Title
Mechanical Evaluation of Polycarbonate Polyurethane for Long-Term Orthopedic Implant Applications

Author
Ford, Audrey

Publication Date
2019

Peer reviewed|Thesis/dissertation

MECHANICAL EVALUATION OF POLYCARBONATE POLYURETHANE FOR LONG-TERM ORTHOPEDIC IMPLANT APPLICATIONS

By

Audrey Christine Ford

A report submitted in partial satisfaction of the

requirements for the degree of

Doctor of Philosophy

in

Engineering - Mechanical Engineering

at the

University of California, Berkeley

Committee in charge:

Professor Lisa Pruitt

Professor Tony Keaveny

Professor Ting Xu

May 2019

Mechanical Evaluation of Polycarbonate Polyurethane for Long-Term Orthopedic Implant Applications

Abstract

Mechanical Evaluation of Polycarbonate Polyurethane for Long-Term Orthopedic Implant Applications

By Audrey Ford

Doctor of Philosophy in Engineering – Mechanical Engineering
University of California, Berkeley
Professor Lisa Pruitt, Chair

There are currently over 2 million total joint replacement procedures completed every year worldwide. The number of total joint replacement procedures is predicted to grow. At the same time, the percentage of younger, more active patients undergoing joint replacement procedures is also predicted to increase. Such predictions motivate a need for joint replacements to last longer and perform better in more active patients. The greatest challenge for current joint replacement device designs is wear-related failures. One potential solution to improve wear performance is to use alternative materials with superior wear performance. Polycarbonate polyurethane (PCU) has been proposed as an alternative material to improve the performance of joint replacements. It is softer and more elastomeric than the current standard polymer, ultra-high molecular weight polyethylene. It has been hypothesized that, due to its lower elastic modulus, PCU will have improved lubrication performance, reducing wear. Historically, improvement to ultra-high molecular weight polyethylene wear performance has come at the expense of fracture resistance. Therefore, in the highly cyclic loading environment of a total joint replacement, the fatigue and fracture properties are also important to consider.

This thesis evaluated the long-term mechanical performance of PCU in orthopedic implant applications. First, we characterized the fatigue crack growth mechanisms in PCU as a function of loading, frequency, hydration, and thermal annealing treatment. We found highly time-dependent behavior as mechanisms of crack growth and failure changed with loading regime. Second, we looked at changes in the structural organization of PCU as a function of thermal treatments and strain. We found trends of increasing ductility with increasing annealing temperature and increasing hydrogen bonding in the ordered hard domain. The amount of hydrogen bonding decreased with increasing strain. Finally, we used an 3D-transient elastohydrodynamic lubrication model to characterize the lubrication regimes in PCU during a simulated gait cycle. Our model contradicts the optimistic predictions of 1D-steady state modeling and may explain the disconnect between early modeling and the experimental wear results for PCU. Moving forward, this work serves as a foundation for many questions that still need to be answered to understand the fatigue, fracture, and tribological performance of this complex material in long-term clinical implant applications.

Acknowledgments

I would like to acknowledge the following people for the support in this research: Professor Lisa Pruitt and the Medical Polymer Group; the larger Berkeley Biomechanics group for collaboration and camaraderie; Dr. Farzana Ansari and Noah Bonnheim for fatigue testing expertise; Samuel Li, Alexandra Belinski, Jessica Sov, Emile Givental, Shan Zhu, and all of the undergraduate assistants that contributed to this work; Dr. John Zupancich of DSM Biomedical Inc. for donating Bionate® material to the project and access to compression molding equipment; Dr. Teresa Chen at Lawrence Berkeley National Labs Molecular Foundry for access to and support with DSC measurements; the Institute for Polymer and Medical Engineering (Medtech) at the Technical University of Munich for hosting me, equipment access, and polymer processing experience and especially to Maximilian Wardenberg for lessons in gratitude; Dr. Ralf Stehle at TU Munich for the SAXS measurements; the Lab of Orthopedic Technology and Professor Stephen Ferguson at ETH Zurich for hosting me and support with computation; Dr. Leiming Gao for collaboration with the EHL model and her support of this project; and Hannah Budinoff, Sarah Frank, and Julia Kramer for their support and review in writing this dissertation.

I would also like to recognize my friends and family for getting me through. I have a wonderful family.

And thank you Pit.

Contents

Chapter 1

Polymers in Total Joint Replacement

1.1 Thesis Overview

The aim of this thesis is to evaluate the mechanical performance of polycarbonate polyurethane with respect to its use as a bearing material in total joint replacements. The first chapter presents a background of total joint replacement (TJR), the current polymers used, and introduce polycarbonate polyurethane (PCU) as a novel material for orthopedics. To motivate the importance of TJR and the need for better material to meet the increasing demand for longer-lasting implants, we begin with the clinical pathology and current treatments. First we introduce the native tissues that are replaced in total joint replacement, the pathologies that lead to the need for total joint replacement, the current treatments, and the materials that are used in total joint replacement. This background will outline the design requirements of total joint replacement, past developments of ultra-high molecular weight polyethylene (UHMWPE), the current gold-standard polymer in the field, and current challenges that limit the current device design, like implant wear. Alternative materials, like PCU, have been proposed as potential solutions to address the wear related challenges and move towards longer lasting implants. The chapter will conclude by introducing the material at the center of this thesis, polycarbonate polyurethane, its properties, and its current uses and performance in orthopedic applications.

The second chapter will present a study on the mechanisms of crack growth in PCU. The chapter first reviews the approaches to fatigue characterization, total-life fatigue and defect-tolerant fatigue. A defect-tolerant approach to fatigue was used for the study, so the linear elastic fracture mechanics theory behind the methods will be introduced. The study evaluates the impact of loading regime, frequency, conditioning, and thermal annealing on the mechanisms of crack growth in PCU. The results of this study led to the hypothesis that structural changes to PCU in the highly constrained crack tip led to highly time-dependent crack growth behavior.

The third chapter seeks to test this hypothesis by exploring the impact of strain on the structural organization of PCU. The chapter reviews the polymer chemistry that drives the phase separated structure of PCU block copolymers and the range of variables that influence the structure. Differential scanning calorimetry, Fourier transform infrared spectroscopy, and small angle X-ray scattering were used to characterize the impact of thermal annealing and strain on the structural organization.

The fourth chapter uses a computational model to predict the lubrication regimes in order to understand the wear performance of PCU in orthopedics. The studies that motivated the interest in more compliant materials in orthopedic applications are reviewed and compared to the experimental wear studies that have been published. The theory of EHL is presented along with its applications to orthopedics. We present a 3D-transient EHL model of PCU compared to UHMWPE acetabular cups.

Finally, the fifth chapter will conclude the thesis and discuss future directions for the research. To motivate the need for improved polymers in TJR, we will begin with the native joint and joint pathologies.

1.2 Articular Cartilage and the Intervertebral Disc

This chapter will provide an overview of the native structure and function of the joints that are currently repaired with total joint replacement, the disease states that lead to the degradation of healthy joints, introduce the methods for repairing diseased joints, and introduce the materials used in total joint replacement to motivate the engineering requirements of orthopedic biomaterials. The musculoskeletal system is the structure that provides protection and motion for the human body. The musculoskeletal system is composed of bones, muscles, and soft tissue. The bones provide structure, the muscles actuate motion, and the soft tissue forms the various types of junctions: tendons connect muscle to bone, ligaments connect bone to bone, and cartilage forms soft structures, complex joints, and cushions bone to bone articulating joints, most generally classified as synovial joints.

Synovial joints compose the articulating joints of the body that provide motion and stability such as knees, hips, shoulders, knuckles, etc. Typically, these joints are categorized as ball-and-socket joints (e.g. hips), hinge joints (e.g. knees), or sliding hinge joints (e.g. shoulders, ankles, wrists) based on their mechanism of motion transfer. Synovial joints provide the relative motion of two bones through the articulation of articular cartilage within a synovial capsule. Articular cartilage covers the surface of the bones to create a bearing surface of all types of synovial joints.

Articular cartilage is a particular type of cartilage that creates the bearing surface for articular joints. More generally, cartilage is a class of soft tissue in joints and structural roles such as the nose, ears, and trachea. The intervertebral disc is cartilage-like and categorized as soft tissue, but has a different and more complex structure than other types of cartilage and sustains more complex loading than other types of cartilage. For that reason the IVD will be discussed separately. Hyaline cartilage is the class of cartilage that plays a structural role such as the nose. However, it does not have the ordered structure that gives articular cartilage the load bearing properties for joints.

1.2.1 Articular Cartilage

The structure of articular cartilage is complex. Articular cartilage is composed of up to 85% water by weight in the most superficial 25% of the tissue and then the percentage of water decreases to 70% near the bone interface [1]. Articular cartilage then contains an extra cellular matrix of approximately 50% collagen and 20-30% proteoglycans by dry weight [1]. The proteoglycan molecules are charged and provide an attractive potential for water absorption into the tissue within the constraining network of collagen fibers creating a pressurized porous matrix.

Collagen provides structure and tensile strength of the tissue and is organized as shown in Figure 1.1. Near the surface, in the superficial zone, collagen fibrils are aligned in parallel to the articulating surface. Moving into the tissue, in the middle zone, the collagen fibrils become randomly ordered and then, as the articular cartilage joins with the underlying bone, in the deep zone, the collagen fibrils align perpendicular to the articulating surface as the material composition becomes more bone-like with the tidemark delineating the transition from cartilage to bone. The transition of collagen structure with depth results in a corresponding transition in the mechanical properties of the tissue [2].

The synovial capsule isolates the joint and synovial fluid provides both lubrication and nutrients for the cartilage. Upon loading, the absorbed water is pushed out of the extra cellular matrix of the cartilage to create a new equilibrium pressure [1]. and a pressurized fluid lubrication layer is created resulting in an extremely low coefficient of friction. Healthy synovial joints, such as the hip and knee, maintain near frictionless articulation for decades through the function of articular cartilage. The coefficient of friction of human articular cartilage has been measured as 0.001 - 0.03 which is an order of magnitude below that of glass (0.15 - 0.35) [3].

Cartilage lacks nerves. This lack of nerves in cartilage allows for load transfer without pain. Consequently, the loss of cartilage leads to pain as the innervated bone begins to bear the load. Cartilage is also an avascular tissue. As an avascular tissue, a tissue without a blood supply to bring nutrients, cartilage relies on diffusion of nutrients from the synovial

fluid. Chondrocytes, cartilage cells, are present in a very low density compared to other tissues and at maturity (1% of tissue volume). Without a blood supply and at such a low density, chondrocytes have minimal remodeling and produce little new tissue, leading to an inability to heal. Therefore when cartilage is damaged or diseased over time, there is a need for surgical repair interventions to alleviate pain because healing in cartilage is minimal [2, 4].

Similar to articular cartilage, the intervertebral disc (IVD), does not have the capacity to self-repair and surgical intervention is needed to treat degeneration. However, the structure of the IVD is unique within the classification of soft tissues due to the unique load transfer requirements of the spine.

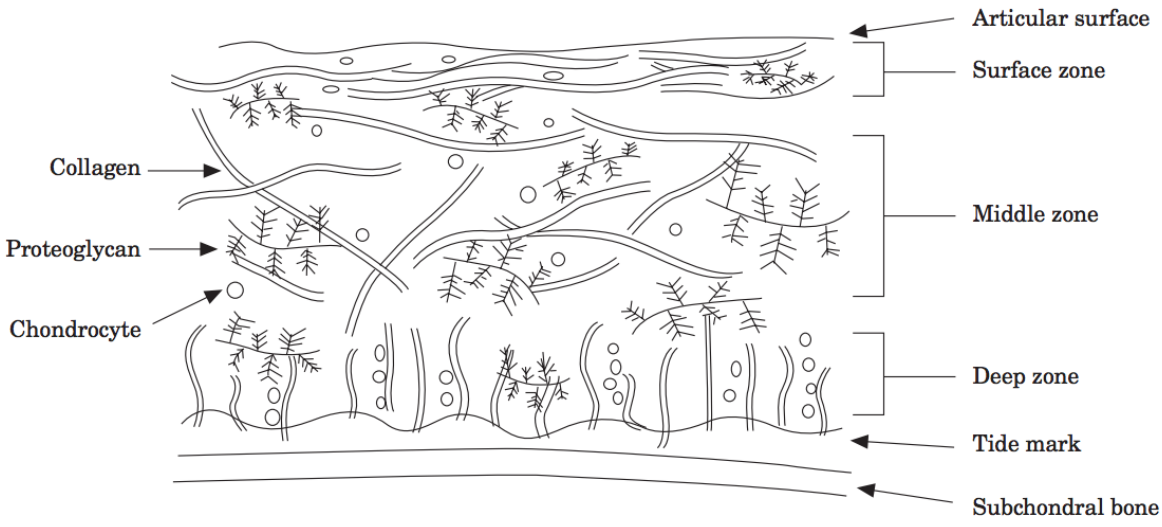

Figure 1.1: Articular cartilage is composed of chondrocytes (1% by volume), proteoglycans (20 - 30 % by dry weight), and collagen (50% by dry weight). The collagen is oriented parallel to the articular surface in the surface zone, becomes randomly oriented in the middle zone, and then orients perpendicular to the surface at the tidemark where the articular cartilage transitions to bone. Reprinted from [5], with permission from Elsevier.

1.2.2 Intervertebral Disc

The intervertebral disc is the tissue that separates each vertebral bone in the space and acts to join the spine, absorb load, and allow for spinal movement [6]. Compared to articular joints were the two bones are articulating in a joint, the IVD spans the entire junction between each vertebral bone in a continuous tissue. The intervertebral disc is type of cartilaginous tissue that is uniquely classified due to its more complex structure. The intervertebral disc is structurally more complex due to the complex loading of the spine. The IVD is composed

of an annulus fibrosis (AF), the outer donut, and the nucleus pulposus (NP), and is joined to a vertebral body on the top and bottom by an end plate (Figure 1.2).

The composition of each component changes with location of the disc within the spine as well as age [7]. The annulus fibrosis is composed of 75-90% collagen in the outer region, 40-75% collagen in the inner region, 10% proteoglycans in the outer region by dry weight, 20-35% proteoglycans in the inner region by dry weight, and 65-80% water by wet weight [6]. At maturity the AF contains 9 x 10^6 cells/cm^3 [7]. The collagen fibers are organized into 15-25 rings in which the collagen fibers are organized at an angle between 62 to 45° from vertical in alternating directions with each concentric ring moving from the outer to inner layers [6, 8]. This complex organization provides resistance to the expansion of the disc upon compression as well as well as tensile strength in bending.

The nucleus pulposus is composed of 25% of collagen by dry weight, 20 - 60% of proteoglycans by dry weight, and 75 - 90% water by wet weight [6]. At maturity the NP contains 4 x 10^6 cells/cm^3 [7]. It is a much more gelatinous material which absorbs load and exudes water under compression. With age the water and proteoglycan content of the IVD decreases with the majority of that loss occurring in the NP [7].

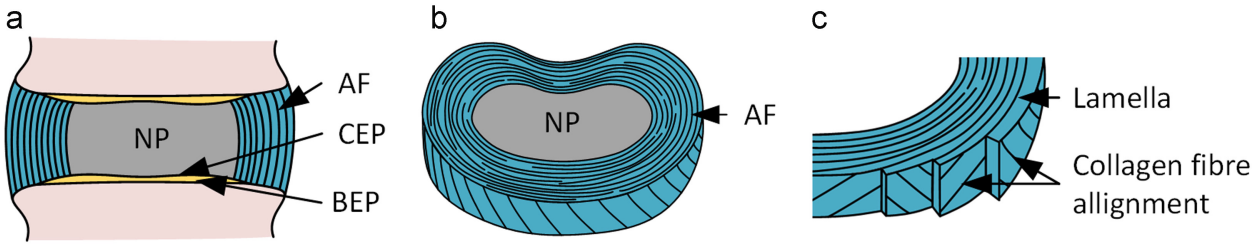

Figure 1.2: The intervertebral disc is a highly ordered cartilage-like structure that provides motion between two vertebra in the spine. It is a disc-like structure that is composed of an outer ring of annulus fibrosis (AF) and an inner, gel-like nucleus pulposus (NP). The annulus fibrosis has lamella of alternating collagen fibers that provide tensile resistance to the pressurization of the nucleus pulposus under load. The disc is joined to the adjacent vertebrae with a cartilaginous and bony end plate (CEP/BEP). Reprinted from [8], with permission from Elsevier.

Similar to articular cartilage, the IVD is avascular and has a low cell density. Due to this, it has an inability to heal and repair following damage. Due to this inability to repair, degeneration of articular cartilage and the IVD, osteoarthritis and degenerative disc disease respectively, lead to a crippling lack of mobility and need for surgical repair and total joint replacement.

1.2.3 Articular Cartilage and Intervertebral Disc Pathologies

Damaged articular cartilage can be classified into three main types: rheumatoid arthritis, osteoarthritis, and traumatic damage. Rheumatoid arthritis is the breakdown of cartilage caused by irregularities in synovial fluid production. Osteoarthritis is the umbrella pathology for the degradation of articular cartilage and is prevalent in over 80% of people aged over 80 years [9]. Damage to the cartilage caused by trauma can occur through any number of joint injuries [10]. It was reported in 2008 that arthritis effects approximately 21% of adults in the US [11]. Native cartilage is not innervated and therefore articulation is pain free. But, during the degradation of articular cartilage and loss of healthy function, load is passed to the innervated bone with a painful result. Severe degradation can result in severely limited motion and even complete lack of activity.

The pathologies that impact the intervertebral disc include: degenerative disc disorder, herniation, and a more general category of lower back pain. Lower back pain affects over 80% of the population [6], but the mechanisms are not well understood. Degenerative disc disorder (DDD) describes the loss of function of the disc. DDD is primarily age related. The nucleus pulposus looses its ability to absorb water and becomes stiffer, and more load is taken up by the annulus fibrosis. Excessive load on the AF can lead to failure and herniation. Herniation occurs when there is a tear or defect in the annulus due to degenerative effects or injury that causes the nucleus pulposus to exude into the spine space. The extruded NP can impinge on nerves and cause pain.

When herniation occurs, there is a clear cause of pain, but lower back pain, as it relates to the degeneration of the intervertebral disc is not well understood. Cases exist with severe degeneration and no back pain while other cases without degeneration or herniation and back pain are reported. Because of the highly complex loading environment of the spine in addition to the high sensitivity of the spinal column to nerve impingement and pain, the pathologies of the spine are not as well understood as those of the synovial joints.

Articular cartilage and the IVD do not have the ability to repair. Therefore, osteoarthritis and DDD must be treated with surgical interventions. The clinically available treatments seek to restore native kinematics and return the patients to mobility. The surgical repairs require engineering materials that can withstand the biological and mechanical demands of the joint function.

1.3 Treatments for Joint Pathologies

In the case of both articular cartilage and the intervertebral disc, the traditional replacement techniques that will be described below do not offer a biomimetic solution to replicate

native tissue structure and function. Rather they employ metals, polymers, and ceramics with vastly different material properties to the native tissue and seek to purely recreate the mechanical function with respect to pain free movement. Total joint replacement is a highly invasive procedure that removes a large amount of native tissue. Therefore, it is only used in very serious cases of debilitating pain. Before turning to TJR, there are other grafting techniques used for small areas of damage or injury. A large research effort in tissue engineering is in progress to restore or replicate the healthy function of the cartilage tissue. However, few tissue engineering solutions have been widely adopted in clinical use.

1.3.1 Total Joint Replacement

The leading standard for treating damaged or degraded articular cartilage is total joint replacement (TJR). TJR was first developed by Sir John Charnley in the 1960s [14, 15, 10]. Today the number of total joint replacements (knee and hip) performed per year numbers between 2 - 3 million worldwide. Device success is reported to be 88% at 10 years for both total hip and total knee replacements [14]. The number of joint replacements is projected to increase with the aging population in the US and Europe (Figure 1.3) [12]. Additionally, it is projected that an increasing number of joint replacements will be done on younger patients (Figure 1.4) [13]. This is driving a demand for devices to withstand the higher loading demands of younger, more active patients, and last longer to avoid multiple revisions during the lifetime of the patient. Therefore, great effort is being made to improve the performance and longevity of the implants.

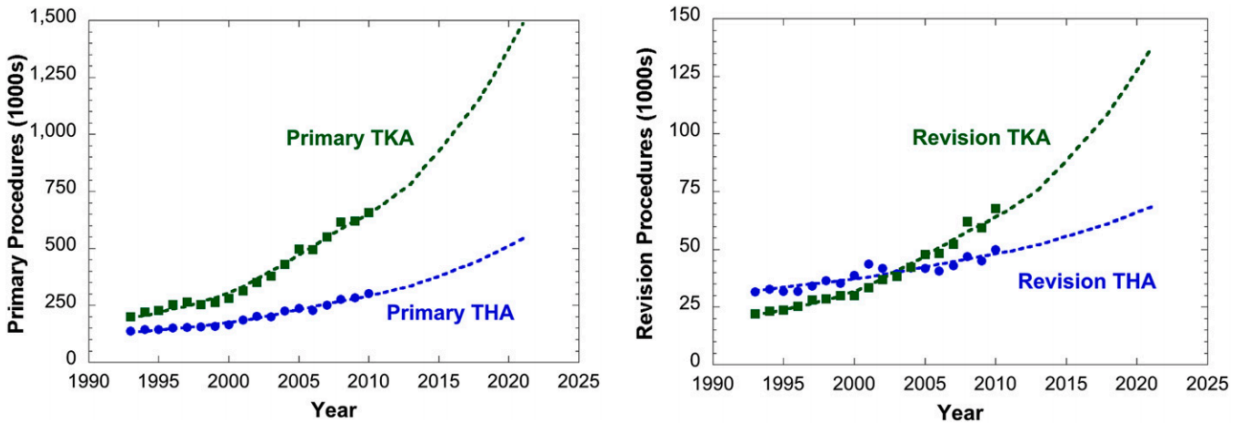

Figure 1.3: The demand for total joint arthroplasty is predicted to increase in the future. This is driving the demand for innovation to make implants last longer under greater loads to meet this increasing demand. Reprinted from [12], with permission from Wolters Kluwer Health, Inc.

The most common joint replacement are, in descending order, hips, knees, spine (IVD), shoulders, elbows, and ankles [10]. Although joint implants are as varied as the anatomy

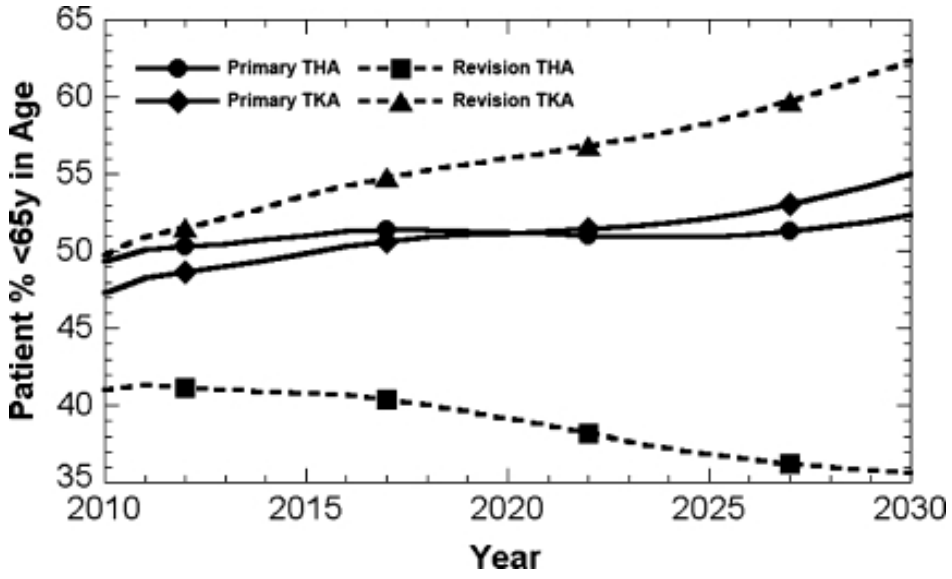

Figure 1.4: In combination with the increasing predicted number of total joint replacements, the percentage of total joint replacements, especially total knee replacements, in patients younger than 65 is expected to increase. Reprinted from [13], with permission from Wolters Kluwer Health, Inc.

that they replace, the materials used are common across most designs. Due to the highly regulated nature of the medical device industry, the materials used are limited a few well studied materials, in the United States, with FDA master files, or other past documentation in other international regulatory agencies. Each design consists of an articulating surface on a bearing material. Common designs include metal on polymer, ceramic on polymer, ceramic on ceramic, and metal on metal. Articulating metals are typically a cobalt chromium alloy [10], ceramics are typically alumina or zirconia [16], and the dominant polymer is ultra high molecular weight polyethylene. These materials are selected to withstand the wear and fatigue loading incurred within the joint. However, when compared the native tissues, the mechanical properties of these materials are orders of magnitude different from that of biological tissue (Figure 1.5).

The geometries and loads of the individual joints lead to a unique stress state in the materials. The conforming geometry of the hip creates low stresses in the range of 2 - 5 MPa, while the less conforming geometry of the knee sees much higher stresses in the range of 20 - 40 MPa [10, 17]. These loads can be highly variable due to the gross heterogeneity of patient's anatomy and gait, device design, and variability caused by surgical techniques such as placement and sizing. The cyclic nature of the stresses must also be considered when evaluating material performance in a given application. In line with the cyclic nature of the stresses, the tribological properties of the materials must also be considered.

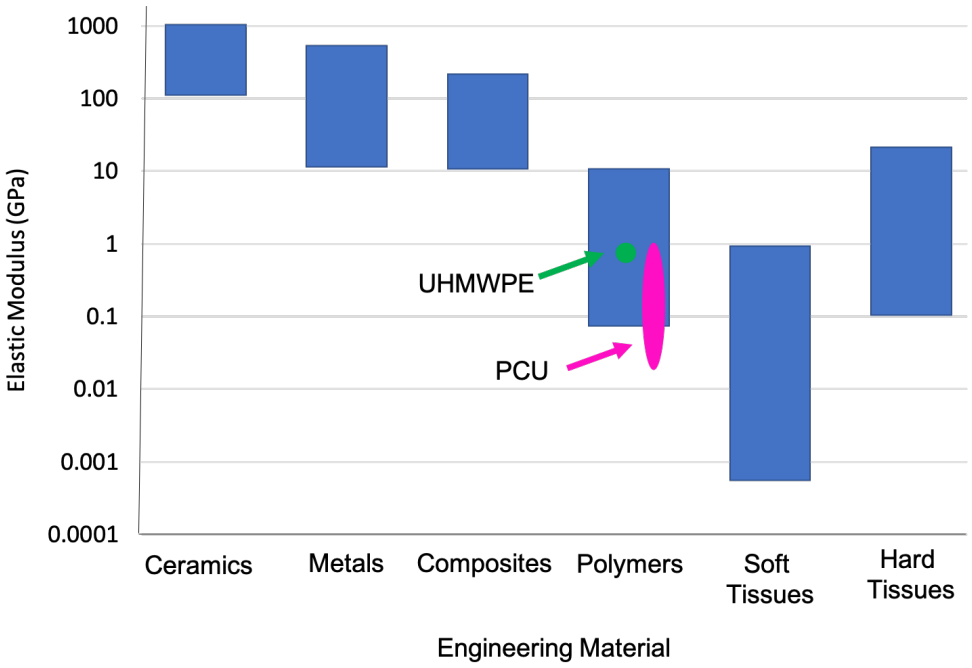

Figure 1.5: Traditional materials used in total joint replacement, ceramics, metals, and UHMWPE (green dot), have moduli orders of magnitude higher than the majority of biological tissues. However, the modulus of PCU (pink oval) can be tuned to better match the moduli of biological tissues. Adapted from [10]

Beyond the mechanical demand on the materials in orthopedic implants, the material must also be biocompatible. Biocompatibility of the bulk material is evaluated by a series of well regulated tests outlined by ISO 10993 (2018): 'Biological Evaluation of Medical Devices' [18]. The strict biocompatibility standards for implantable materials limits the number of materials that can be used in device design. And even those materials that are approved by regulatory bodies for use face challenges with immune response and adverse biological reaction. In orthopedic implants, the size scale of materials plays a large role. The biologic response to small wear particles has proven to be a limitation of device life [19].

Causes of Failure in Total Joint Replacement

Hard-on-hard couple designs (metal on metal and ceramic on ceramic) have the lowest wear rates, followed by ceramic on highly crosslinked UHMWPE, metal on highly-crosslinked UHMWPE, and then ceramic and metal on untreated UHWMPE show the worst wear rates (Table 1.1, Figure 1.6) [20]. Although ceramic and metal couples have better wear performance, UHMWPE couples are still preferred in certain applications. In the case of metal on metal implants, small scale metallic wear particles have been correlated to adverse systemic responses [21, 22]. Ceramic implants have faced challenges of rare, but catastrophic fractures.

Newer formulations are less prone to fracture, but remain more expensive than UHMWPE designs. Ceramic on ceramic implants also have a low, but unpredictable incidence (0.7 - 2.9 %) of audible squeaking [14]. In polyethylene implants, wear particles remain more localized within the joint capsule. However, the wear particles begin a biological cascade that has been shown to lead to osteolysis, or bone resorption, inflammation, device loosening, and ultimately cause the device to fail [23, 24, 25].

Table 1.1: Wear rates for different bearing couples in orthopedic implants [20].

Bearing couple	Wear rate ($\frac{mm^3}{10^6 cycles}$)	
	Ceramic	Metal (CoCr)
UHMWPE	1 - 63	14 - 201
Highly Crosslinked UHMWPE	0 - 7	0 - 11.7
Ceramic	0 - 5	-
Metal (CoCr)	-	0.2 - 25

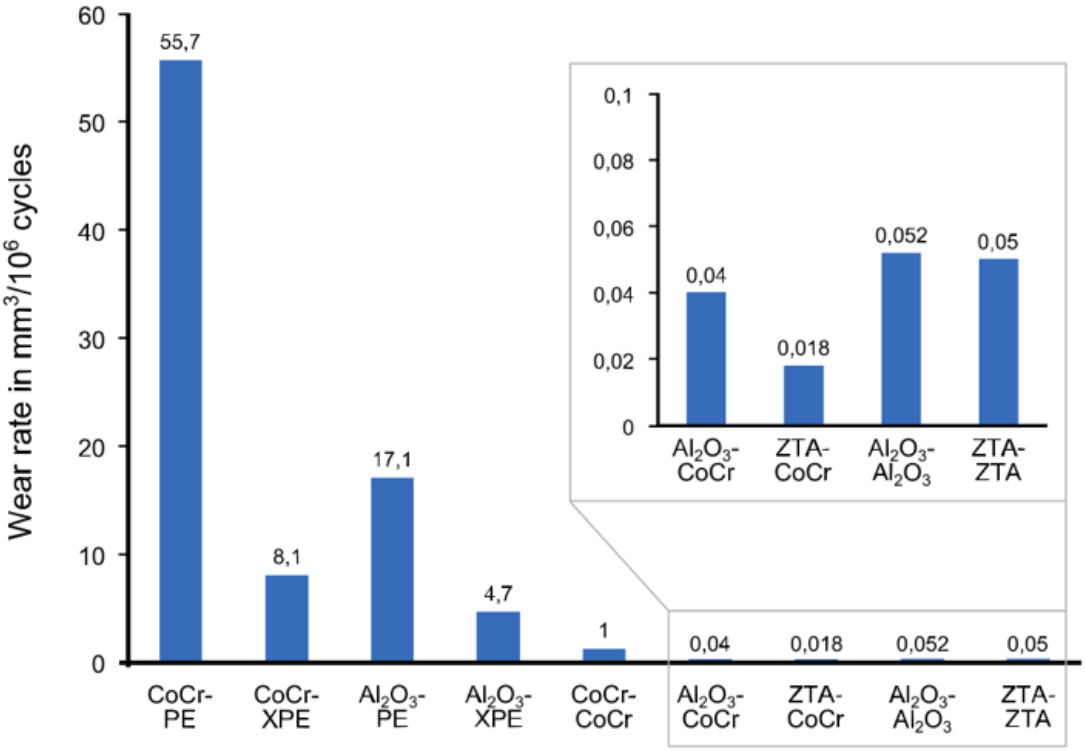

Figure 1.6: Wear rates for polyethylene (PE) and metal (CoCr) are significantly higher than that of polyethylene and ceramic (Al_2O_3). Crosslinking (XPE) greatly improved the wear rate of polyethylene, but all polyethylene combinations are much higher than the hard on hard combinations of metal and ceramic (CoCr, Al_2O_3, ZTA). Reprinted from [14], with permission from Elsevier.

1.3.2 Autonomous and Autologous Grafting Treatments

A small defect in the cartilage leads to an increased risk for development of osteoarthritis. Damage to one area of cartilage creates a cascade of altered load bearing and wear that accelerates the degradation of surrounding cartilage. Therefore, early treatment of small defects is an effective way to reduce the risk of osteoarthritis and avoid the need for an early total joint replacement.

For treatment of local defects, autonomous and autologous grafts have shown positive results, but are limited by tissue availability [2]. Grafts are taken from undamaged regions or donor tissue and pressed into a damaged region. The osteochondral autograft transfer (OATS) technique takes one large graft or several round biopsy punches (called mosaicplasty) of healthy cartilage and presses them into a defect (Figure 1.7) [26, 27]. Autologous chondrocyte implantation (ACI) is a technique in which the patients stem cells are cultured and then injected into the defect. A cover is required to hold the stem cells in place [28].

Another commonly used technique is micro-fracture. The process of micro-fracture punches down through the damaged cartilage to the underlying bone to release marrow derived stem cells into the defect [29, 30]. These stem cells create fibrocartilage tissue. The resultant tissue is cartilage-like but it has the unorganized structure of scar tissue and cannot function as the surrounding cartilage. Many studies have evaluated these methods and they all have positive outcomes although microfracture has shown to have worse outcomes with larger defects [28].

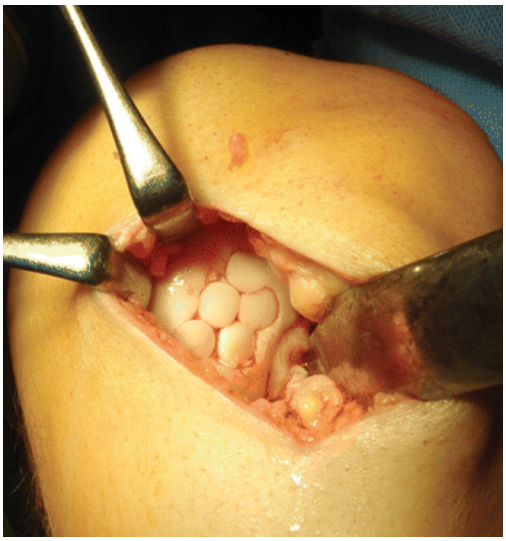

Figure 1.7: Example of mosaicplasty repair of a focal osteochondral defect. Reprinted from [26] with permission Sage Publishing.

Although successful in the short-term at repairing a small defect, these grafting procedures do not identically recreate the structure and mechanical function of the native cartilage. The challenges of tissue availability for grafting and poor mechanical function of repaired tissue motivates a need for better repair techniques for small defects and damaged cartilage to slow the progression of osteoarthritis or degeneration and delay the need for TJR. Researchers have long targeted cartilage for tissue engineering therapies. They aim to create a viable cartilage structure *ex vivo* that can be implanted to provide the mechanical function of native cartilage.

1.3.3 Tissue Engineering

Articular cartilage has long been a target of tissue engineering because of its relatively low cell density, simple structure, and avascular nature. Tissue engineering strategies are focused on using a range of cell sources from juvenile bovine and adult canine chondrocytes, to autologous, self-sourced, human chondrocytes, and mesenchymal stem cells from adipose, bone, or

synovium. The cells are then cultured *in vitro* or *in vivo* as pellet cultures or in conjunction with a matrix structure to encourage matrix synthesis to achieve native properties [31, 32].

More recently, 3D bioprinting techniques have shown promise for controlled production of highly complex tissues [4, 2]. A combination of growth factors and biophysical stimuli further contribute to the production of optimized tissues [4]. Native levels of glycosaminoglycans and compressive mechanical properties have been achieved, but collagen production remains a challenge. Additionally, when constructs are scaled up ($>$ 4 mm diameter), nutrient diffusion into the center of the construct becomes increasingly inhomogeneous. This nutrient gradient leads to inconsistent matrix production with more matrix deposited on the outside of the scaffold than in the center. Different methods to address the limitation of nutrient diffusion include: macro-channels introduced after casting the scaffolds, dynamic loading of the scaffolds, and perfusion of media during culture, and modular manufacturing techniques [31, 33, 34, 35].

Modular manufacturing techniques are one strategy to address the challenge of scaffold size being limited by low nutrient diffusion. As demonstrated by Ford et. al., modular fabrication exploits the well-known affinity of tissue engineered constructs to stick to each other in culture. Initially, small diameter constructs are cultured individually to promote access to nutrients. After 14 days of culture, constructs are then placed in 3D printed molds (porous baskets) to encourage the formation of controlled bonds between the constructs which strengthened throughout the culture period. This process automatically leaves channels between the bonds in the constructs maintaining nutrient channels in the bonded surface [35]. These channels were observed to remain open for longer throughout culture compared to channels that had been punched into large bulk constructs at the beginning of culture [33].

This technique was further shown to be extrapolated to create patient specific geometries. Molds were 3D printed based on a CT scan on a human tibial plateau. Then a modular surface 950 mm^2 was created based on that patient geometry. The modular approach produces a construct that is similar in composition to the clinically used mosaicplasty technique in which multiple round punches of grafted tissue are pressed into a focal defect [26, 27].

Although promising results have been shown, the clinical translation of this technology is not yet widely successful. Some technologies have been approved at varying levels for clinical use. The following tissue engineered cartilage therapies are available at various stages of clinical trials and use: BioCart®II (Histogenics, Waltham, MA), Bioseed®-C (BioTissue Technologies GmbH, Freiburg, Germany), CaReS® (Arthro Kinetics Biotechnology, Krems, Austria), Cartipatch® (Tissue Bank of France, Lyon, France), Chondrosphere® (co.don AG, Teltow, Germany), Hyalograft® C (Anika Therapeutics, Bedford, MA), INSTRUCT, MACI (MACI; Vericel, Cambridge, MA), NeoCart® (Histogenics, Waltham, MA), NOVOCART® 3D (TETEC, Melsungen, Germany) , and RevaFlex™/DeNovo® ET (Isto Technologies, St. Louis, MO). Challenges remain in developing a reliable cell source, understanding the in-

teractions between the native tissue and scaffold, understanding construct development and functional biomechanics, and improving fixations methods. Additionally, large regulatory hurdles exist for these novel repair methods [36].

Tissue engineering and grafting techniques focus on focal defect and small areas of injured or damaged cartilage and do not address the challenge of degradation of the entire cartilage surface. Tissue engineering solutions for full joint degradation are even further from clinical translation. Therefore, a parallel effort to improve the well established total joint replacement technologies is important to proceed in parallel to the tissue engineering strategies with an unknown timeline to clinical application.

1.4 Polymers in TJR

Total joint replacement continues to be the most successful treatment for severe osteoarthritis. Historically, UHMWPE replacements have been the most commonly implanted devices and continue to be the gold standard by which new designs will be evaluated against.

1.4.1 UHMWPE

The primary polymer used in TJR is ultrahigh molecular weight polyethylene (UHMWPE). The first hip implants, performed by Sir John Charnley in 1959, utilized a polytetrafluoroethylene bearing surface to provide a low friction surface. These early implants failed due to creep, wear, and resulting immune response. However, Sir John Charnley succeeded in the 1960's, using UHMWPE, which has become the industry standard. Total knee replacements soon followed in the 1970s by adopting an UHMWPE bearing surface for a sliding joint that replaced the fully constrained joint designed in the 1950's [10]. Since then, a great deal of research on UHMWPE has gone into understanding the complex trade-offs between material performance, biological response, and longevity of the implant.

UHMWPE is a homopolymer with identical chemistry to the lower density polyethylenes commonly used in consumer products (carbon backbone with hydrogen side units). However, compared to low density polyethylene, which has a molecular weight of 30,000 - 50,000 g/mol, UHMWPE has a molecular weight of 2 - 6 million g/mol (density = 0.925 - 0.935 g/cm^3). The long polymer chains of UHMWPE organize into a semicrystalline structure with ordered lamellar structures within amorphous regions (Figure 1.8). The percent crystallinity of UHMWPE ranges from 45% to 60% [10]. Two UHMWPE resin types are commonly used in medical applications, GUR 1020 and GUR 1050. They differ in their molecular weights, 2-4 million g/mol and 4-6 million g/mol for 1020 and 1050 respectively. At a lower molecular weight, GUR 1020 has a greater capacity to crystallize and therefore a higher degree of

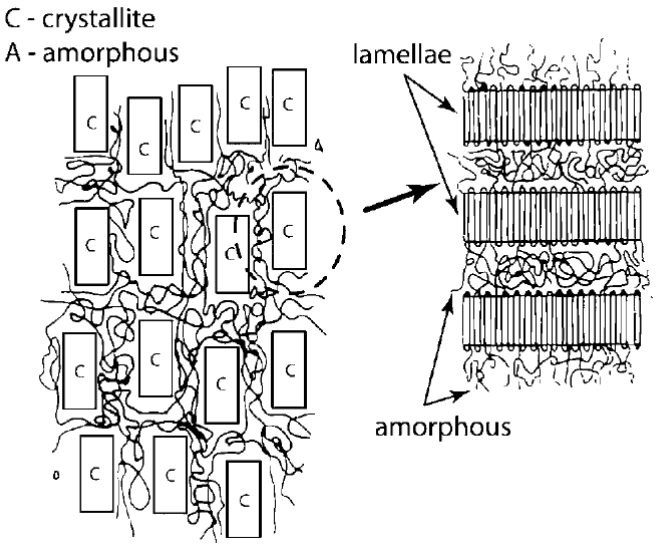

Figure 1.8: UHMWPE is a semicrystalline polymer. Crystalline lamellae (40% to 60%) are surrounded by unstructured amorphous regions. This order plays a large role in the mechanical performance of the material. Reproduced from [10] with permission of Cambridge University Press through PLSclear.

crystallinity. This gives it superior yield strength, modulus, and fatigue crack propagation resistance to that of GUR 1050 [37].

The mechanical properties of UHMWPE are highly dependent on the molecular weight and crystallinity. Semicrystalline UHMWPE typically has a modulus on the order of 1 GPa, a yield strength of 20 MPa, and an ultimate strength of 30 MPa as well as favorable energetic toughness and a low coefficient of friction that contribute to its success in orthopedic implants [10]. However, the microstructure of UHMWPE, dictated by the degree of crystallinity, drives the performance of the material as it relates to wear, fatigue crack growth, and oxidation.

Understanding the connection between the material behavior and device performance has been essential in developing successful devices through an improved understanding of the failure mechanisms. Ultimately, the majority of these total joint replacements fail due to 'loosening'. Loosening, a broad descriptor for many failures related to a loss or weakening of the bone around the implant. Loosening has been correlated to the UHMWPE particulate wear debris and the resulting biological inflammatory response [14]. Controlling the wear in UHMWPE and improving its longevity *in vivo* has driven a series of changes to the material composition over its years of use in TJR.

Over its years of use, many changes have been made to UHMWPE to improve the performance of the material in orthopedic devices. Different sterilization methods, manufacturing methods, base resins, and additives have been used. Sterilization methods include gamma radiation in air, ethylene oxide gas sterilization, gamma radiation in inert atmosphere, and gas plasma. UHMWPE implants have been manufactured using ram extrusion and compression molding. Base resins including (1020 and 1050 GUR) have been used and carbon fibers have been included [38]. Each of these changes impact the crystallinity and structure of the material and influence clinically relevant performance parameters such as wear resistance and fracture resistance.

A significant body of research has characterized the tradeoffs between processing changes on the clinical performance of UHMWPE. Crosslinking through gamma irradiation, annealing processes, antioxidant additives, and mechanical deformation have been used to address the wear related concerns of UHMWPE [38]. Although crosslinking (5 - 10 Mrad gamma-irradiation) increased the wear performance of UHMWPE (Figure 1.9), it also caused a loss of oxidative resistance and fatigue crack resistance (Figure 1.10) [37, 38].

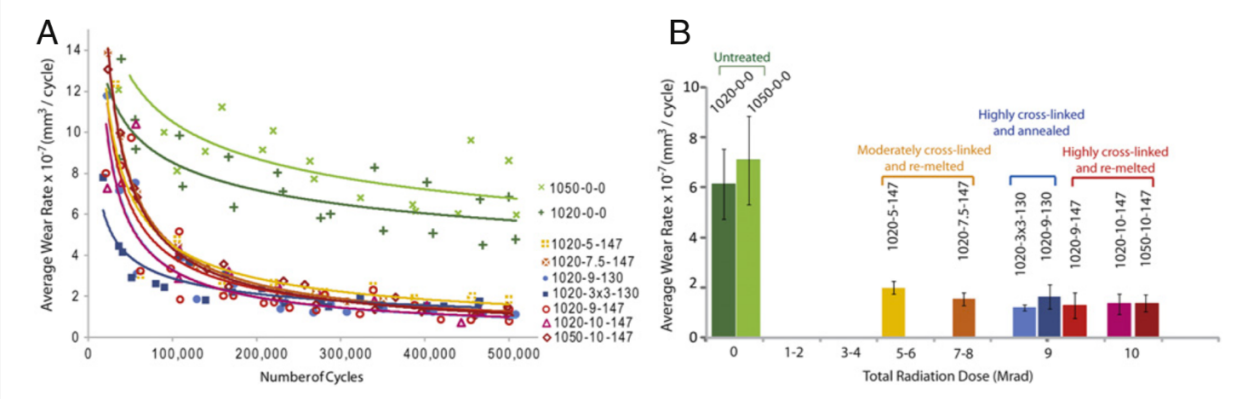

Figure 1.9: Crosslinking with gamma irradiation was shown to improve the wear performance of the UHMWPE. Reprinted from [37], with permission from Elsevier.

Post irradiation annealing processes limited the effect on oxidative resistance, but did not improve the lost fatigue crack resistance [38]. These tradeoffs are driven by the microstructural properties of the material. The crystallinity, quantity and quality of lamellar structures drives these tradeoffs [38] and is central in predicting the impact of future changes to the material on the mechanical performance *in vivo* (Figure 1.11).

As researchers investigate alternative materials for use in TJR, the lessons learned from decades of UHMWPE use must be considered. New materials offer new and interesting properties and potentials. But still, tradeoffs between functional properties must be considered when making alterations to material composition or structure. This must all be taken into

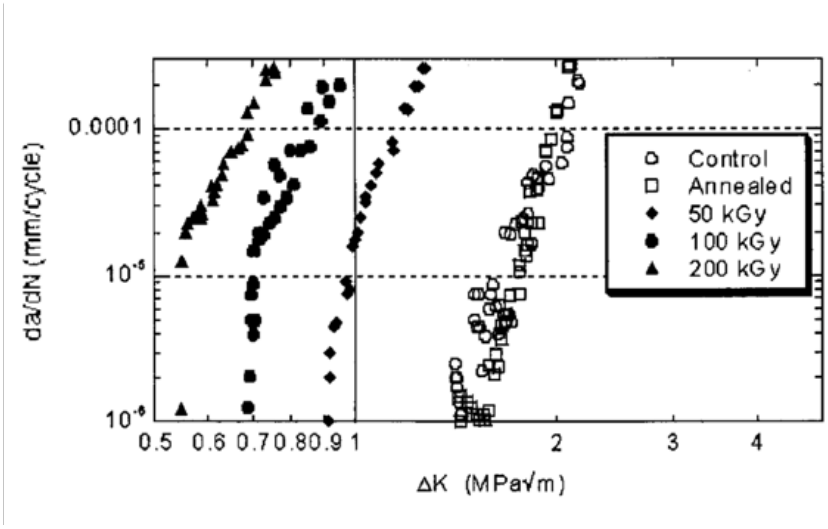

Figure 1.10: Crosslinking through gamma irradiation was used to improve the wear performance of UHMWPE, but led to a reduction in the fatigue crack propagation resistance, requiring a lower cyclic stress to drive an equivalent crack growth rate and shifting the da/dN vs ΔK curve to the left. Reprinted from [39], with permission from Elsevier.

account within a scope of long-term, high-cycle use *in vivo*.

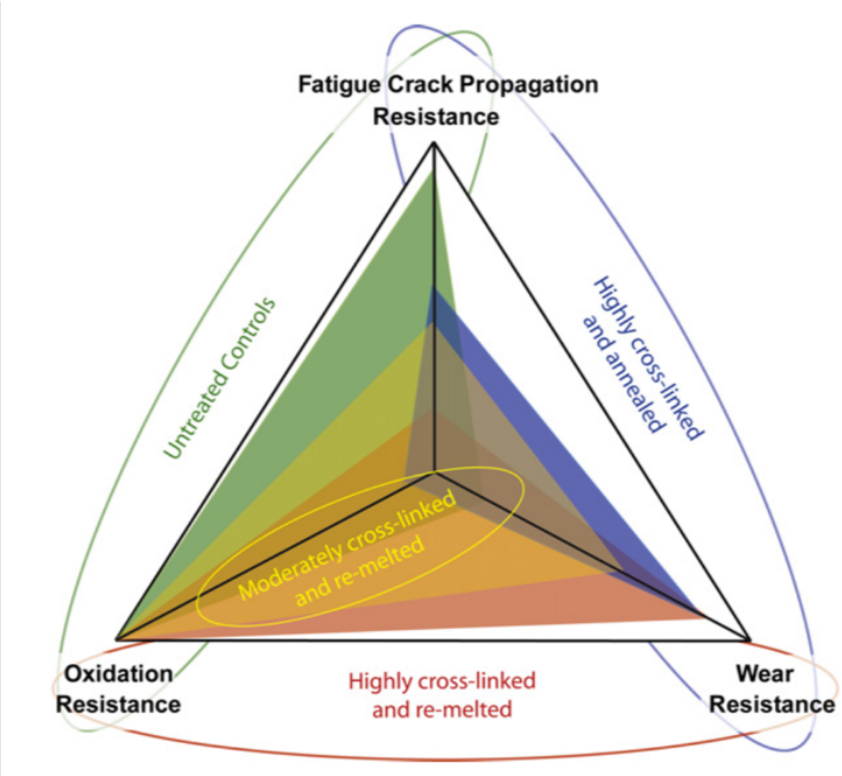

Figure 1.11: As UHMWPE treatments and compositions were changed and developed over the years, the performance results showed a tradeoff between oxidation resistance, wear resistance, and fatigue crack propagation resistance. An improvement in one typically led to a reduction in one or two of the others. Reprinted from [37], with permission from Elsevier.

1.4.2 Alternative Materials to UHMWPE in Total Joint Replacement

With the success of TJR, there is a demand for implants that last longer and perform under higher loading situations. It is projected that now over half of patients receiving total hip and total knee replacements and revisions are under the age of 65 [13]. In order to meet this rising demand, designs that address the current failure mechanisms, such as wear, must be found. Alternative materials and coatings have been the main focus of the effort to improve the longevity and load capacity of total joint replacements.

Current alternatives to UHMWPE bearing surfaces can be grouped into surface modifications or coatings and new bulk materials [14]. Surface modifications and coatings include diamond-like carbon, nano-crystalline diamond, pyrolytic carbon, nitrated and carbonated surfaces, surface oxidized zirconium, and oxidized titanium. New bulk materials include non-oxide ceramics, carbon fiber reinforced PEEK, polyurethane, and hydrogels. Based on an evaluation of use in other fields, *in vitro* evaluation, clinical use, chemical stability, and

mechanical stability, the leading alternatives were reported in a review by [14] to be nitrated and carbonated surfaces, surface oxidized zirconium, and polyurethanes (Figure 1.12). In evaluating the performance of hard on soft implant designs, the former two alternatives are surface modifications or coatings that increase the wear resistance of the hard articulating surface. The use of polyurethane was found to be the most promising polymeric alternative to UHMWPE as a new soft bearing surface material [14].

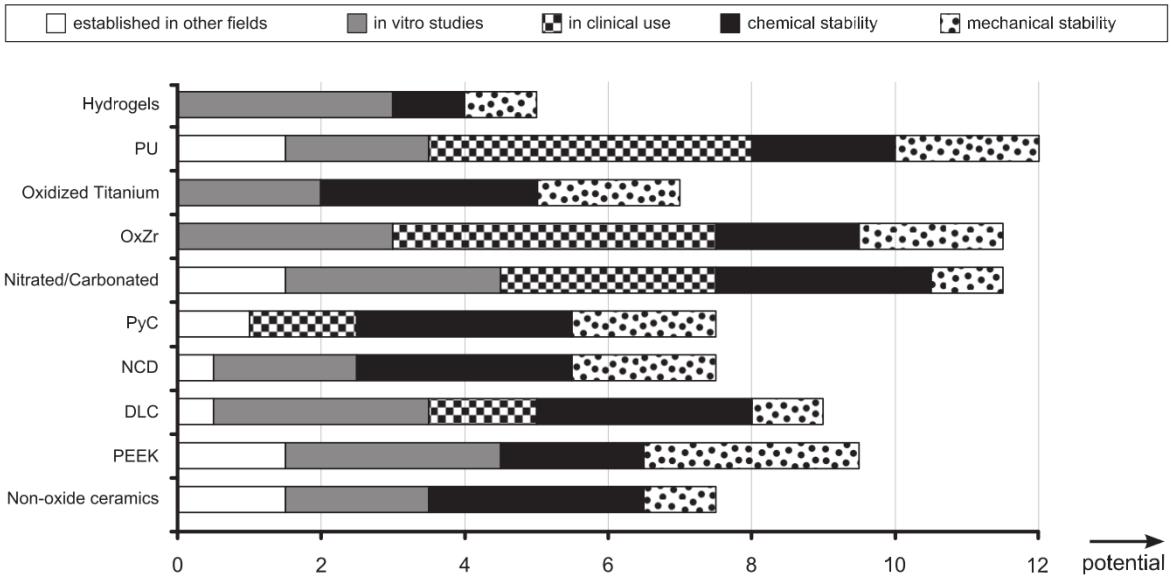

Figure 1.12: Rating of the potential of alternate materials in total joint replacement by Sonntag et. al. 2012 Fig 3. Materials were evaluated based on established history in other fields, *in vitro* studies, clinical use, chemical stability, and mechanical stability. PU - polyurethanes, OxZr - oxidized zirconium, nitrated/carbonated - titanium coatings, PyC - pyrolytic carbon, NCD - nano crystalline diamond, DLC - diamond like carbon, PEEK - Polyetheretherketone). Reprinted from [14], with permission from Elsevier.

1.5 Polycarbonate Polyurethane in Total Joint Replacement

1.5.1 Previous Use of Polyurethanes in Medicine

Polyurethanes are a broad class of polymers that are known for a large number of compositions, properties, and applications. The wide range of properties are a result of the many combinations in the ratio and respective molecular weights of the two components that make up the copolymer [10]. More details on the polymer chemistry will be outlined in Chapter

3. Controlling these parameters dictates the hardness and modulus of the material as well as lubricity, opacity, and biocompatibility [40]. Additionally, the phase-separated structure that results from the separation of the two blocks of the polyurethane copolymers create a quasi-rubber reinforced composite behavior. Because of their toughness and highly tailorable properties, they are used in applications that range from car bumpers in the automotive industry, to skate board wheels in the consumer goods industry. For the same reasons, their high toughness and mechanical tailorability, polyurethane elastomers are also attractive materials for use in medical devices.

Due to their tuneable mechanical properties, along with relatively good hemo- and biocompatibility, polyurethanes are good candidates for use in the medical industry. Polyurethane copolymers were first introduced into the medical device industry in the 1970's. Polyether polyurethanes were used in neurological leads in 1975, cardiac leads in 1977, and then connector modules for implantable cardiac pacemakers, defibrillators, and neurologic stimulators [40, 41]. Polyester polyurethanes have been used in breast implants.

However, both polyether and polyester polyurethane copolymers underwent failures due to unforeseen biodegradation mechanisms [40, 41, 42]. Polyester polyurethane underwent hydrolytic degradation and polyether polyurethane underwent stress corrosion cracking [40]. Polyurethane pacemaker leads in pacemakers failed due to hydrolytic degradation and stress corrosion cracking [40]. Polyurethane films in early breast implants degraded and leached silicone [40, 43]. Degradation in both cases was due to oxidative attack of the soft segment chemistry. In order to combat this degradation mechanism, the soft segment was replaced with the more stable polycarbonate [44].

1.5.2 Polycarbonate Polyurethane Properties

Polycarbonate polyurethane was introduced in the 1990's as a more biostable alternative to polyether and polyester polyurethane biomaterials. Polycarbonate urethane (PCU) contains a polycarbonate soft segment, poly(1,6 hexyl 1,2-ethyl carbonate) diol (PHECD) with similar hard segment components to polyether urethanes commonly used in medical devices [43, 44]. The polycarbonate soft segment is less susceptible to hydrolytic attack and degradation yet still biocompatible [45, 46, 47, 40, 48, 49, 50].

As will be discussed in Chapter 3, polycarbonate polyurethane (PCU) is a block copolymer. Thermodynamic interactions between the polyurethane (hard) and polycarbonate (soft) segments create phase separation into amorphous regions of mixed hard and soft segments and regions of ordered hard segments that dictate the structure of the material [51, 52, 53]. The exact degree of phase separation is dependent on thermal and temporal processing [53, 54]. Correspondingly, the mechanical properties of PCU are dependent on the degree of phase separation [52, 53, 55, 44]. The ordered hard segments effectively create a quasi-

rubber-reinforced energetic toughening mechanism that enables an increased ductility while maintaining strength in the polymer. Hard segments form highly ordered structures with a high degree of hydrogen bonding within the domain. The remaining amount of hard segments in the amorphous mixture of soft segments determines the degree of phase separation of the material [40, 43, 51, 54, 56].

PCU has also been shown to be more resistant to oxidation caused by sterilization and aging than UHMWPE. PCU was found to have no impact on mechanical properties following irradiation or accelerated aging alone, but lost 9% of ultimate strength following both irradiation and 5 years of accelerated aging. UHMWPE (1050 GUR extruded) was found to have a 70% reduction in ultimate load following the same procedure [41]. With improved stability, PCU is an attractive material for load bearing orthopedic applications.

As stated previously, PCU has been introduced due to its attractive elastomeric properties. It has a high toughness and a low modulus. The range of moduli for PCU is more similar to the moduli of soft tissues (1 MPa) than the traditional materials used in TJR (1 - 200 GPa) (Figure 1.5). The mechanical properties of PCU, like other polyurethanes, can be tuned by changing different variables in the chemical composition. By varying the ratio of hard to soft segments in the polymer chain, the Shore hardness of PCU can go from 80A to 75D. Similarly, the modulus of the material can range from 11 MPa to over 1 GPa. Elastic modulus values that have been published for Bionate® 80A and 75D are summarized in Table 1.2. As will be addressed in the following sections, the modulus of PCU is highly dependent on hydration and is viscoelastic.

Table 1.2: Summary of measurements of the elastic modulus Bionate® polycarbonate polyurethane

Modulus (MPa)		Testing Condition				
Bionate® 80A	**Bionate® 75D**	**Test**	**Conditioning**	**Strain Rate (mm/min)**	**Temp.**	**Ref.**
	335	Tension	Hydrated	10	Room	[57]
	493			75		
	562			150		
	1560			500		
22 - 24	131-328	Compression	Dry	0.5	37°C	[58]
16 - 25		Compression	Hydrated	32	37°C	[59]

Hydration

Polycarbonate polyurethane is also hygroscopic. Absorbed water disrupts the hydrogen bonding in the ordered domains of PCU and has a plasticizing effect on the polymer. It takes up to two weeks of soaking to reach steady hydrated state of approximately 1.3 wt % for both Bionate® 80A and 75D [56, 57]. This absorption of water has a significant influence on mechanical properties of PCU [60]. Conditioning reduces the modulus [47, 61] and reduces the ultimate strength of 75D by more than 50% compared to dry material [47, 56]. This drop in stiffness was correlated with a decrease in glass transition temperature observed after hydration in PBS and indicated an increase in phase separation and order in the hard domain [47]. A significant drop in tensile properties following 3 - 5 months of hydration has been reported. This suggests that, although no significant additional water is being absorbed, interactions with water and the domain structures are occurring on different time scales [47, 56].

Hydration also influences the surface organization of polyurethane copolymers. The thermodynamics driving phase separation also dictates the order at the surface. The segment orientation that lowers the surface free energy will be favored. An experiment by Xu et al. 2009 showed a dynamic restructuring of the hydrophilic hard segments during hydration. They showed that for biological applications, this change in surface energy led to a change in the conformation of adsorbed fibrinogen and corresponded to a decrease in platelet adhesion [62].

Viscoelasticity

As an elastomer, PCU exhibits highly time dependent behavior characterized by its viscoelastic properties [63, 64, 65, 66, 67]. Viscoelasticity describes both the elastic and viscous components that make up the mechanical behavior of most polymers. The elastic response of a polymeric material is attributed to the entropic stretching of the polymer chains beyond their equilibrium length. This has been shown to be a linear elastic response. However, polymer chains also have the capability to move in relations to each other. This response is the viscous nature of the polymer and is time dependent. Longer time periods provide the opportunity for chains to move relative to one another. This manifests itself in different stiffnesses and ultimate properties of a single material when exposed to variable strain rates. Viscoelasticity can also manifest itself in stress relaxation or creep under constant loading.

For Bionate® specifically, Shemesh et al. characterized the viscoelastic response of the material in the NuSurface® meniscal implant in a simulated device setup. They found a stiffening response with increasing strain rate, see in a reduction of the maximum strain from 1 mm/min to 100 mm/min. Following hydration the maximum strain at all strain rates decreased significantly as the modulus increased signaling a embrittling effect. Under

dynamic loading the maximum strain was further reduced. Under fatigue loading all properties initially changed in the first 300,000 cycles, and then remained constant up to 2 million cycles. However, following fatigue loading, permanent plastic deformation was observed [65].

Wear Performance

Early friction and lubrication experimental studies and computational modeling suggest that PCU has potential to have better wear performance than UHMWPE. PCU can be formulated to have a much lower modulus of elasticity than UHMWPE. Theoretically, a lower modulus will reduce the contact stresses and increase the potential for a full fluid film lubrication regime. Initial models of the elastohydrodynamic lubrication (EHL) regimes (discussed further in Chapter 4) in a PCU hip implant predicted a lubricating film that was 1.5 - 3.4 times thicker than that of UHMWPE, suggesting better wear performance [68].

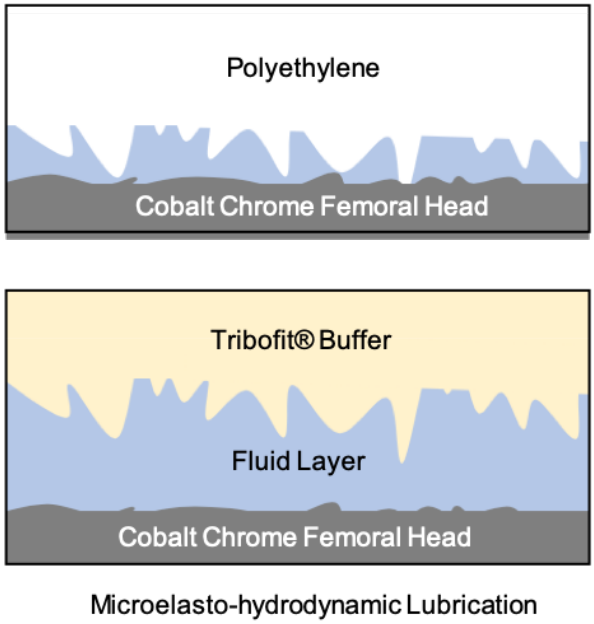

Figure 1.13: Promotional material for Tribofit® depicts an increased lubrication layer in PCU acetabular cups compared to UHMWPE based on EHL modeling. Adapted from promotional material [69].

This has initiated the introduction of orthopedic implants with PCU bearing materials. Several medical companies use PCU in spine devices with various indications. Active Implants Inc. (Memphis, TN) has led the market with a PCU hip and knee implant. They have also led the publication of *in vitro* wear testing that shows improved wear performance of PCU over UHMWPE [70, 71, 72]. Each of these publications state that polycarbonate

promotes fluid film lubrication to reduce wear citing: [73, 74, 75]. Additionally, the promotional material from Active Implants Inc. [69] cites improved EHL as a marketing point for PCU citing [74] (Figure 1.13).

1.5.3 Polycarbonate Polyurethane: Clinical Applications and Performance

PCU, produced under the name Bionate® by DSM in Berkeley, California, has been used in the acetabular cup of hip replacements by Active Implants Inc. since 2006, in the European market [76, 14, 77, 78] and is in a meniscus implant in clinical trials in the United States (Figure 1.17, right). Outside of TJR, PCU is also approved by the FDA for use in the Dynesys spine stabilization device, with a temporary indication [78, 79, 80] (Fig.1.18) and the the Bryan cervical disc replacement device [81, 82]. The initial data for each clinical application will be reviewed below. A summary of mechanical and thermal properties of Bionate® can be found in Table 1.3. Early results show promise, but long term performance is unknown [79, 78, 77, 76].

Table 1.3: Summary of selected mechanical and thermal properties of Bionate® polycarbonate polyurethane.

Property	**Bionate® 80A**	**Bionate® 75D**	**Reference**
Hardness	84A	73D	[83]
Density (g/cm^2)	1.19	1.22	[83]
UTS (MPa)	46.6	63.2	[83]
Ultimate strain (%)	531	241	[83]
Water absorption (%)	1.2	0.8	[83]
Coefficient of friction	1.52	0.64	[83]
Poisson's ratio	0.4924 - 0.4926	0.3844 - 0.4254	[58]
Glass transition temperature (°C)	17	76	[56]

PCU Total Hip Implants

The low and evenly distributed contact stresses in the highly conforming ball and socket hip joint are ideal conditions for the hypothesized improved fluid lubrication layer of a more compliant PCU bearing surface (Figure 1.14) [84, 85, 72, 86]. The Tribofit® acetabular hip

component (Active Implants, Memphis, TN, USA), is a 3mm thick PCU liner designed to be press fit directly into the pelvis, or with a metal liner [87].

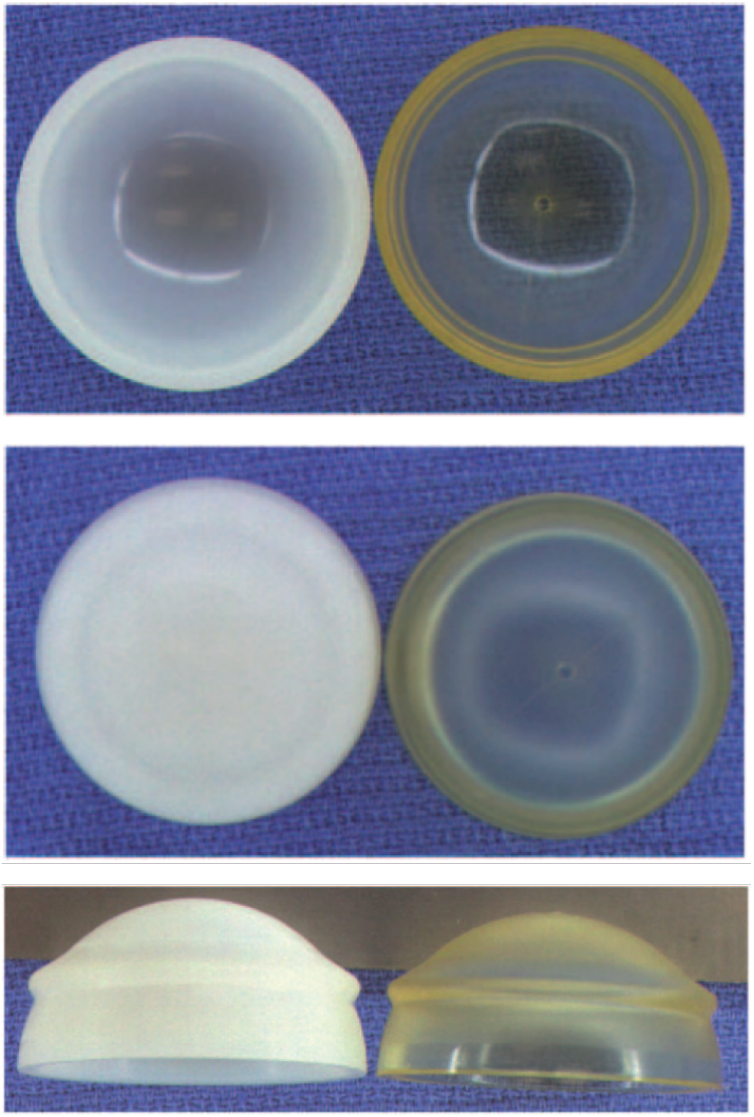

Figure 1.14: Example of a PCU acetabular cup compared to an UHMWPE cup of the same dimensions. Reprinted from [72] with permission from Sage Publishing.

Large animal studies showed promising results. A four year ovine study using PCU acetabular cups observed no physical or chemical degradation, little immune response, and minimal wear. Of 37 implants, fracture was observed in the hard backside of one device, but did not continue into the compliant bearing material (Figure 1.16) [60]. Additionally, the hardness of the material increased after one year of implantation and then remained constant. Correspondingly, the phase separation of the material increased with implantation

time [60]. Another two year ovine study showed similar positive results with no observed fracture and acceptable wear. Asperities on the initial implant wore down to a smoother bearing surface than when initially implanted [88].

Isolated human explant case studies, though limited in implant time, have also been positive. The first human explant after 10.5 months showed wear rates (1.4 - 14 mm^3/year) [77] similar to what was predicted in the wear simulator studies, but wear particle size smaller than was predicted *in vitro*: average = 2.9 μm, range = 0.5 - 90 μm, with one particle at 200 μm [70, 71]. A second explant, at 1 year, showed a similar wear rate (15 mm^3/year) on the front side, though 10% of thickness was lost on the superior side [76]. A third explant study of a Tribotfit® cup that was implanted without a metal backing directly into the acetabulum showed heavy wear on the backside. Movement and wear against the native acetabulum was indicated as the cause of a wear rate of $160\pm45 mm^3$ in 11 months. This is significantly more than had been previously reported for metal backed acetabular cups (Figure 1.15) [89].

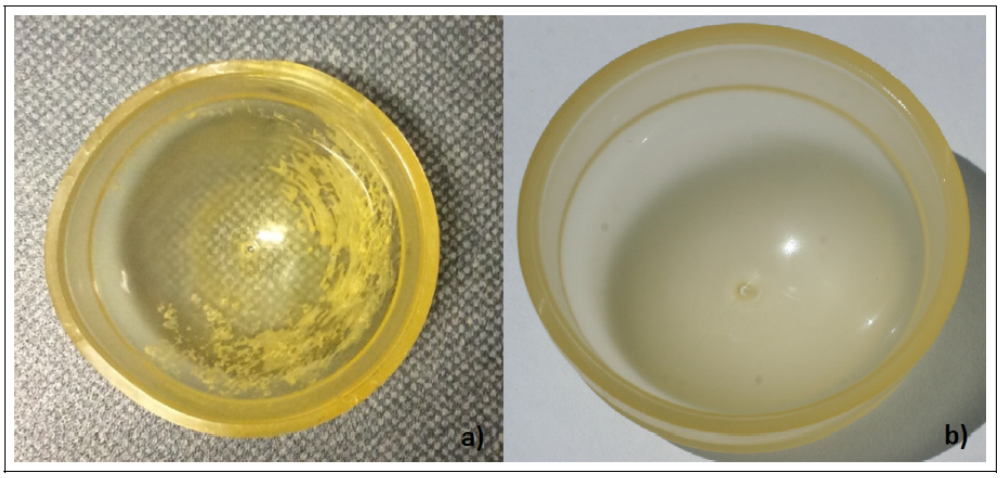

Figure 1.15: A PCU acetabular cup before implantation (right) and after 11 months of implantation (left) showing the deposits of biological material on the back of the cup. Reprinted from [89] with permission from Sage Publishing.

Results from the first early clinical studies contradicted some findings in the *in vitro* and animal studies. One study compared PCU THA implants to hemiarthroplasty in the treatment of femoral neck fractures in elderly osteoporotic patients. They found no difference in Harris Hip Score for function and pain between PCU THA and hemiarthroplasty [90]. Another study, comparing PCU THA to metal-on-metal THA systems found equivalent performance between the two, with less metal ion levels in the serum of the PCU implants [91]. However, a third study, comparing the use of PCU implants to hemiarthroplasty to treat femoral neck fractures in elderly osteoporotic patients, showed higher pain reported in the PCU implants with only a 84% three-year-survival rate. Of the 42 patients, 6 required

revisions. Dislocation and wear were the main causes of revision. Of the six revisions, two were acutely dislocated, but did not have signs of wear, and two had heavy signs of wear. One instance of a 2.5 cm^2 hole was reported [92].

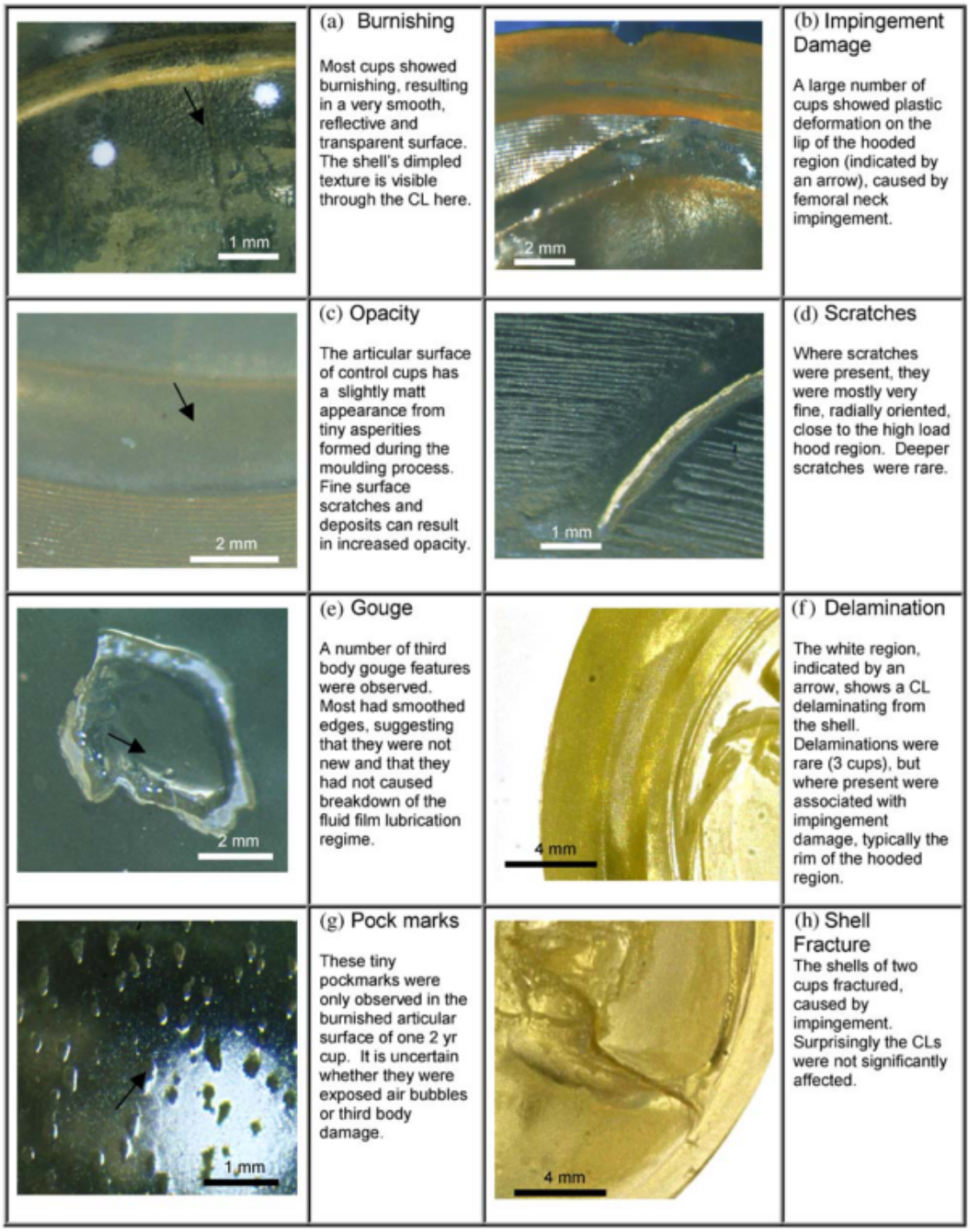

Figure 1.16: Examples of the modes of damage that were observed in a 4 year ovine study of 37 total implanted PCU acetabular cups. Although damage was observed, overall good function and satisfactory wear outcomes were seen. Reprinted from [60], with permission from Elsevier.

PCU Meniscus Implants

The NuSurface® meniscal implant is produced by Active Implants, Memphis, TN, USA, as a replacement meniscus. The device is made of Bionate® 80A reinforced with circumferential high modulus UHMWPE fibers (Dyneema Purity®, DSM Biomedical, Geleen, NL) (Figure 1.17, right) [93]. These fibers mimic the native collagen architecture of the meniscus and resist bulging under the hydrostatic pressure of axial loading. The device aims to reduce the contact forces in the knee following meniscectomy [94, 65, 95]. A six-month sheep study using an early design showed positive results [96]. In a one-year goat study (Figure 1.17, left), the PCU meniscus device was found to perform similarly to an allograft control. However, a tearing failure was observed in one of seven implants [94]. The incidence of failures in these studies, with limited sample size, highlights the need for further study of the failure mechanisms of PCU.

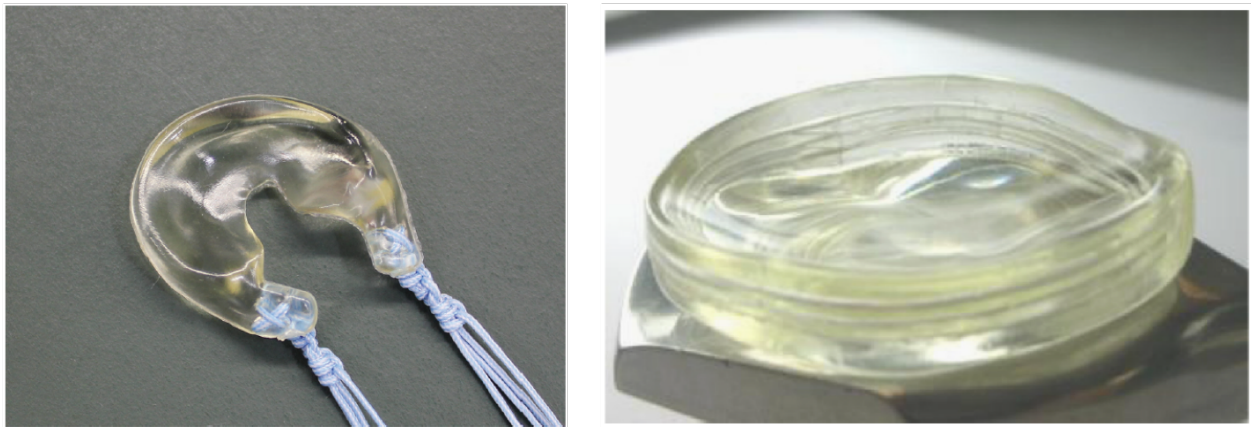

Figure 1.17: Examples of PCU meniscus devices. The image on the left shows an PCU meniscus implant adapted for an *in vivo* goat study. Reprinted from [94] with permission from Sage Publications. The image on the right shows the Nusurface® device from Active Implants in *in vitro* viscoelasticity testing. Reprinted from [65] with permission from Elsevier.

PCU in Spinal Implants

PCU has also been of much interest as a tough, impact-absorbing, and elastomeric intervertebral disc replacement for spine devices. The spine stabilization device, Dynesys® (Zimmer Biomet, Warsaw, Indiana, USA), is an alternative to stabilize a motion segment in place of fusion. It allows for limited motion while providing support and stability [97] (Figure 1.18). The Dynesys® device consists of two pedicle screws that fix a PCU spacer on a poly(ethylene-terephalate) (PET) cord. The PCU spacer supports compressive loads while the PET cord resists tensile loading.

Figure 1.18: Example of a Dynesys spine stabilization device. The screws are put into adjacent vertebra and the PCU spacer allows for limited mobility of a degenerated intervertebral disc. Reprinted from [78], with permission from Wolters Kluwer Health, Inc.

One explant case with two spacers, implanted for 5.5 years and removed due to an abscess near one likely caused by infection, reported evidence of hydrolysis at the surface in one of the two spacers. However, no damage was observed at a depth of 100 μm [97]. This finding was supported by work by Ianuzzi et al. who found surface level chemical modification in 2 of 44 retrieved devices where the device was in contact with bodily fluid [97, 78]. Gross deformation and abrasive wear were observed (Figure 1.19). Additionally, one spacer had cracks that extended from the surface to the center (Figure 1.20) [78]. Similar findings were made in another set of explant devices. Gross deformation, surface ($< 10\mu$m) chemical modifications attributed to oxidation, and surface cracking were observed [79].

There are other, though less studied, spine stabilization devices containing PCU that are in various stages of regulatory approval. Other devices include: Transistion® (Globus Medical, Audubon, PA, USA), NFix®, II/NFlex/NGarde® (Synthes GmbH, Oberdorf, Switzerland), Total Posterior Spine® (Impliant Ltd, Netanya, Israel, now Premia Spine Ltd, Herzeila, Israel), and the PDS System® (Interventional Spine, Irvine, CA) [80].

Beyond spine stability, PCU has been used to mimic the function of the IVD in cervical intervertebral disc replacement devices. The Bryan cervical disc replacement (Medtronic, Minneapolis, MN, USA) (Figure 1.21), utilizes a PCU core and sheath between two tita-

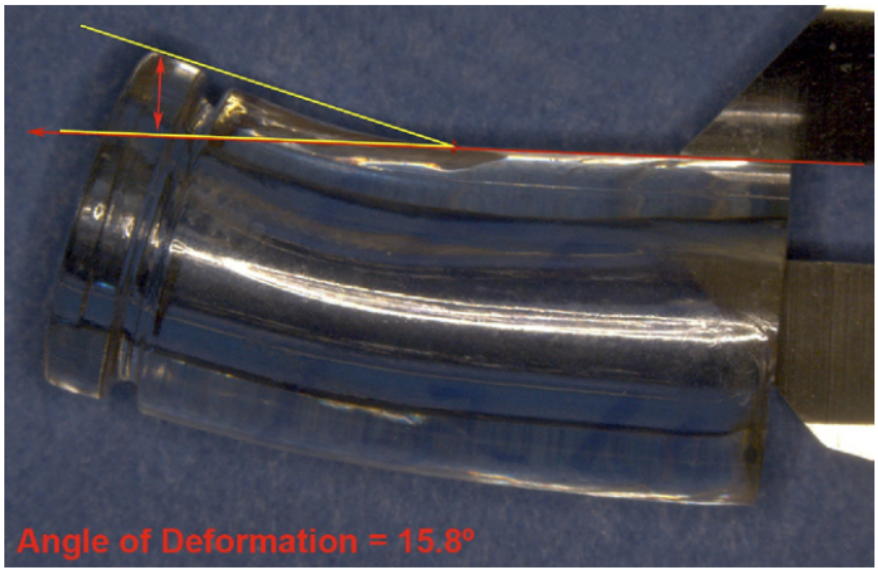

Figure 1.19: Example of plastic deformation observed in the PCU spacer of a Dynesys spine stabilization device implanted for one year. The deformation was the result of bending in addition to the compressive loads that the PCU component of the device is designed to sustain. Reprinted from [97], with permission from Elsevier.

nium plates [97]. Animal studies found satisfactory immune response and wear rates of 1.2 mg/million cycles with an average particle size of 3.9 μm. Loss of height, largely due to creep, was measured at 0.02mm [81]. Clinical trials began in Europe in 2000 and early prospective clinical trials also reported satisfactory results similar to those seen with anterior discectomy and fusion [98, 82]. Movement was preserved in 87.3% of patients with a single level replacement [82]. However, complications have been identified related to: operative approach, spinal chord or neural root injury related to inadequate decompression, loosening and failure of the device, postoperative kyphosis or unwanted spinal curvature, heterotrophic ossification or growth of bone cells, and loss of movement through fusion [82]. One explant study reported on a device failure after 8 years of implantation. Upon investigation, a 5 mm crack was found in the PCU sheath. A cyst (2 x 1 x 1 cm) was found adjacent to the Bryan disc that may have been related to the release of wear debris from the fractured sheath [99].

Another disc replacement that utilizes PCU is the LP-ESP device (FH Orthopedics, Chicago, IL, USA) for lumbar disc replacement. Positive results were reported following 7-years post implantation [100, 80]. Further disc replacement devices that utilize PCU are available at different levels of regulatory approval including: M6 Cervical and Lumbar discs (Spinal Kinetics, Sunnyvale, CA, USA), Theken eDisc^{TM} (Theken Disc, Akron, OH), and the Freedom® Lumbar Disc (Axiomed Spine Corp., Garfield Heights, OH, USA) [80].

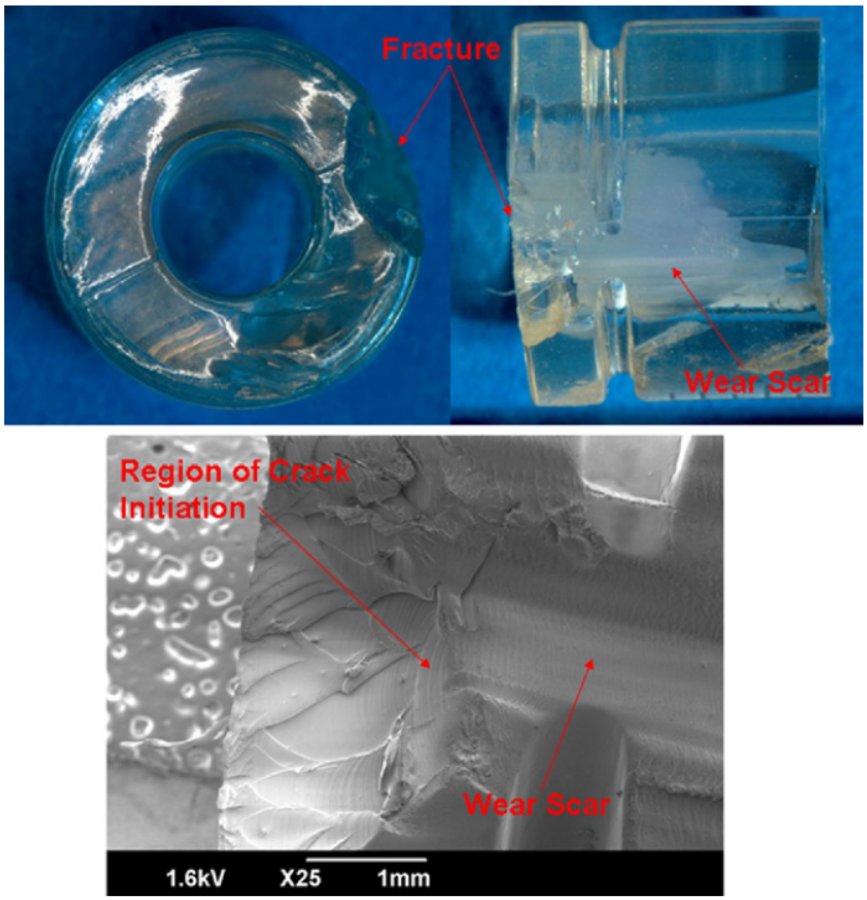

Figure 1.20: Example of fatigue fracture observed in the PCU spacer of a Dynesys spine stabilization device implanted for over 1 year. The PCU spacer provides resistance to compressive loading to give support to a diseases intervertebral disc in place of a spinal fusion. Reprinted from [97], with permission from Elsevier.

Figure 1.21: The Bryan cervical intervertebral disc implant (Medtronic, Minneapolis, MN, USA) includes a PCU core and sheath 'IVD' between two titanium plates. The implant allows for motion to be maintained following disc degeneration rather than immobilizing the segment through a fusion. Reprinted from [98], with permission from Elsevier.

1.6 Summary

In synovial joints and the spine, cartilage is the soft tissue that allows for motion and provides pain free articulation. Cartilage does not have the ability to heal and repair itself, so with injury or damage over time, it degrades. The degradation of cartilage leads to painful bone-on-bone contact in the case of articular joints, or nerve impingement in the spine.

The current gold standard to treating osteoarthritis is total joint replacement. The gold standard in total joint replacement material design is crosslinked UHMWPE on a hard articulating surface. Current UHMWPE hip replacements designs have a 1% per year or less revision rate in the first 10 years [15]. However, with increasing demand, devices are being pushed to perform better and last longer. Currently, wear related failure in total joint replacements is the greatest challenge. In order to rival or exceed the performance of UHMWPE, PCU needs to show promise at implantation times at or exceeding those currently reported for UHMWPE.

PCU has been introduced as an alternative material to UHMWPE with the potential for improved wear performance. PCU is more compliant than UHMWPE and is marketed as having better lubrication. *In vitro* wear studies have shown promising results, but not as great of an improvement as predicted.

Historically, improvements to the wear performance of UHMWPE, through crosslinking, has led to tradeoffs with fracture resistance and oxidation resistance. Moving forward, these lessons must be applied in new materials. Even though PCU has been presented as a potential good alternative material with respect to wear performance, the fatigue and fracture resistance is also important to consider.

Clinical data on PCU remains limited especially in the long-term. However, there are clinically available devices using PCU in hip, knee, and spine applications. Therefore, extensive *in vitro* testing must seek to explore the behavior of PCU under high cycle fatigue and wear.

This thesis will evaluate the mechanical performance of PCU with respect to its use in load bearing medical implants. The research questions investigated are: 1) What factors influence the mechanisms of fatigue crack growth in PCU? 2) How does strain impact the structural organization of PCU? 3) What is the lubrication regime in a PCU hip implant under transient 3D walking gait?

Chapter 2

Micromechanisms of Fatigue Crack Growth in Polycarbonate Polyurethanes

2.1 Introduction

The loading environment of an orthopedic implant is highly cyclic in nature. It is commonly estimated that, based on the average number of steps per year, an implant will undergo at least 1 million loading cycles per year. The loading is highly variable due to the inter-patient differences in activity levels, weight, stride etc. Loading is further variable with type of activity. For example, walking, stair ascent, standing from seated, etc. all create different loading patterns. In addition to this heterogeneity of loading, the design requirements of a medical implant are highly safety critical. Due to the highly invasive nature of the surgery required to access the implant, there is no ability to inspect the implant after implantation. An implant must perform for years without the maintenance or inspection available in other safety critical industries (i.e. aerospace).

Unlike wear, which causes progressive failure of the device, fracture can require an immediate revision surgery. In the hip, a more conforming geometry reduces the contact stress and reduces the likelihood of fracture. However, notches and features designed to provide mechanical fixation into the metal backing, create stress concentration locations that have led to fracture (Figure 2.1). In the knee, designs that aim to recreate the native kinematics have a less conforming design and therefore higher contact stresses. These contact stresses have led to subsurface cracking and delamination in the material.

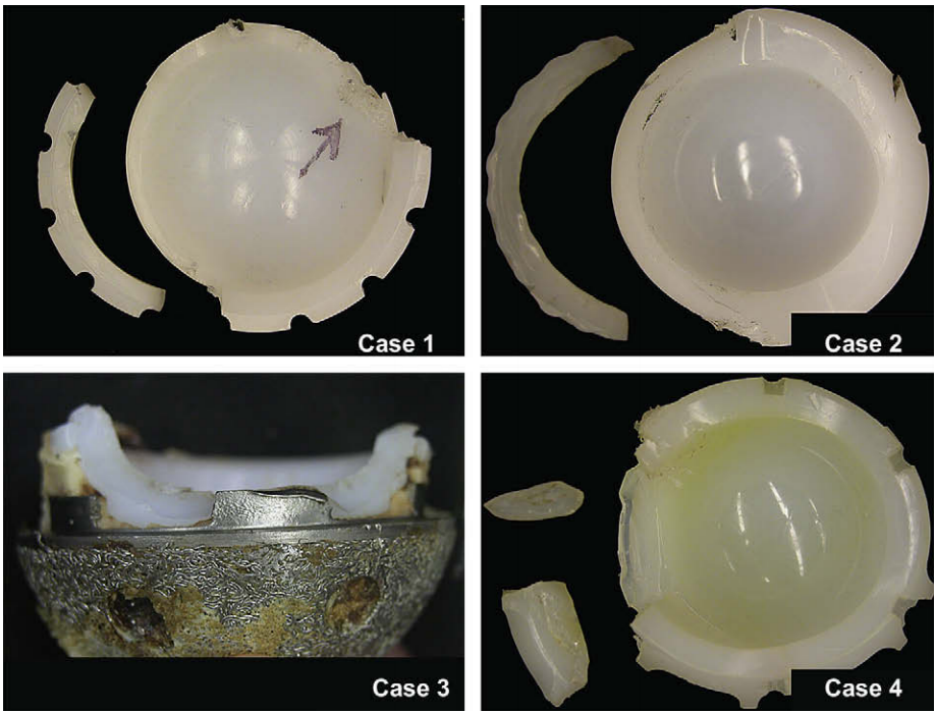

Figure 2.1: Example of clinical fractures observed in crosslinked UHMWPE acetabular cups. Reprinted from [101], with permission from Elsevier.

Due to the high-cycle loading environment facing total joint replacements, it is crucial to characterize the long-term fatigue performance of a candidate material for long-term implantation. A linear elastic fracture mechanics (LEFM) approach has historically been used to compare new formulations of UHMWPE for use in orthopedic implants. For a safety critical applications, fatigue crack growth characterization studies how flaws in the material can grow under cyclic loading and potentially lead to failure.

The cartilage-like modulus and elastomeric properties of PCU make it an attractive material for orthopedic joint replacement applications. As introduced in Chapter 1, PCU has been introduced as an alternative polymer to ultra high molecular weight polyethylene as the bearing surface in hip, knee, and spinal implants [76, 14, 77, 78, 79, 80]. Initial clinical data on PCU device performance is limited [76, 78, 79, 97, 99] and there is no long-term clinical data. The development of PCU has been motivated by improving the wear performance of total joint replacements (TJR). However, the polymer bearing surface must provide both good wear resistance and fracture resistance.

Although PCU is an elastomer and promoted for its high toughness, examples of fracture of PCU have been reported in explant case studies and *in vivo* animal studies. In a case study, Ianuzzi et al. reported fracture in a PCU spacer of a Dynesys spine stabilization device

explanted after 0.7 years (Figure 2.2) [78]. Khan et. al. reported fracture in the Bionate® 75D backing of an acetabular cup lined with Bionate® 80A. The fracture occurred in 1 of 37 cups in a 3 year sheep study [60]. Finally, Vrancken et al. reported fracture of a PCU total meniscus prosthesis in 1 of 7 implants in a 12 month goat study [94]. These examples underline the importance of understanding the fracture and fatigue mechanisms of PCU to predict the long-term performance of PCU implants.

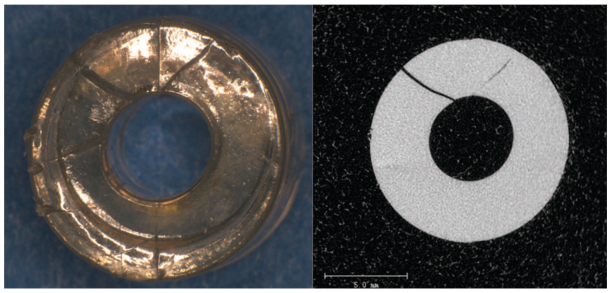

Figure 2.2: Fracture was observed in the PCU spacer of a Dynesys spine stabilization device explanted after 0.7 years. The crack in the fractured spacer (right) was confirmed to be through the full thickness in a CT scan (left). Reprinted from [78], with permission from Wolters Kluwer Health, Inc.

This chapter presents a LEFM-based approach to characterize the fatigue crack propagation mechanisms in PCU. This approach investigates the mechanisms that control and propagate a flaw under the fatigue conditions similar to those faced in orthopedic implant applications. By characterizing the way cracks grow to failure in PCU, we can better predict potential long-term failure mechanisms of this material. This chapter will first review fatigue characterization methods and the theory of a LEFM approach to fatigue. It will then introduce previous work characterizing fatigue in PCU. Finally, we report the results of a study testing variables including temporal loading effects, frequency, hydration, and thermal annealing on the fatigue crack propagation mechanisms in PCU.

2.2 Fatigue of Polymers: Theory

Fatigue characterization is typically divided between two distinct approaches, total life fatigue and defect tolerant fatigue. Total life fatigue, also referred to as the stress-life approach, measures the number of cycles to failure at a given load. It assumes the material is initially defect free, that life encompasses flaw initiation and growth, and does not emphasize mechanisms of failure. In contrast, the defect tolerant approach to fatigue assumes that the material has an initial defect and then characterizes the growth of that defect until failure,

emphasizing the mechanisms of growth.

2.2.1 The Total Life Approach

Total life fatigue looks at the relationship between applied load and number of cycles until failure. This is done experimentally by testing a sample in cyclic fatigue at a given stress level and recording the number of cycles until failure. Repeating this process at a range of stress levels results in a relationship between stress and number of cycles until failure. This curve, known as the stress-life curve, is used to fit the Basquin equation (Equation 2.1):

$$\sigma_a = \sigma'_f (N_f)^b \tag{2.1}$$

where σ_a is the cyclic stress, σ'_f is the stress coefficient, b is the Basquin exponent, and N_f is the number of cycles to failure. The number of cycles to failure is written as N_f or $2N_f$ depending on the curve is calculated based on the number of full reversals or full cycles. To create the S-N curve, multiple samples are tested at various σ_a, resulting in multiple numbers of cycles to failure. A series of such tests produce sufficent data point to predict σ_f and b, and creating a relationship to predict the life of a part under a known load (Figure 2.3) [10].

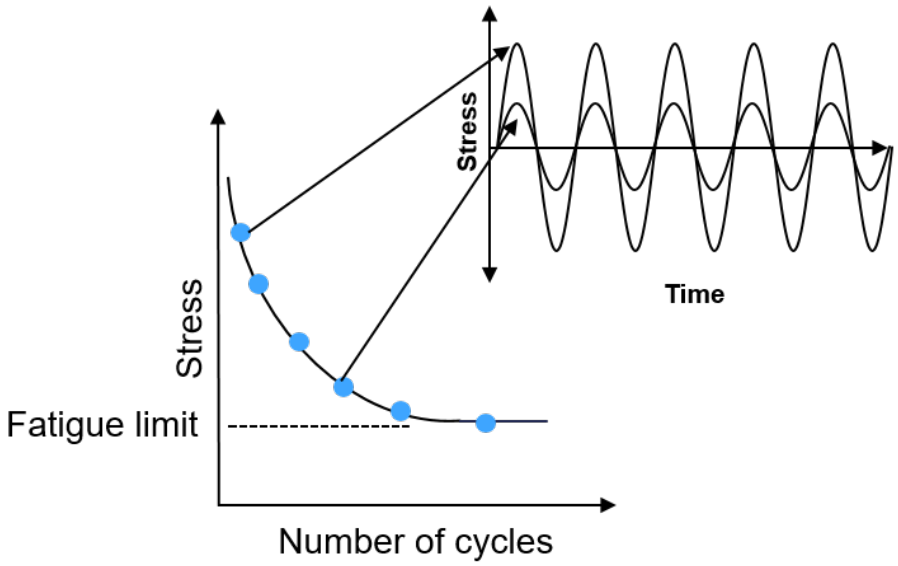

Figure 2.3: Each data point in the S-N curve represents the number of cycles sustained until failure of a sample tested at a given cyclic stress. Many sample points form the curve which, for many materials, plateaus at a minimum stress level after which failure is not observed, referred to as the 'fatigue limit'.

The lower stress bound of the curve is known as the 'fatigue limit' of the material. Under that stress, the part is not expected to fail within the maximum number of cycles tested. Applying an appropriate safety factor to this fatigue limit is used in design. Although some materials do not exhibit a fatigue limit, if a finite number of cycles is expected, statistical confidence can be established for non-safety critical designs.

The stress-life curve is only appropriate for the specific cyclic loading that was used to generate the curve (i.e. fully reversed loading or zero to tension loading). The application of a mean stress, variable amplitude loading, or a geometry with stress concentrations can change the stress-life relationship. Adjustments to the Basquin equation can be made to account for mean stress effects. However, the more accurate method is to recreate the stress-life curve for a given design and loading case. This is not always possible because experimentally creating a stress-life curve is time and sample intensive. Multiple samples are needed at each stress level, and a long time can be required to reach high cycle failure at low stresses. High amounts of scatter is commonly observed and is linked to inter-sample variability due to manufacturing and material defects [10].

Various cycle counting techniques can be used in applications where variable amplitude loading occurs, such as the highly heterogeneous loading of orthopedic implants. One commonly used technique is Miner's rule of damage accumulation (Equation 2.2):

$$1 = \sum_{i=1}^{m} \frac{n(\sigma_i)}{N_f(\sigma_i)} \tag{2.2}$$

where: $n(\sigma_i)$ is the number of cycles that occur at σ_i and $N_f(\sigma_i)$ is the number of cycles to failure at σ_i.

Miner's rule assumes that there is a finite life of the part. Loading at a finite number of cycles a given cyclic stress takes a fraction of the life of the device proportional to the number of cycles to failure at that stress. Loading at each cyclic stress is then summed to estimate the total stress-life of the part. This method to accommodate variable loading is a first pass at predicting failure in a material, but there is a high statistical scatter based on the existence of flaws in the material. For safety-critical applications, this estimate can only serve a limited predictive role.

Total life fatigue assumes that the initial material is flawless. The presence of a flaw reduces the fatigue life because, under cyclic loading, flaws (cracks) can grow towards a length that can cause failure. Flaws and inconsistencies due to manufacturing defects and variability are inevitable in most materials. This is not accounted for in total life fatigue beyond the statistical scatter in the stress-life curve. But, in parts where the fatigue is safety critical, such as airplanes, nuclear applications, and medical devices, more robust testing techniques are used to predict failure.

2.2.2 Defect Tolerant Fatigue

Linear Elastic Fracture Mechanics

Predicting and understanding fracture is the goal of the defect tolerant approach to fatigue. The defect tolerant approach assumes that there is a defect in the material, either from manufacturing or damage, and seeks to understand the stress state and material response at the crack tip that lead to crack growth and, finally, to fracture. To do this, the defect tolerant approach to fatigue utilizes LEFM. Although polymers are typically not linear elastic materials, LEFM has proven to be useful in characterizing their behavior. This will be further addressed later in the chapter. This section will introduce the theory behind LEFM, but is not an exhaustive review. For further reference see [102].

The field of LEFM began with the development of Griffith's energy balance. The Griffith energy balance approach quantifies crack growth within the global stresses of a linear elastic solid. The Griffith energy balance describes crack growth as a lowering of the energy of a system (ϵ) through the work required to release strain energy (Π) and to create new surfaces (W_S) (Equation 2.3, Figure 2.4).

$$\Delta\epsilon = \Delta\Pi + \Delta W_S \tag{2.3}$$

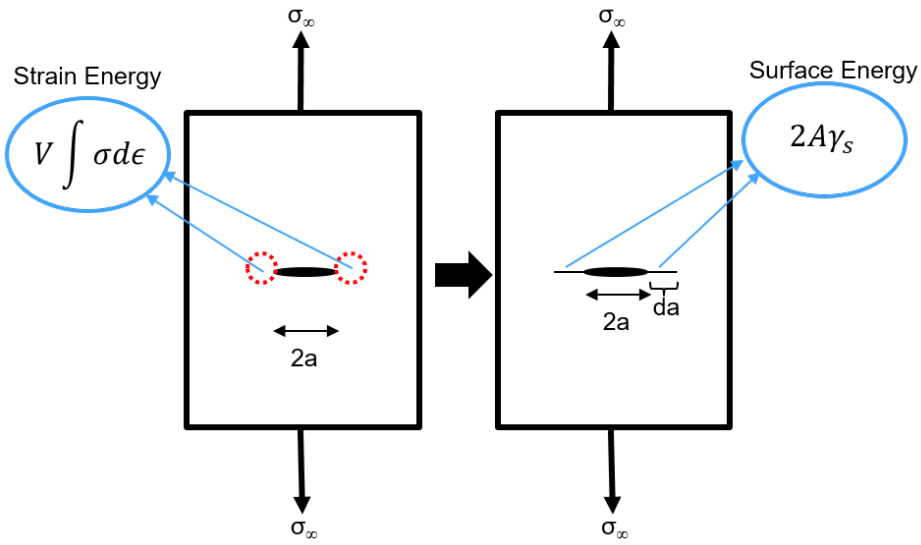

Figure 2.4: The Griffith energy balance states that crack growth will occur when the strain energy exceeds the energy of the new surface. Thickness (t) is the dimension into the page.

As the crack grows (da), the crack area (dA), product of the crack growth and thickness (t), also increases (Equation 2.4):

$$dA = (2da)t \tag{2.4}$$

The energy balance, with respect to the changing area is then:

$$\frac{d\epsilon}{dA} = \frac{d\Pi}{dA} + \frac{dW_S}{dA} = 0 \tag{2.5}$$

Inglis estimated the strain energy as a function of changing crack area. The strain energy ($\int \sigma_\infty d\epsilon = \sigma_\infty^2/E$) can be estimated by considering the area of a cylinder around the crack area (Figure 2.4 right, Equation 2.6):

$$\Pi = \pi a^2 t \frac{\sigma_\infty^2}{E} \tag{2.6}$$

where σ_∞ is the far field stress, a is half the crack length, t is the thickness of the material, and E is the modulus of elasticity.

The change in strain energy per change in crack area is then given in Equation 2.7:

$$\frac{d\Pi}{dA} = \frac{-\pi\sigma_\infty^2 a}{E} \tag{2.7}$$

The change in surface energy (W_s) is equal to 2 times the crack length, to account for both top and bottom surfaces, multiplied by the thickness and a surface energy parameter (γ_s):

$$W_s = 4at\gamma_s \tag{2.8}$$

The derivative with respect to crack area is then given by Equation 2.9.

$$\frac{dW_s}{dA} = 2\gamma_s \tag{2.9}$$

Using the elastic energy to define the work, fulfilling the Griffith Energy balance gives the following relation:

$$\frac{-\pi\sigma_\infty^2 a}{E} = 2\gamma_s \tag{2.10}$$

Irwin named the left value of equation 2.10 the energy release rate (G) and the right term the material resistance. The strain energy release rate (Equation 2.11) provides a failure criteria based on the global stress state in the material and the flaw size:

$$G = \frac{-\pi\sigma_\infty^2 a}{E} \tag{2.11}$$

A strain energy that exceeds the surface energy will lead to fracture, while the opposite will remain intact.

The strain energy release rate failure criteria does not account for material ductility and therefore is applicable only to brittle materials. Further, this method uses global stresses

and does not address the stress state at the crack tip where ductility plays a key role. In order to move towards a description of the stress state at the crack tip we can consider the stress concentration impact of notches and other geometric irregularities.

Geometric irregularity, holes, or cracks create areas of stress concentration with respect to a far field load. The stress concentration factor (k_t) describes this increase of the local stress with respect to the global stress (σ_{local}, Figure 2.5):

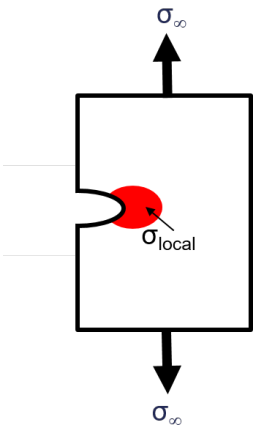

Figure 2.5: The stress concentration factor (k_t) is the ratio of the stress at a local point of stress concentration (σ_{local}) to the global stress in the body away from the concentrated point (σ_∞).

$$k_t = \frac{\sigma_{local}}{\sigma_\infty} \tag{2.12}$$

The stress concentration factor can be solved for analytically for simple geometries and was also studied by Griffith. For an elliptical hole in an infinite plate, he found the stress concentration factor to be a function of the notch root radius (ρ) (Equation 2.13 & 2.14, Figure 2.6).

$$\sigma_x = 2\sigma_\infty \sqrt{\frac{a}{\rho}} \tag{2.13}$$

$$\rho = \frac{b^2}{a} \tag{2.14}$$

For an atomically sharp crack, a crack that has no curvature beyond that on the atomic scale, the notch root radius goes to zero, making the limit of the stress infinite at the crack tip (Equation 2.13).

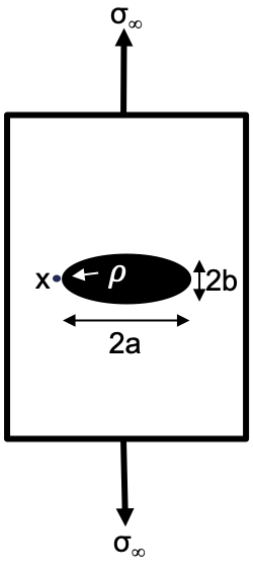

Figure 2.6: The stress concentration factor solved by Griffith for an elliptical center crack in an infinite plate is a function of the notch root radius or 'sharpness' of the notch. The sharper the notch is the higher the stress concentration at point x.

Infinite stress should cause any material to fail. However, from experience, cracks do not immediately cause failure in a material, therefore there is another mechanism at play that prevents failure in the presence of a crack.

Irwin and Williams proposed the stress field in front of a crack tip. They defined the stress field as a function of a stress intensity (K_I), the radial distance from the crack tip (r), and the angle from the direction of crack growth (θ) (Equation 2.15 - 2.17, Figure 2.7).

$$\sigma_{xx} = \frac{K_I}{\sqrt{2\pi r}} cos\frac{\theta}{2} 1 - sin\frac{\theta}{2} sin\frac{3\theta}{2} \tag{2.15}$$

$$\sigma_{yy} = \frac{K_I}{\sqrt{2\pi r}} 1 + sin\frac{\theta}{2} sin\frac{3\theta}{2} \tag{2.16}$$

$$\sigma_{xy} = \frac{K_I}{\sqrt{2\pi r}} sin\frac{\theta}{2} sin\frac{3\theta}{2} \tag{2.17}$$

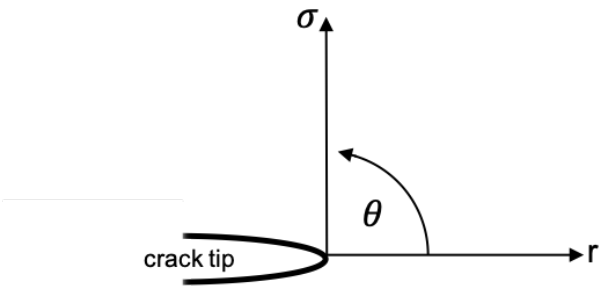

Figure 2.7: The stress field is defined as a function of stress intensity (K), radial distance from the crack tip (r), and the angle from the direction of the crack tip (θ).

The stress intensity factor is unique for different loading modalities. K_I, K_{II}, and K_{III} correspond to tensile, sliding, and shear motions, as outlined in Figure 2.8. Mode I stress intensity (K_I) is a function of the geometry (F), far field stress (σ_∞), and crack length (a) (Equation 2.18).

$$K_I = F\sigma_\infty\sqrt{\pi a} \tag{2.18}$$

The geometry factor (F) is calculated for standard compact tension specimens (ASTM D5045). The stress intensity factor can be similarly defined for each mode of loading and combined for cases of complex loading. However, because the tensile loading of Mode I represents a worst case for fatigue crack growth, we will focus on this case. The stress intensity factor (K) is not equivalent to the stress concentration factor (k_t) which describes a ratio of local to global stresses. Instead, stress intensity describes the driving force of crack growth for a given loading type in the form of the global stress and corresponding strain field in front of the crack.

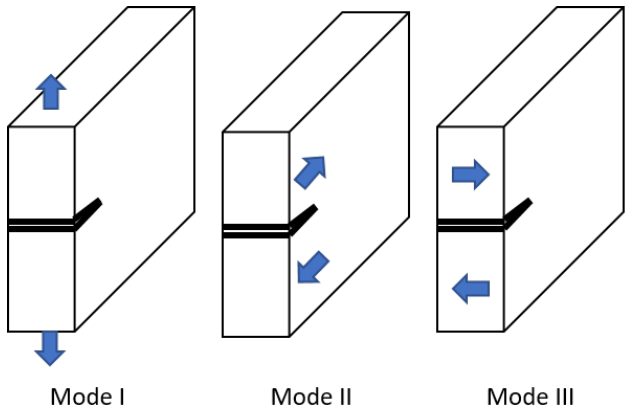

Figure 2.8: The stress intensity factor is unique for each of three loading modes: tension (I), sliding (II), and shear (III).

Stress intensity can be correlated to the strain energy release rate through:

$$\frac{K_I^2}{E} = G \tag{2.19}$$

Like the solution for the stress concentration at an elliptical hole, the analytical description of the stress field in front of the crack (Equation **??**) produces a singularity at the crack tip ($\lim_{r\to\ 0}\sigma(r) = \infty$). However, in many materials, localized ductility acts to reduce the stress at the crack tip. In ductile materials, local yielding ahead of the crack tip creates a so-called plastic zone (Figure 2.9).

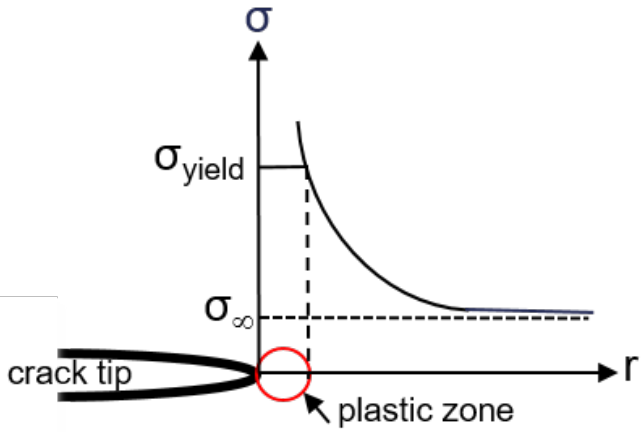

Figure 2.9: For an infinitely sharp crack the theoretical stress concentration should go to infinity. However, plasticity of the materials changes the response at a yield stress. This results in a plastic zone (circled in red) around the crack tip in which plastic deformation occurs controlling crack growth and fracture.

From empirical observation, stress intensity (K) still governs the crack growth rates as long as the local yielding and plasticity effects are small with respect to the linear elastic region where K describes the stress state. In practice, K can be used as a parameter to predict fracture and failure based on this LEFM approach when the condition of small scale yielding,

$$B, a, (W - a) \geq 2.5\left(\frac{K_{IC}}{\sigma_{yield}}\right)^2 \tag{2.20}$$

based on sample geometry (W, a, and B, Figure 2.10) and material properties (critical stress intensity: K_{IC} and yield strength: σ_{yield}) is met (Equation 2.20).

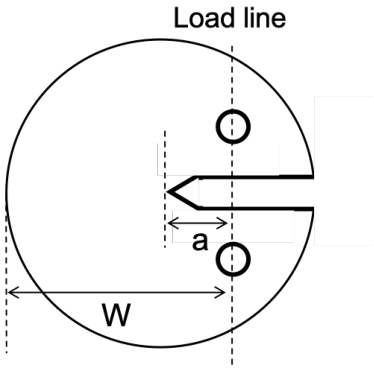

Figure 2.10: The geometry parameters that are used to determine conditions of small scale yielding include sample thickness (B, dimension into figure), distance from load line to edge of sample (W), and crack length measured from the load line (a).

The stress intensity (K) quantifies the crack tip driving force. In order to predict fracture, a criteria for a critical value of stress intensity must be established. The critical stress intensity (K_{IC}) is the stress intensity at which fracture occurs. This can then be used along with Equation 2.18 to predict a critical crack length for a given stress state and geometry or vice versa. In conditions of plane stress, the critical stress intensity remains dependent on the geometry of the sample. In plane strain conditions, the critical stress intensity is independent of geometry and can be used as a material property.

In conditions of plane stress (thin samples), the dominant yielding is at 45° to the thickness axis (Figure 2.11, left). This leads to an inconsistent stress field through the thickness and a large plastic zone relative to the thickness of the material. In conditions of plane strain (thick samples) the ductile failure planes at 45° form in the direction perpendicular to the thickness (Figure 2.11, right). This creates symmetric planes of ductile yielding with respect to the crack growth. In plane strain conditions, Poisson contraction and changing stress state at the edges are negligible relative to a homogeneous stress state through the thickness of the material at the crack tip and the plastic zone is small relative to the thickness. Consequently, the stress intensity is a function of the sample geometry (Equation 2.18).

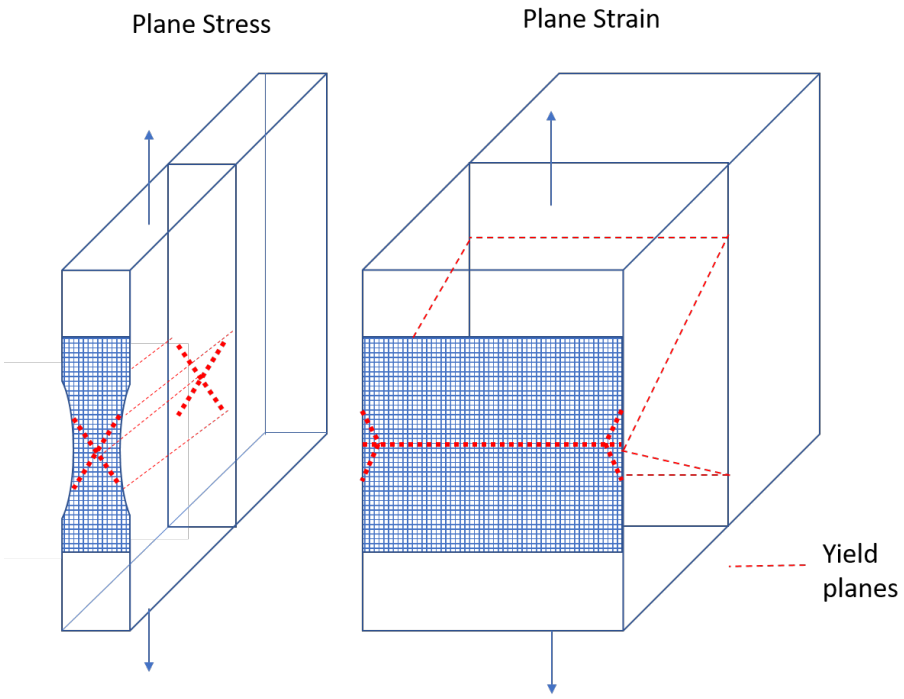

Figure 2.11: In thin samples the Poisson contraction at the edges is large relative to the total thickness and the planes of maximum shear are at 45° to the axis of load. However, in plane strain, when the sample is thick, the dominant yielding is also at 45°, but in parallel to the direction on load which leads to a symmetric highly constrained stress state at the crack tip that is independent of geometry.

In conditions of plane stress, typically thin specimens, K_I is a function of geometry. However, in conditions of plane strain, the value of K_I is constant (Figure 2.12). Since the stress intensity factor (K_I) is constant in plane strain conditions, the critical stress intensity, the stress intensity at which fracture occurs, can be considered a material property.

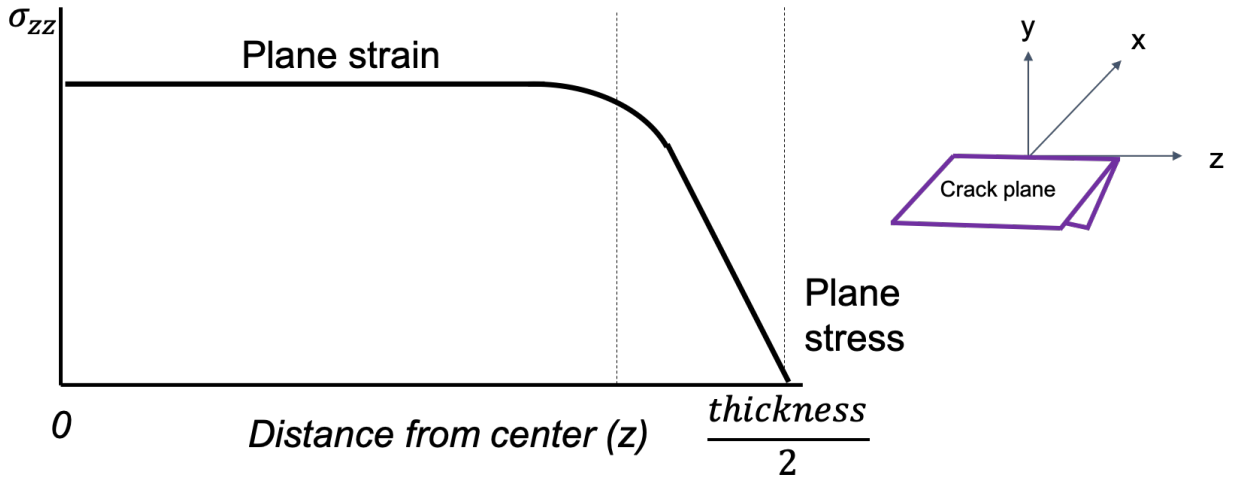

Figure 2.12: The critical stress intensity can be considered a constant material property if conditions of plane strain are met and the stress state is homogeneous throughout the thickness of the sample. In conditions of plane stress, this is not the case and the stress intensity remains a function of the specimen geometry. Adapted from [102]

Application of LEFM to Fatigue

We have introduced stress intensity as a failure criteria to predict fracture under a static applied far field stress. Stress intensity can also be used to describe the driving force for crack growth under cyclic loading, such as the loading present in orthopedic implants. Like in the static case, in cyclic loading, stress intensity is a function of geometry (F) and crack length (a). The difference is that rather than a monotonic far field stress, cyclic stress ($\Delta\sigma_\infty$) is used (Equation 2.21).

$$\Delta K_I = F\Delta\sigma_\infty\sqrt{\pi a} \tag{2.21}$$

The relationship between crack growth rate ($\frac{da}{dN}$) and the cyclic stress intensity (ΔK) characterizes fatigue crack propagation. Paris was the first to define a linear relationship between the log-log plot of ΔK and $\frac{da}{dN}$ (Equation 2.22, Figure 2.13):

$$\frac{da}{dN} = C(\Delta K)^m \tag{2.22}$$

The region below the linear region is referred to as the threshold. Generally, no crack growth is observed below $\Delta K_{threshold}$. This region can be compared to the fatigue limit of the total life approach. However, studies of small crack behavior show that this is not a true

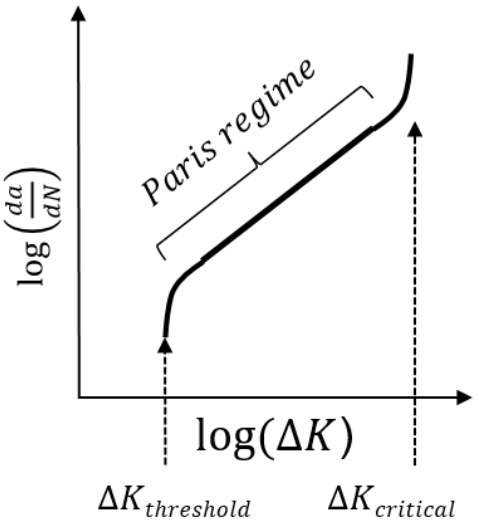

Figure 2.13: The Paris regime describes the linear relationship between cyclic stress intensity (ΔK) and the crack growth rate ($\frac{da}{dN}$) between the initiation of crack growth ($\Delta K_{threshold}$) and fast fracture ($\Delta K_{critical}$).

limit to crack growth and different mechanisms operate at small length scales. At high values of ΔK, runaway crack growth occurs as the material fails in fast fracture. This critical limit ($\Delta K_{critical}$) is loosely related to the monotonic K_{IC}.

The fatigue crack growth properties for a given material are used to predict the life of a material based on a known initial crack size and critical stress intensity, K_{IC}, at which failure will occur. The Paris relationship can be integrated to obtain an initial or final crack length or number of cycles between two given crack lengths. This approach can be used to establish inspection regimes to detect potentially critical cracks in a safety critical design.

The assumptions inherent in a LEFM approach to fatigue are the following: 1) ductile yielding at the crack tip is small relative to the region described by the stress intensity factor and 2) the material behavior is linear elastic. These assumptions must be considered when applying a LEFM approach to characterize crack growth in medical polymers.

The first assumption of a LEFM approach to fatigue is that ductile yielding at the crack tip is small relative to the region described by the stress intensity factor. This can be met by using specimen geometries that meet the condition of small scale yielding (Equation 2.20). The standard geometries used are outlined in ASTM 647 - Standard Test Method for Measurement of Fatigue Crack Growth Rates and ASTM D5045 - Plane-Strain Fracture Toughness and Strain Energy Release Rate of Plastic Materials.

The second assumption of LEFM is that the material behavior is linear elastic. A criteria for the validity of a linear elastic approximation for non-linear materials is presented in ASTM D5045 Section 9.1.1.

As discussed in Chapter 1, LEFM has been used in orthopedics to predict the fracture behavior and fatigue life of UHMWPE. Yet, UHMWPE, as a polymer, is not a linear elastic material, violating an assumption of LEFM. Rather, the material response of UHMWPE is nonlinear and viscoelastic. However, at relevant strain rates, a linear approximation of the material properties is close enough to make the predictions of LEFM useful for design. UHMWPE exhibits a linear Paris regime as do other polymeric materials that do not adhere to linear elastic behavior [103].

2.2.3 The Application of LEFM to Orthopedic Polymers

Little is known about the mechanisms of fatigue crack growth in PCU biomaterials. Historically, LEFM has been used to study the impact of different processing techniques on the fatigue crack resistance of UHMWPE. Therefore, this study seeks to apply LEFM to study fatigue crack growth in PCU.

Extensive work has been done in studying the fatigue crack growth and fracture behavior of UHMWPE using a LEFM approach beginning in the early 1980's [104]. As outlined in Section 1.4.1, various changes the the microstructure of UHMWPE have been made over the years in attempt to improve the wear and oxidation resistance of the material. These changes have come at the cost of a loss in resistance to fatigue crack growth leading to premature fracture [38, 15, 37, 105, 106, 107].

The microstructure of UHMWPE is characterized by crystalline lamellar regions within regions of amorphous polymer chains. Other variables that impact the microstructure of UHMWPE are the degree of crosslinking within the amorphous region of the polymer as well as the overall molecular weight of the polymer chains [38]. The degree of crosslinking is controlled by irradiation applied during sterilization or specifically to increase the crosslink density of the material. The percent crystallinity and lamellar thickness can be impacted by irradiation, high pressure molding processes, annealing, and post-annealing remelting processes. Finally, post-synthesis changes to the molecular weight of the polymer through oxidation can be impacted by irradiation, annealing, post-annealing remelting processes, and the addition of antioxidants (Vitamin E) into the material. All of these parameters can then be correlated to a change in the fatigue resistance of UHMWPE [38].

UHMWPE is a nonlinear and viscoelastic material. However, the application of a LEFM approach to describe its fracture and fatigue crack resistance has been shown to be informative in studying the impact of structural changes on the material performance. Reproducible

Paris behavior has been reported by numerous groups [106, 105, 37, 107]. It has been shown that the crack growth in UHMWPE dominates any viscoelastic creep or relaxation effect [108]. It does not exhibit many mechanisms commonly seen in polymers like crazing ahead of the crack tip or shear banding. This results in crack growth that is dominated by the peak load rather than the cyclic loading magnitude [108].

Like PCU, the properties of UHMWPE that make it an effective material in TJR are based on the structure of the polymer. UHMWPE has crystalline regions within an amorphous matrix that provide the high energetic toughness of the material. PCU has a phase-separated structure giving it a high toughness as well. In a similar parallel, it is likely that the fatigue crack resistance of the material will be highly sensitive to the structural organization of PCU. Therefore, it is important to explore the mechanisms of fatigue crack growth in PCU.

Miller et al. used a stress-based total life fatigue evaluation of injection molded polycarbonate polyurethane to show that the fatigue life was positively correlated with the hard segment content (Figure 2.14). The stress life curve shifted higher with increased hard segment content and higher effective hardness [109, 110, 111]. Wiggins et al. did a study using a diaphragm to study the impact of fatigue loading on biodegradation of PCU. Although this is not a direct evaluation of the mechanical properties of the material, they found that strain rate and stress state (uniaxial vs. biaxial loading) were important factors impacting degradation [112, 113].

This study uses a safety-critical, defect-tolerant approach to characterize fatigue in PCU. This approach investigates the mechanisms that control and propagate a flaw under fatigue conditions that mimic orthopedic implant applications. Understanding the mechanisms that propagate a flaw under cyclic loading, we can better predict potential long-term failure mechanisms of this material. The objective of this study is to explore the impact of time-dependent effects and hydration on the ability for cracks to propagate in PCU.

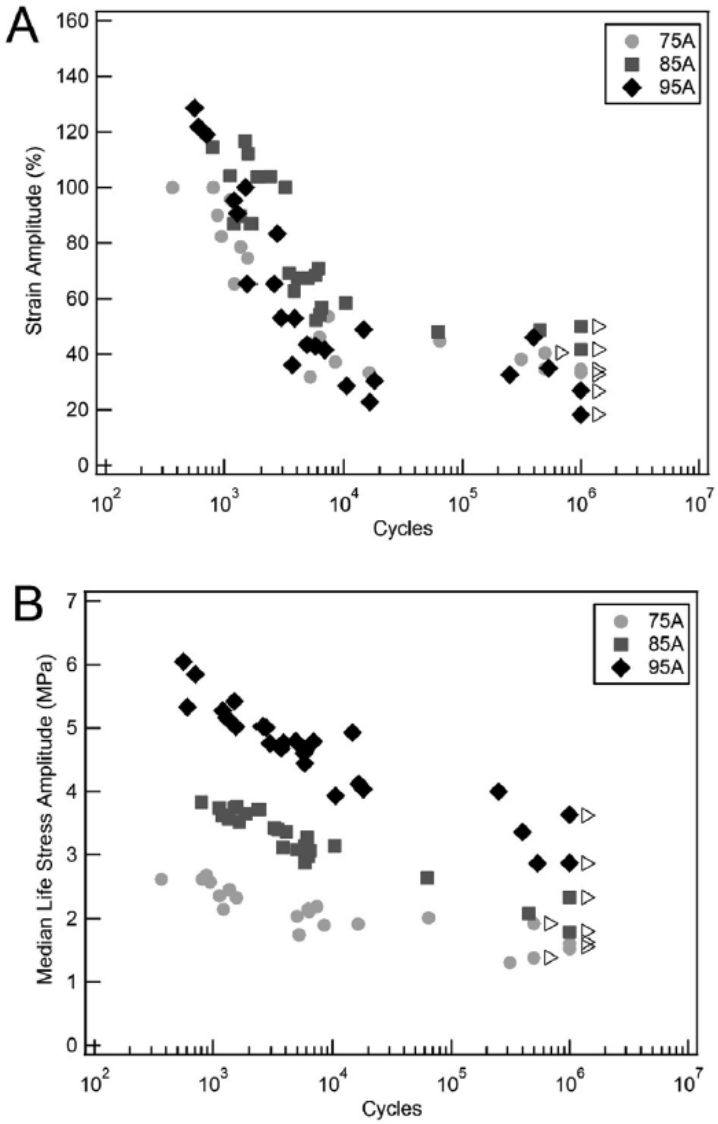

Figure 2.14: The stress-life relationship between cyclic load and number of cycles to failure for three polycarbonate polyurethane copolymers. Arrows at the end of the curves indicate that failure was not observed. Reprinted from [111], with permission from Elsevier.

2.3 Methods

Polycarbonate polyurethane, trade name Bionate® 75D (named for its Shore hardness value), was obtained from DSM Biomedical, Berkeley, CA. Extruded rod stock of UHMWPE 1020 GUR was obtained from Orthoplastics, Lancashire, UK.

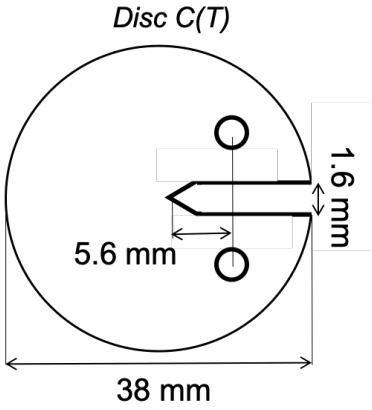

Figure 2.15: Geometry of compact tension disc specimens based on guidelines of ASTM E647 (thickness = 3.3 mm).

Compact tension disc specimens were machined from injection molded Bionate® 75D discs (3.3 mm thick, 38 mm in diameter) and machined from rod stock of UHMWPE 1020 as guided by ASTM E1820 and E647 (Figure 2.15). A 1.0 ± 0.2 mm pre-crack was started with a razor blade in the 0.005 in radius notch. The samples were cyclically loaded in tension (loading ratio F_{max}/F_{min}: R = 0.1, number of samples: n = 3 - 4) using a servohydraulic Instron 8871 (Norwood, MA). Unless otherwise specified, testing was done in air at room temperature, with a forced air-cooling system to reduce hysteretic heating, and under cyclic loading from 14 - 140 N. Crack growth was recorded optically (Infinivar CFM-2/S, 5 μm/pixel and Sony XCD-SX910 camera) and a custom MATLAB code was used for crack tip image processing.

Five test sub-groups were evaluated to test the effects of material, loading, frequency, conditioning, and annealing, respectively, as outlined in Table 2.1. First, compact tension specimens of PCU and UHMWPE with identical geometries were compared. Loading was applied with an increasing ΔK in order to avoid crack blunting in the UHMWPE. Samples were loaded with increasing ΔK stepped from 10 - 100 N in increments of 1 - 10 N every 30,000 cycles until failure (i.e 10 - 100 N, 11 - 110 N, ...). The goal of this test was to compare PCU to the current clinical standard, UHMWPE, for which extensive fatigue crack growth characterization has been performed.

Second, samples were tested both intermittently, continuously, and with increasing ΔK at 5 Hz in air. Intermittently loaded samples were loaded 8 - 10 hours/day and unloaded completely overnight (1 - 4 nights). Continuously loaded samples were loaded 24 hours/day. Ramped samples were loaded intermittently, but with only one period of unloading. This test was run based on time observations made during testing and is relevant to potential

Table 2.1: Outline of the test variables studied

Test Group	Material	Loading	Frequency	Conditioning	Annealing
1	UHMWPE PCU	Ramped	5 Hz	Dry	None
2	PCU	Ramped Continuous Intermittent	5 Hz	Dry	None
3	PCU	Intermittent Continuous	2 Hz 5 Hz 10 Hz	Dry	None
4	PCU	Continuous	5 Hz	Dry Hydrated	None
5	PCU	Continuous	5 Hz	Hydrated	None 140°C

relaxation effects that could occur in an *in vivo* loading situation.

Third, the effect of frequency was evaluated by testing samples at 2, 5, and 10 Hz. Samples tested at 2 Hz were tested intermittently while samples tested at 5 and 10 Hz were tested continuously. Following the time depending observations of the second test group, frequency was investigated to further understand the viscoelastic impacts on fatigue crack growth in PCU.

Fourth, the effect of hydration was evaluated by testing conditioned samples fully submerged in a phosphate buffered saline (PBS) bath at room temperature. Crack measurements were performed while samples were loaded in the environmental bath chamber (acrylic walls). Hydrated samples were soaked in PBS and the mass was measured daily (to ensure that equilibrium had been reached). All samples were tested after more than 30 days of conditioning. This test was run because of the known impact of hydration on the mechanical properties of PCU. The *in vivo* environment is hydrated, therefore understanding the impact of hydration is highly relevant.

Fifth, the effect of annealing was evaluated by testing hydrated samples that had been annealed at 140°C for 24 hours. The goal of this test was to evaluate the impact of a different structural organization on the mechanical response to crack growth. Different thermal and temporal processing during manufacturing can lead to a range of phase-separated structures in PCU. Therefore, the goal of looking at a different heat treatment was to understand how much the mechanical response could potentially shift.

After fatigue failure, the fracture surfaces were sputter coated and imaged with a Hitachi 2460 Scanning electron microscope (SEM). In order to compare the fatigue fracture surfaces to monotonic failure, a single compact tension specimen of equivalent geometry was tested at a strain rate of 50 mm/min until failure, sputter coated and imaged with the SEM.

Results are presented as average ± standard deviation. A Student's t-test and one-way ANOVA with post hoc analysis were used to compare means.

2.4 Results

2.4.1 Test Group 1: PCU vs. UHMWPE

Table 2.2: Summary of Test Group 1

Test Group	Material	Loading	Frequency	Conditioning	Annealing
1	UHMWPE PCU	Ramped	5 Hz	Dry	None

The aim of the first test group was to compare the fatigue crack propagation in PCU to the 'gold-standard' polymer in the orthopedics industry, UHMWPE (Table 2.2). The UHMWPE samples did not meet conditions of small scale yielding and PCU samples only met the conditions of small scale yielding for approximately the first 1.4 mm of crack growth. Therefore, with the presence of plane stress conditions, an equivalent geometry, at clinically relevant thickness, was used to compare crack growth. The presence of plane stress conditions is reflected in the high stress intensity values measured for UHMWPE. Previously reported stress intensity values, for fatigue crack growth of UHMWPE under small scale yielding conditions, was in the range of 0.5 - 2 MPa$\sqrt{m}$ [39, 37]. The plane stress fatigue crack growth data was, as expected for plane stress conditions, observed in a higher range of stress intensities (2 - 8.5 MPa$\sqrt{m}$, Figure 2.16).

The rationale for using thin specimens was due to the limitations of injection molding PCU samples. The PCU samples had to be thin in order to obtain specimens that had a homogenous structural organization. Thicker samples resulted in a gradient in phase separation through the thickness of the sample, due to uneven cooling gradients, that was optically observable in the opacity of the sample. A distribution in structural organization was expected to impact the mechanical response and was therefore undesirable. A 3.3 mm thick disc was decided upon as a thickness that already had an existing mold made and produced an optically homogenous structure.

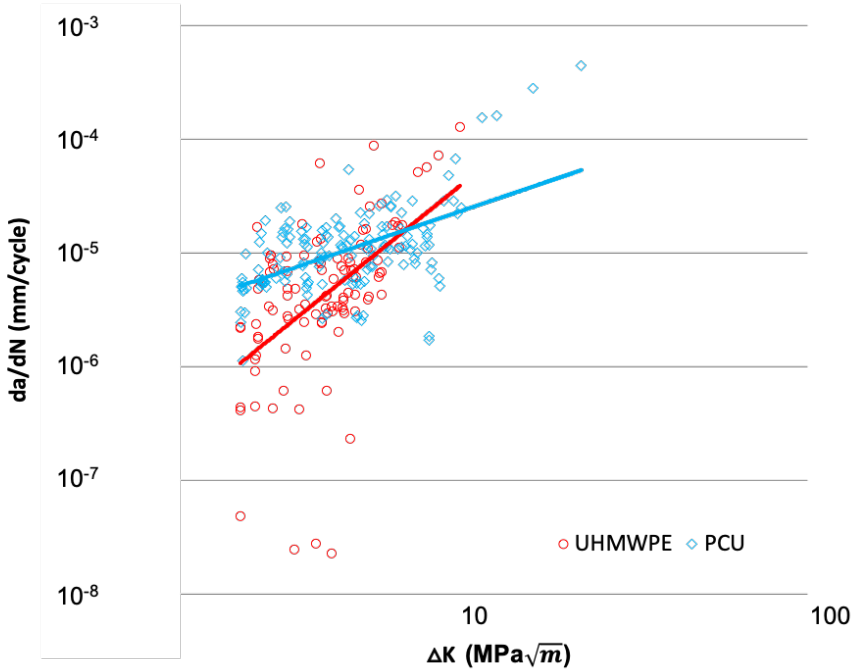

Figure 2.16: Fatigue crack growth in PCU compared to UHMWPE. A strong Paris regime was not observed for either material, but the slope of the data was higher for UHMWPE than for PCU. Crack growth occurred at a similar range of ΔK for both materials, but UHMWPE showed a larger range of crack speeds. (n = 3)

The results of test group 1 found that neither material exhibited a strong linear Paris regime, but the Paris coefficient, m, is higher for UHMWPE (Figure 2.16). The crack growth rate as a function of number of cycles of PCU proceeded at a very consistent rate as ΔK increased (slope = 1 x 10^{-5} ± 0, R^2 = 0.91 ±0.1). In comparison, UHMWPE crack growth proceeded very slowly at first before accelerating at higher values of ΔK (slope = 4.3 x 10^{-6} ± 0, R^2 = 0.85 ± 0.1, Figure 2.17). Although crack growth proceeded with largely different rates, both PCU and UHMWPE have a similar number of cycles to failure and crack length at failure ($p > 0.05$, Figure 2.18). In PCU, the crack remained sharp throughout crack growth with little crack mouth opening displacement (CMOD). However, crack growth in UHMWPE was characterized by a process of blunting and sharpening with much greater CMOD and crosshead displacement (Figure 2.19).

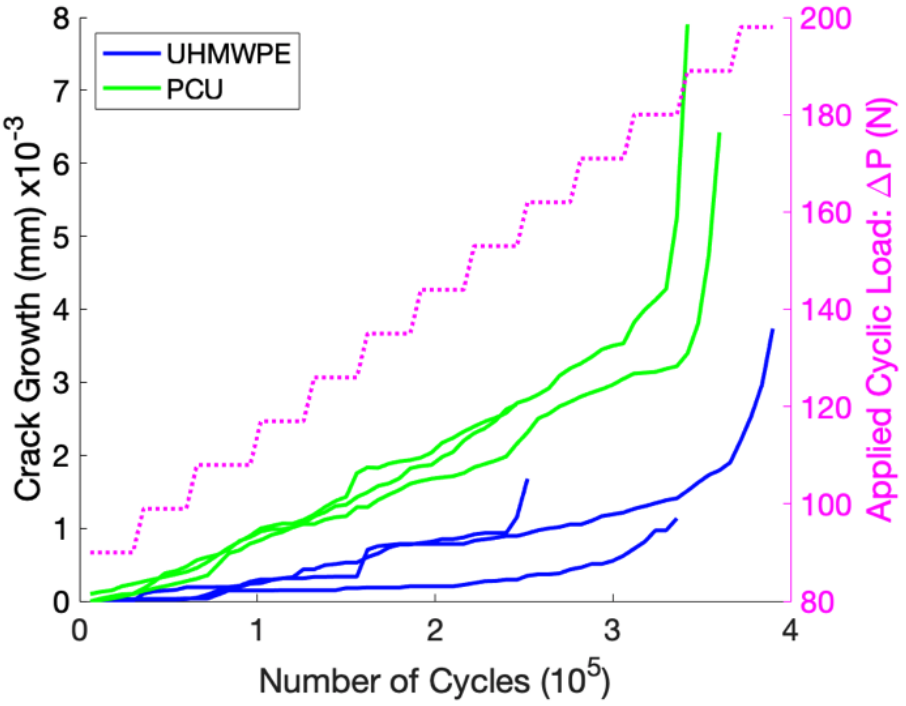

Figure 2.17: Crack growth as a function of number of cycles. Individual lines represent individual samples (n = 3).

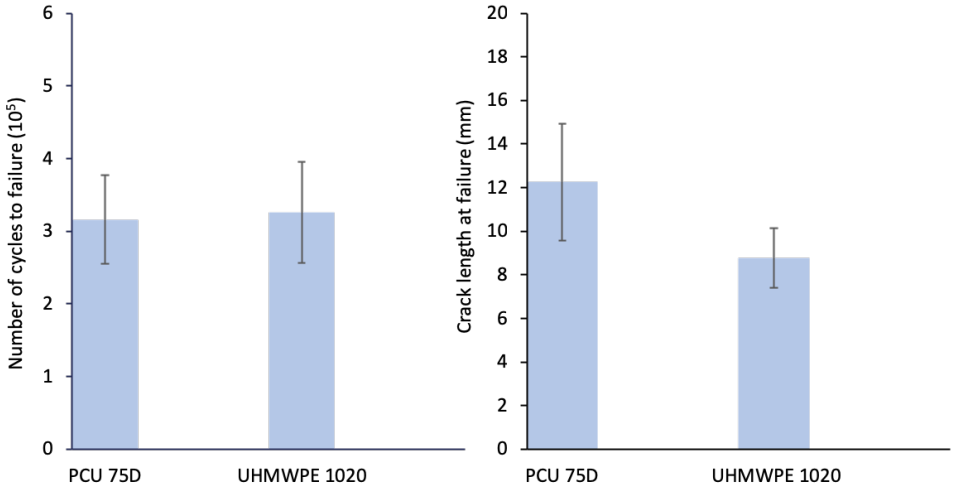

Figure 2.18: Number of cycles to failure (left) and crack length at failure (right) for PCU and UHMWPE.

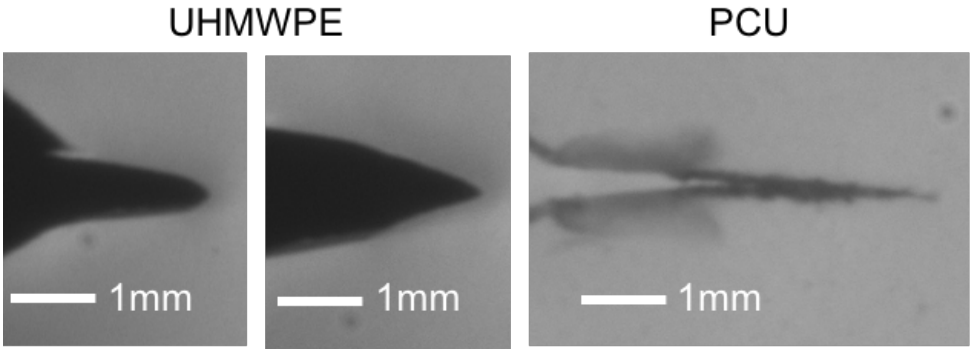

Figure 2.19: Crack growth in representative samples was characterized in UHMWPE (left two images) by blunting and sharpening of the crack tip, while in PCU (right) the crack tip remained sharp throughout growth.

2.4.2 Test Group 2: Intermittent vs. Continuous Loading

Table 2.3: Summary of Test Group 2

Test Group	Material	Loading	Frequency	Conditioning	Annealing
2	PCU	Ramped Continuous Intermittent	5 Hz	Dry	None

The second test group looked at the impact of continuous loading (24 hours/day), intermittent loading (8 - 10 hours/day, allowing for relaxation overnight), and ramped loading (increasing ΔK by 10 - 100 N every 30,000 cycles) (Table 2.3).

Similar to samples loaded continuously, samples loaded intermittently and with ramped loading did not exhibit a strong Paris relationship between $\frac{da}{dN}$ and ΔK. However, comparing the Paris data for samples loaded continuously and samples tested under ramped loading shows that neither group shows significant crack acceleration with increasing ΔK. However, the range of crack growth rates in continuously loaded samples was much greater for continuously loaded samples than for ramped samples. Crack speeds of 10^{-8} - 10^{-6} mm/cycle were observed for continuously loaded samples, but not ramped samples where all crack growth proceeded closer to 10^{-5} mm/cycle until failure (Figure 2.20). This highlights the fact that ΔK is not the dominant variable controlling crack growth when the applied load can alter crack growth speeds.

Crack growth in samples tested intermittently was observed to proceed linearly (Figure 2.21A). Stress shielding mechanisms evidenced by crazing, out of plane crack deflection, and

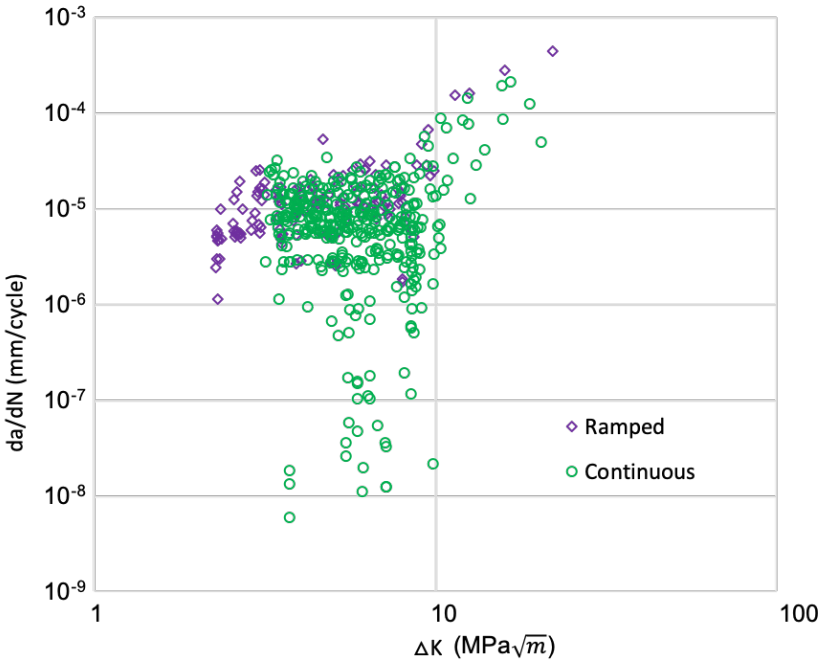

Figure 2.20: Comparison of crack velocity (da/dN) and stress intensity factor (ΔK) range between samples loaded with a constant cyclic load (continuous) and increasing cyclic load (ramped). In the case of continuous loading, the increase in stress intensity (ΔK) was driven by crack extension. In the case of ramped loading, an increasing applied load the increase in stress intensity (ΔK) was a combination of crack extension and increasing cyclic load (reference Equation 2.21).

the presence of multiple initial crack tips, that ultimately resulted in the dominance of one, were observed. Additionally, crack growth did not proceed evenly through the thickness of the sample. Fatigue crack propagation proceeded without an increase in crack mouth opening displacement or crosshead displacement.

Following a period of unloading, samples failed in fast fracture upon reloading. For example, samples were tested 8 - 10 hours (144,000 - 180,000 cycles) per day and testing was stopped and the samples were unloaded overnight. After 1 - 4 days of this regimen, upon reloading, the samples failed before 1000 cycles had been completed. Failure occurred after 3 - 6 mm of stable crack growth. The abrupt brittle failure is clear on the fracture surface with a transition from a rough to a smooth surface (Figure 2.22). The initial crack growth exhibits a classically rough crazed fracture surface attributed to the fibril fracture during craze failure. At failure, the crazed fracture surface transitions to a smooth and largely featureless surface characteristic of brittle failure [103].

Crack growth in samples tested continuously as a function of number of cycles was linear until failure. In continuously tested samples, the first 2 - 4 mm of crack growth proceeded

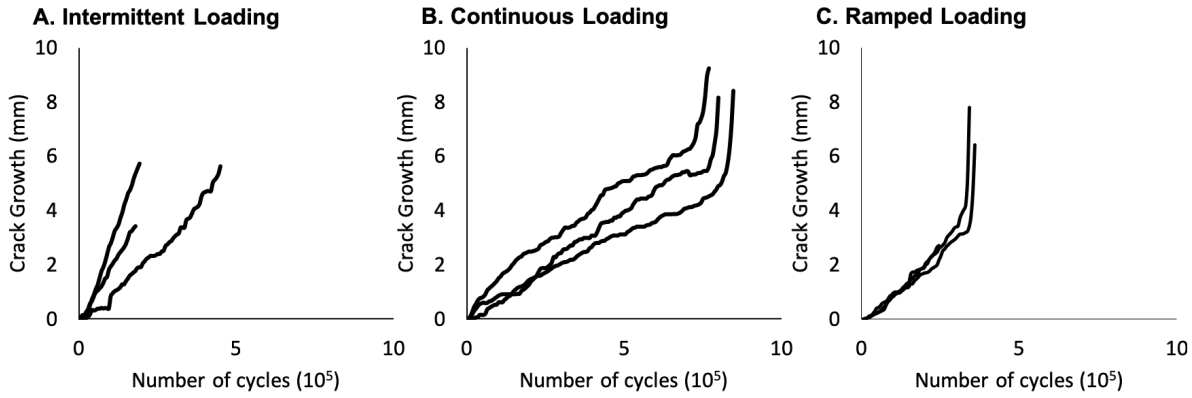

Figure 2.21: Crack growth per number of cycles for PCU samples with intermittent, continuous, and ramped loading. Each line represents individual samples [57].

without discernible CMOD. After 2 - 4 mm, the crosshead displacement increased, but the crack tip remained sharp for a total crack length of greater than 10 mm before opening into a mode of ductile tearing with visible gross deformation at the crack. Multiple crack tips were observed in one one sample. Otherwise, crack growth was largely Mode I. In contrast to the fracture of the intermittently loaded sample, the continuously loaded samples never completely fractured, but, at large crack lengths, proceeded to tear until opening to 180° (seen in Figure 2.21B as abrupt increase in crack length at failure). In the continuously loaded samples, fractography showed a continuous crazed surface, 7 - 9 mm long, with regular bands perpendicular to crack growth at longer crack lengths (Figure 2.23). Both the number of cycles until failure and the crack length at failure for continuously loaded samples was statistically significantly greater than intermittently loaded sample (Student's t-test: $p \leq 0.05$, Figure 2.24). Samples continuously loaded sustained approximately twice as many cycles until failure as those samples that were intermittently loaded and underwent brittle fracture.

In samples that were loaded with increasing ΔK, ramped from 10 - 100 N by 1 - 10 N every 30,000 cycles, the crack growth was linear. The crack growth rate had a constant slope similar to that of samples loaded continuously at a constant ΔK (Figure 2.21C). The formation of multiple crack tips was observed in 2 of 3 of the samples. Both crack tips were traveling perpendicular to the direction of loading and one quickly dominated. Ramped samples were also loaded over two days and so had a period of relaxation similar to the intermittently loaded samples. However, ramped samples were unloaded after over 17 - 170 N of cyclic loading which is significantly higher than the constant 14 - 140 N of the intermittently loaded samples. Samples with ramped loaded exhibited both tearing and brittle fracture. One sample underwent fast fracture upon reloading at 18 - 180 N. Two samples underwent tearing failures after being reloaded at 20 - 200 N. Irregardless of the difference in failure modes, the total number of cycles to failure and crack length at failure for sam-

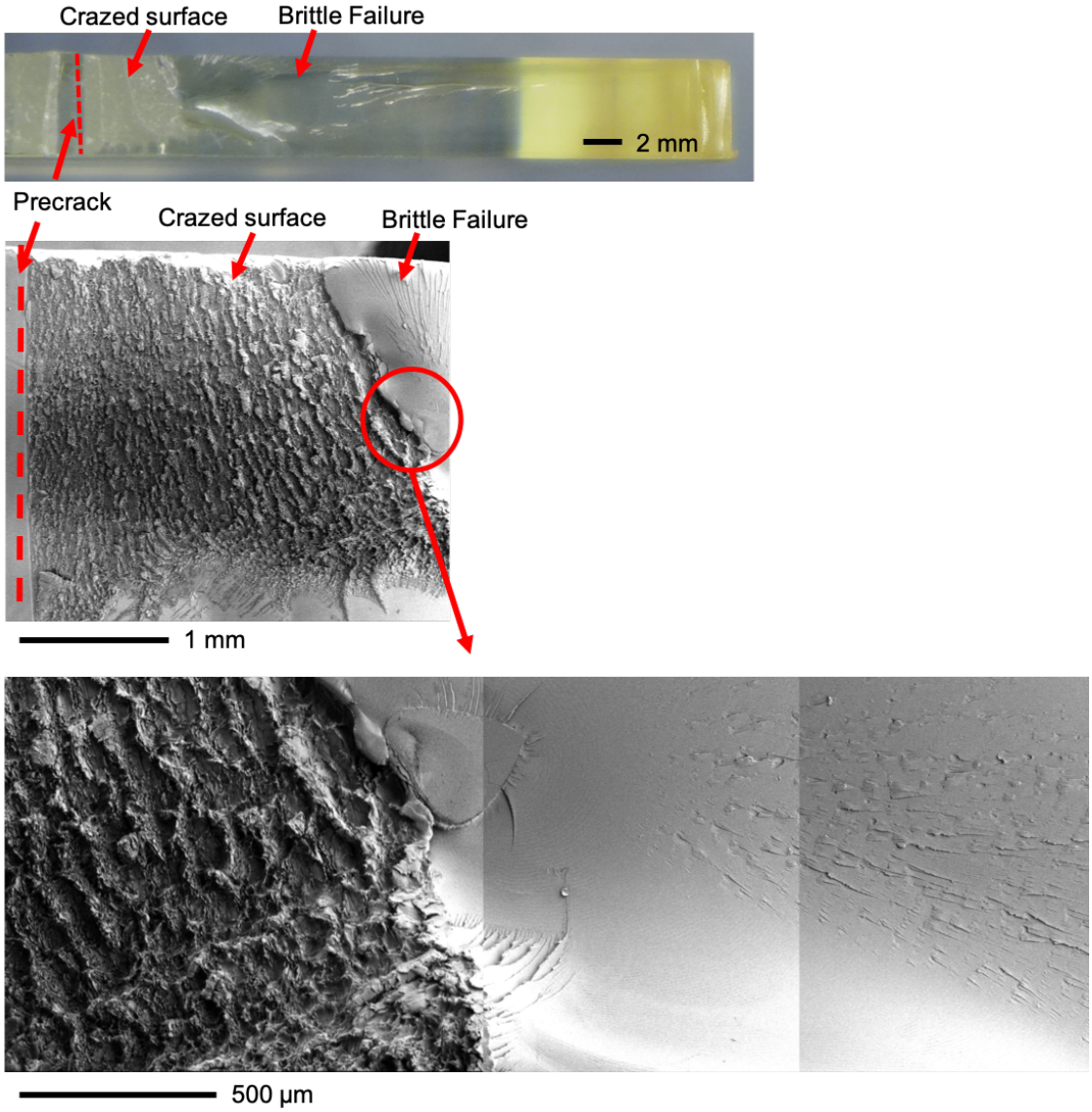

Figure 2.22: Fractography of a sample that was loaded intermittently shown at three size scales. A clear transition can be seen between the rough crazed fracture surface where crack growth was slow and the smooth, brittle, fast-fracture surface [57].

ples with ramped loading were statistically similar to that of samples loaded intermittently (ANOVA: $p \geq 0.05$), but statistically different than samples loaded continuously (Figure 2.24).

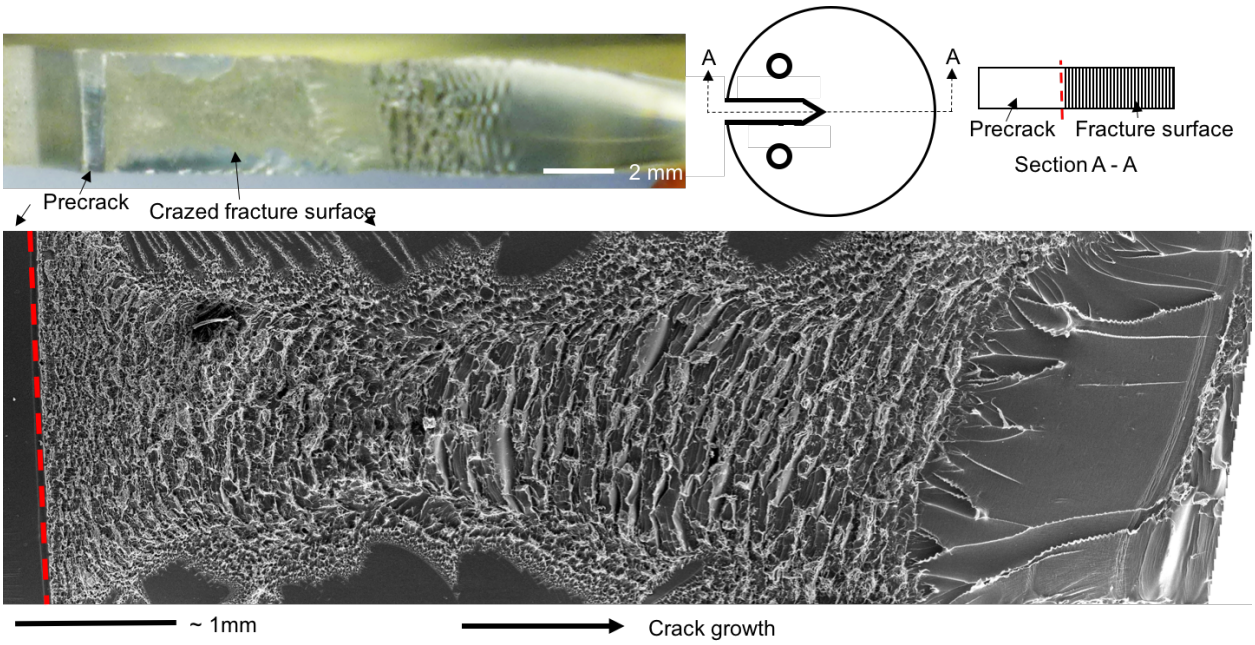

Figure 2.23: Fractography of a sample that was continuously loaded. Compared to the intermittently loaded sample, the crazed region extends much further with features increasing in size until it recedes into ductile lips as the sample tore open to 180°. (note: the SEM image was stitched together from multiple images so the scale is inconsistent) [57].

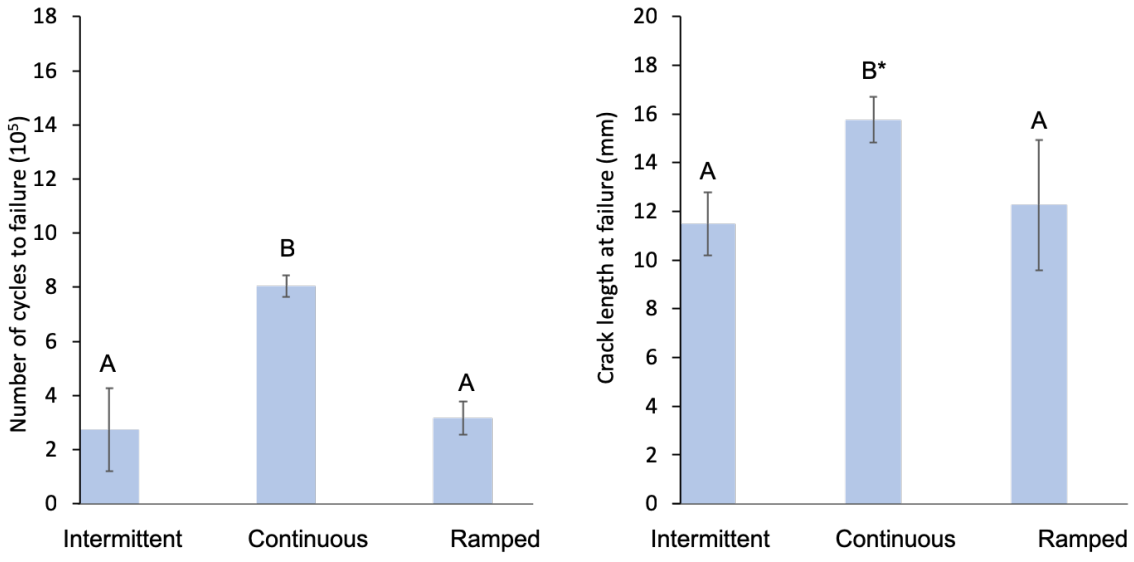

Figure 2.24: Number of cycles to failure (left) and crack length at failure (right) was significantly greater for samples with continuous loading than those with intermittent or ramped loading (*individual Student's t-test: $p \leq 0.004$, one-way ANOVA for crack length: $p = 0.0575$) [57].

2.4.3 Test Group 3: Frequency

Table 2.4: Summary of Test Group 3

Test Group	Material	Loading	Frequency	Conditioning	Annealing
3	PCU	Intermittent Continuous	2 Hz 5 Hz 10 Hz	Dry	None

The third test group investigated the effect of frequency on the fatigue crack growth in PCU (Table 2.4). Crack growth proceeded largely linearly for samples tested at 5 Hz while greater variability in crack growth rates was seen at both 2 and 10 Hz (Figure 2.25).

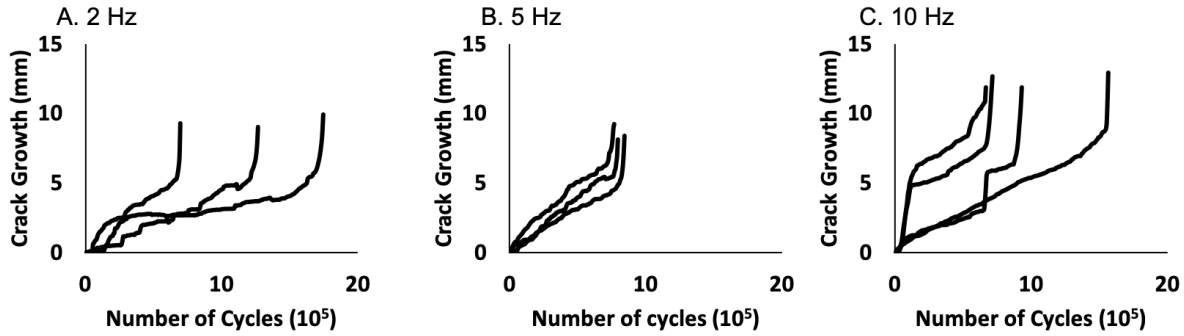

Figure 2.25: Crack growth as a function of number of cycles for samples tested at 2, 5, and 10 Hz. Multiple lines represent individual samples [57].

Crack growth for samples evaluated at 2 Hz was largely Mode I, perpendicular extension with respect to the direction of tensile loading, with little out of plane crack advance (Figure 2.26A). Crack growth in samples tested at 5 Hz was also largely Mode I, but multiple crack tips were present in 1 of 3 samples. In contrast, crack growth in samples tested at 10 Hz did not remain in the plane normal to the load. Rather, crack growth in 3 of 4 samples tested at 10 Hz exhibited crack tip deflection, when the direction of crack growth deviated from growth normal to the loading direction. Additionally, multiple crack tips and non planar growth through the thickness of the sample were observed in 4 of 4 samples (Figure 2.26B). The high prevalence of stress shielding mechanisms at 10 Hz is also seen in the variable crack growth rates .

No significant differences ($p > 0.2$) were observed between the number of cycles to failure and crack length at failure between 2 Hz (1,236,000 $\pm$ 525,642 cycles and 16.0 $\pm$ 0.5 mm) and 5 Hz (804,000 $\pm$ 39,344 cycles and 15.8 $\pm$ 1.0 mm). Samples evaluated at 10 Hz, compared

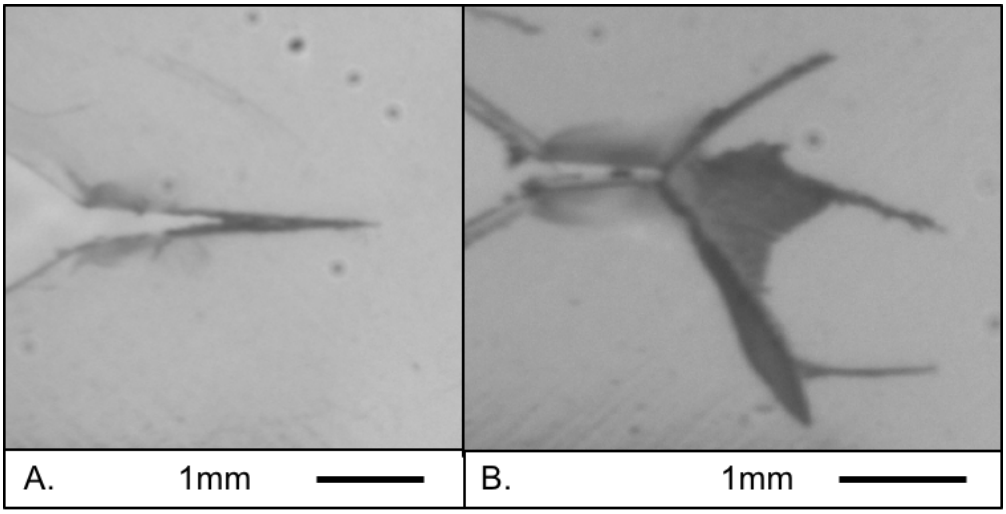

Figure 2.26: Representative images of the growing crack in a sample tested at 5 Hz (A) and 10 Hz (B). The sample at 5 Hz has a single crack growing in Mode I while the sample at 10 Hz shows the growth of multiple crack tips out of plane [57].

to samples tested at both 2 Hz and 5 Hz, had a similar number of cycles to failure (969,000 $\pm$ 414,231 cycles), but sustained a longer crack length at failure (18.9 $\pm$ 0.5 mm, $p < 0.002$, Figure 2.27). Although samples tested at 2 Hz were tested intermittently, no brittle fracture was observed upon reloading.

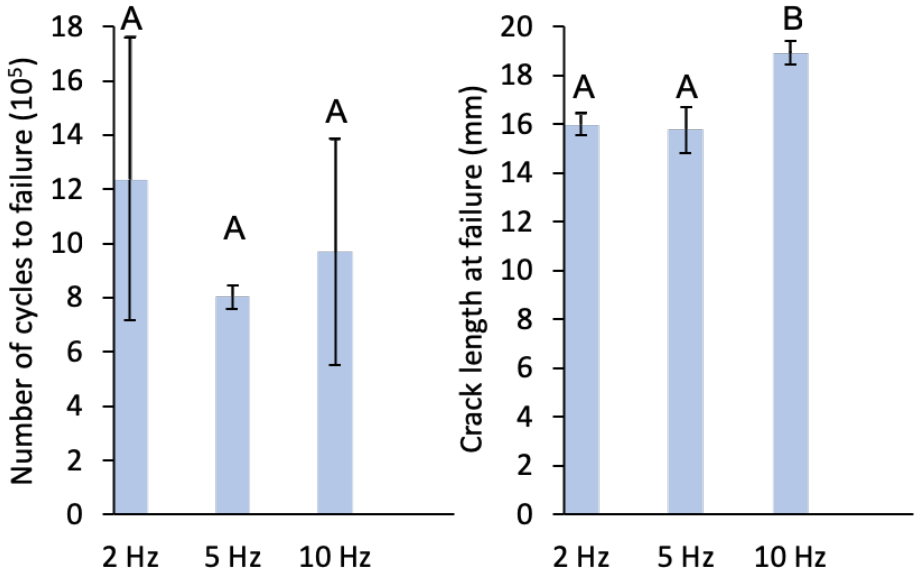

Figure 2.27: Number of cycles until failure and crack length at failure for PCU testing at 2, 5, and 10 Hz (mismatched letters indicate significant difference: $p = 0.0006$) [57].

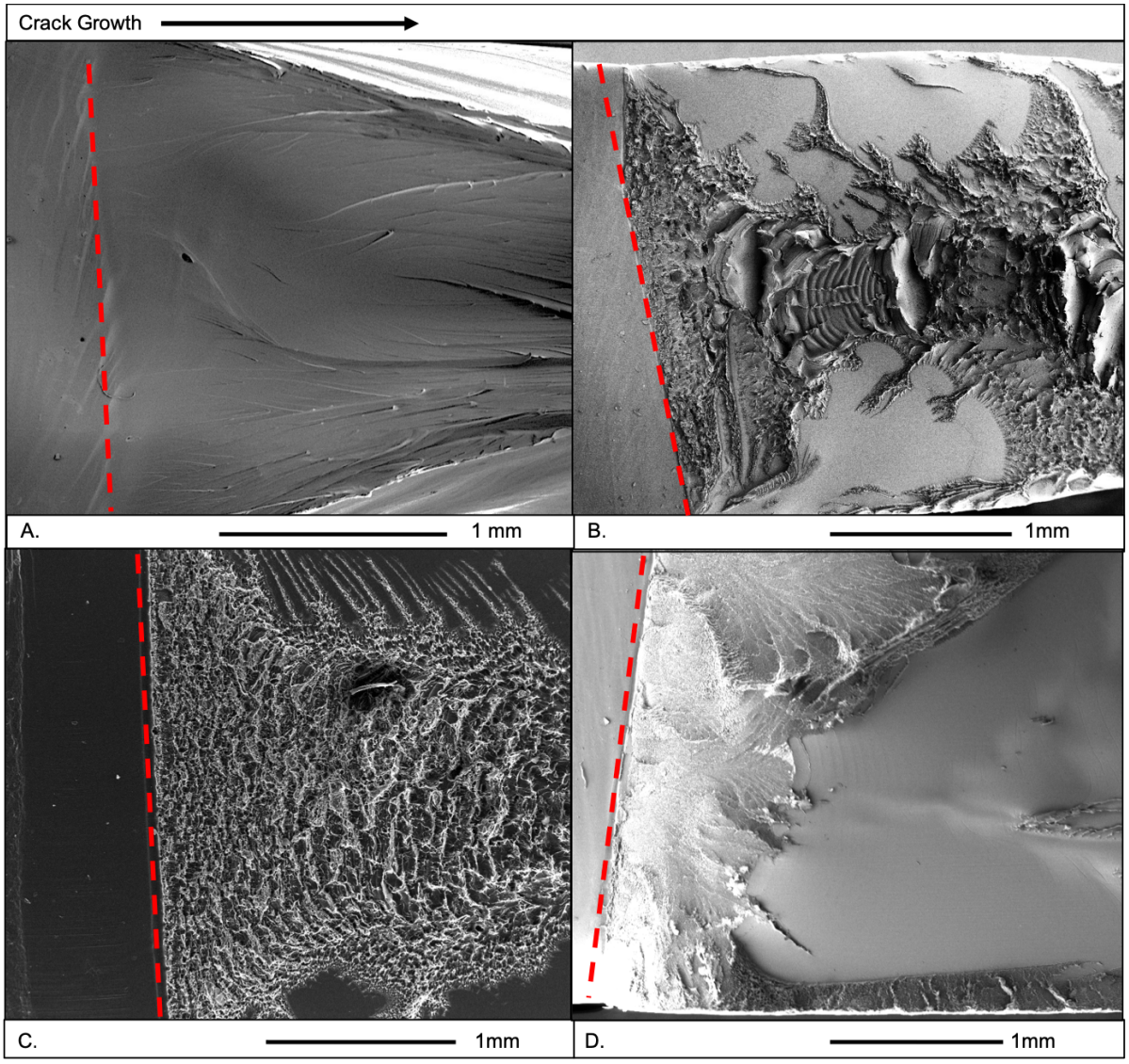

Figure 2.28: Fracture surfaces for disc compact tension specimens tested in monotonic tension at 50 mm/min (A), in cyclic fatigue at 2 Hz (B), 5 Hz (C), and 10 Hz (D). Dotted line indicates start of crack [57].

The testing frequencies resulted in three distinct fracture surfaces. A reference fracture surface of a PCU sample of equivalent geometry pulled in monotonic tension to failure at 50 mm/min is shown in Figure 2.28. The tensile reference has a classically ductile failure surface with evidence of tearing (Figure 2.28A).

In contrast, fractography of samples tested at 2 Hz showed evidence of crazed failure, but features were less evenly distributed. The craze-like features were coarser than that of 5 Hz and coupled with larger-scale ductile features (Figure 2.29B, Figure 2.30). Additionally,

large edge effects were observed where smooth areas rise towards the ductile features in the center of the specimen. Samples tested at 5 Hz show a very consistent craze pattern of fibrillated failure (Figure 2.23, shown in previous section). The size scale of the pattern increases with crack growth. Samples tested at 10 Hz show multiple different failure regions consistent with the growth of multiple crack tips (Figure 2.29A). Additionally, the changes in crack growth rate are apparent in the smooth, brittle region of crack growth which transitioned abruptly to a craze surface more similar to that observed in the 5 Hz samples.

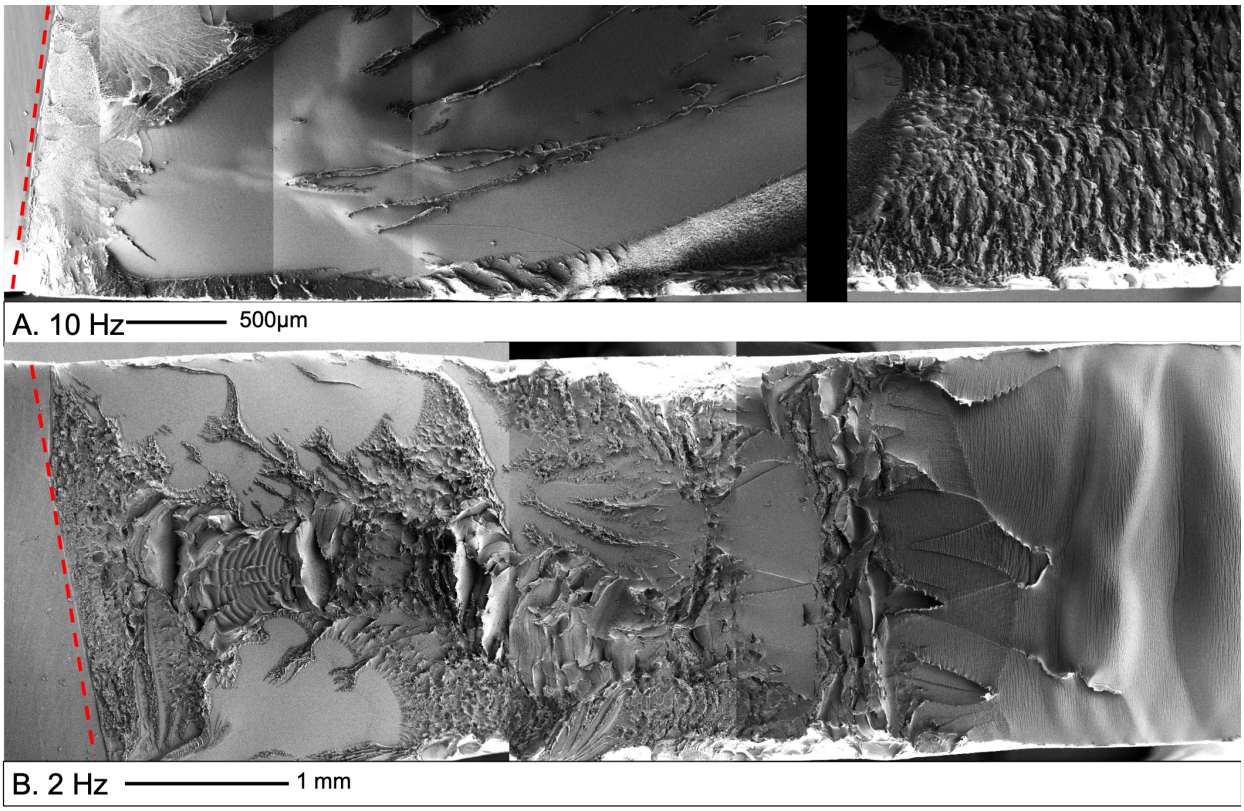

Figure 2.29: Comparison of the fracture surface of a sample loaded at 10 Hz (top) and 2 Hz (bottom). The sample loaded at 10 Hz shows inconsistent features with large areas of smooth brittle failure that return to a crazed surface later on. Fracture on different planes in visible close to the beginning of fracture due to the presence of multiple crack tips. The sample loaded at 2 Hz shows craze like features, but with overall larger features and strong transverse edge effects [57].

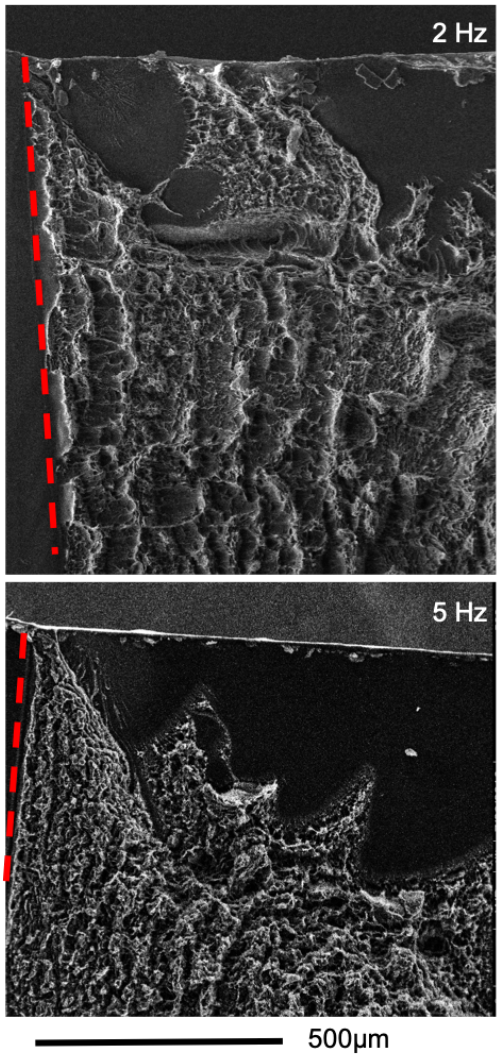

Figure 2.30: Crazing was observed in samples tested at both 2 Hz (top) and 5 Hz (bottom). This image compares the size of the craze features on the same length scale. The crazed features in the sample tested at 2 Hz are larger with a striated pattern perpendicular to the direction of crack growth that is spread further apart than the similar pattern perpendicular to the direction of crack growth. In both samples a smooth surface is observed on the edge of the sample. This is likely due to a different stress state in which poisson effects play a more significant role than in the more constrained middle of the sample [57].

2.4.4 Test Group 4: Hydration

Table 2.5: Summary of Test Group 4

Test Group	Material	Loading	Frequency	Conditioning	Annealing
4	PCU	Continuous	5 Hz	Dry Hydrated	None

The fourth test group explored the impact of hydration on the fatigue crack growth in PCU (Table 2.5). Hydrated samples were conditioned in PBS for over 30 days prior to testing. During which time the water uptake reached equilibrium at an average of 0.72 wt.% increase. Hydration resulted in smoother and more exponential crack growth rate than the discontinuous FCP observed in dry specimens (Figure 2.31).

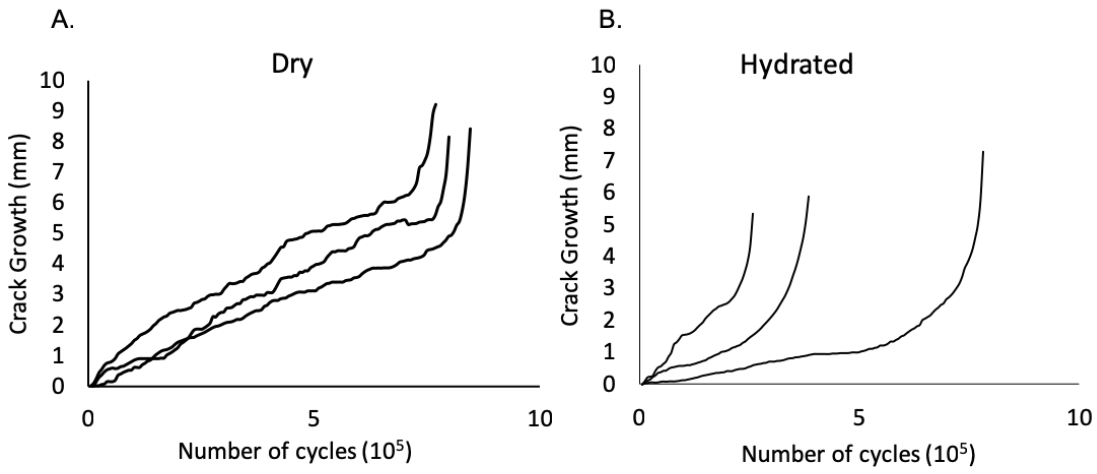

Figure 2.31: Crack growth as a function of number of cycles for dry versus hydrated samples. In dry samples, crack growth is largely linear, but proceeds in jumps. In hydrated samples, crack growth proceeds in a much smoother manner with more exponential growth than dry samples [57].

At small crack lengths (< 1 mm), craze mechanisms (fibrillation) were observed as darker bands at the crack tip ahead of the crack mouth opening. At longer crack lengths, there was an increase in crack mouth displacement with extension compared to dry samples (Figure 2.32). Crack growth to failure was only seen in three of five tested samples. In two samples, the crack blunted and no further crack growth was observed for approximately 700,000 cycles.

The number of cycles to failure for hydrated sample was not statistically different than that of dry samples, but the crack length at failure of hydrated samples was significantly

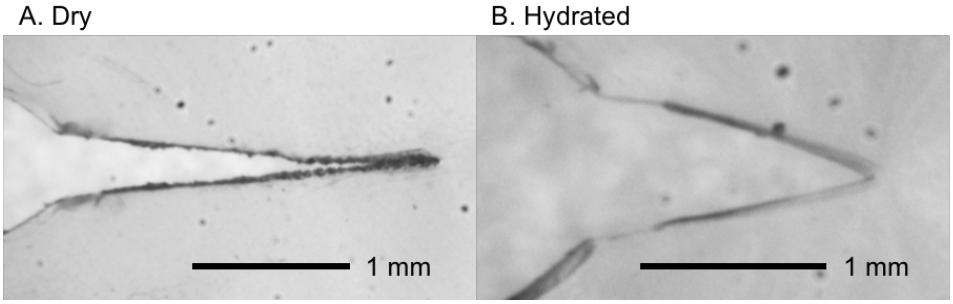

Figure 2.32: Crack growth in dry sample (A) proceeded with less crack mouth opening displacement than hydrated sample (B) [57].

lower than those observed for dry samples ($p = 0.02$, Figure 2.33C & F).

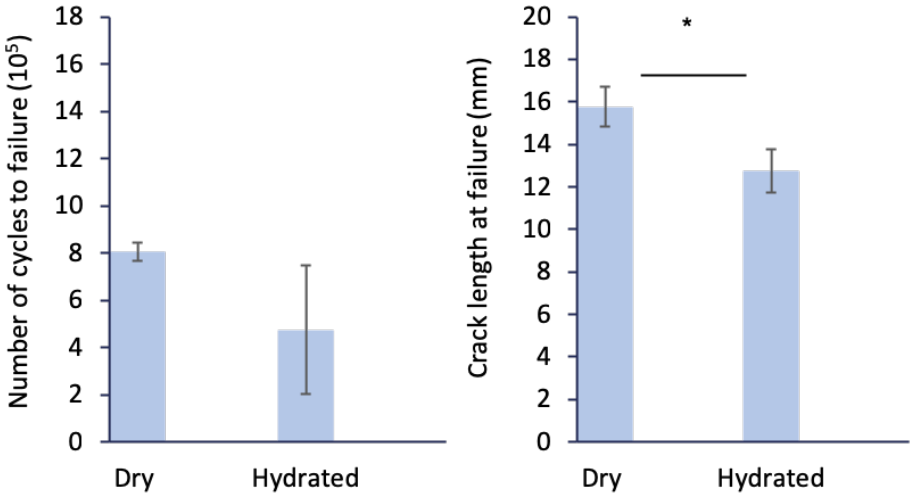

Figure 2.33: Number of cycles and crack growth at failure for dry and hydrated PCU. No significant difference was observed in number of cycles to failure, but hydrated samples had a significantly lower crack length at failure ($^*p = 0.02$) [57].

Fractography for the hydrated samples showed a rough fracture surface for the first 0.5 - 2 mm of crack growth with larger and more regularly spaced surface features than the crazed surfaces observed in dry samples (Figure 2.34A). The surface then transitioned into a smooth surface with ductile chevrons for the remainder of crack growth (Figure 2.34B).

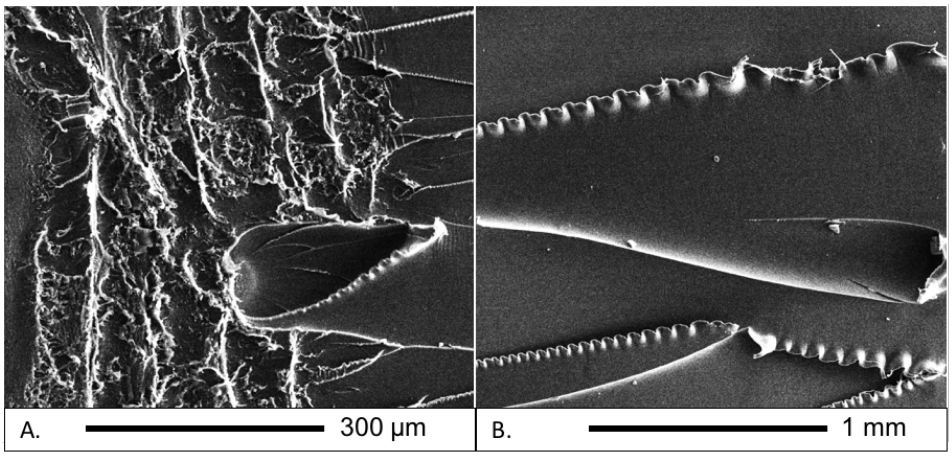

Figure 2.34: Representative fracture surface of a hydrated sample. Evidence of fibrillation was seen for a short distance at the very beginning of crack growth (A), but quickly opened to a smooth characteristically ductile fracture surface for the remainder of crack growth (B) [57].

2.4.5 Test Group 5: Annealing

Table 2.6: Summary of Test Group 5

Test Group	Material	Loading	Frequency	Conditioning	Annealing
5	PCU	Continuous	5 Hz	Hydrated	None 140°C

The fifth test group explored the impact of annealing on fatigue crack growth in hydrated PCU (Table 2.6). One sample annealed at 140°C demonstrated behavior very similar to that of hydrated unannealed samples (Figure 2.35).

However, the other two samples annealed at 140°C initially blunted and then cracks began to form on the shear planes at 45° to the direction of loading (Figure 2.36, top). These cracks then began to grow together as the crack progressed until they joined to form a blunt crack with a large CMOD (Figure 2.36). This behavior is seen as the very low initial crack growth in two of the annealed samples followed by an increase in crack growth around 400,000 cycles (Figure 2.35 B).

Due to high variability, both crack length at failure and number of cycles at failure were statistically similar, though the number of cycles until failure for two annealed samples was much greater due to the blunting effect (Figure 2.37).

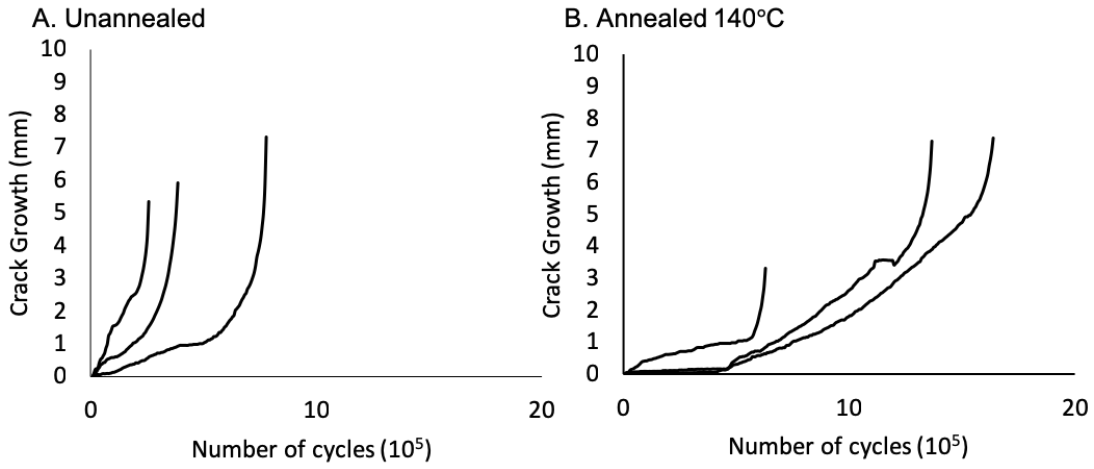

Figure 2.35: Crack growth as a function of number of cycles for unannealed and annealed PCU.

The initiation of two cracks is apparent in the presence of two fracture planes in the fractography (Figure 2.38). Fractography from a blunted sample also reveals a much more textured surface (Figure 2.38 A) compared to the highly ductile markings on the unannealed sample (Figure 2.38 B). Little evidence of crazing exists (Figure 2.39).

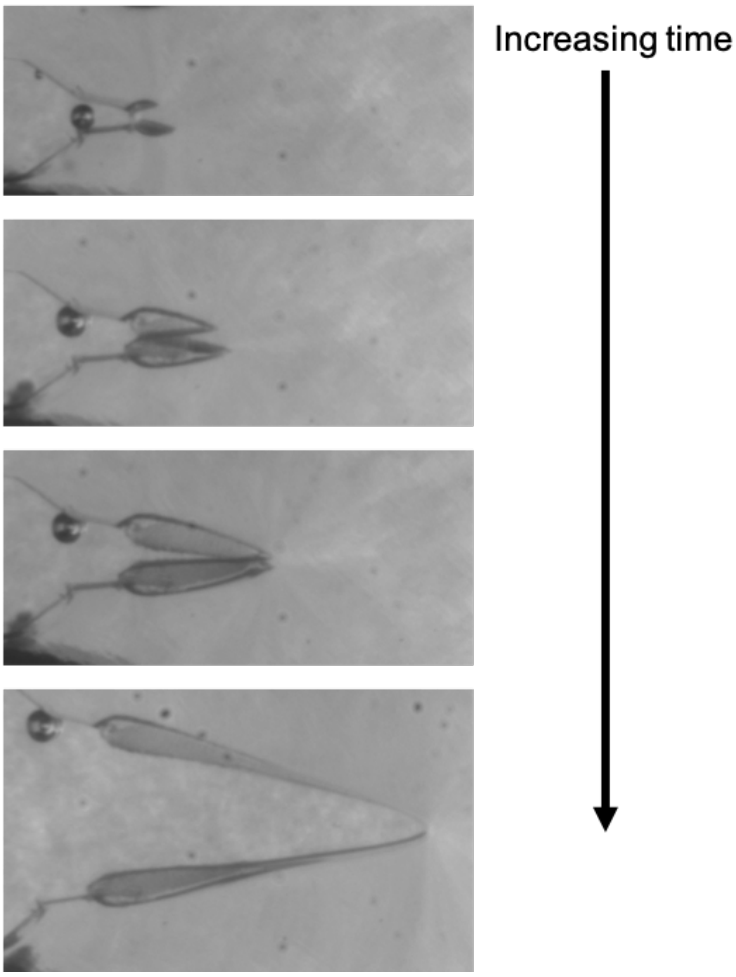

Figure 2.36: Annealed samples initially blunted. Cracks then grew at 45° to the direction of load, began to extend in the crack direction, and ultimately grew together into a single crack. Images are in temporal order top to bottom.

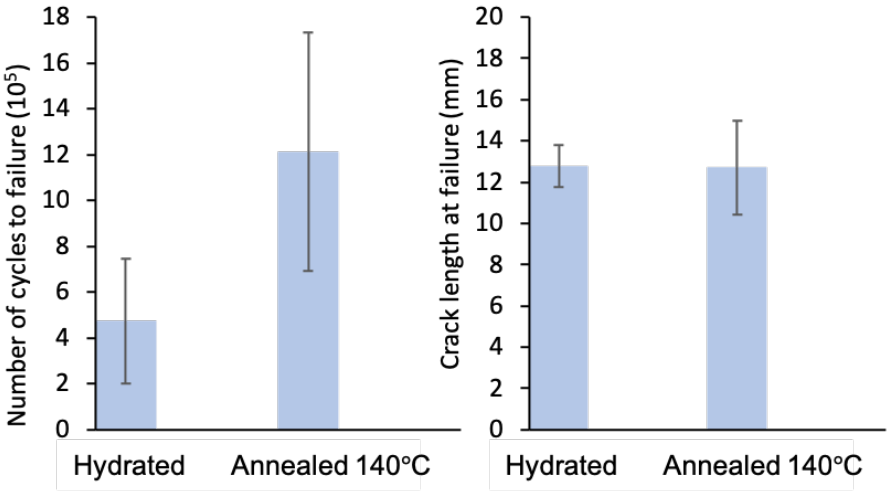

Figure 2.37: Number of cycles to failure and crack length at failure for unannealed and annealed PCU.

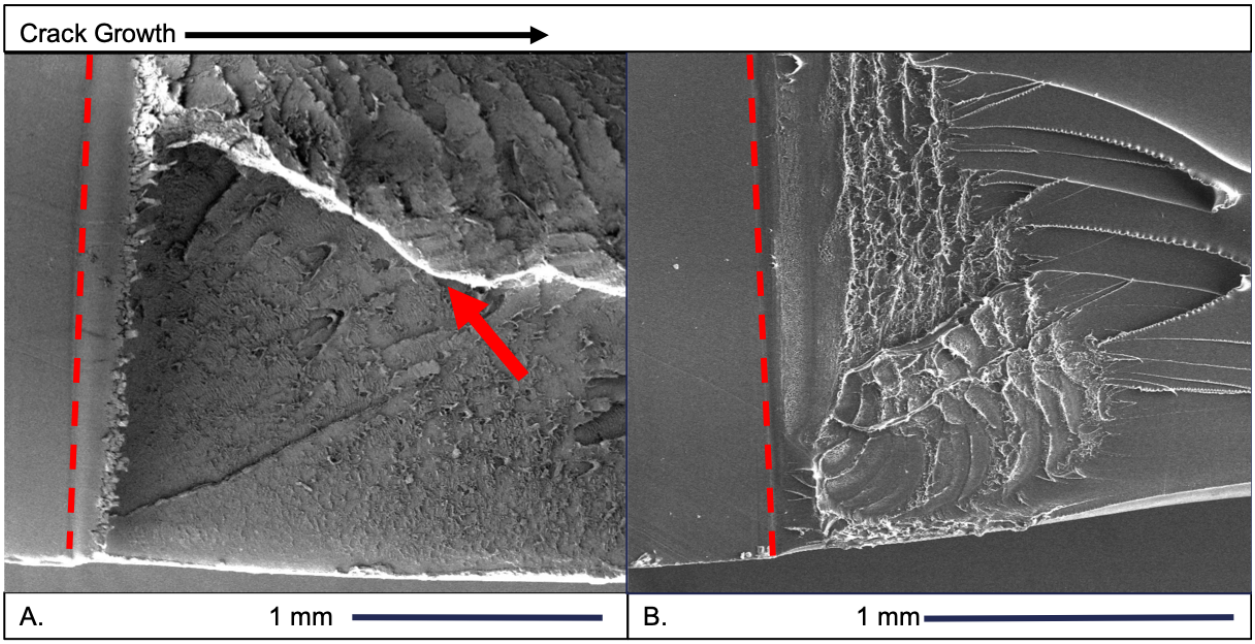

Figure 2.38: Fractography of annealed samples (A) shows a separation between the planes of growth of two cracks (arrow). The surface shows little evidence of crazing, but a more featured surface than the ductile failure surface of unannealed samples (B).

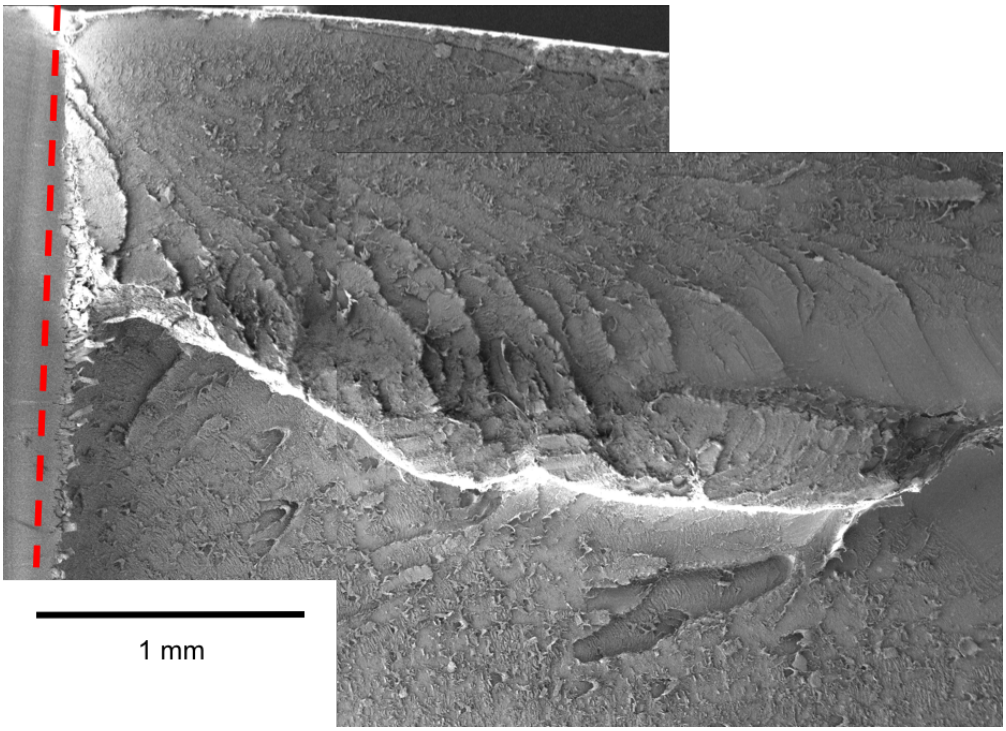

Figure 2.39: Fractography of an annealed sample shows two separate fracture planes from the two crack tips that merged after several millimeters of crack growth.

2.5 Discussion

The primary objective of this study was to explore the variables that control the mechanisms of fatigue crack growth in PCU for its use in medical devices. It has been well established that the tensile mechanical properties of PCU are dependent on a wide range of temporal, thermal, and chemical variables. In agreement with the complex interactions between chemical, structural, and mechanical properties of PCU, the fatigue behavior of the material was impacted by loading manner, rate, hydration, and annealing. These studies point to a need to better understand these interactions with respect to their impact on the clinical performance of PCU.

The aim of the first test group was to understand how PCU compares to UHMWPE, a well-characterized benchmark in the orthopedic polymer industry. Due to dimensional limitations, identical compact tension geometries were used to compare PCU and UHMWPE. The stress state for UHMWPE was too thin to meet the conditions of plane strain and the PCU sample transitioned out of conditions of plane strain at crack lengths over 1.4mm. This geometric constraint confounds the comparison at a consistent highly constrained stress state, especially at long crack lengths. However, a thickness of 3.3 mm is relevant to the geometries of medical devices where cracks may be growing in thin sections or features.

The range of crack speed and ΔK in which crack growth was stable was similar for both PCU and UHMWPE, but the mechanisms were largely different. Compared to UHMWPE, PCU exhibited less uniform and in-plane crack growth. Stress shielding mechanisms such as crack tip deflection, multiple crack tips, out-of-plane crack growth, and crazing were observed. Comparatively, in UHMWPE, only crack blunting was observed as crack growth progressed straight and uniformly. This is reflected in the more linear $\frac{da}{dN}$ versus ΔK relationship in UHMWPE compared to more scatter seen in the crack growth of PCU with the exception of the few points of ductile tearing before failure. In UHMWPE, an increasing cyclic load was required to maintain a sharp crack and progress crack growth. In contrast, in PCU a crack could be propagated to failure at a constant cyclic load without blunting. In order to investigate the impact of a ramped loading to drive ΔK, a comparison of ramped versus un-ramped loading was incorporated into the second test group.

Compared to UHMWPE, PCU had a smaller range of crack growth rates ($\frac{da}{dN}$). Similarly, there was little positive correlation between $\frac{da}{dN}$ and ΔK for PCU. This suggests that the stress shielding mechanisms were more dominant than the stress driving force (ΔK). This is further supported by the fact that the crack growth rate remained constant for samples that underwent ramped loading (increasing cyclic load) compared to the samples tested at a constant cyclic load. Clinically, this may have negative implications if crack growth proceeds at a similar rate regardless of the applied cyclic load. It would suggest that a larger range of loads would be equally problematic for damage. Future work should investigate of the

influence of K_max versus ΔK on the crack growth in PCU.

Based on this study, a LEFM approach could not be used to quantitatively compare the fatigue crack resistance of PCU to UHMWPE by means of the Paris law. Although the crack growth mechanisms were very different between PCU and UHMWPE, comparing cycles to failure and crack length to failure, there is no clear benefit of PCU over UHMWPE from a fatigue resistance perspective. It should be noted that the PCU used here is 75D, a harder formulation of PCU than the 80A commercially used in orthopedics so a direct clinical prediction is not valid. The fatigue character of PCU is further complicated by the variables evaluated in the other following test groups.

The aim of the second test group was to explore the effect of loading on crack growth in PCU. Previous studies have explored the tensile and viscoelastic properties of polyurethane copolymers outside of fracture and fatigue applications [56, 50, 53, 52]. Based on the observations of the impact of strain rate and conditioning on the tensile properties of PCU, it is expected that, under a highly-constrained stress state of a crack tip, the same factors would influence the fatigue crack growth in the polymer.The rate-dependent response of PCU is important with respect to the performance of the polymers in long-term load bearing orthopedic implants where load magnitude and rate can be highly variable.

Unloading the samples overnight resulted in premature brittle failure. This brittle failure was not observed in samples loaded 24 hours a day. This result suggests the existence of a localized transformation at the crack tip due to the highly concentrated stress state or hysteretic heating caused by the cyclic loading. Fatigue-loading and thermal treatments have been shown to impact the structural organization of polyurethane copolymers [54, 114, 115]. Therefore, we hypothesize that this localized transformation causes a shift in the structural organization of the polymer surrounding the crack tip. A shift in the structural organization of the polymer at the crack tip would lead to a different mechanical response of the material at the crack tip than that of the bulk material. When the sample was removed and allowed to relax overnight, any temperature increases were lost and/or any strain effects were allowed to relax. Then upon reloading, the stress state at the crack tip was not the same as when the sample was removed from testing and a different failure mechanism was observed.

A counterargument to this hypothesis could be that there was an external test-setup effect that caused the samples to fail upon reloading such as a jump in the equipment at startup, etc. First, the failure did not occur immediately upon reloading, but within the first 1000 cycles of loading. Making it unlikely that a jump in the first few cycles created the failure. The ramped samples were also tested intermittently, which allows us to check if this phenomena was due to testing conditions or the relaxation overnight.

The ramped samples were tested intermittently and brittle failure upon reloading was observed in 1 of 3 of the samples. The lack of brittle failure in two the the three samples may

be explained by the fact that they only underwent one overnight relaxation cycle compared to multiple unloading cycles for the intermittently loaded samples. Additionally, the ramped samples had already reached a high K_{max} (loaded at 20 - 200 N compared to 14 - 140 N for the un-ramped samples) before being unloaded. The ramped sample that failed was relaxed at 17 - 170 N of loading. Therefore, the state of stress at the crack tip in the samples that did not fail brittlely likely had transitioned to a different stress state at the crack tip than the samples that failed after relaxation.

Samples tested intermittently at 2 Hz further support the hypothesis that there was a thermal or strain induced transformation at the crack tip leading to brittle failure. Brittle failure upon reloading was observed at 5 Hz, but not at 2 Hz. The slower loading would create less hysteretic heating and reduce thermal differences between the continuously loaded and relaxed state.

It is not clear if the relaxation effects are dependent on the crack length, the number of cycles sustained, temperatures, or length of time unloaded. However, a dramatic shift in failure mechanisms due to time dependent loading effects could have serious implications for device design. More testing is required to understand what controls this response especially with respect to physiologically relevant parameters.

Crack growth in PCU that was loaded at a constant ΔK was similar to PCU loaded with an increasing ΔK. The range of ΔK for which crack growth occurred was similar between both loading conditions with the exception of crack growth ΔK's below that of the constant loading case. This suggests that it is the stress shielding mechanisms that are determining the crack growth rate rather than the stress intensity. This supports the poor applicability of Paris behavior in classic LEFM and suggests that it is the cyclic nature of the loading that is more important than the magnitude. Further work should investigate the relative contribution of creep induced by static loading on a crack versus cyclic loading at a given magnitude of loading.

The aim of the third test group was to investigate the influence of loading frequency on the crack growth rate of PCU at clinically relevant levels. Loading frequency was also observed to change the mechanism of fatigue crack growth in PCU. At 2 and 5 Hz, crazing and nonplanar crack growth were observed, but overall, a single crack tip dominated in Mode I (orthogonal to the loading axis and in plane with the initial notch). In contrast, at a frequency of 10 Hz, multiple crack tips, nonplanar crack growth, crazing, and discontinuous FCP were observed. We hypothesize that this behavior is related to the ability of the well-ordered hard phase and amorphous soft phase to accommodate the stress state at the crack tip. At lower effective strain rates the amorphous soft phase has sufficient time to deform in the direction of applied stress creating a crazed fracture surface; whereas, at higher strain rates, brittle fracture processes and the nucleation of multiple crack tips become dominant as the amorphous regions do not have the time to deform and fracture occurs in regions

where the structural organization is weakest.

Most of the frequencies used in this study are higher than what is physiologically relevant (≤ 1 Hz). The baseline was set at 5 Hz based on pervious experience with UHMWPE which indicated that 5 Hz was the highest frequency that would not induce hysteretic heating effects. This has been shown to not be the case with PCU, which shows frequency effects below 5 Hz.

The fourth aim of this work was to understand the changes to fatigue crack growth in PCU following hydration. Fatigue crack growth in conditioned PCU, with a 50% reduction in elastic modulus [56], proceeded at a slower rate, as would be expected with a more elastomeric material. The mechanism of FCP was much different than in dry samples. Notably, the fatigue crack grew with a large crack opening displacement. It should be noted, however, that in highly-constrained clinical applications, large tensile displacements may not be relevant. These findings suggest that in a constrained clinical application conditioned PCU may offer greater fatigue crack growth resistance when the mechanism of ductile tearing is not available. However, a reduced presence of the stress shielding mechanisms that were observed in dry PCU may also negatively influence the ability to resist crack growth.

The final aim of this work was to investigate the effect of annealing on the FCP in hydrated PCU. Annealing has been shown to increase the phase separation in PCU [54]. Therefore, it would be expected that, if the fatigue crack growth behavior is dictated by the phase separation at the crack tip, annealing should influence fatigue crack growth. This is in line with the hypothesis from test group 2, that hysteretic heating or strain induced changes to the structure at the crack tip resulted in the change in failure behavior. A change in crack growth behavior between annealed and unannealed material was observed. Annealed material initially blunted and then cracks nucleated at 45° from the direction of loading, grew, and eventually joined together into a single crack. The blunting of the primary crack was likely due to the more ductile mechanical behavior of the annealed material. However, the appearance of the secondary cracks at 45° to the direction of loading aligns with the planes of maximum shear in the plane strain configuration of a compact tension specimen. Failure along this plane shows low shear strength relative to the strength in the principal direction. At longer crack lengths, when the two crack tips rejoined into a single crack front, the stress state had moved from plan strain towards plane stress, where the planes of maximum shear are rotated. This curiously different behavior from an unannealed sample highlights that the thermal history is important to the fatigue resistance of PCU.

Future work will focus on understanding how the phase separation of PCU is impacted by hysteretic heating and cyclic strain under fatigue loading. Understanding the relationship between the degree of phase separation of PCU and applied cyclic loading is essential to elucidate the mechanisms of fatigue failure. In clinical applications thermal treatments occur throughout device production, from manufacturing to sterilization. The complex interactions

between many variables in PCU and its fatigue performance underscore the importance of understanding how the processing of the material could impact its clinical performance.

Overall, it is important to understand the failure mechanisms of PCU in order to successfully predict its long-term performance as a load-bearing implantable biomaterial. This study explores potential failure mechanisms of the PCU rather than prediction of clinical outcomes. This study is a first look at what parameters might be important to characterizing the fatigue behavior of PCU. In this study we sought to explore the mechanisms that control crack growth and failure in PCU. We must first understand the structure-function relationships of the material to understand what is important to control clinically to accurately design load-bearing implants comprising PCU.

2.6 Conclusions

This study showed the impact of hydration and time dependent effects on fatigue crack growth in PCU. Samples unloaded overnight experienced premature brittle failure compared to those tested continuously. Higher loading frequencies resulted in the formation of multiple crack tips, variable crack growth rates, and out of plane crack growth. Finally, conditioning resulted in highly ductile crack growth with large crack mouth opening displacement. Dry crack growth was characterized with evidence of crazing and less crack mouth opening displacement. These results suggest that there is a strong time dependent interaction between the fatigue crack growth in PCU and the microstructural organization at the crack tip. Understanding this interaction and the mechanisms that control crack growth in PCU is important to inform the design of PCU devices used in long-term implant applications.

Chapter 3

The Impact of Strain on the Structural Organization of Polycarbonate Polyurethane

3.1 Introduction

Chapter 1 reviewed PCU in its commercial uses in spine, hip, and knee implant designs [97, 77, 78, 76, 79, 80]. A large body of work has explored the mechanical performance of PCU for long-term orthopedic implant applications, but heavily focuses on the wear performance [116, 117, 71, 70, 118, 119, 72]. As discussed in Chapter 2, less work has focused on the fatigue behavior of PCU [111, 110, 112, 113, 50, 120, 57].

Previous work (Chapter 2) demonstrated highly time dependent fatigue crack growth and failure behavior in PCU [57]. We hypothesized that this behavior was a result of shifting structure caused by the highly-constrained stress state at the crack tip. Our results from a material-level fatigue test motivate a study to understand the interaction between stress and structure of PCU. Additional motivation is found clinically in an *in vivo* study of PCU acetabular cups in sheep by Khan. Khan et al. reported a significantly lower glass transition temperature, correlated to an increase in phase separation, in PCU following implantation [47]. This suggests that clinically-relevant loading can alter the structure of PCU. Therefore, it is important to understand how *in vivo* loading can impact the structure and correlated properties of PCU for its use in long-term medical implants. The objective of this study is to understand the impact of strain on the structural organization of PCU.

The introduction will review the phase-separated structure of polyurethane block copolymers, from intrinsic properties, like chemistry and thermodynamic interactions, to the extrinsic variables, such as processing. Next, we introduce the impact of structure on the mechanical properties of polyurethanes. Finally, we review previous studies of the impact of mechanical deformation and fatigue on the structural organization of segmented

polyurethanes in general. Then we present our findings on the impact of strain on the structural organization of PCU.

3.1.1 Polyurethane Chemistry

Polyurethane copolymers are of interest in many applications, ranging from automotive to medical, because of their wide range of tuneable properties. This wide span of mechanical and chemical properties derives from the range of chemical combinations allowed by the copolymerization of hard diisocyanates with chain extenders and soft macrodiol segments [121, 122]. The thermodynamic incompatibility of the two blocks leads to a phase-separated structure, as the hard and soft segments agglomerate with like-blocks. The phase-separated structure of the material dictates the unique elastomeric mechanical properties with high toughness while maintaining rubber-like extension [43, 54, 51].

The degree of phase separation for a given polyurethane copolymer is dictated by many variables. Intrinsic parameters, like block chemistry, weight fraction of each block, and molecular weight and polydispersity of each block all impact the resulting structure. Additionally, extrinsic parameters, like thermal and temporal treatment, hydration, and mechanical loading all contribute to determining the final structure of the copolymer [54, 51, 123, 55, 53, 62, 124, 52, 125, 115, 114]. Because all of these variables can change the physical properties of the material it is important to understand their potential influence on an end point application, such as a medical implant.

Polymers are chains of covalently bonded repeat units, 'mers', that form structures based on the makeup of the backbone of the chain as well as secondary interactions between and within chains. Polymers can be made up of only a single repeat unit (A-A-A...) or multiple repeat units (A-B-A-B... or A-A-B-B-B-A...) in many permutations (Figure 3.1). The thermodynamic interactions of the chain chemistry and lengths of the chain (molecular weight) play a role in dictating the structure and properties of the material.

Polyurethanes were developed by Dr. Otto Bayer in 1937. They are a broad class of polymers classified by the presence of a urethane linkage in the polymer chain and are derived from carbamic acids. The generalized urethane unit is polymerized with repeating urea, ester, ether, or aromatic units, typically of lower glass transition temperature. The linkage is formed with the reaction of an isocyanate -N=C=O with an alcohol -OH. This forms the generalized polyurethane repeat unit (Figure 3.2) [42, 44].

Polyurethane block copolymers, or segmented polyurethanes can be synthesized using addition products of the soft segment component with terminal hydroxyls and diisocyanate to produce alternating blocks. These are then chain extended with a short chain diol to the desired ratio (Figure 3.3). The end groups can then be terminated, used to form crosslinks,

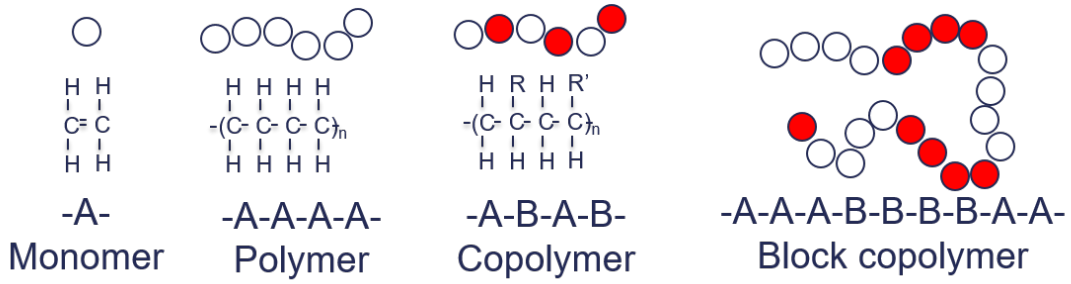

Figure 3.1: Polymers are chains or repeat 'mer' units. Monomers are combined into chains. Chains of a single monomer or multiple monomers or blocks of monomers can be combined to change the properties of the material.

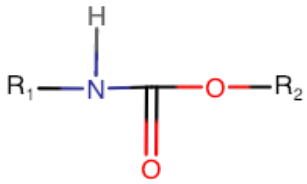

Figure 3.2: The chemical structure of a urethane monomer. Adapted from [40].

or add an end group [40]. The wide range of chemical, mechanical, electrical, and optical properties of polyurethanes derive from the range of combinations of hard segments, soft segments, and chain extenders that this process allows. The combination of potential diisocyanates, polyols, and chain extenders is exponentially increased with the combination of different molecular weights of each component and stoichiometric ratios between each.

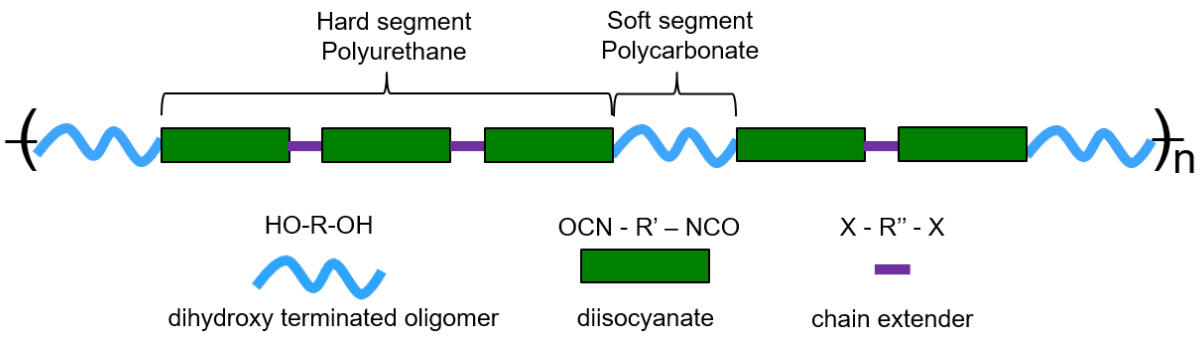

Figure 3.3: Polyurethane block copolymers are composed of a hard (polyurethane) and soft (polycarbonate) segment. The soft segment is generally a dihydroxy terminated oligomer. They are polymerized with a diisocyanate and then chain extended. This process gives the high degree of tailorability of the composition and properties of the polyurethane copolymers.

3.1.2 Structural Organization of Polyurethanes

The block chemistry of polyurethane copolymers creates a phase-separated structure. The phase separation creates an effective physical crosslinking mechanism like that which exists in lightly crosslinked rubbers and provides the elastomeric properties of polyurethanes [51]. The crystalline phase of the diisocyanate with a chain extender is referred to as the hard segment, while the polyol phase that forms an amorphous matrix is referred to as the soft segment [42]. The phase separation of the segments is dependent on both intrinsic and extrinsic variables such as chemistry and molecular weight and thermal processing (annealing) and hydration respectively [43, 54, 40, 51, 55, 53]. Although a number of variables can alter the structure of polyurethanes, these interactions are thermodynamically driven. The hard and soft segments in polyurethanes are thermodynamically incompatible and fundamentals of polymer chemistry describe the interactions.

The degree of separation is thermodynamically-driven to minimize free energy (ΔG) through a balance of enthalpy (ΔH) and entropy (ΔS) (Equation 3.1).

$$\Delta G = \Delta H - T\Delta S \tag{3.1}$$

The chemistry and molecular weight of each block dictates the inter- and intra-segment interactions. This affinity is described by χ in Flory Huggins Theory of phase separation of copolymers (Equation 3.2).

$$\Delta G = \frac{kT}{a^2}\sqrt{\frac{\chi_{AB}}{6}}\frac{Na^3}{\frac{\lambda}{2}} + \frac{3}{2}kT\left[\frac{\frac{\lambda^2}{2}}{Na^2}\right] \tag{3.2}$$

The enthalpic term describes the relative affinity of each segment to itself and the other segment (first term of Equation 3.2). The enthalpic contribution is dependent on characteristics of the polymer chemistry such as degree of polymerization (N) and domain periodicity (λ). The parameter χ is a function of the number of neighboring available free sites (z), temperature (T), and a parameter describing the pairwise interactions of each segment (w) (Equation 3.3).

$$\chi = \frac{z\Delta w}{kT} \tag{3.3}$$

The entropic contribution describes the state of deformation of the polymer chain relative to its equilibrium state (second term of Equation 3.2). The entropy is related to the degree of polymerization (N), domain periodicity (λ), and Kuhn step size (a), a measure of chain flexibility.

The molecular weight is additionally dependent on both processing temperature and method [56, 54, 51]. The polyurethane organizes into amorphous regions of rubbery soft segment interspersed with semicrystalline regions of hard segment stabilized by hydrogen bonding (Figure 3.4). In different polyurethane copolymers, an increase in molecular weight of the soft segment while maintaining hard to soft segment ratio was found to increase the degree of phase separation, inter-domain spacing, and order in the hard domains [55, 122, 120]. An increase in hard segment content also creates larger hard domains, but the total degree of phase separation is dependent on the mobility and composition of the segments. [122, 51]. The size scale of the hard domains and domain separation ranges based on the variables described above, but using atomic force microscopy has been estimated to be on the order of 10 - 100 nm scale for different polyurethane copolymers (Figure 3.5) [126].

Initially after molding or being taken out of solution, the polymer is randomly mixed. As the polymer cools and with increased time, the phase separation increases (Figure 3.4) [44]. The mechanical properties of the material are dependent on the size, concentration, and level of order in the hard segment domains which drives their ability to orient and crystallize upon the application of strain [44]. After or during processing, annealing and curing temperatures can affect the degree of phase separation, especially at temperatures above the glass transition temperature [40, 54, 123, 53]. The structures formed in the hard domains are also dependent on thermal processing. Kojio et al. found that spherical structures formed in a polyurethane elastomer cured at a lower temperature, while larger and more regular tilted cylinder structures formed when cured at a higher temperature [123].

Like other polyurethane copolymers, PCU is organized into a phase separated structure. In the case of Bionate®, the exact ratios of hard to soft segment, molecular weights, and polydispersity is unknown due to the proprietary nature of the material. However, it will be

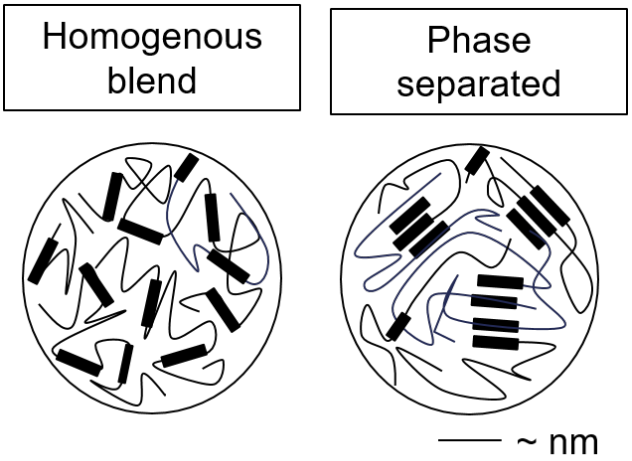

Figure 3.4: The hard and soft segments in the polyurethane copolymer are thermodynamically incompatible and therefore separate into ordered regions of hard blocks and amorphous regions of soft segments. The degree to which this occurs depends on thermal and temporal treatments.

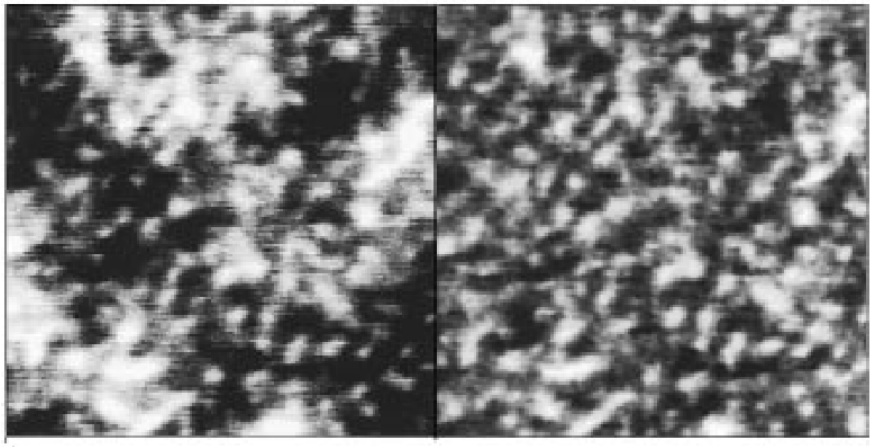

Figure 3.5: Tapping mode atomic force microscopy has been used to probe the size scale of the structure of polyurethane copolymers. The image shows topographical data (left) with a height range from 0 - 5 nm in Pellethane, a polyurethane copolymer. The image on the right is phase data that has been correlated to the hard and soft domains of the copolymer showing the distribution of phase separated domains. The images widths are 250 nm. Reprinted with permission from [126]. Copyright (1997) American Chemical Society.

similarly influenced by the extrinsic parameters previously discussed such as thermal treatments and hydration. Therefore, understanding the structure-function relationships of the material with respect to processing is important in order to design for a desired mechanical performance in medical applications.

3.1.3 Impact of Structure on the Mechanical Properties of Polyurethanes

The degree of phase separation dictates the mechanical behavior of the material. The mechanics are controlled by size and concentration of hard segments, strength of segment adhesion, and segment mobility [44]. Phase separation is required to impart elastomeric behavior [51]. Although the specific interactions are further dependent on the polymer composition, trends have been reported in many different polyurethane copolymers. An increased ratio of hard to soft segment increases the tensile strength of the material, but reduces the ductility [52, 122, 109]. Similarly, increasing the molecular weight of the soft segment increases the tensile strength, stiffness and hardness with greater ability to form crystal structures within the soft segment domains. This crystallinity also contributes to greater ductility as well [52, 51, 55]. In contrast, with some soft segment chemistries this can lead to a decrease in modulus [122]. Increased phase separation in PCU compared to PEU leads to higher modulus and lower ultimate elongation from reduced flexibility of carbonate soft segment. [49, 55]. An increase in hard segment content led to an increase the tensile modulus and decrease in elongation at break [51]. The influence of microstructure on the material properties is important to understanding and predicting the long-term performance of the material *in vivo*.

3.1.4 Impact of Mechanical Deformation on the Structure of Polyurethanes

The structure of polyurethanes is what dictates the material properties, but it is also impacted by mechanical deformation. Most semicrystalline polymers and elastomers have some degree of strain induced crystallization and a stiffening effect at high strains as polymer chains align in the direction of the strain. In the case of semicrystalline polymers, the amorphous regions provide the flexibility for the crystalline regions to orient normal to the direction of strain, and eventually the amorphous regions also crystallize as they are drawn out in the direction of the strain (Figure 3.6).

The phase-separated structure of polyurethanes has a similar behavior. The ordered hard domains act as 'crosslinks' restricting the relative motion of regions of amorphous soft phase. With the application of strain, the inter-domain spacing in a polyurethane elastomer was shown to increase in the direction of strain and decrease normal to the direction of strain (Figure 3.7). This effect was found to be greater in polyurethanes with larger and more ordered hard domains [123]. Strain induced crystallization of the soft phase was observed at large strains and this was inhibited by the presence of increased crosslinking limiting the motion of the amorphous soft phase [123].

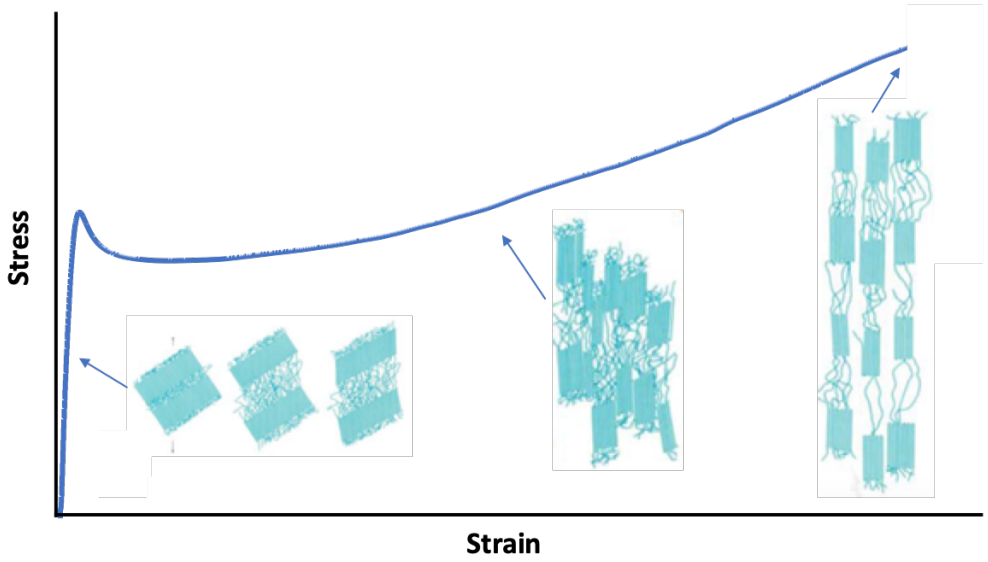

Figure 3.6: In semicrystalline polymers, like UHMWPE, increasing strain is taken up first by the entropy of the chains in the 'elastic' region. This is followed by the region of greatest strain with stretching of the amorphous regions, eventually leading the the break up of crystalline regions as the chains aline in the direction of strain before failure when the backbone of the chains ruptures. Adapted from [127].

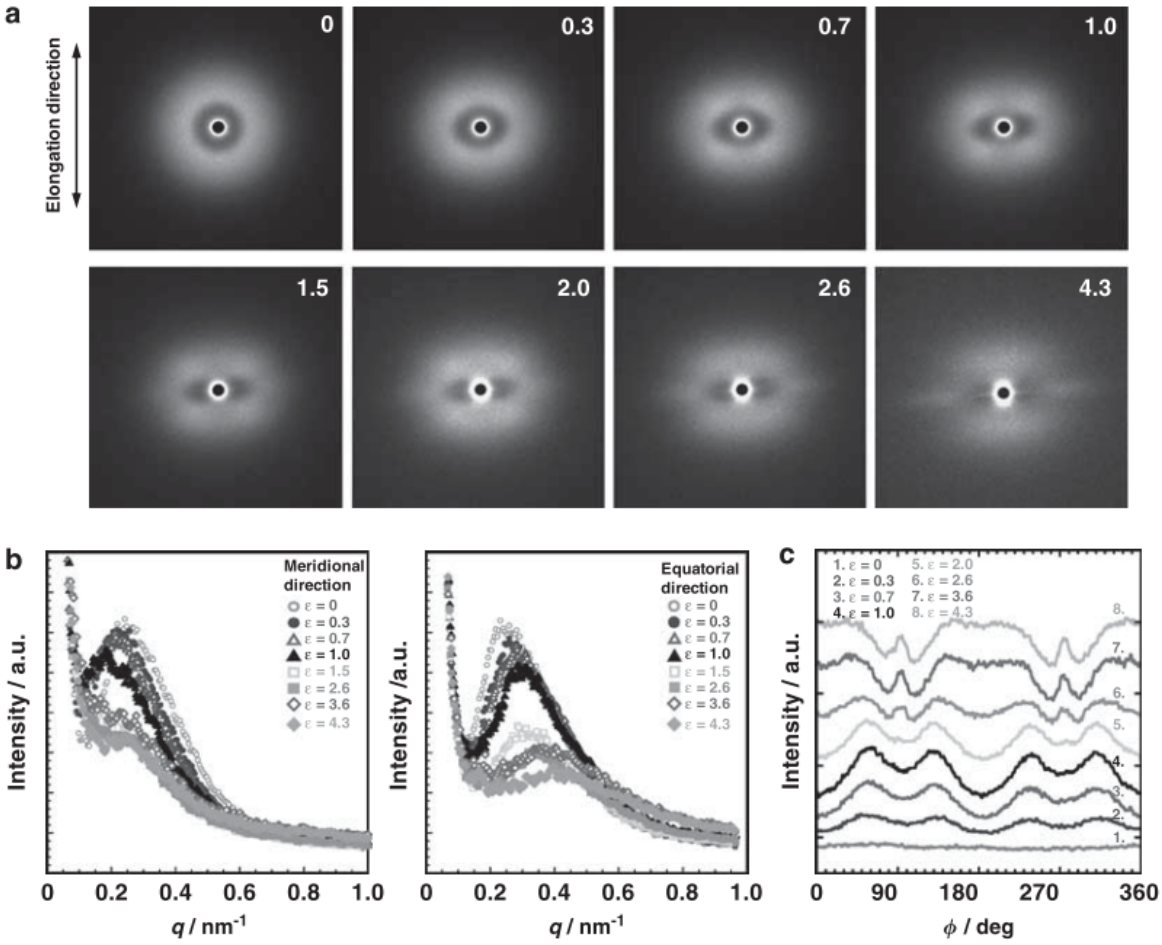

Figure 3.7: The impact of strain on the 2D SAXS diffraction patterns of a polyurethane elastomer showing a change in the structure with applied strain. Reprinted by permission from Springer Nature: [123] (2011).

3.1.5 Fatigue Effects on the Structure of Polyurethanes

In addition to static strain, the impact of cyclic loading has also been explored, though to a lesser extent, in segmented polyurethanes. One model, showing the effect of cyclic strain (± 20% strain with a mean strain of 100%) in polyurethane ureas, describes a three stage response (Figure 3.8 & 3.9). During the initial phase the structure is unaffected. In the second phase the phase separation begins to decrease the phases mix. This occurs as the lamellar structures in the axis of spherulitic structures normal to the applied strain break apart and lamellar domains orient normal to the direction of applied strain. Finally, in the third phase, domain separation is largely lost and the segments orient and align in the direction of strain [114, 115].

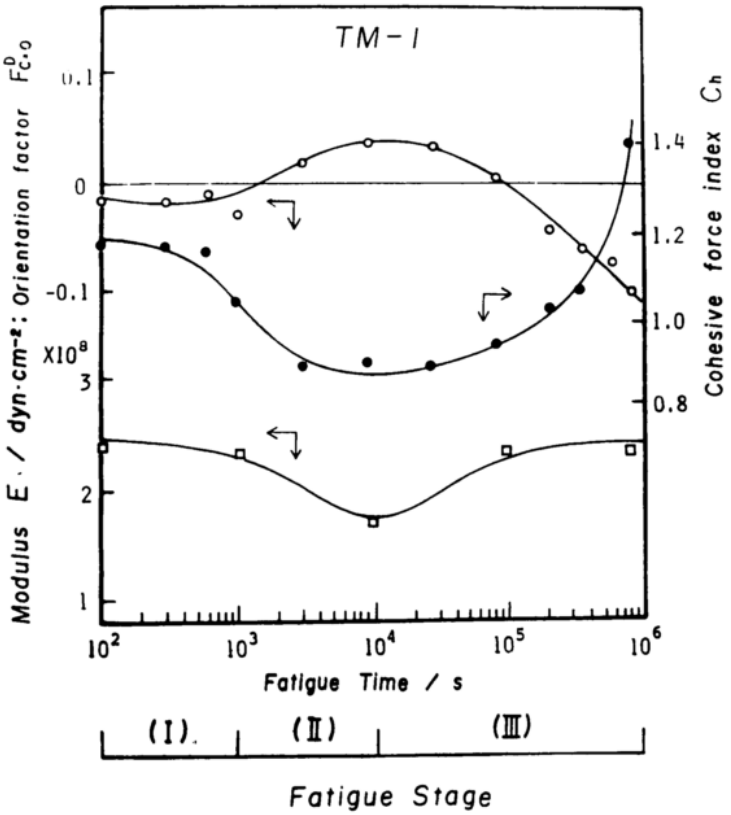

Figure 3.8: Impact of strain of the elastic modulus, the orientation factor, and cohesive force index (the latter two both related to the structure of the domains) in a polyurethane urea. Reprinted by permission from Springer Nature: Polymer Journal [114], (1986).

However, testing of another polyurethane copolymer at lower mean strains and strain amplitude showed more complex behavior. Jimenez et al. tested segmented polyurethanes with variable soft segment molecular weights at a strain of ± 20% with a mean strain of

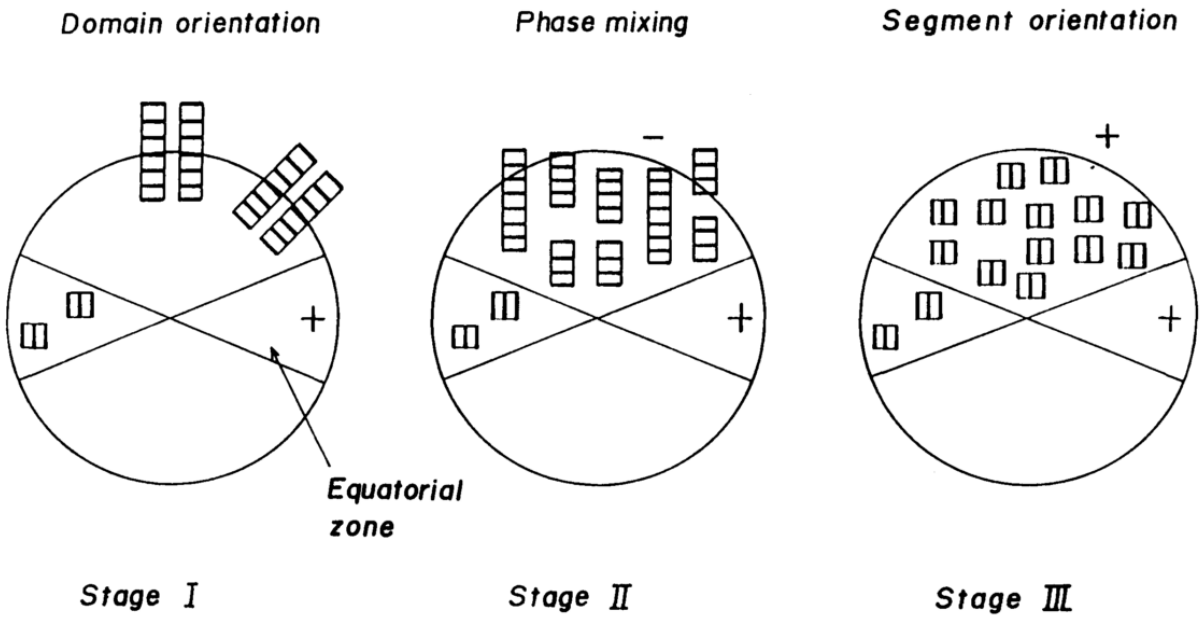

Figure 3.9: Schematic showing the impact of fatigue on the structural organization of polyurethane ureas hypothesized by Shibayama et al. Reprinted by permission from Springer Nature: Polymer Journal [115], (1987).

3%. This study found that, depending on the soft segment molecular weight, the phase separation and order in the hard domains could either increase or decrease following fatigue loading [120]. This suggests that fatigue at lower strains can play a more subtle role in manipulating the microstructure than the destruction seen with static strain.

It is well established that fatigue and static strain can impact the structure of polyurethane copolymers. It is equally established that the complex interaction of many variables dictating the ultimate structure, such that the trends observed for one copolymer cannot be generalized to other chemistries and blends.

3.1.6 Polycarbonate Polyurethane Chemistry and Structure

Polycarbonate polyurethane, trade name Bionate®, DSM Biomedical, Berkeley, CA, is the specific copolymer that is currently utilized broadly in orthopedics. In Bionate® the hard segments are a 4,40-diphenyl- methane-diisocyanate (MDI), the chain extender is 1,4-butanediol (BD), and the soft segments are composed of poly(1,6-hexyl 1,2-ethyl carbonate) diols (PHECD) (Figure 3.10) [54]. Bionate® is produced in several ratios of hard to soft segments. They are named for the Shore hardness durometer and range from 80A to 75D.

Although the exact chemistry and synthesis processes are proprietary, a body of work has been published characterizing the performance of the material with respect to its use in the medical industry (See Chapter 1).

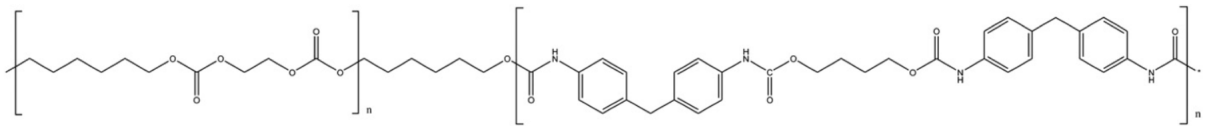

Figure 3.10: The chemical structure of Bionate® polycarbonate polyurethane. Reprinted from [54] with permission from Elsevier.

3.2 Methods

This study uses differential scanning calorimetry (DSC), Fourier transform infrared spectroscopy (FTIR), and small angle X-ray scattering (SAXS) to characterize the impact of static strain on the structural organization of PCU. Table 3.1 summarizes the samples that were characterized with each technique.

Table 3.1: Study Testing Summary

		Characterizations		
Annealing Condition	**Strain Condition**	**DSC**	**FTIR**	**SAXS**
Unannealed	Unstrained	x	x	x
	Failure	x	x	
70°C	Unstrained	x	x	x
	Yield	x	x	x
	100%	x	x	
	200%	x	x	x
	Failure	x	x	x
100°C	Unstrained	x	x	x
	Failure	x	x	x
140°C	Unstrained	x	x	x
	Failure	x	x	

3.2.1 Materials

Polycarbonate polyurethane, trade name Bionate® 75D was obtained from DSM Biomedical (Berkeley, CA). Bionate® 75D films (0.3 mm thick) were compression molded at 460°C (485 °C top plate and 435°C bottom plate) and 19000 lbf. Tensile dog bone specimens (ASTM D1708) were punched from the films. The dogbones were annealed at variable temperatures (70°C, 100°C, and 140°C) for at least 4 hours and compared to an unannealed control.

3.2.2 Tensile Testing

The samples were pulled to variable strains at a strain rate of 102 mm/min (4 in/min) using an Instron 5566 (140°C samples were pulled using a Zwick-Roell testing machine) at room temperature and ambient humidity. All annealing conditions were strained to failure and unstrained. Samples annealed at 70°C were strained at approximately yield strain (12.5% ± 0.7%), 100% strain (102.5% ± 0.2%), 200% strain (202.4% ± 0.8%), and failure strain (258.3% ± 10.1%) and compared to an unstrained control. At the given strain, testing was stopped, and the samples were unloaded. Total relaxation strain was recorded after more than 30 days after loading. Elastic modulus was calculated as a linear regression from the yield point of the material.

3.2.3 Differential Scanning Calorimetry

Differential Scanning Calorimetry (DSC) was performed using a Thermal Analysis Q2000 to collect DSC thermograms from -75°C to 220°C in a heat-cool-heat cycle at 20°C/min in an atmosphere of nitrogen or helium. A sample mass of 7 - 10 mg was used.

A heat-cool-heat DSC curve for Bionate® 75D (Figure 3.11) shows four main signals in the first heat ramp: an endotherm around 55°C (T_0), a secondary endotherm (T_I), and then two endotherms at 180°C and 204°C (T_{II} and T_{III}). T_0 was not reported in Bionate® 80A [54]. It is likely related to enthalpic relaxation following molding, and masked the T_g of 75D on the first ramp. The T_I endotherm has been related to the presence of hydrogen bonding in highly ordered structures and has been shown to be highly dependent on the thermal history of the material [54]. T_{II} and T_{III} are related to the loss of order between the hard and soft segments and are independent of the thermal history of the material [54]. In the cooling ramp there is a single exothermic peak which is attributed to re-crystallization of the domains or the appearance of ordered structures. In the second heating ramp the T_0 and T_I endotherms are indistinct suggesting that the order that was present in the hard domains was lost by heating over the T_{II} temperature and was not reformed in the rapid cooling. The appearance of these peaks in the first but not the second heating ramp suggests that they are related to hydrogen bonding in the hard domain. A T_{III}' peak is present near the location

of the peaks attributed to loss of order in the first cycle, but it appears at a higher temperature. Without the T_0 endotherm, the glass transition temperature (T_g) is distinguishable in the second heating ramp. For samples annealed at 70°C the T_g was between 22.5°C and 24°C.

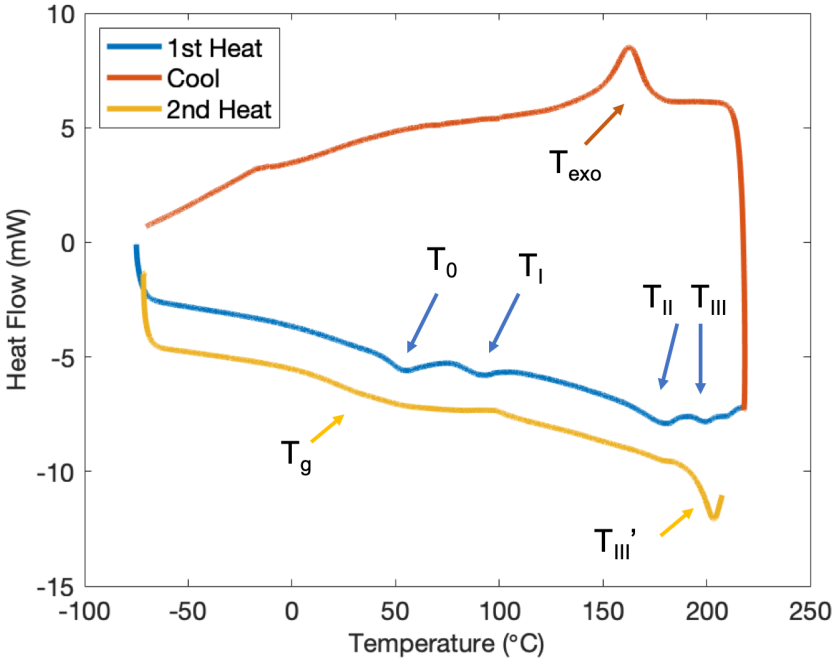

Figure 3.11: A representative DSC heat-cool-heat curve for Bionate® 75D (unstrained and annealed at 70°C). The second heating ramp is shifted down 2 mW for better visualization. The first heat ramp shows four characteristic endotherms. T_0 was attributed the the enthalpic relaxation of the material and masks the glass transition temperature. T_I is related to the thermal history of the material and degree of hydrogen bonding in ordered domains. T_{II} and T_{III} are independent of thermal history and mark a loss of phase separation. The cooling ramp has an exothermic peak attributed to re-separation or recrystallization of order in the domains (T_{exo}). The second heating ramp does not have T_0 and T_I endotherms suggesting that they are processing related. Without these endotherms, the T_g is distinguishable in the second heating.

3.2.4 Fourier Transform Infrared Spectroscopy

A Brucker Spectrum ATR Vertex 70 Fourier Transform Infrared Spectroscopy machine (FTIR) was used to collect spectra from 600 cm^1 to 4000 cm^1 in attenuated total reflectance (ATR) mode using a sample scan rate of 32 scans and a resolution of 4 cm^1.

The broad carbonyl peak gives information about the relative influence of free carbonyls and those involved in hydrogen bonding in both ordered hard domains and in the amorphous

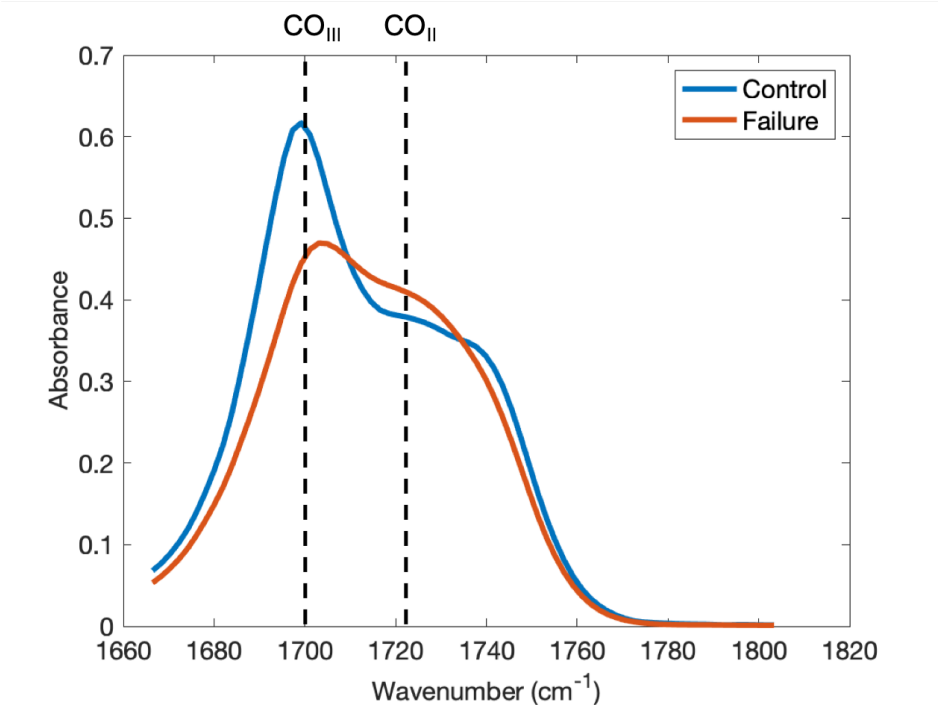

Figure 3.12: Hydrogen bonded carbonyls in ordered hard domains is attributed to the peak at 1700 cm^{-1} and hydrogen bonded carbonyls in the amorphous matrix are attributed to the peak at 1722 cm^{-1}. The ratio of these peaks (CO_{II}:CO_{III}) is used to describe changes in the hydrogen bonding with strain and annealing condition. The example shown is sample annealed at 70°C at control and strain to failure conditions.

soft matrix. The peak at 1737 cm^{-1} (CO_I) is attributed to free, non-hydrogen bonded carbonyls, the peak at 1722 cm^{-1} (CO_{II}) to hydrogen bonded carbonyls in the amorphous matrix, and the peak at 1700 cm^{-1} (CO_{III}) to hydrogen bonded urethane carbonyls in the ordered hard domains [54]. The ratio between the relative number of carbonyls that are hydrogen bonded in the amorphous matrix to the number in ordered hard domains (CO_{II}:CO_{III}) will be used for comparisons. Since these peaks are very close together they cannot be resolved independently and result in one broad peak. Figure 3.12 shows two example peaks where the relative contribution of each peak is shifted. A higher value of CO_{II}:CO_{III} corresponds to relatively less order in the hard domains.

3.2.5 Small Angle X-ray Scattering

Small angle X-ray scattering (SAXS) was performed using an Itaku BioSAXS 1000 with a Pilatus detector (79 μpixels). The maximum scattering angle was 0.7 $Å^{-1}$ using a Cu K(α) source with a wavelength of 1.52 Å.

The peak width is correlated to the disparity of size of features [123]. The peak in the intensity versus scattering angle at 0.05 Åhas been attributed to the distance between hard domains [52, 123, 53]. Bragg's law (Equation 3.4) was used to estimate this inter-domain spacing [120].

$$d_{bragg} = 2\pi/Q_{max} \tag{3.4}$$

3.3 Results

3.3.1 Tensile Testing

Annealing was found to significantly reduce the yield stress and Young's modulus of Bionate® 75D (Figure 3.13). Samples annealed at 140°C compared to samples that were not annealed had a drop in yield stress and modulus from 46.75 ± 0.8 MPa to 14.4. ± 4.0 MPa and 980.1 ± 24 MPa to 354.1 ± 126.0 MPa respectively. Additionally, the distinct peak in stress at the yield point was reduced with increasing annealing to no peak observed at 140°C. The trend of lower modulus with increasing annealing temperature is consistent with the findings of Cipriani et al. for Bionate® 80A and indicates more ductile behavior with increasing annealing temperature. The ultimate stress and strain was only significantly different for PCU annealed at 140°C where ultimate stress decreased while the ultimate strain increased (Figure 3.14, $p \leq 0.0006$) further indicating more ductile and elastomeric material with increasing annealing temperature.

The distinct 'waves' or 'bumps' observed in the unannealed stress-strain curve after yielding was repeatable and attributed to the material and not a machine effect. At the yield point, a very distinct transition to necking was observed as a 'pop' as the shaft of the dog bone specimen formed at necking region at an observable angle to the direction of load. The neck then began to extend as the region of large strain post yield. The waves in the curve are a result of the dynamic response of the sample following this formation of a neck and quick increase in strain. Although other samples had similar necking behavior, the transition was less dynamic and this recoil behavior was not observed.

The samples annealed at 70°C and strained at intermediate steps before failure exhibited some relaxation following unloading. Some plasticity was observed following strain to the yield point because the test was stopped shortly after yield. The recovery at higher strains was also significant (40% - 50%) showcasing the highly nonlinear behavior of the material (Table 3.2). This residual plastic deformation is expected to then correlate to a change in the structural organization of the material.

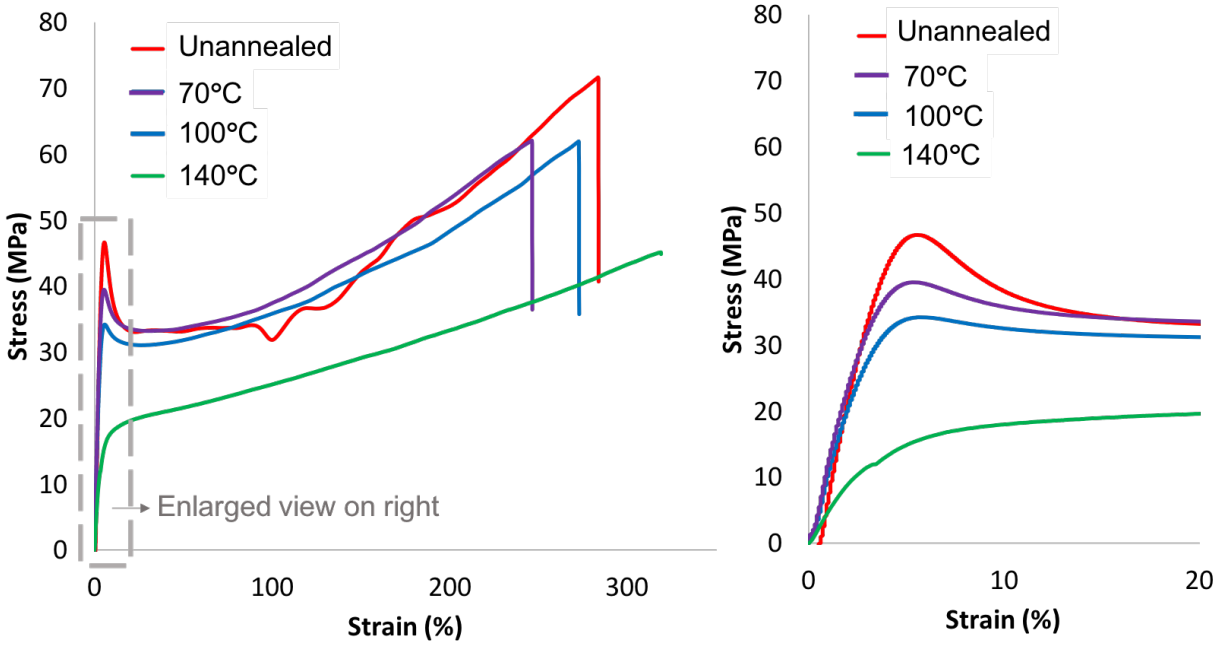

Figure 3.13: Tensile behavior of Bionate® 75D annealed at various temperatures after molding. With increasing annealing temperature, the Young's modulus and yield strength of the material decreased as characteristic of a more ductile and elastomeric material.

Table 3.2: The final recovered lengths of samples annealed at 70°C and loaded to yield, 100%, and 200% strain.

Sample Strain Condition	Initial Length (mm)	Average Applied Strain (%)	Average Final Strain (%)	Average Recovered Length (mm)	Recovery (%)
Yield	22	12.5	1.2	22.4 ± 0.4	90.2
100%		102.5	44.9	32.6 ± 0.8	56.2
200%		202.4	124.5	48.9 ± 0.6	38.5

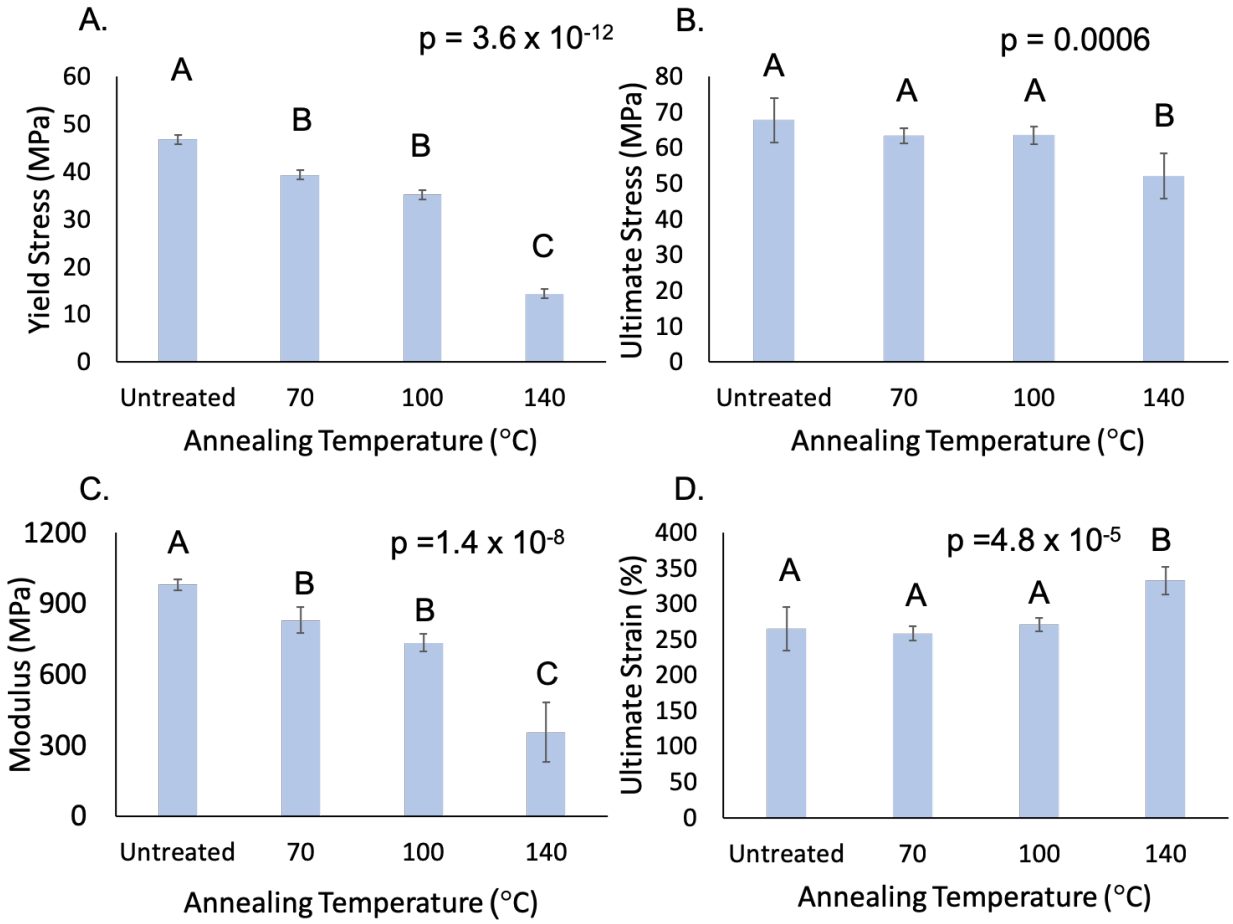

Figure 3.14: Mechanical properties of Bionate® 75D annealed at various temperatures following molding. These results point to more ductile and elastomeric material behavior following annealing compared to a more brittle response with less annealing. Mismatched letters signify statistically significant difference ($p < 0.05$, ANOVA). Error bars represent ± 1 standard deviation.

3.3.2 Differential Scanning Calorimetry

Based on previous studies, it was expected that annealing would increased the amount of order in the hard domains of PCU which would correlate to an increase of the T_I endotherm in the DSC signature. As expected, DSC characterization showed an increase in T_I with annealing in the unstrained specimens (Table 3.3, Figure 3.15A). This is indicative of increased hydrogen bonding and the development of more ordered hard domains. As expected, T_{II}, attributed to a loss of order and independent of thermal history, was unchanged with annealing. The T_0 endotherm masked the T_g.

After strain to failure, the DSC signature was similar for all annealing conditions. All annealing conditions also exhibited a prominent endotherm around 55°C that is likely due to the enthalpic relaxation following the release of strain. No distinct T_I was observed, but T_{II} was broadened in all samples (Figure 3.15B). Given that all post-failure curves were similar, the final structure is independent of the initial degree of phase separation.This suggests that, following failure, the order in the hard domains is lost.

The impact of strain on the DSC endotherms was smaller than that of annealing. In Bionate® 75D samples annealed at 70°C, the T_I endotherm was not appreciably affected with increasing strain (Figure 3.16). An ANOVA analysis showed a statistical difference ($p = 0.04$), but in a post hoc analysis, no individual groups were different. The lack of observable change suggests that there is no measurable loss of order in the hard domains following strain using this indirect measurement technique. This suggests that strain is accommodated by the amorphous soft segment regions of PCU.

Table 3.3: The location of the T_I endotherm in unstrained Bionate® 75D as a function of annealing temperature.

Annealing Condition	**T_I (°C) Average ± St. Dev.**
Untreated	84.9 ± 0.3*(exo)
70°C	92.2 ± 2.1
100°C	124.0 ± 0.7
140°C	166.9 ± 0.7

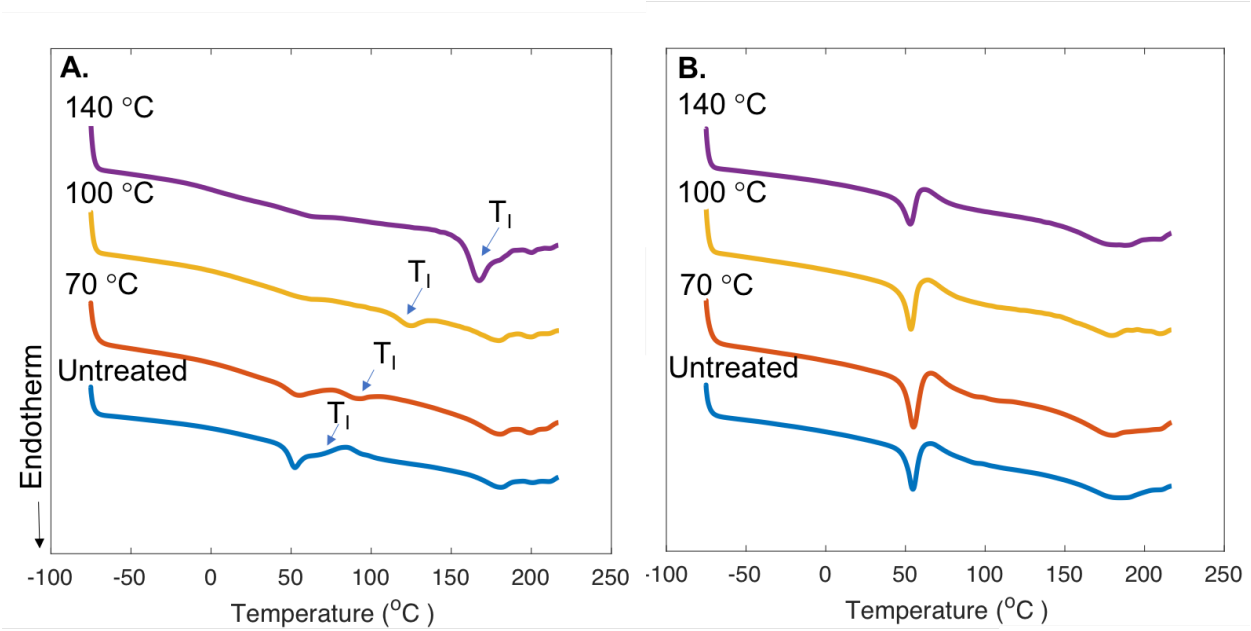

Figure 3.15: The DSC curves for unstrained Bionate® 75D annealed at increasing temperatures (A) show a correlated increase in T_I marking increased hydrogen bonding in the hard domains and no change in T_{II} and T_{III}. After strain to failure (B) T_0 is increased due to relaxation effects, and T_{II} is broader, but there are no notable differences between annealing conditions.

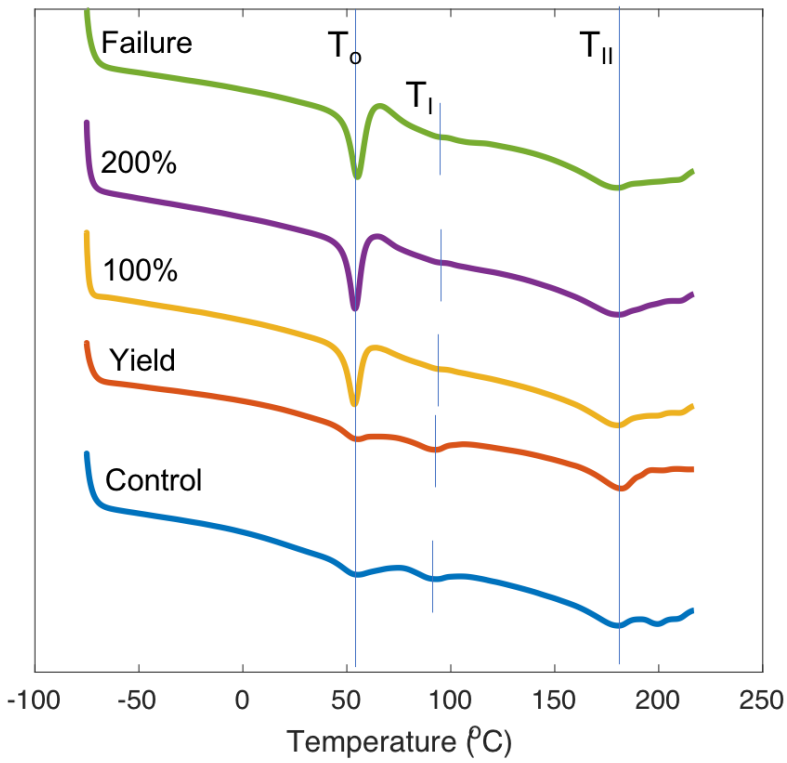

Figure 3.16: Impact of strain on the DSC curves of PCU.

3.3.3 Fourier Transform Infrared Spectroscopy

In line with the results of DSC, it was expected that FTIR would show an increase in order in the hard domain with increasing annealing. Such behavior would be indicated by a shift in the the ratio of the carbonyl peak for hydrogen bonded carbonyls in the amorphous region to hydrogen bonded carbonyls in the ordered hard domains (CO_{II}:CO_{III}). A lower CO_{II}:CO_{III} ratio suggests more hydrogen bonding in the hard domain and therefore a more ordered hard domain.

In unstrained samples, annealing reduced the number of free carbonyls (1737 cm^1) and hydrogen bonded carbonyls in the amorphous matrix (1722 cm^1) relative to the number of strongly hydrogen bonded carbonyls (1700 cm^1) (Figure 3.17, left). This suggests that annealing increased the order in the hard domains with more hydrogen bonding in the ordered domains relative to the amorphous regions. Unlike the results of DSC, there was no observable difference between different annealing temperatures. Samples annealed at 70°C, 100°C, and 140°C all showed a similar shift compared to the unannealed control. Following strain to failure, the carbonyl peaks were similar for all annealing conditions (Figure 3.17, right). The difference between the control and failed curves in the annealed samples was more pronounced than the difference for unannealed samples (Figure 3.18).

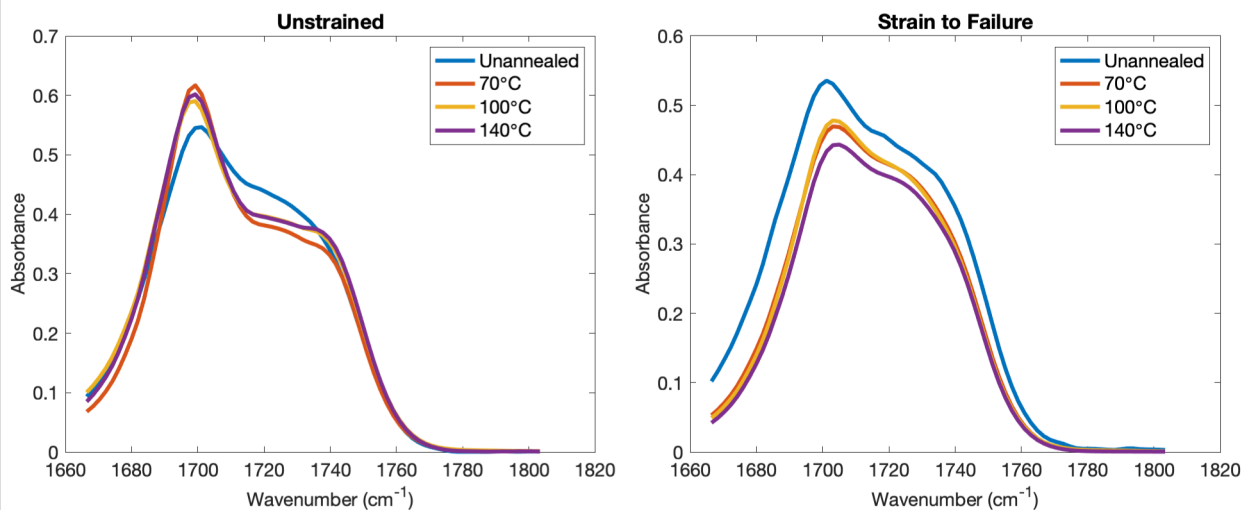

Figure 3.17: The carbonyl peak of unstrained Bionate® 75D (left) shifted with annealing to indicate fewer free and hydrogen bonded carbonyls in the amorphous matrix compared to those strongly hydrogen bonded. Peak shown normalized at 1700 cm^{-1}. When strained to failure (right), hydrogen bonds in the amorphous matrix and free carbonyls increase relative to hydrogen bonded carbonyls in the ordered domains for all annealing conditions.

Following strain to failure, CO_{II}:CO_{III} was similar for all annealing conditions (Figure 3.19, ANOVA $p = 0.22$). The CO_{II}:CO_{III} for unstrained and strained to failure unannealed

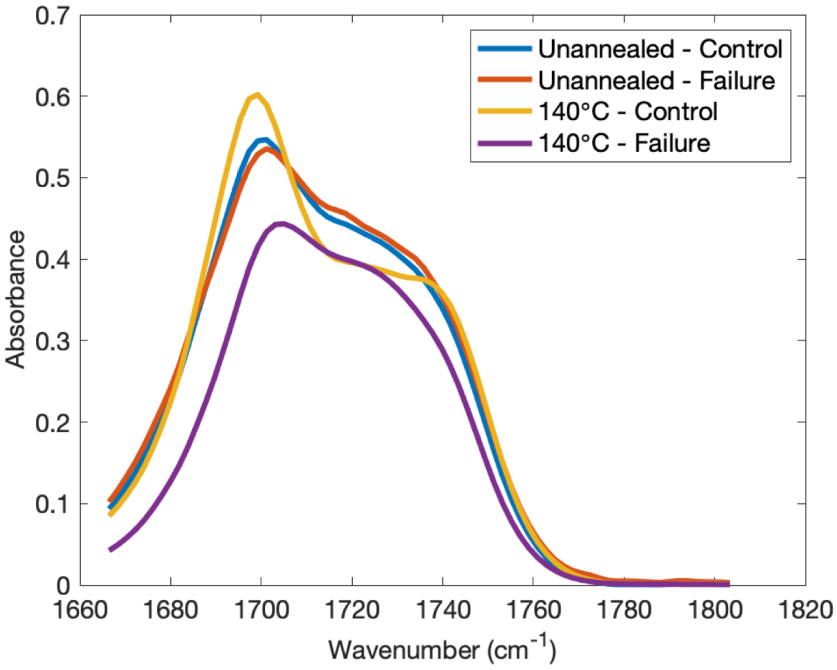

Figure 3.18: Comparison between no strain and strain to failure for unannealed samples and samples annealed at 140°C.

75D was similar (Figure 3.19, Student's t-test $p = 0.38$). For all other annealed conditions, the CO_{II}:CO_{III} ratio was significantly higher following strain to failure (Figure 3.19, Student's t-test $p < 0.008$). These results support what was seen in DSC. Annealing increases the amount of hydrogen bonding present in the ordered domains and, following strain to failure, all hydrogen-bonding-induced order is lost. The final state following strain to failure is independent of the initial degree of order in the hard domains.

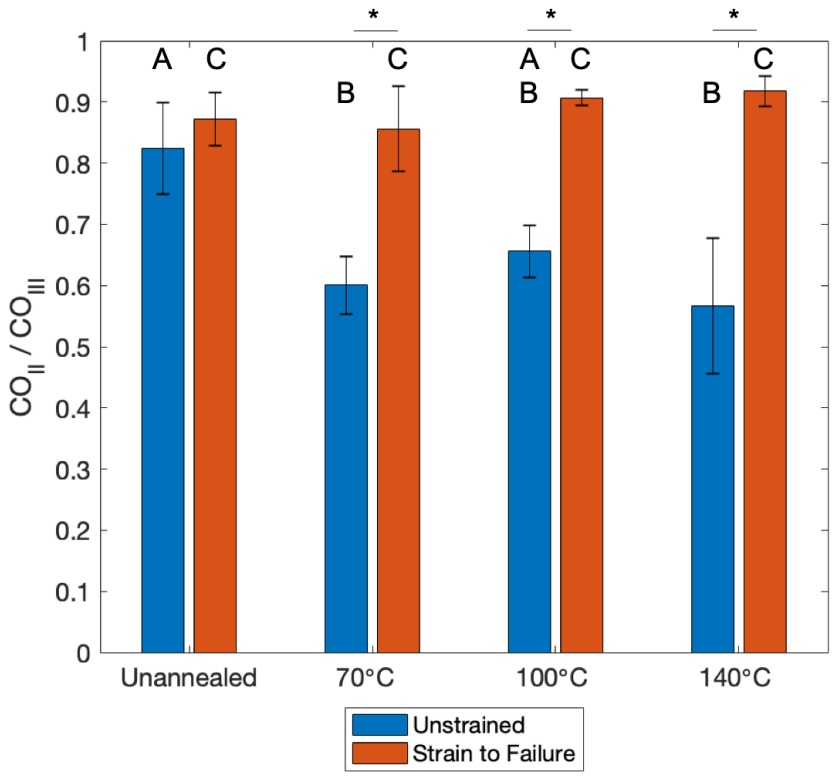

Figure 3.19: In unstrained 75D, the ratio of the carbonyls involved in hydrogen bonds in the amorphous matrix compared to those in ordered domains (CO_{II}:CO_{III}) decreased with annealing temperature. Following strain to failure, in all annealed samples, CO_{II}:CO_{III} increased compared to the unstrained condition and no difference was seen with annealing temperature. Mismatched letters (ANOVA) and *(Student's t-test) indicate statistical difference.

In contrast to the results of DSC, FTIR resolved some differences between strain conditions. Increasing strain in the samples annealed at 70°C increased the number of free carbonyls and hydrogen bonded carbonyls in the amorphous matrix relative to the number of strongly hydrogen bonded carbonyls in ordered domains (Figure 3.20). The pattern was not linearly correlated, but qualitatively showed lower hydrogen bonding in the hard domain at yield strain and 100% strain compared to the control and then another increase in 200% strain and failure strain compared to the control. Quantitatively, this correlates to a significant increase in CO_{II}:CO_{III} with strain (Figure 3.21, ANOVA $p = 0.003$).

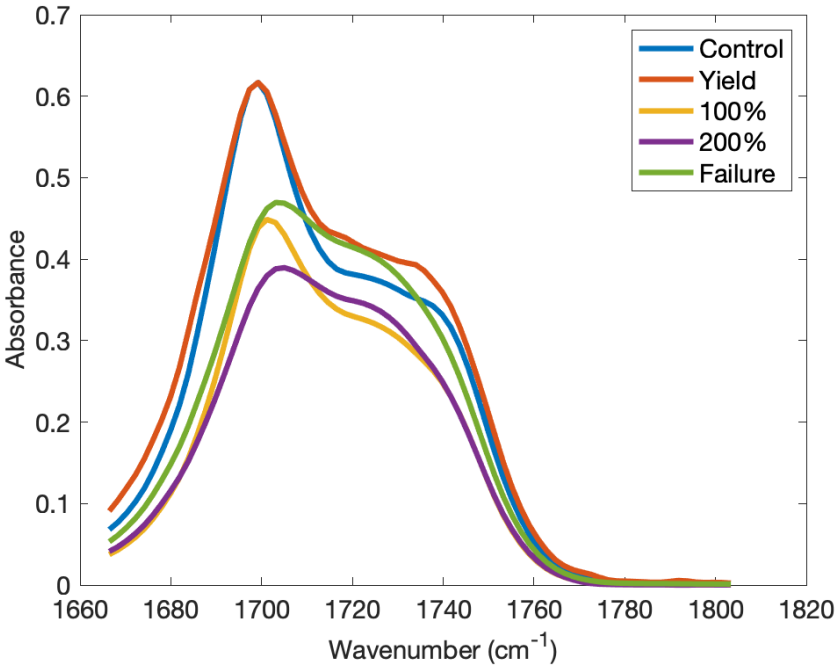

Figure 3.20: The carbonyl peak shifts from less contribution of hydrogen bonded carbonyls in the matrix and free carbonyls to more with increasing strain indicating a loss of order in the hard domains.

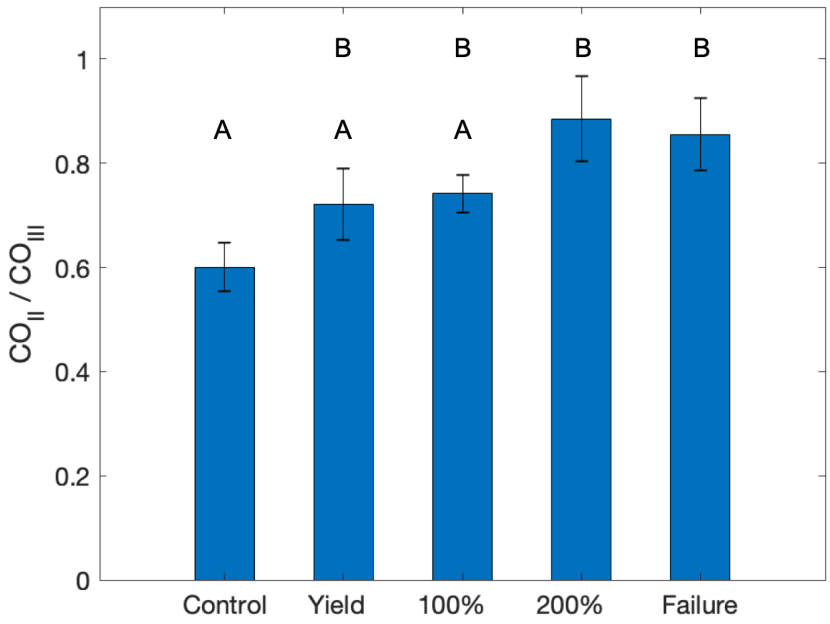

Figure 3.21: In 75D annealed at 70°C, the ratio of the carbonyls involved in hydrogen bonds in the amorphous matrix compared to those in ordered domains (CO_{II}:CO_{III}) increased with increasing strain indicating loss of order in the hard domains. Mismatched letters indicate statistical significance (ANOVA, $p = 0.003$).

3.3.4 Small Angle X-ray Spectroscopy

Compared to DSC and FTIR which indirectly correlate to hydrogen bonding in the hard domains, SAXS directly measures the domain spacing. We observed that inter-domain spacing decreased with increasing annealing temperature as indicated by the shift in the location of the peak in scattering intensity (Figure 3.22). Using Bragg's Law, the domain spacing was estimated to be between 11.4 - 14.3 nm (Table 3.4). No trend was observed with respect to the distribution of the domain sizes. The width of the scattering intensity peak can be correlated to the distribution in domain sizes. Peak width increased at annealing temperatures of 70°C and 100°C with respect to the unannealed control, but decreased again at 140°C. Scattering intensity images show symmetric scattering patterns for the unstrained control samples indicating an isotropically distributed structure (Figure 3.23).

Table 3.4: The domain spacing calculated form Bragg's law and width of the peak for each annealing condition, related to the distribution in spacing.

Annealing Condition	**Domain Spacing** $\AA$	**Peak Width** $\AA^{-1}$
Untreated	139	0.047
70°C	143	0.060
100°C	114	0.053
140°C	120	0.041

Following failure, we were no longer able to measure the inter-domain spacing due to the fact that we only had measurements in 1D. Comparing the scattering patterns between the unstrained and failed samples shows symmetric patterns in the unstrained sample for all annealing conditions and a non-symmetric scattering pattern emerged following failure for all annealing conditions (Figure 3.23). This asymmetric pattern indicated anisotropic distribution of the domains. This is likely a result of alignment of the domains in the direction of strain.

For samples annealed at 70°C the scattering patterns show a symmetric scattering pattern for both the control and yield conditions. However, after yield, the 200% strain and failure strain conditions show increased asymmetry in the scattering patterns (Figure 3.24). This suggests that the yield point is the transition where chain alignment begins as the structure orients in the direction of strain. Such behavior is similar to what is reported in semicrystalline polymers.

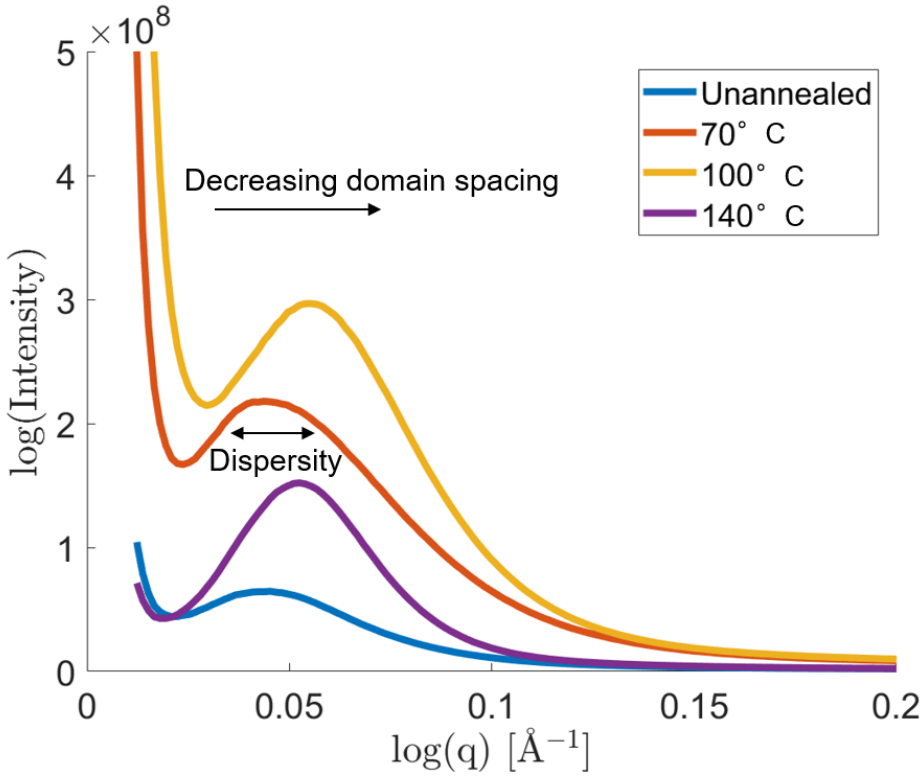

Figure 3.22: The maximum intensity shifted right with increasing annealing temperature indicating a reduction in domain spacing. The peak widths increased with annealing temperatures of 70°C and 100°C indicating a broader distribution of spacing dimensions, but then decreased again at 140°C.

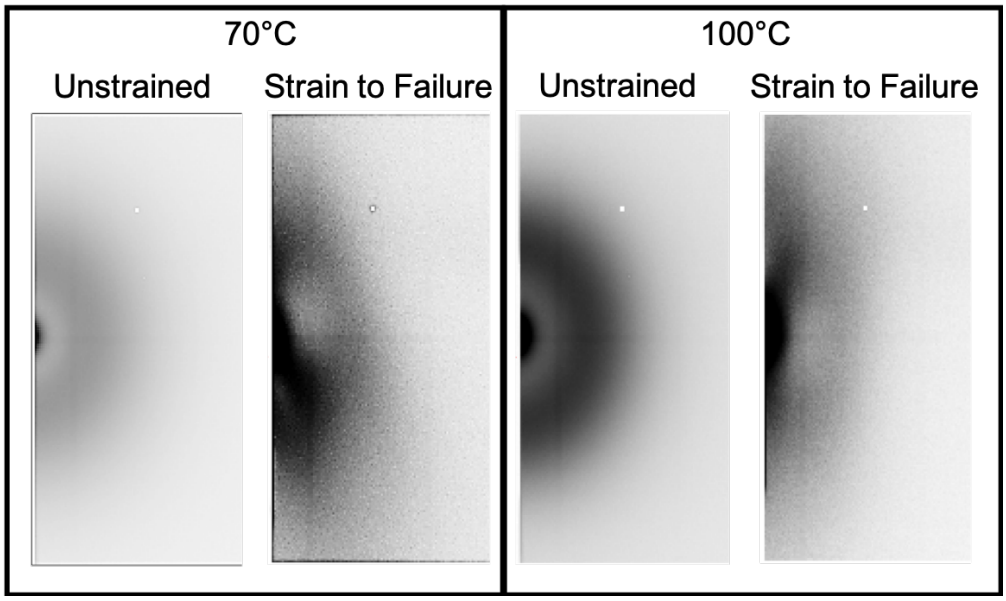

Figure 3.23: SAXS scattering patterns for unstrained and strained to failure and samples annealed at 70°C (left) and 100°C (right). For both annealing conditions, samples show symmetric scattering patterns before strain followed by asymmetric patterns after strain indicating a shift from isotropic to anisotropic structure.

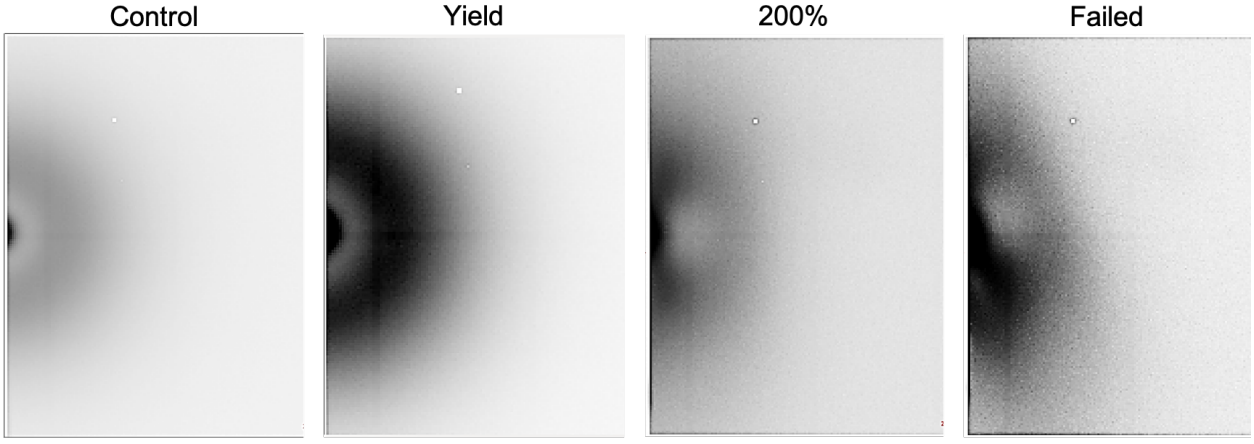

Figure 3.24: SAXS scattering patterns for samples annealed at 70°C at control, yield, 200%, and failure strains. The control and yield strains show symmetric patterns indicating isotropy, while the 200% and failure strain show increasing degrees of anisotropy as would be expected.

3.4 Relating Structure to Mechanical Properties

The correlation between structure and mechanical properties, although well known to exist within polyurethane copolymers, has not been well documented for the particular formulation of Bionate® PCU. This study begins to relate thermal processing (annealing) with mechanical properties (yield stress, modulus) through measurable metrics of the structure (DSC, FTIR, SAXS). Yield stress and modulus decrease with increasing order in the hard domains shown by a decrease in the T_I endotherm, measured from DSC (Figure 3.25), and increasing $CO_{II} : CO_{III}$ ratio, measured with FTIR (Figure 3.26). The relationship between domain spacing, measured by SAXS, and mechanical properties, modulus and yield stress was less clear, but the highest moduli and yield stress correlated with larger domain spacing, suggesting more ordered domains (Figure 3.27). These relationships are important to inform design with PCU biomaterials where material properties of a part post injection molding could differ from test specimens molded in a different geometry with different molding temperatures and cooling times. Further, any heating during sterilization and post processing could also impact the properties of the end device.

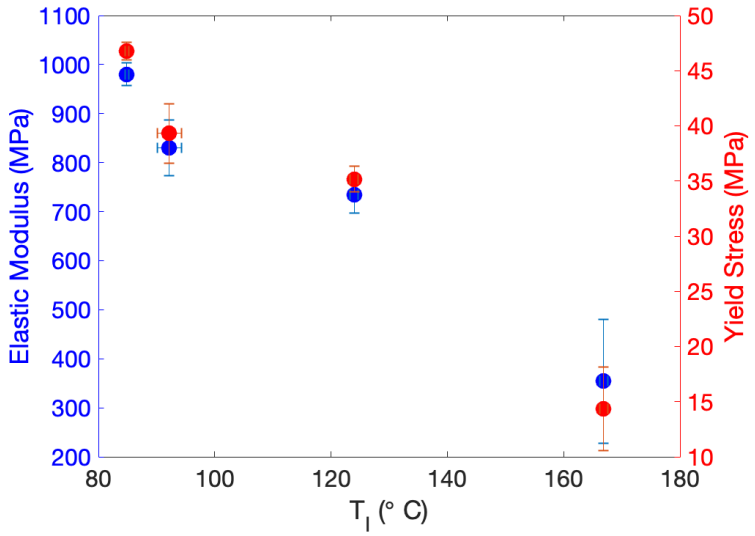

Figure 3.25: The yield stress and elastic modulus were found to be negatively correlated with the T_I endotherm relating more order in the hard domain to more ductile material (R^2: elastic modulus = 0.95, yield stress = 0.95).

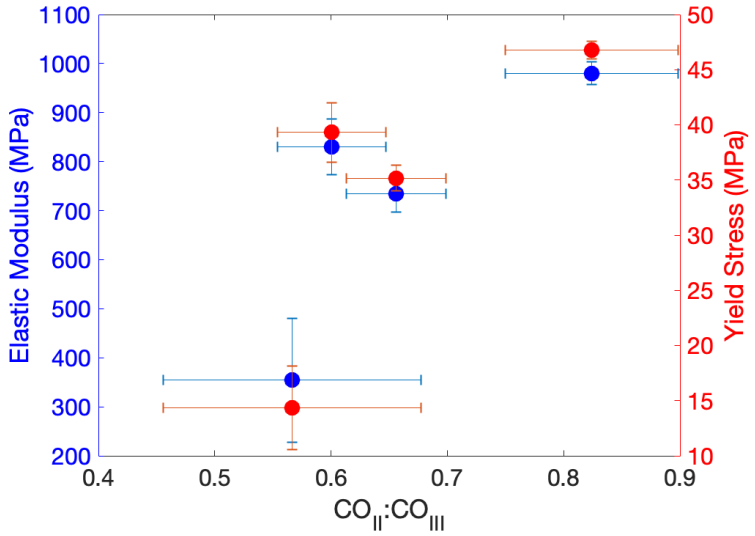

Figure 3.26: The yield stress and elastic modulus did not have a strong correlation to the CO_{II} : CO_{III} ratio, but the trend was positive suggesting that more order in the hard domain to more ductile material (R^2: elastic modulus = 0.59, yield stress = 0.57).

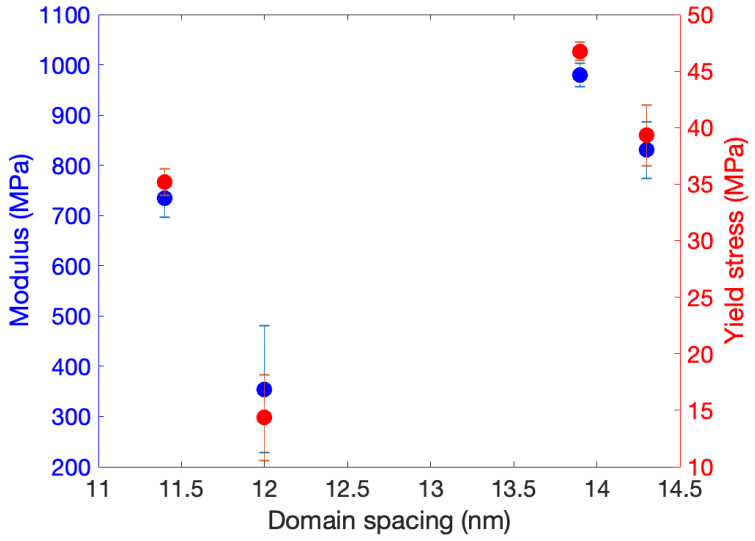

Figure 3.27: The domain spacing did not correlate linearly with material properties, but the maximum modulus and yield strength had higher domain spacing suggesting more ordered domains (R^2: elastic modulus = 0.41, yield stress = 0.37).

3.5 Discussion

The objective of this study was to investigate the impact of static mechanical strain on the structural organization of polycarbonate polyurethane with respect to the impact of *in vivo*

loading of medical devices. DSC and FTIR, indirectly probe the order in the copolymer through relative amounts of hydrogen bonding as a proxy for amount of order in the hard domain. SAXS gives a more quantitative measure of the size scale and organization of structural features in PCU.

Results from both FTIR and DSC suggest an increase in hydrogen bonding in the hard domains, following post-molding annealing treatments, correlating positively with temperature. Higher annealing temperatures lead to more hydrogen bonding. This result is in agreement with well documented behavior of polyurethane copolymers [54]. Further, both FTIR and DSC indicate a loss of order in the hard domains from hydrogen bonding following strain to failure which is independent of the initial degree of phase separation. Both DSC and FTIR showed a difference in hydrogen bonding between the control and yield strain. SAXS results confirmed the finding by showing a decreasing domain spacing which could imply an increase in hard domain size with increasing annealing treatment. SAXS qualitatively shows a disruption in the isotropy of the structural organization at 100% and 200% strain.

The finding that structural changes occur post yield also aligns with the results found in Chapter 2. The highly constrained stress state in the plastic zone ahead of the crack tip likely undergoes structural changes as the order in the hard domain is disrupted. The combination of strain and hysteretic heating effects combine to alter the structure ahead of the crack tip and control crack extension. This further supports that following relaxation, these effects are diminished and the mechanisms of crack growth are changed. Beyond the fracture implications previously discussed, a strain induced change to the structure of the material over time could change the overall mechanical behavior of a device over time. This has larger implications for contact stresses in the device that, if greater than the yield stress, could lead to the accumulation of bulk structural changes in the material structure over time.

This study shows that DSC, FTIR, and SAXS can resolve some differences in structure following annealing. However, the resolution of these methods is not high enough to create truly mechanistic understandings. The indirect approximation of hydrogen bonding is not correlated well enough to structure to show clear trends. For example, the different relative changes between strain conditions were not resolved by DSC, and FTIR differentiated only between large steps in strain. Therefore, DSC and FTIR could likely not resolve the impact of more subtle changes, for example as a result of fatigue. SAXS has a greater capacity to elucidate for quantitative features in the structure and using 2D SAXS would be ideal to characterize the structures.

The resolution of DSC, FTIR, and SAXS were even more limited with respect to strain induced changes. There was little measurable impact at very high strains. Therefore, it is unlikely that DSC and FTIR would be able to capture more subtle changes to the structure as a result of bulk cyclic loading as had originally been proposed for this study. Similarly, SAXS might be able to capture these changes, but 2D would be required to take quantitative

measurements on anisotropic order. Other methods such as AFM might be alternatives to characterize the structure.

The study aims to investigate the complex interactions between strain and the structural organization of PCU. We recognize that the geometry of the samples and the simplicity of uniaxial tensile loading, limit the clinical applicability of the results. Clinical loading is not only multi-axial and highly constrained, but also cyclic in nature. This is more relevant in the highly constrained geometries of medical devices where large plastic strains are limited, but long device lives are required. However, based on the findings here, in order to pursue future work focusing on investigating the impact of multi-axial and cyclic strain on the structural organization of PCU, structural characterization methods must first be developed.

3.6 Conclusions

The results of this study demonstrate that, like other copolymers, the order in the phase-separated domains of Bionate® 75D is dependent on thermal annealing and mechanical strain. Annealing had a strong impact on the stress-strain response of PCU. Samples annealed at higher temperatures had an increasingly ductile response. Hydrogen bonding in the ordered hard domains increased with increasing annealing temperature and decreased with increasing strain. A lack of resolution in the characterization methods limit the creation of detailed structure-function relationships between these parameters. Therefore, additional study is needed to understand the complex structural organization of PCU with respect to its use in medical devices where thermal processing during manufacturing and *in vivo* loading could change the structure and, consequently, the mechanical response of the material.

Chapter 4

Elastohydrodynamic Lubrication in PCU Hip Implants

4.1 Introduction

As discussed in Section 1.3.1, the leading cause of failure in polymeric hard on soft total joint replacements is loosening, a wear related failure. Wear of the ultra-high molecular weight polyethylene (UHMWPE) bearing surface creates particulate debris that is released into the joint cavity. On small size scales, these particles initiate an immune response. The immune response begins a biological cascade, releasing cytokines that can then lead to bone resorption and further accelerate implant failure [19]. Therefore, the primary target in moving toward PCU as an alternative material is to improve the wear performance. Reducing wear would increase the lifespan of the device and meet the increasing demand for longer lasting implants.

The use of a softer, more compliant, bearing surface has, therefore, been proposed as a potential solution to improve the wear performance of total joint replacements. The only commercialized compliant bearing material is polycarbonate polyurethane (PCU). As an elastomer, PCU has a high energetic toughness, while also having a lower modulus (20 MPa) than UHMWPE (1 GPa). It is marketed as having a lower contact stress and increased lubrication thickness to improve wear performance (See Chapter 1). The Tribofit® acetabular cup (Active Implants, Memphis, TN, USA) has been available in the EU since 2006 and the Nusurface® meniscus implant (Active Implants, Memphis, TN, USA) has been available in the EU since 2008 and is currently undergoing FDA clinical trials. Other devices using PCU were reviewed in Chapter 1.

In the previous chapters we investigated the fatigue performance of PCU with respect to its clinical use in orthopedic implants. However, given that wear related failures present the largest challenge for current UHMWPE implants, the tribological performance of PCU is central to the application of orthopedic implants. Theoretical elastohydrodynamic lubrication (EHL) models of the lubricant thickness, initially showed great promise predicting

full fluid lubrication and low wear for PCU systems [73, 74, 75]. *In vitro* experimental hip simulator studies have not shown as large of an improvement as was predicted [70, 71, 72]. We hypothesize that the loading assumptions in early lubrication models led to an over prediction of the lubrication regimes. Simplified models predicted thick lubricant films, which would reduce surface contact and improve wear performance.

The aim of this chapter is to apply a more physiologically accurate 3D-transient EHL model to reassess lubrication thicknesses of lower modulus materials in hip implants compared to an UHMPWE cup. First, an overview of wear studies related to PCU will be presented. The theory of contact, wear, and lubrication modeling will be reviewed. Then the theory of EHL modeling will be introduced. Finally, we will present simulated lubrication results using an existing 3D-transient EHL model with a compliant, PCU, acetabular cup in a hip implant.

4.2 Experimental and Simulated Wear Performance of PCU

EHL modeling has been used to evaluate the impact of using a compliant bearing material, like PCU, in orthopedic implants. Early studies predicted that a more compliant bearing surface would lead to lower contact pressures and thicker lubrication layers than with UHMWPE [74, 128]. However, these studies were limited in that they used a model fit for the solution of the Reynold equation and used a non-physiologically high viscosity for convergence stability. These models predicted film thicknesses on the order of 0.2 μm.

Wang et al. used a 1D steady-state EHL model to model a generic polyurethane elastomer with a linear elastic modulus of 20 MPa and Poisson's ratio of 0.4999 versus UHMWPE. He found that the polyurethane designs with radii of 16mm and 23mm had fluid film thicknesses of 0.166 μm and 0.364 μm respectively compared to a fluid film thickness of 0.110 μm for the UHMWPE design with a radius of 14 mm (Figure 4.1) [68]. This corresponded to a reduction in the fluid pressure distribution in PCU implants (Fig. 4.2). This model suggested that while the lubrication thickness of UHMPWE (0.11 μm) is lower than the surface roughness (0.1 - 2.5 μm) [129], it is operating in a mixed mode lubrication regime and susceptible to wear. A thicker film for PCU suggested a better lubricated regime compared to its surface roughness (reported as 26.6 - 783.0 nm) [71].

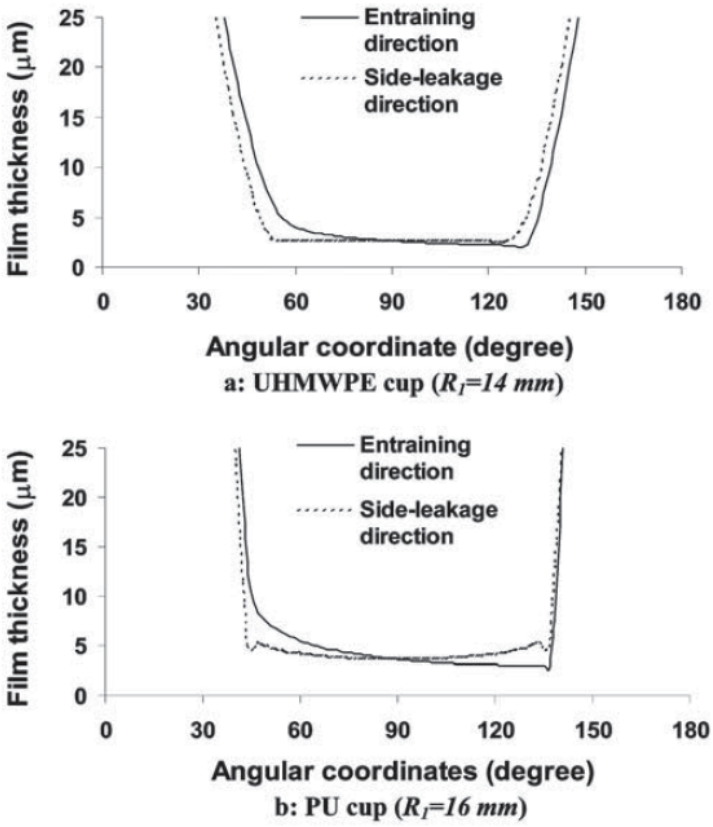

Figure 4.1: The film thickness distribution in UHMWPE and PCU for a steady state model with only flexion and extension motion at a load of 1456 N and viscosity of 0.5 Pa·s. Reprinted from [68], with permission from Sage Publishing.

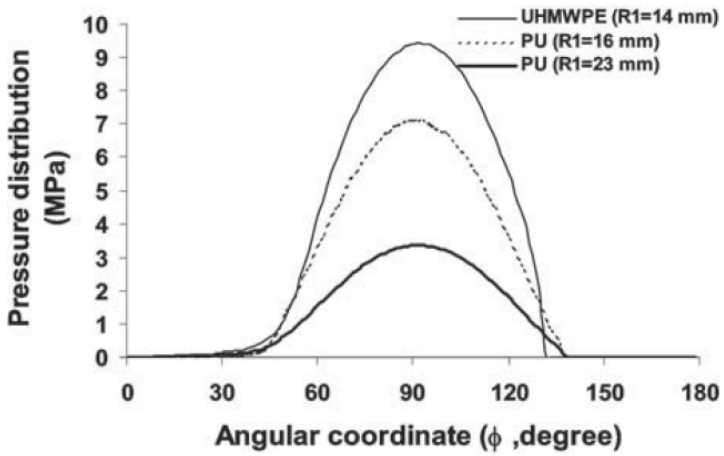

Figure 4.2: The lower modulus of polyurethane reduced the fluid pressure distribution compared to UHMWPE. Increasing the radius further reduced the peak pressure. Reprinted from [68], with permission from Sage Publishing.

A full fluid film lubrication regime is how native cartilage maintains such low coefficients of friction. The two articulating surfaces are separated by the lubricant and do not come into contact. As the lubricant thickness decreases within the range of the surface roughness, some of the higher asperities (peaks) come into contact and wear can occur. With thinner lubricant thicknesses, more and more asperities come into contact, increasing wear until a boundary lubricated regime is reached and only a thin layer of the lubricant exists. Early EHL studies predicted full fluid film lubrication regimes to mixed lubrication (but better than UHMWPE) and led to the promotion of the material as 'biomimetic' and 'cartilage-like', implying that it utilizes the same mechanisms as native cartilage to maintain its incredible friction and wear resistance [69]. These early models were used to motivate the study of PCU and many publications looking at PCU as a candidate material for medical devices cite improved lubrication regimes as a motivation [116, 130, 70, 71, 72, 14, 84, 131]. However, experimental data does not fully align with these predictions.

Simulation and experimental studies of PCU have shown low friction levels and full or partial lubrication regimes in PCU bearing [116, 131]. Bionate® articulating on cartilage also showed good results with a low coefficient of friction and limited wear to the cartilage [86]. The measured coefficients of friction were 0.24 - 0.5 compared to 0.0005 - 0.04 for native cartilage on cartilage articulation [86].

There is no clinically acceptable wear rate or failure criteria. Therefore, wear is typically assessed in comparison to the current standard, UHMWPE. Since UHMWPE is known to fail due to wear related issues, a lower wear rate than UHMWPE would signal promise for the material.

Initial data from *in vitro* wear studies suggests that the wear properties of PCU are similar to or slightly lower than those of UHMWPE. Two studies by Elsner, of Active Implants Inc, using the ISO 14242 gait loading curve with a maximum load of 3000 N for 8 and 20 million cycles, report a volumetric wear rate for PCU of 5 - 11 mm^3/million cycles (2 - 3 x 10^6 particles/million cycles) [70, 71, 132]. Another hip simulator study by Active Implants Inc, used direct UHMWPE control with a Paul loading curve and 3000 N max loading for 5 million cycles. This study reported a higher wear rate for PCU, at 19.1 mm^3/million cycles compared to a control of UHMWPE at 25 - 27 mm^3/million cycles [72]. Other studies report positive results for PCU compared to UHMWPE in a less clinically relevant dual axis pin-based wear simulator [133].

Compared to crosslinked UHMWPE, the wear rate of PCU is less promising. Wear rates of UHMWPE have been significantly lowered with the addition of crosslinking. Wear rates of conventional UHMWPE range from 17.1 - 56.7 mm^3/million cycles with metal and ceramic respectively. Crosslinking reduces these rates to 4.7 - 8.1 mm^3/million cycles for UHMWPE on metal and ceramic respectively [14]. The reported wear rates for PCU of 5 - 19.1 mm^3/million cycles [70, 71, 72] falls within and above the range reported for crosslinked

UHMWPE (Figure 4.3). There is not a clear improvement in wear performance of PCU over UHMWPE based on wear volumes in experiments as was predicted by lubrication models.

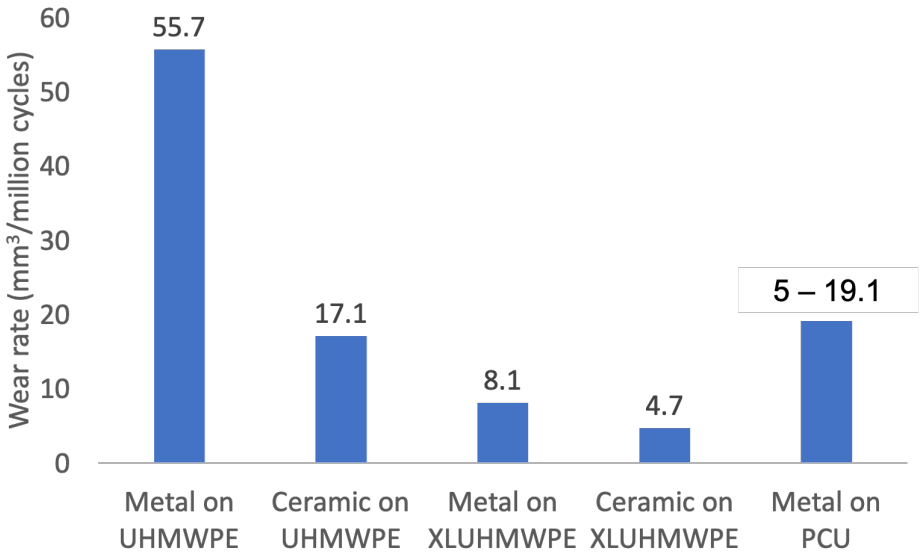

Figure 4.3: The wear rate of PCU reported from *in vitro* studies is comparable to current wear rates in crosslinked UHMWPE. Adapted from [14].

Although explant data is very limited, wear estimates from *in vivo* data estimates similar wear to what has been reported *in vitro*. One study reported a wear rate of approximately 13.4 mm^3/year after 10.5 months on implantation [77]. Another study of an explant from 12 months of implantation estimated a wear rate of less than 15 mm^3/year [76].

Beyond wear volume, the size of the PCU particles, from *in vitro* hip simulator testing, was also found to be different from that of UHMWPE [70, 71]. Generally, small wear debris 0.2 - 10 μm triggers immune cells to start an inflammatory response [70]. Therefore, if PCU wear particles are larger, macrophage inflammatory response to PCU may be lower than the inflammatory response to smaller UHMWPE wear particles [19]. The inflammatory cell response has been correlated with changes in osteoclast function and long-term bone resorption. This can lead to loosening and failure of a device. The large size of the PCU particulate debris is therefore less likely to initiate the adverse biological cascade. However, larger particles could produce additional tribological challenges.

PCU particles in a wear simulator study were found to be 8 - 13 μm (Figure 4.4) compared to the reported size of UHMWPE (0.1 - 5 μm) and metal debris (0.051 - 0.116 μm) [70, 71]. In contrast to what was found in simulator studies, in an explant study, Wippermann found significantly smaller wear particles than reported by Elsner. After 10.5 months *in vivo*, Wippermann reported average particles sizes of 0.9 and 2.9 μm using filtration and

SEM with a range of 0.5 - 30 μm (plus a single particle of 200 μm) [77].

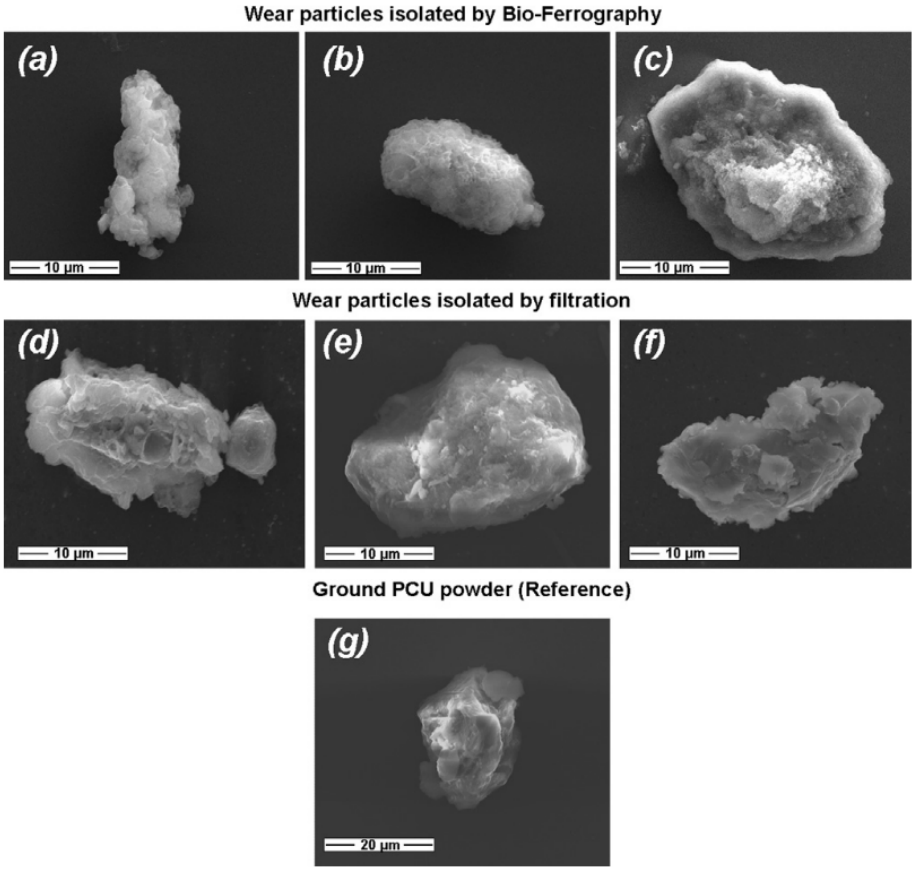

Figure 4.4: The wear particles in PCU were reported to be larger on average than those in UHMWPE or metal on metal implants. Larger wear particles are hypothesized to have lower inflammatory potential. Reprinted from [70], with permission from Elsevier

Overall there is a conflict between the optimistic predictions of EHL modeling and the outcomes of *in vitro* wear studies for PCU in orthopedic implant applications. In this chapter we present the results of a collaboration between the author and Dr. Leiming Gao. We apply a more clinically relevant 3D loading EHL model, developed by Dr. Gao, to revisit the mechanics of lubricated contact with a compliant surface. The goal of this study is to align the simulations with the *in vitro* experimental studies to understand the tribological characteristics of using compliant materials, like PCU, in orthopedic implants.

4.3 Theory of Elastohydrodynamic Lubrication Modeling

The best way to reduce wear in engineering contact systems is through lubrication. In the case of a total joint replacement, the lubricant, synovial fluid, is naturally available. However, the presence of a lubricant does not ensure better tribological performance. The lubricant must be able to maintain separation of the two contacting surfaces under an applied load and relative motion. Hydrodynamic lubrication/mixed lubrication describes the fluid layer that separates or partially separates two surfaces based on the relative velocity and applied load of one of the surfaces based on lubrication approximation theory. The Reynolds equation can be solved to determine the fluid thickness and pressure distribution in the fluid based on a given applied load, geometry, fluid viscosity, and velocity. EHL couples the solution for the elastic deformation of the materials due to the applied pressure with the film thickness of the lubricant. EHL uses the finite difference method to solve the highly non-linear coupled problem in lubricated contact. Along with the stability challenges of the nonlinear nature of the problem, efficient solvers are required for convergence.

Lubrication in bearing contacts is well studied from the perspective of classical mechanical bearings and acts to limit the direct interaction between asperities of the two contacting surfaces through the balance between mechanical deformation of the surfaces and the flow of the fluid. For contacts where the load is high and relative motion is low, the material deformation dominates the fluid lubrication layer. Therefore, the dry contact approximation for deformation can be used to typify the physical character of the contact. But fluid lubrication effects are still important to consider. Examples of such bearing surfaces include roller bearings and cams in which the contact areas are small and the pressures are high leading to deformation of the contacting surfaces. Such classic mechanical examples have strong analogies to a ball-in-socket hip implant.

Lubrication modeling is so well studied because it is impractical to measure lubricant thickness and pressure in many applications. To measure lubricant thicknesses, white light interferometry is used which requires on of the bearing couples to be optically clear. In the case of total joint replacement, EHL provides the ability to model complex lubrication regimes that cannot be experimentally measured and have important implications to device life and performance.

The results of EHL approximate the lubrication regime and are related to wear, but do not directly predict the wear potential of the material. We begin by motivating the use of EHL for approximating wear performance by outlining the relationship between lubrication, contact, and wear.

4.3.1 Lubrication Regimes

In an effort to reduce wear, lubrication is employed to reduce contact between articulating surfaces. Lubrication reduces the frictional force which correlates to wear. It also physically separates regions of the contacting surfaces, reducing adhesive effects and contact stresses. Lubrication is described as three main regimes, boundary lubrication, mixed lubrication, and full film lubrication.

The Stribeck curve describes the interaction between the lubrication regimes and the resultant coefficient of friction for a given system as a function of the relative velocity between the surfaces, applied pressure, and viscosity of the fluid (Figure 4.5). Boundary lubrication occurs when there is a majority of contact between the two surfaces, mixed lubrication is a middle state where some regions are lubricated, while some asperities of the surfaces are in contact, and full fluid lubrication is a regime where the lubricant fully separates the surfaces and no solid-solid contact occurs (Figure 4.6). Elastohydrodynamic lubrication is the ideal state for reducing wear of a system. However, the lubrication regime is a function of velocity, and when velocity goes to zero the system tends toward boundary lubrication.

In the case of total joint replacement, where loading is highly variable, even if a bearing couple provides good lubrication in a steady state case, there will exist time points of start-up and reversal of motion, where the lubrication regime will tend towards mixed or boundary lubrication.

The hydrodynamic lubrication regime (λ) is dictated by the ratio between the minimum film thickness (h_{min}) of the lubrication layer and the composite surface roughness (average roughness: R'_a or rms roughness: R'_q) (Equation 4.1).

$$\lambda = \frac{h_{min}}{R'_{(a)}} \tag{4.1}$$

A boundary lubrication regime is defined as systems where $0.1 \leq \lambda < 1$, a mixed lubrication regime is defined as $1 \leq \lambda < 3$, and a full fluid film lubrication regime is defined as $\lambda \geq 3$.

For materials with low modulus subjected to high contact pressures, microelastohydrodynamic lubrication may reduce the roughness height. The theory of microEHL is that the high contact pressures deform asperities in the contact region to create a more uniform and smooth surface and decrease the potential for mixed lubrication regimes. This theory has been cited in support of the use of compliant bearing surfaces like PCU.

The lubrication regime is based on fluid behavior, but in EHL, the relative displacement due to material deformation typically dominates compared to the undeformed fluid thickness.

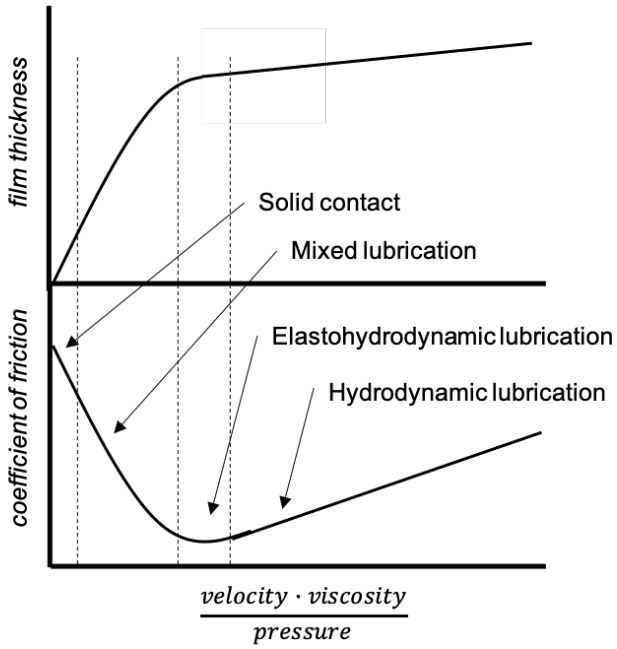

Figure 4.5: The Stribeck curve shows that lubrication regime and coefficient of friction are a function of the relative velocity, lubricant viscosity, and applied pressure of the contact system. The coefficient of friction is highest in boundary lubrication, then lower in mixed lubrication, and then lowest in elasto- and hyrodynamic lubrication or full-fluid lubrication. Adapted from [134].

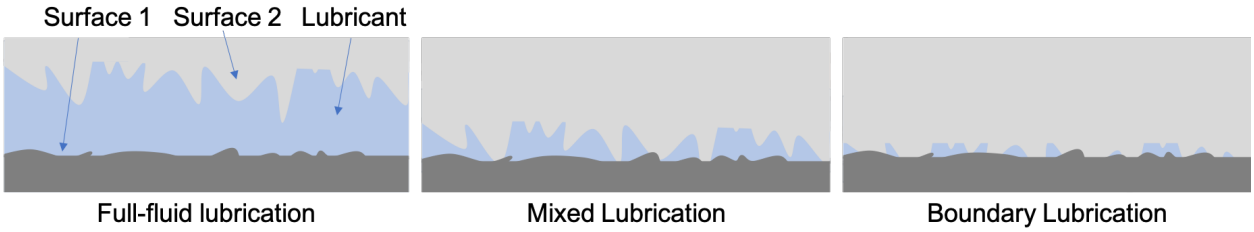

Figure 4.6: Lubrication regimes are defined as full-fluid lubrication, also referred to as hydrodynamic lubrication or elastohydrodynamic lubrication (left), mixed lubrication when some asperities are in contact while other areas are lubricated (center), and boundary lubrication, where little lubricant separates the surfaces and a large portion are in direct contact (right).

In an EHL model, different methods have been developed to calculate the elastic deformation in the acetabular cup based on a given pressure distribution. The contact problem was first

solved analytically by Hertz. The Hertzian contact solution relates the loading, geometry, and material properties of two contacting bodies and the resulting contact area, contact stress, and deformation. These relationships between load, contact area, contact stress, and deformation provide context for the results of the EHL model with respect to wear potential.

4.3.2 Hertzian Contact Theory

As will be presented in the next section, the wear rate has generally been shown to be a function of contact pressure, sliding distance, and contact area. Hertzian contact theory provides an analytical model to understand the interaction of contact stress, material properties, contact area, and geometry in a given contact. Hertz was the first to find an analytical solution to the problem of two contacting spheres assuming a parabolic approximation for the bodies. The gap between the two bodies can be described by:

$$h(x,y) = h_0 + \frac{x^2}{2R_x} + \frac{y^2}{2R_x} + \frac{2}{\pi E'} \int_{-\infty}^{+\infty} \int_{-\infty}^{+\infty} \frac{p(x',y')dx'dy'}{\sqrt{(x-x')^2 + (y-y')^2}} \tag{4.2}$$

where h is the gap between the two bodies, h_0 is the initial distance between two relative points in the two bodies, $R_x = R_y$ which are the equivalent radii, E' is the equivalent modulus of the two body system, and p is the pressure distribution in the contact area.

According to Hertzian contact theory, contact stress and the resulting material deformation is a function of the modulus of the contacting material, applied load, geometry, and the contact area. When two surfaces are pressed together in contact, both bodies deform to give a contact area with a pressure distribution that balances the applied load (Figure 4.7).

In contact, the gap (h) is equal to zero and pressure is positive. Where the gap (h) is greater than zero, no contact occurs and the pressure is zero. The force balance between the applied load (w) and the pressure distribution in the area of contact is given as:

$$w = \int \int_{\Omega} p(x,y)dA \tag{4.3}$$

where Ω is the contact area.

The analytical solution by Hertz for two spheres of equal radius in contact results in a contact area disc of radius a. The central deformation is given as:

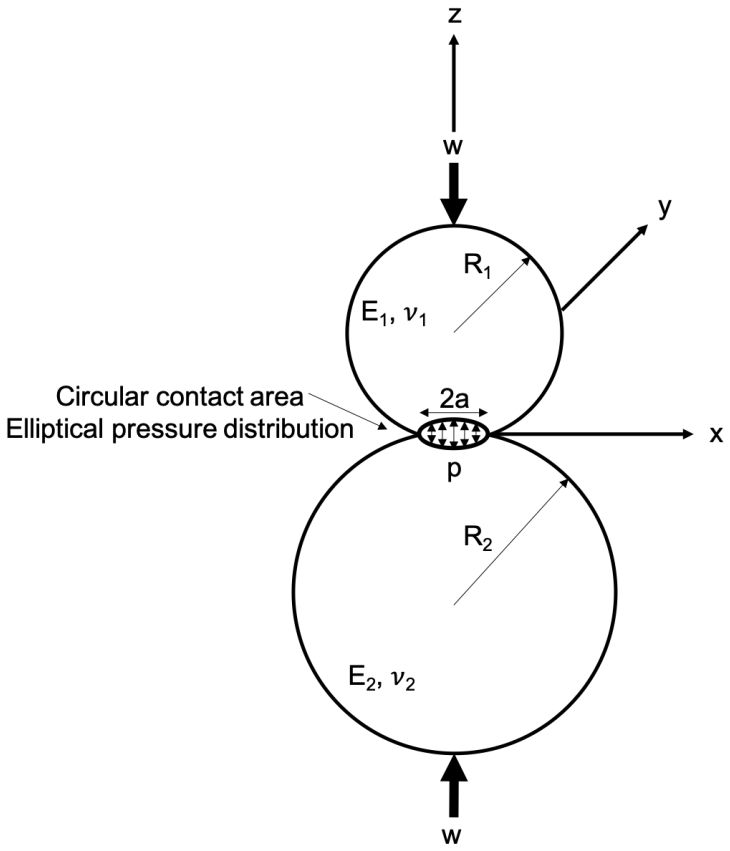

Figure 4.7: Hertzian contact theory for two spheres gives an analytical solution for the contact area and pressure distribution based on the radii of each sphere (R), the applied load (F), and the elastic modulus and Poisson's ratio of each sphere (E and ν).

$$h_0 = \frac{-a^2}{R_x} \tag{4.4}$$

and the resulting pressure distribution in the contact area is given as:

$$p(x,y) = p_h\sqrt{1-(x/a)^2-(y/a)^2} \tag{4.5}$$

Both these results are in terms of only two variables, the contact radius (a) and the central contact pressure (p_h). These variables are defined as:

$$p_h = \frac{3w}{2\pi a^2} \tag{4.6}$$

$$a = \sqrt[3]{\frac{3wR_x}{2E'}} \tag{4.7}$$

$$where: \frac{2}{E'} = \frac{(1-\nu_1^2)}{E_1} + \frac{(1-\nu_2^2)}{E_2} \tag{4.8}$$

The Hertzian contact solution provides a relationship between the contact pressure and the modulus of the material based on this simplified geometry. A reduction in modulus increases the contact area which in turn reduces the contact pressure. Although the solution is less straight forward for a conforming geometry, in the case of orthopedic implants, the reduction in modulus of PCU (24 MPa) from that of UHMWPE (1 GPa), would then also reduce the maximum contact pressure. However, a reduced contact stress does not directly correlate to lower wear. Material interactions, surface roughness, and lubrication can all influence the wear rate. In a conforming contact, a lower modulus will also increase the contact area leading to statistically more opportunity for interaction of surface asperities and wear to occur.

Hertzian contact has many simplifying assumptions that enable its analytical solution. It assumes similar material properties, low contact areas, and linear elastic material behavior. In early EHL models, Hertzian contact for a ball-on-plane geometry was used to estimate the elastic deformations under hydrodynamic pressure. To improve the fidelity of the model other analytical approximation such as the constrained column model were incorporated. Other analytical approximations of elastic deformation and finite element methods will be discussed in the solution of the EHL model. However, Hertzian contact provides a simple basis to understand the complex relationships between the variables that ultimately influence the lubrication regimes that are modeled in EHL.

4.3.3 A Generalized Wear Model

Archard's wear law provides an empirical wear relationship to understand what variables play a role in the wear rate of a material. Archard's law relates the wear rate (V) to a wear rate coefficient (C), the contact load (P), and the sliding distance (L) [135]:

$$V = CPL \tag{4.9}$$

Variations of Archard's Law have been adopted for modeling wear of UHMWPE joint replacements, incorporating material parameters such as hardness, yield strength, and cross

shear ratio [136, 137, 138, 139]. Liu et al. showed that for UHMWPE, the linear wear rate (δ = volumetric wear rate per area) was independent of contact pressure, but dependent on the cross shear ratio (C_o, Equation 4.11), contact area, and sliding distance. The cross shear ratio is the ratio of the frictional work component normal (W_{ti}) and parallel (W_{pi}) to the principal molecular orientation to the total frictional work discretized across a motion cycle [138, 139], leading to the relationship:

$$\delta = C(C_o)L \tag{4.10}$$

$$C_o = \frac{\Sigma W_{ti}}{\Sigma(W_{ti} + W_{pi})} \tag{4.11}$$

Although these wear laws can be informative in modeling and predicting wear, they rely on empirically derived relations rather than material properties or damage mechanisms. Some studies of UHMWPE have aimed to look more mechanistically to understand wear in UHMWPE, but without establishing a fundamental relation [140].

For PCU, although many simulator wear studies have been done [70, 71, 72], none have used the Archard wear model or a derivative of the model. Instead, wear rates have been reported in volume or mass per year or million cycles. Since the wear coefficient captures all the mechanistic information of the wear process, it is an oversimplification to assume that a lower contact stress could reduce the wear rate in PCU. Further, it has been shown that in UHMWPE, the wear rate is independent of contact pressure [139]. Therefore, to understand the long-term wear potential of PCU, a more detailed model is needed to capture the contact in a PCU joint replacement.

Wear has been incorporated into EHL models through the application of Archard's law iteratively with the transient EHL solution for metal on metal implants [141]. A wear model for metal was developed based on a modified Archard's Law which incorporates material thickness and surface roughness to predict wear rates. This model was able to capture the two regimes of wear observed in hip simulator studies: the 'wear-in' regime of a higher wear rate and 'steady-state' period with a lower equilibrium wear rate [142, 143].

Fundamentally, Archard's wear law relates the contact load (P) and the sliding distance to the wear rate through a coefficient that incorporates material, lubrication, and mechanistic effects. The results of EHL produce an estimate of the contact load (P), a direct variable in the wear law, and the lubrication regime, which is incorporated into the wear coefficient. Therefore, indirectly, the results of EHL can be used to predict changes in wear performance.

4.3.4 Elastohydrodynamic Lubrication

Next we will outline the components of the EHL model: hydrodynamic lubrication, elastic deformation, force balance, and numerical methods. Hydrodynamic lubrication consists of the fluid dynamic equations that approximate the film thickness and pressure based on an applied load and velocity. Elastic deformation considers the amount of deformation in the acetabular cup as a result of the fluid pressure. The force balance ensures equilibrium is maintained between the fluid pressure and applied loading. Finally, the numerical methods used to solve the highly nonlinear problem will be reviewed. The following overview serves to provide a basic foundation to understand the results of EHL modeling. For a more detailed overview of the problem and numerical methods employed in the solution see [144].

Hydrodynamic Lubrication

EHL simultaneously solves the Reynolds equation for fluid thickness and pressure distribution as well as elastic deformation of the material. It must first solve for the fluid thickness and pressure an initial thickness, then calculate the material deformation due to the pressure, and then iterate until a converged film thickness and pressure is reached. In some cases, the relationship between pressure and the viscosity and density of the fluid may need to be accounted for. However, that is not the case for total joint replacements where the viscosity can be approximated as Newtonian at the loads and velocities of motion.

Hydrodynamic lubrication refers to the uncoupled case without the consideration of elastic deformation. In hydrodynamic lubrication, the Reynolds equation (Equation 4.12) describes the pressure distribution in a viscous fluid flow through a small gap. The Reynolds equation can be derived from the Navier Stokes equations assuming negligible inertial and external forces, large planar dimensions relative to height, and no slip boundary conditions:

$$\frac{\partial}{\partial x}\left(\frac{\rho h^3}{12\eta}\frac{\partial p}{\partial x}\right)+\frac{\partial}{\partial y}\left(\frac{\rho h^3}{12\eta}\frac{\partial p}{\partial y}\right)-\frac{\partial(u_m\rho h)}{\partial x}-\frac{\partial \rho h}{\partial t}=0 \tag{4.12}$$

where p is the pressure, h is the total film thickness, u_m is the mean surface velocity, η is the viscosity, ρ is the density, and t is time (Figure 4.8).

A cavitation boundary condition is applied to ensure that no negative pressures exist in the solution. This results in the creation of a complimentary problem in which the Reynolds equation is valid when $p(x,y) > 0$ and set to $p(x,y) = 0$ everywhere else [144].

In the case of a total joint replacement (Figure 4.9), a spherical coordinate system is adopted [145, 146, 147] .

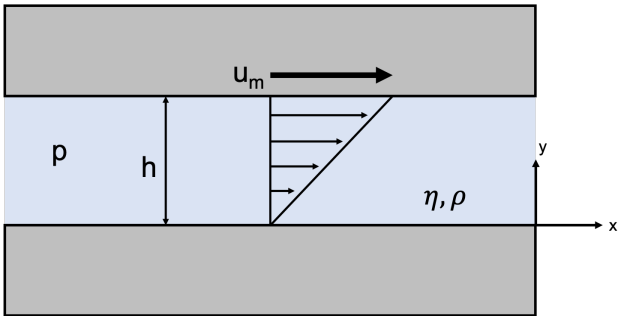

Figure 4.8: The Reynolds equation solves for the fluid thickness (h) and pressure (p) under the average velocity (u_m) considering the fluid viscosity (η) and density (ρ).

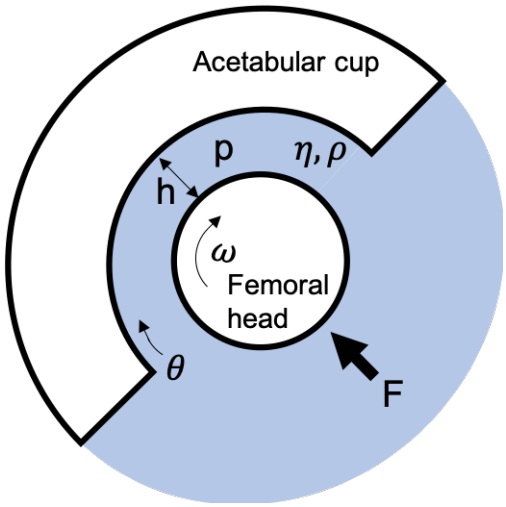

Figure 4.9: In the hip geometry, the Reynolds equation includes the rotation motion (ω) of the gait cycle considering that the fluid pressure must be in equilibrium with the applied load (F) from the gait cycle. The θ direction is along the arc shown and ϕ is normal to θ.

Solid Elastic Deformation

EHL couples the hydrodynamic lubrication problem with the elastic deformation of dry contact. In order to solve this coupled problem, the solver must iterate between a current solution for the film thickness and pressure and an updated solution accounting for material deformation as a result of that pressure. The elastic deformation has been incorporated into the EHL solution in several different ways, using analytical models, like the Hertzian contact solution, or, as used in this study, through relationships derived from finite element models [147].

The elastic deformation of the two bodies, the acetabular cup and femoral head, can be most simply approximated based on Herztian contact theory as described in Section 4.3.2. However, that is only valid for the limited geometries for which the assumptions

of the analytical solution apply. Another analytical method to approximate the elastic deformation based on a linear elastic response is through the constrained column model [145, 17]. In spherical coordinates the deformation based on the constrained column model can be calculated as:

$$\delta = \frac{R_2\left[(\frac{R_3}{R_2})^3 - 1\right]}{E\left[\frac{1}{1-2\nu} + \frac{2}{1+\nu}(\frac{R_3}{R_2})^3\right]}p \tag{4.13}$$

Another method to solve the elastic deformation is to use the finite element method to create a relationship between pressure and displacement based on an assumed symmetry and linear elastic material behavior. This method is used in Dr. Gao's 3D-transient EHL model [147]. First, a finite element model is used to solve for the deformation that results from a unit pressure applied at a single element area in the center of the cup. The deformation at every point due to a unit pressure at the center can then be used to generate a map between the distance of one point from another and the relative displacement [148]. A matrix mapping the displacement at every point in the mesh relative to a unit pressure at any other given point is created. The map is then incorporated into the model using the equivalent spherical discrete convolution (ESDC) technique and fast Fourier transform (FFT) to calculate displacement from a pressure distribution [148, 147]. This method assumes perfect symmetry such that no edge effects occur to change the material deformation as the load moves away from the center of the cup. This finite element approach allows for factors like supporting material and thickness to be incorporated in the elastic deformation.

Force Balance

Finally, a force balance between the fluid pressure and the applied load boundary condition must also be satisfied, incorporating the applied load from the gait cycle into the solution (Equation 4.14):

$$F = \int_{-\infty}^{+\infty}\int_{-\infty}^{+\infty} p(x', y')dx'dy' \tag{4.14}$$

where F is the total external applied load and p is the fluid pressure.

Numerical Methods of the Solution

In joint replacement models, a spherical mesh is adopted such that the element size in equal in both the θ and ϕ direction ($\Delta\theta = \Delta\phi$). Finite difference discretization schemes are used to discretize each equation. Typically, multiple finite difference schemes are applied to the Reynolds equation to promote stability. Gauss Seidel or Jacobi relaxation is used in the pressure iteration of the fluid solution. Multi-grid methods are used to accelerate the solution by relaxing different error frequencies on different mesh densities. Multi-level multi-integration methods are used to incorporate the elasticity solution into the solver. Convergence is then set as a limit on the change in the pressure error over one cycle, typically error $\leq 10^{-4}$ [144].

4.4 Elastohydrodynamic Lubrication in Orthopedic Implants

EHL theory can be applied to many examples of friction, wear, and contact in biology including, microcirculation of red blood cells in capillaries, the blinking of an eye and contact lens, respiratory motion between pleural surfaces, and articulation in synovial joints [149, 150, 151]. Its application to synovial joints and subsequently, artificial joint replacements provides a tool to study the complex *in vivo* environment [152, 153]. The designs that have been modeled include, metal on metal, ceramic on ceramic, metal on UHMWPE, and metal on polyurethane. Within more general EHL solutions, orthopedic applications have highly conforming bearing surfaces (i.e. ball-in-socket), synovial fluid as the lubricant, and highly variable and heterogenous loading patterns based on the gait cycle [129, 153].

EHL solves the coupled problem of the thickness of a pressurized fluid (the synovial fluid under loading) and the elastic deformation of the contacting surfaces. The governing equations and solution will be outlined below. The output of the EHL model is an approximation of the lubricant fluid thickness throughout the area of contact and the pressure distribution in that fluid. The fluid thickness can then be used to estimate the lubrication regime as outline in Section 4.3.1. The lubrication regime can then be related to the coefficient of friction and propensity of the system to undergo wear.

4.4.1 Geometry

EHL models of hip implants typically use a ball-in-socket geometry assuming a highly constrained geometry. In some cases, such as hard contacts (i.e. metal-on-metal), a ball on plane assumption can be used to simplify the problem (Figure 4.10, right). For soft contact, such as metal on polymer, a ball-in-socket geometry must be used to improve the accuracy of the results (Figure 4.10, left) [129, 145]. Another geometrical consideration is the position

of the acetabular cup. Anatomically the cup is typically positioned at an angle of 45° with respect to the horizontal [152].

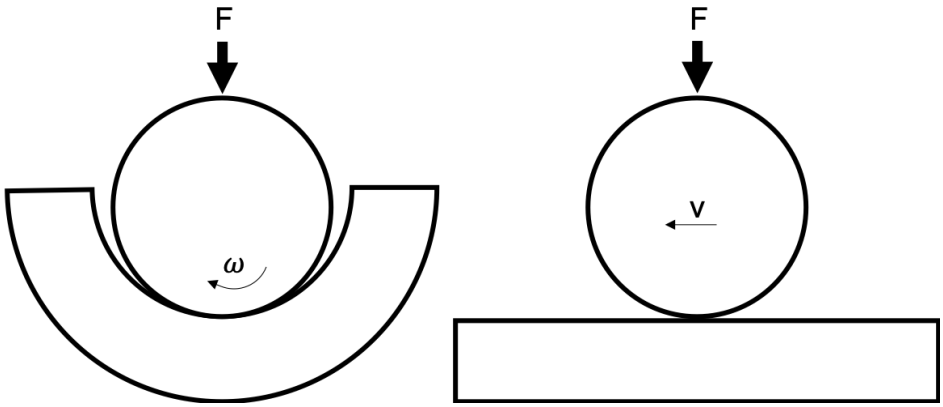

Figure 4.10: A ball-on-plane geometry can be assumed for hard-on-hard couples where the contact area is much smaller than the radius. Assuming ball-on-plane allows simple analytical models to be used to calculate elastic deformation. However, for soft contact, a ball on plane model is required to improve accuracy.

4.4.2 Lubricant

The lubricant used in orthopedic EHL models is synovial fluid, present in both the natural hip joint and TJR. Synovial fluid is known to decrease in viscosity as a results of disease (Figure 4.11) [154]. Synovial fluid is typically modeled as a Newtonian fluid with a representative viscosity of 0.002 - 0.0025 Pa·s or 0.0009 Pa·s for 25% bovine serum typically used in simulator studies. In reality, synovial fluid is non-Newtonian and experiences shear thinning. However, at physiological shear rates ($10^5 s^{-1}$) and contact pressures below 100 MPa, a Newtonian approximation without piezo-viscous effects is applicable [152, 153, 129]. In many models, especially earlier models, a higher than physiological viscosities (0.01 - 0.1 Pa·s) were used for convergence stability [68]. Higher viscosities will result in higher film thicknesses [68]. Therefore, it is important to consider the solution viscosity when comparing results of EHL models.

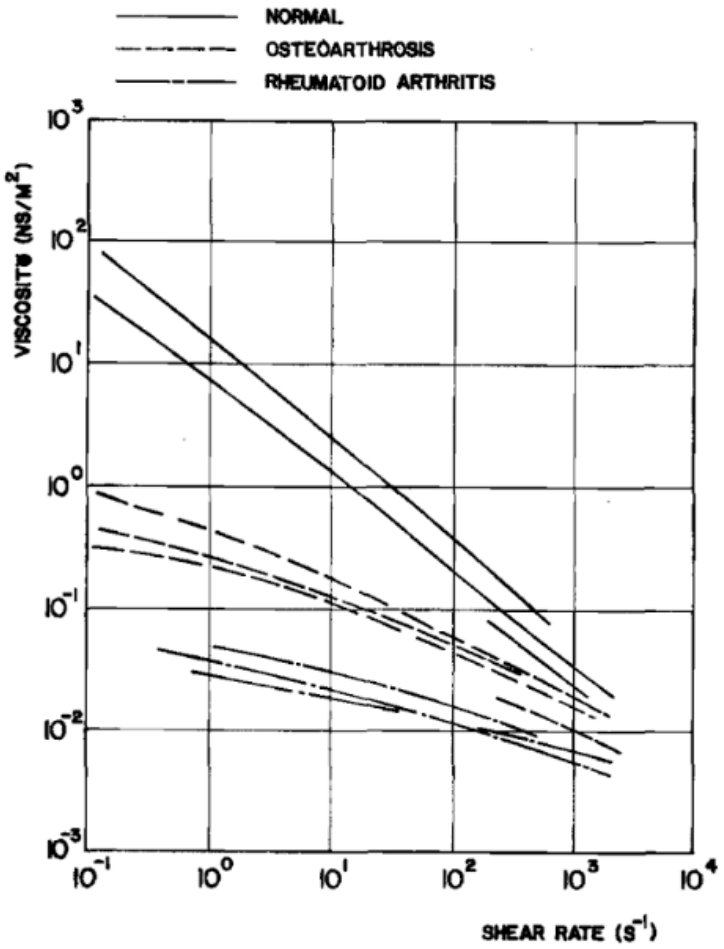

Figure 4.11: EHL modeling models synovial fluid as Newtonian and constant at physiological loads and shear rates. However, the viscosity of synovial fluid is shear thinning and lowered by the onset of osteoarthritis. Reprinted from [154] with permission from John Wiley and Sons.

4.4.3 Loading Conditions

The loading conditions in orthopedic EHL models have progressively become more sophisticated. Early models began with 1D quasi-static loading and 1D rotation. The model progressed to a 1D transient analysis, which revealed the role of squeeze film action in maintaining the film thickness during walking and a higher film thickness than quasi-static analysis [155]. EHL modeling of joint replacements has evolved to include a 3D gait cycle incorporating 3D loading and rotation. This allows the same loading pattern, for example the ISO14242 gait pattern (further detailed in the Methods Section), to be used in EHL models as is used in experimental wear simulator studies. Further development has incorporated load data collected from *in vivo* instrumented implants [156]. It has been shown that the film thickness in a metal on metal hip implant increases with 3D loading compared to

an equivalent 1D case [147]. Typical loads applied range from 300 - 3000 N with a steady state angular rotation of 2 rad/s [157, 155, 158].

4.4.4 Previously Studied Material Couples

The results of EHL studies on the different material types follow the trends expected from theory. The harder materials have smaller contact areas and lower film thicknesses. Metal on metal implants have the highest contact pressures and lowest film thickness, then UHMWPE on metal, and finally PCU on metal with the lowest contact pressures and largest film thickness. Within each of these designs, variations in the geometry of the device can further impact the character of the contact.

Metal on metal hip prostheses have lubrication film thicknesses in the range of 0.1 μm and contact pressures of 20 MPa - 55 MPa [155, 158]. It has been shown that the film thickness increases with increasing femoral head diameter and decreasing radial clearance [155, 159]. The thickness of the acetabular component also plays a role in dictating the EHL character [155]. However, other studies have shown little impact of the underlying material [159, 158]. It has been shown that accounting for the underlying bone compliance does not have a significant impact on the contact mechanics [158].

EHL studies of metal on UHMPWE hip prostheses have approximated a film thickness on the order of 0.2 - 0.3 μm with maximum contact pressures of 8 - 12 MPa [157, 145]. There was no observed difference in the predicted film thicknesses between quasi-static and transient analysis [157]. As stated earlier, this film thickness is lower than the average surface roughness of UHMWPE (0.5 μm) suggesting a mixed lubrication regime facilitating the wear issues seen in current implants. In mixed lubrication, some asperities are in contact with the opposing surface and there is not continuous lubrication. This mixed lubrication regime has been studied using a sinusoidally varying radial surface. This resulted in a reduced film thickness and a mixed lubrication regime at viscosities higher than physiological [152].

EHL solutions for a hip implant with a more compliant bearing surface material, using 1D-steady state loading, predicted lower contact pressures and thicker lubrication layers than with UHMWPE [74, 160, 68]. Early models, that ran parametric studies, predicted an increasing film thickness with reducing modulus [74].

Wang et al. modeled a generic polyurethane elastomer with a linear elastic modulus of 20 MPa and Poisson's ratio of 0.4999 versus UHMWPE using a 1D-steady state model. They found that the polyurethane designs with radii of 16 mm and 23 mm had fluid film thicknesses of 0.166 μm and 0.364 μm respectively compared to a fluid film thickness of 0.110 μm for the UHMWPE design with a radius of 14 mm [68]. This corresponded to a reduction

in the fluid pressure distribution.

In summary, 1D-steady-state EHL models have predicted that softer PCU acetabular cups will promote full-fluid lubrication and reduce wear in total hip replacements. However, experimental wear studies have shown less promising results. The aim of this study is to apply a 3D-transient model of the physiological gait cycle to explore the impact of 3D motion, reversals, and time dependance on the lubrication predictions of PCU hip implants.

4.5 Methods

4.5.1 Geometry and Materials

A PCU total hip replacement and a UHMWPE total hip replacement were modeled by Dr. Gao using her 3D-transient EHL model [147]. A cobalt chromium femoral head, typical for hip implant designs, was assumed to be articulating on the polymer. Due to the mismatch in stiffnesses, the femoral head was assumed to be rigid. Similarly, the titanium metal lining between the polymeric acetabular cup and the bone of the pelvis was assumed to be rigid. This assumption was validated by comparing displacements in the acetabular cup with a rigid surface or a titanium back.

The clinically available sizes of PCU acetabular cup range from 34 mm - 50 mm diameters. The diameter of commercial PCU implants are larger, to accommodate larger femoral heads, than a typical UHMPWE implant (28 mm), to provide a higher thickness, which is designed to accommodate the known wear that will occur. The outer diameter is fixed by the anatomical constraints of the pelvis. We modeled a 34 mm diameter PCU implant and an equivalently sized UHMWPE liner in order to compare the film thicknesses directly. The radial clearance that was modeled was 0.5 mm. The cup thickness was 3 mm for the 34 mm diameter devices. The geometries and material properties that were modeled are summarized in Table 4.1.

4.5.2 Loading

A steady state solution was used as the initial guess for the solution of the transient model. The steady state condition was with w_y = -300 N and an angular velocity ω_x = -2 rad/s. Figure 4.12 shows the loading and rotations with respect to the cup geometry. The transient solution was based on loading parameters that are used in hip simulator studies to mimic the 3D loads of a single walking gait cycle. This 3D loading curve was based on ISO 14242 (Figure 4.13). The total cycle was solved discretely in 100 time steps.

Table 4.1: Summary of the geometry, fluid properties, and material properties modeled in this study.

	Material	
Property	**UHMWPE**	**PCU**
Radius (mm)	17	
Cup thickness (mm)	3	
Clearance (mm)	0.5	
Viscosity (Pa·s)	0.01	
Elastic Modulus (MPa)	1000	24
Poisson's Ratio	0.4	0.4924

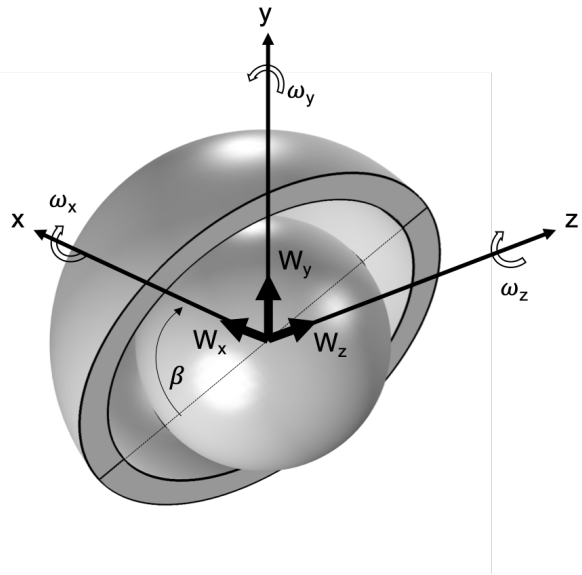

Figure 4.12: The ISO14242 load was applied to the acetabular cup via the femoral head in the coordinate system shown here. The rotations correspond to the anatomical motions of flexion-extension (ω_x), internal-external rotation (ω_y), and adduction-abduction (ω_z). The angle β represents the 45° anatomical angle of implantation with respect to the face of the cup.

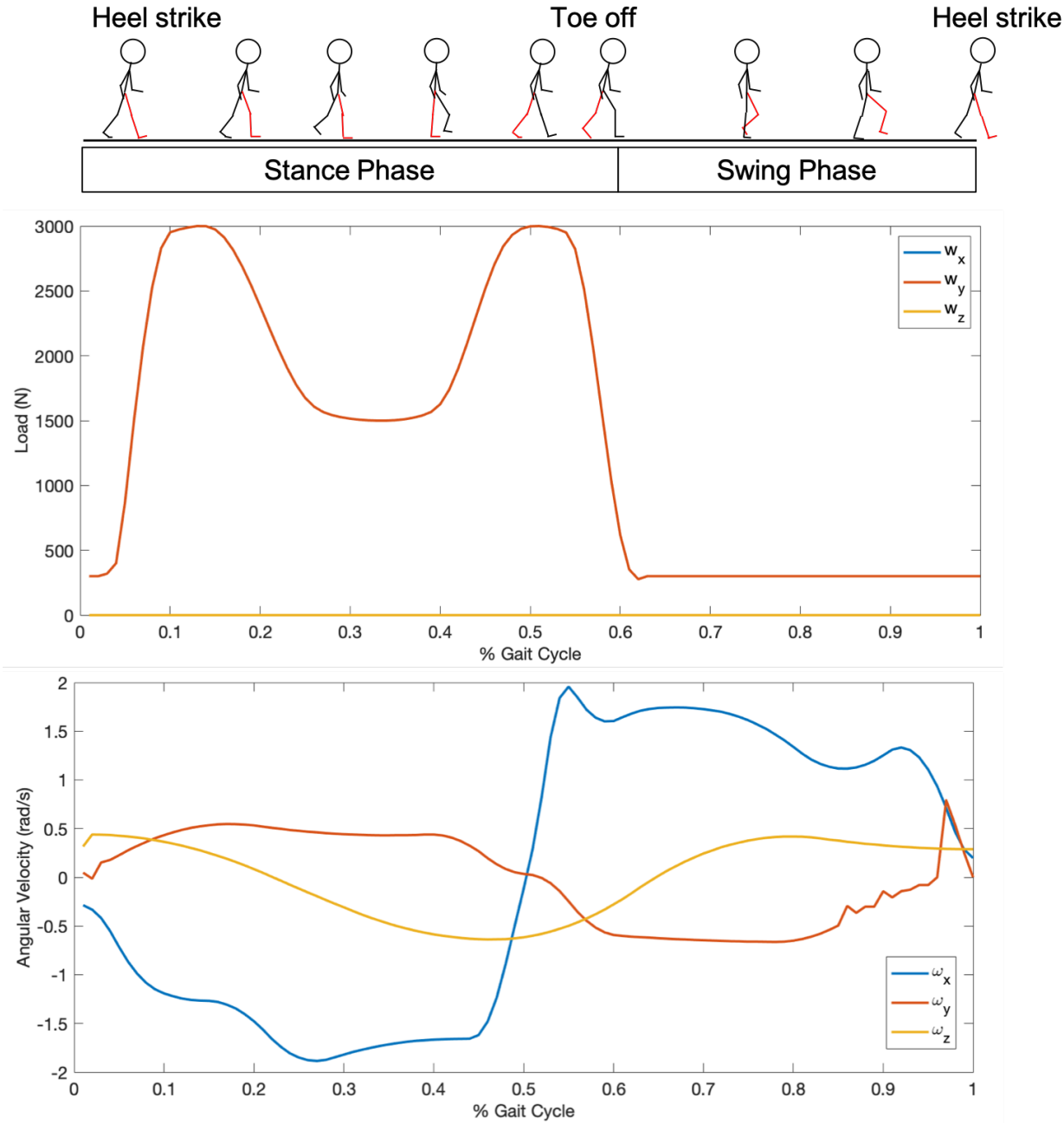

Figure 4.13: The standard loading curve for joint simulator studies per ISO14242 was used as the 3D load input into the model. One gait cycle was modeled at a rate of 1 Hz. At the top a schematic of the corresponding motion (red leg) is shown. The gait cycle is typically divided into the stance phase where the majority of loading occurs when the leg is on the ground and swing phase when the leg is swinging forward for the next step.

4.5.3 EHL Solution

This work employed a EHL model of a hip implant. For further details of the method reference previously published work [147, 142, 143]. This model simultaneously solves the Reynolds equation for the pressure distribution under the applied load and assumed fluid thickness. The pressure distribution is then used to update the elastic deformation which increases the fluid thickness and the two equations are iteratively solved until a converged solution in reached for each time point in the gait cycle. The transient 3D Reynolds equation in spherical coordinates (ϕ and θ) is given in Equation 4.15.

$$\begin{aligned}\frac{\partial}{\partial\phi}\left(h^3\frac{\partial p}{\partial\phi}\right)+sin\theta\frac{\partial}{\partial\theta}\left(h^3sin\theta\frac{\partial p}{\partial\theta}\right)=6\eta R_c^2sin\theta\Bigg[&-\omega_x\left(sin\phi sin\theta\frac{\partial h}{\partial\theta}+cos\phi cos\theta\frac{\partial h}{\partial\phi}\right)\\&+\omega_y\left(cos\phi sin\theta\frac{\partial h}{\partial\theta}-sin\phi cos\theta\frac{\partial h}{\partial\phi}\right)\\&+\omega_z sin\theta\frac{\partial h}{\partial\phi}\Bigg]\\&+12\eta R_c^2sin^2\theta\frac{\partial h}{\partial t}\cdot dyn\end{aligned} \tag{4.15}$$

where h is the fluid thickness, p is the fluid pressure, η is the fluid viscosity, R_c is the cup inner radius, ω is the rotational velocity in x, y, and z directions in the global coordinate frame of the applied load (Figure 4.12), and dyn is a switch parameter to switch between steady state ($dyn = 0$) and transient conditions ($dyn = 1$). A zero pressure boundary condition is used to ensure that all pressures in the solution are non-negative. The spherical mesh in ϕ and θ is shown in Figure 4.14.

The total fluid thickness (Equation 4.16) is a function of the radial clearance (c) and geometric gap between the femoral head relative to the cup in the x, y, and z directions (e_x, e_y, and e_z) and elastic deformation of the surfaces ($\delta(\phi,\theta)$).

$$h(\phi,\theta)=c-e_xsin\theta cos\phi-e_ysin\theta sin\phi-e_zcos\theta+\delta(\phi,\theta) \tag{4.16}$$

The elastic deformation of the surfaces (δ, Equation 4.17) is calculated as a function of the influence coefficient (K) as a function of pressure, spherical coordinate location, and mean fixed latitude (θ_m).

$$\delta(\phi,\theta)=\int_\phi\int_\theta K(\phi-\phi',\theta-\theta',\theta_m)\cdot p(\phi',\theta')d\theta d\phi \tag{4.17}$$

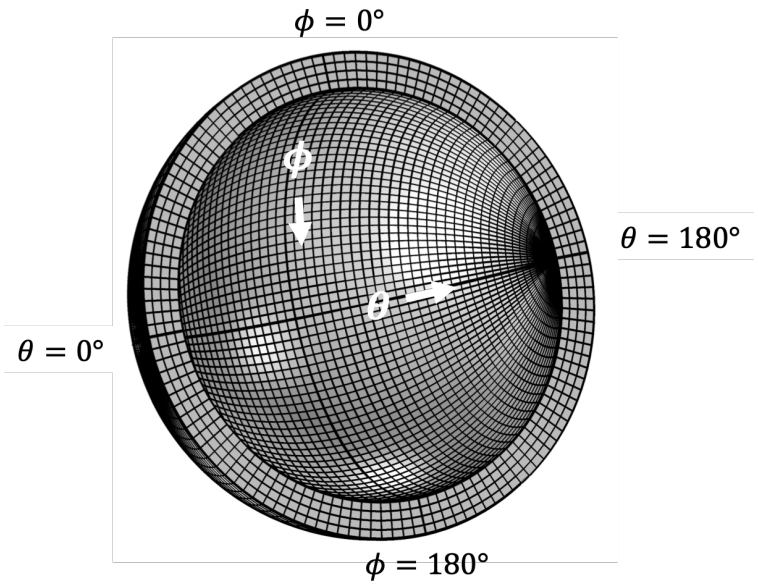

Figure 4.14: The mesh used for the finite difference discretization was a n x n spherical mesh in the ϕ and θ directions.

The influence coefficient matrix (K) for estimating the elastic deformation of the cup based on a given pressure was based on previously published method [68]. To create the influence coefficient matrix, a COMSOL model of the acetabular cup was created with a mesh equivalent to spherical mesh that would be used in the multi-grid solution. A unit pressure with area $\Delta\phi$ x $\Delta\theta$ was applied at the center node (Figure 4.15). The resulting displacement field on the surface was exported. From the displacement field with an n x n mesh, a n^2 x n^2 matrix was created mapping the deformation as a function of distance from the node where the pressure was applied was created. The equivalent spherical discrete convolution (ESDC) technique and fast Fourier transform (FFT) technique is used to calculate the elastic deformation from this matrix as previously described by [68, 147].

In order to maintain equilibrium, the pressure solution ($p_{x,y,z}$) must be equivalent to the applied load from the walking motion ($w_{x,y,z}$), in this case the ISO standard loading curve:

$$f_{x,y,z} = R_c^2 \int_{\phi} \int_{\theta} p_{x,y,z} d\theta d\phi = -w_{x,y,z} \tag{4.18}$$

The pressure transformation from the surface spherical cup mesh (θ, ϕ) to the global cartesian coordinate system (x, y, z) of the applied loading is defined as:

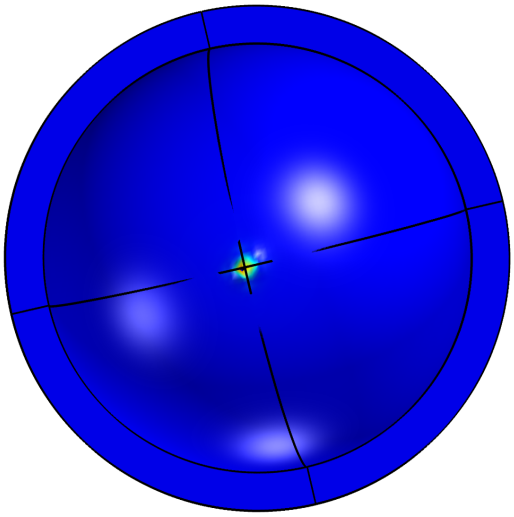

Figure 4.15: A unit pressure was applied to an area of $\Delta\phi$ x $\Delta\theta$ to calculate the displacement field resulting at that node.

$$\begin{aligned} p_x &= psin^2\theta cos\phi \\ p_y &= psin^2\theta sin\phi \\ p_z &= psin\theta cos\theta \end{aligned} \tag{4.19}$$

The above governing equations are non-dimensionalized using the modulus (E), radial clearance between femoral head and acetabular cup (c), radius of the cup (R_c), viscosity of the fluid (η), and a unit rotational velocity (ω_o):

$$
\begin{aligned}
P &= \frac{p}{E} \\
H &= \frac{h}{c} \\
\Delta &= \frac{\delta}{c} \\
W_{x,y,z} &= \frac{w_{x,y,z}}{ER_c^2} \\
F_{x,y,z} &= \frac{f_{x,y,z}}{ER_c^2} \\
\epsilon &= \frac{c^2 E \cdot H^3}{6\eta R_c^2 \omega_o} \\
\Omega_{x,y,z} &= \frac{\omega_{x,y,z}}{\omega_o} \\
T &= t \cdot \omega_o \\
\bar{e}_{x,y,z} &= \frac{e_{x,y,z}}{c}
\end{aligned}
\tag{4.20}
$$

Additionally, non-dimensionalization was done such that all variables are on the order of 1 in effort to reduce error and improve numerical stability. The non-dimensional parameters in Equation 4.20 were used to non-dimensionalize the Reynolds equation (Equation 4.21), the film thickness equation (Equation 4.22), the elastic deformation equation (Equation 4.23), and the force balance equation (Equation 4.29 and 4.31).

$$
\begin{aligned}
\frac{\partial}{\partial\phi}\left(\epsilon\frac{\partial P}{\partial\phi}\right) + sin\theta\frac{\partial}{\partial\theta}\left(\epsilon sin\theta\frac{\partial P}{\partial\theta}\right) = &-\Omega_x\left(sin\phi sin^2\theta\frac{\partial H}{\partial\theta} + sin\theta cos\phi cos\theta\frac{\partial H}{\partial\phi}\right) \\
&+\Omega_y\left(cos\phi sin^2\theta\frac{\partial H}{\partial\theta} - sin\theta sin\phi cos\theta\frac{\partial H}{\partial\phi}\right) \\
&+\Omega_z sin^2\theta\frac{\partial H}{\partial\phi} \\
&+2sin^2\theta\frac{\partial H}{\partial T}\cdot dyn
\end{aligned}
\tag{4.21}
$$

$$
H(\phi,\theta) = 1 - \bar{e}_x sin\theta cos\phi - \bar{e}_y sin\theta sin\phi - \bar{e}_z cos\theta + \bar{\delta}(\phi,\theta) \tag{4.22}
$$

$$
\bar{\delta}(\phi,\theta) = \frac{E}{c}\int_\phi\int_\theta K(\phi-\phi',\theta-\theta',\theta_m)\cdot P(\phi',\theta')d\theta d\phi \tag{4.23}
$$

$$F_{x,y,z} = \int_{\phi} \int_{\theta} P_{x,y,z} d\theta d\phi = -W_{x,y,z} \tag{4.24}$$

$$\begin{aligned} P_x &= P sin^2\theta cos\phi \\ P_y &= P sin^2\theta sin\phi \\ P_z &= P sin\theta cos\theta \end{aligned} \tag{4.25}$$

The EHL problem was solved numerically using the finite difference method. The cup surface was discretized into a spherical mesh of equal sizing in the ϕ and θ directions as shown in Figure 4.14. In the case of the Reynolds equation, multiple finite difference schemes were applied to different parts of the equation in order to support stability and convergence of the solution (Equation 4.26). In order to solve the transient cases, the film thickness from the previous time step ($\bar{H}_{i,j}$) was used.

$$\begin{aligned} &\frac{1}{\Delta_\phi^2}\Big[\epsilon_{i-0.5,j}P_{i-1,j} - (\epsilon_{i-0.5,j} + \epsilon_{i+0.5,j})P_{i,j} + \epsilon_{i+0.5,j}P_{i+1,j}] \\ &\quad + \frac{sin\theta_j}{\Delta_\theta^2}[\epsilon_{i,j-0.5}sin\theta_{j-0.5}P_{i,j-1} - (\epsilon_{i,j-0.5}sin\theta_{j-0.5} \\ &\quad + \epsilon_{i,j+0.5}sin\theta_{j+0.5})P_{i,j} + \epsilon_{i,j+0.5}sin\theta_{j+0.5}P_{i,j+1}\Big] \\ &= -\Omega_x\left[sin^2\theta_j sin\phi_i\frac{H_{i,j} - H_{i,j-1}}{\Delta_\theta} + sin\theta_j cos\theta_j cos\phi_i\frac{H_{i,j} - H_{i-1,j}}{\Delta_\phi}\right] \\ &\quad + \Omega_y\left[cos\phi_i sin^2\theta_j\frac{H_{i,j} - H_{i,j-1}}{\Delta_\theta} - sin\theta_j sin\phi_i cos\theta_j\frac{H_{i,j} - H_{i-1,j}}{\Delta_\phi}\right] \\ &\quad + \Omega_z sin^2\theta_j\frac{H_{i,j} - H_{i-1,j}}{\Delta_\theta}\Big] + 2sin^2\theta_j\frac{H_{i,j} - \bar{H}_{i,j}}{\Delta_T} \cdot dyn \end{aligned} \tag{4.26}$$

The half step discretization for the second-order discretization is defined as:

$$\begin{aligned}
\epsilon_{i-0.5,j} &= \frac{\epsilon_{i-1,j} + \epsilon i,j}{2} \\
\epsilon_{i+0.5,j} &= \frac{\epsilon_{i+1,j} + \epsilon i,j}{2} \\
\epsilon_{i,j-0.5} &= \frac{\epsilon_{i,j-1} + \epsilon i,j}{2} \\
\epsilon_{i,j+0.5} &= \frac{\epsilon_{i,j+1} + \epsilon i,j}{2} \\
sin\theta_{j-0.5} &= \frac{\theta_{j-1} + \theta j}{2} \\
sin\theta_{j+0.5} &= \frac{\theta_{j+1} + \theta j}{2}
\end{aligned} \tag{4.27}$$

$$\bar{\delta}_{i,j} = \frac{E}{c} \sum_{k=1}^{N_\phi} \sum_{l=1}^{N_\theta} K_{i-j,k-l} P_{k,l} \Delta_\theta \Delta_\phi \tag{4.28}$$

The force balance was discretely approximated using a simplified 9-point weighted summation (Equation 4.29).

$$\begin{aligned}
F_{x,y,z} = \frac{\Delta_\phi \Delta_\theta}{9} \sum_{i=1}^{N_\phi} \sum_{j=1}^{N_\theta} [16 P_{i,j}^{x,y,z} + 4(P_{i-1,j}^{x,y,z} + P_{i+1,j}^{x,y,z} + P_{i,j-1}^{x,y,z} + \\
P_{i,j+1}^{x,y,z} + P_{i-1,j-1}^{x,y,z} + P_{i+1,j-1}^{x,y,z} + P_{i-1,j+1}^{x,y,z} + P_{i+1,j+1}^{x,y,z}] = -W_{x,y,z}
\end{aligned} \tag{4.29}$$

$$\begin{aligned}
P_{i,j}^x &= P_{i,j} sin^2\theta_j cos\phi_i \\
P_{i,j}^y &= P_{i,j} sin^2\theta_j sin\phi_i \\
P_{i,j}^z &= P_{i,j} sin\theta_j cos\theta_j
\end{aligned} \tag{4.30}$$

Gauss-Seidel relaxation is used to solve the Reynolds equation. The non-dimensional eccentricities ($\bar{e}$) were adjusted based on the error between the calculated (F) and applied load (W) multiplied by a factor (μ) to accelerate convergence.

$$\bar{e}_{x,y,z} = \bar{e}_{x,y,z} - \mu_{x,y,z}(F_{x,y,z} + W_{x,y,z}) \tag{4.31}$$

Multigrid methods were used to solve the problem. Two grid levels, 65 x 65 and 129 x 129, were used. The convergence criteria that were used are outlined in Equation 4.32 and 4.33.

$$errw_{x,y,z} =\mid \frac{f_{x,y,z} + w_{x,y,z}}{w_{x,y,z}} \mid < 0.05 \tag{4.32}$$

$$errp = \frac{\sum_{i=1}^{257}\sum_{j=1}^{257} p_{i,j}^{new} - p_{i,j}^{old}}{\sum_{i=1}^{257}\sum_{j=1}^{257} p_{i,j}^{new}} < 0.05 \tag{4.33}$$

4.6 Results

We solved the transient 3D EHL problem for a acetabular cup made of either PCU or UHMWPE. All geometry and fluid variables were held constant except the material properties (elastic modulus and Poisson's ratio) for the different materials. The results will be presented at key points within the gait cycles highlighted in Figure 4.16, heel-strike, mid-stance, toe-off, and swing.

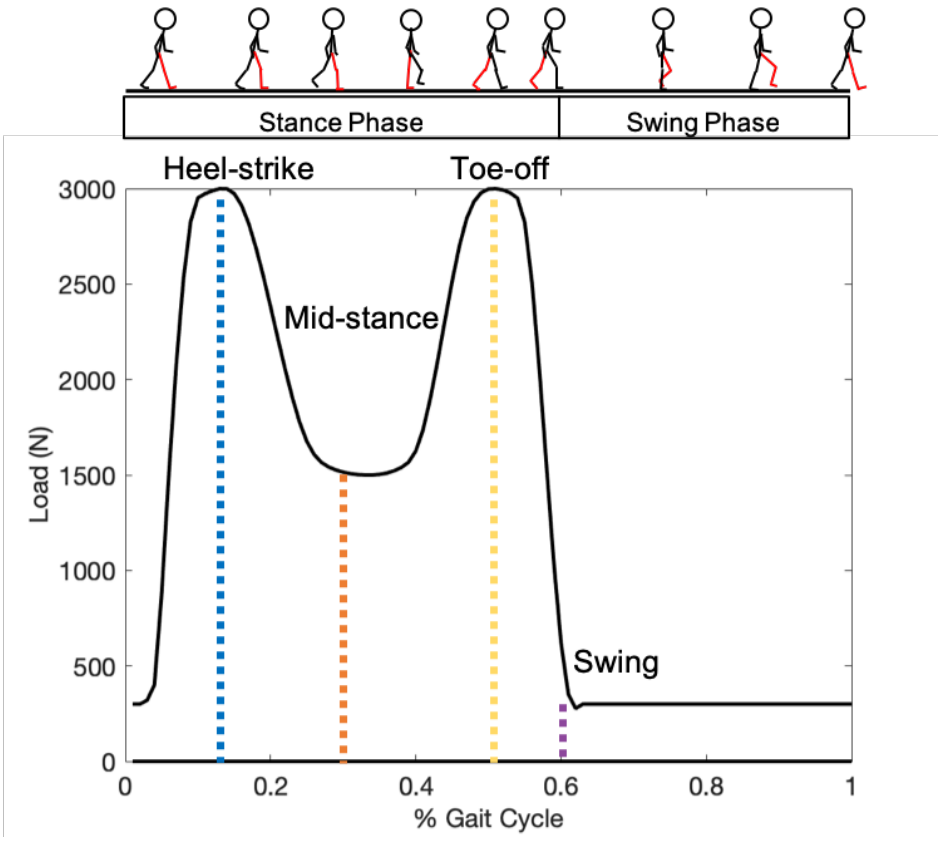

Figure 4.16: The film thickness and pressure distributions will be presented at the time points of the gait cycle (heel strike, mid-stance, toe off, and swing) marked in this figure. Colors of the lines will match the color of the results curve.

4.6.1 UHMWPE

The minimum film thickness along a central cross section for UHMWPE ranged from 2.53 μm to 3.78 μm throughout the gait cycle (Figure 4.17, left). The maximum pressure in the fluid reached a peak at 12.7 MPa and followed the loading pattern of the applied loads from the gait cycle (Figure 4.17, right). The film thickness increased at the peak loads. This might be due to the fact that the minimum film thickness occurred at a ring around the central area of maximum pressure such that at higher loads, as the contact area increased, there was sufficient central film thickness to support the increasing load.

The distribution of the film thickness and pressure at a central cross section in the entraining direction (direction parallel to dominant rotation) is shown in Figure 4.18. The region of minimum film thickness does not correspond to the region of maximum pressure, but the distributions are symmetric around the center of pressure even under varying rotation in 3D. The mismatch between pressure distribution and film thickness distribution may seem counterintuitive, but is due to the complex interactions between the rotations in 3D

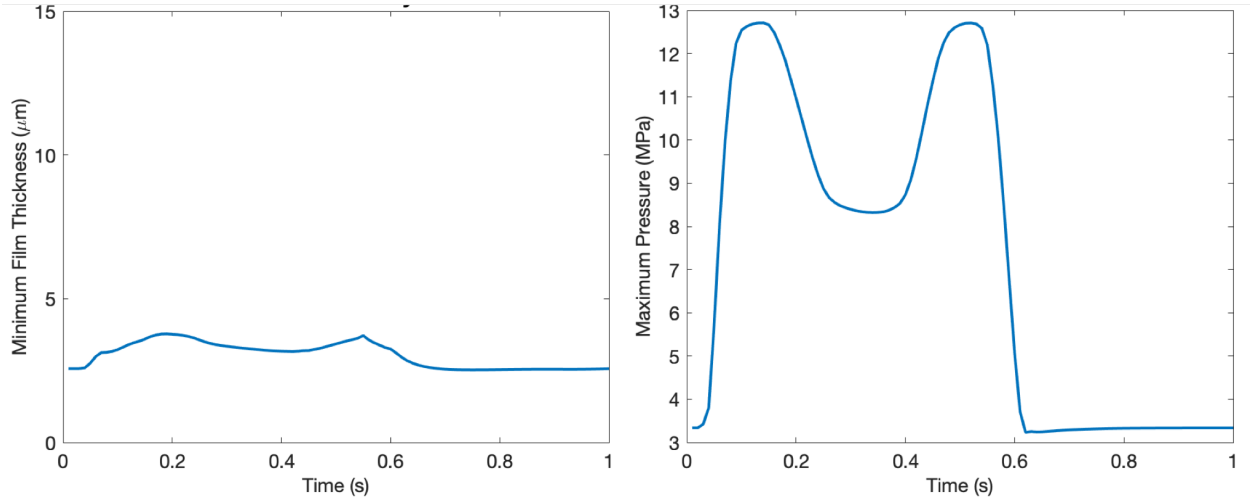

Figure 4.17: The minimum film thickness in the UHMWPE cup throughout the gait cycle (left) and corresponding maximum pressure (right).

changing the direction from which new lubricant is pulled into the pressurized area relative to what is squeezed out.

The film thickness and area under loading both vary with respect to applied loading of the gait cycle. The distribution of the film thickness and pressure at a cross section normal to the direction of dominant rotation (squeeze direction) are shown in Figure 4.19. There is little difference between the two directions, because the distributions are symmetric around the center of loading. The near symmetry is clearly seen in the distributions of film thickness and pressure shown in Figures 4.20 & 4.21.

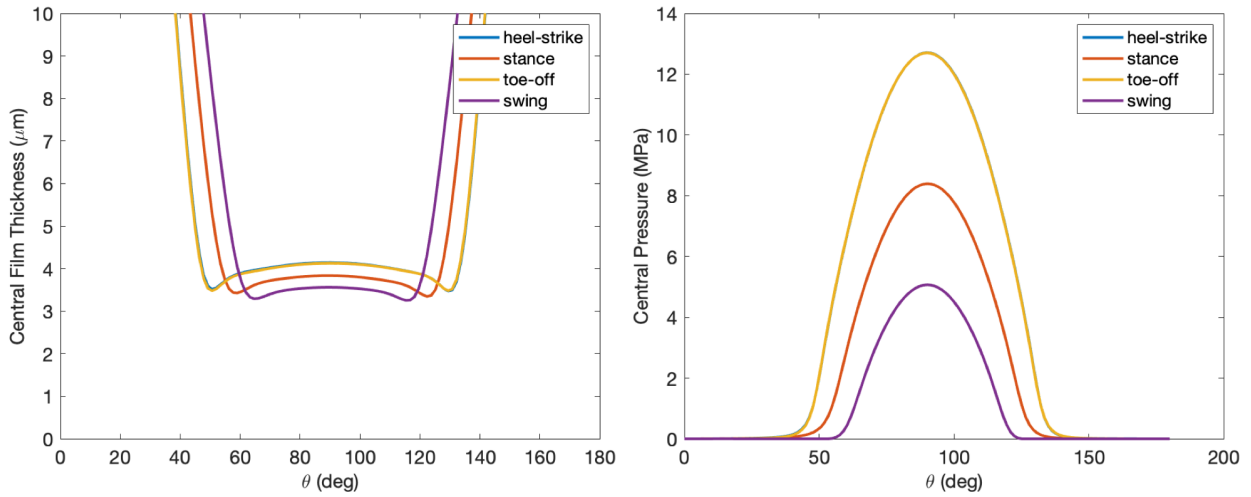

Figure 4.18: The film thickness and pressure distribution at the mid-line in the entraining direction of the UHMWPE cup at the major inflection time points in the gait cycle. Note: heel-strike and toe-off curves overlap.

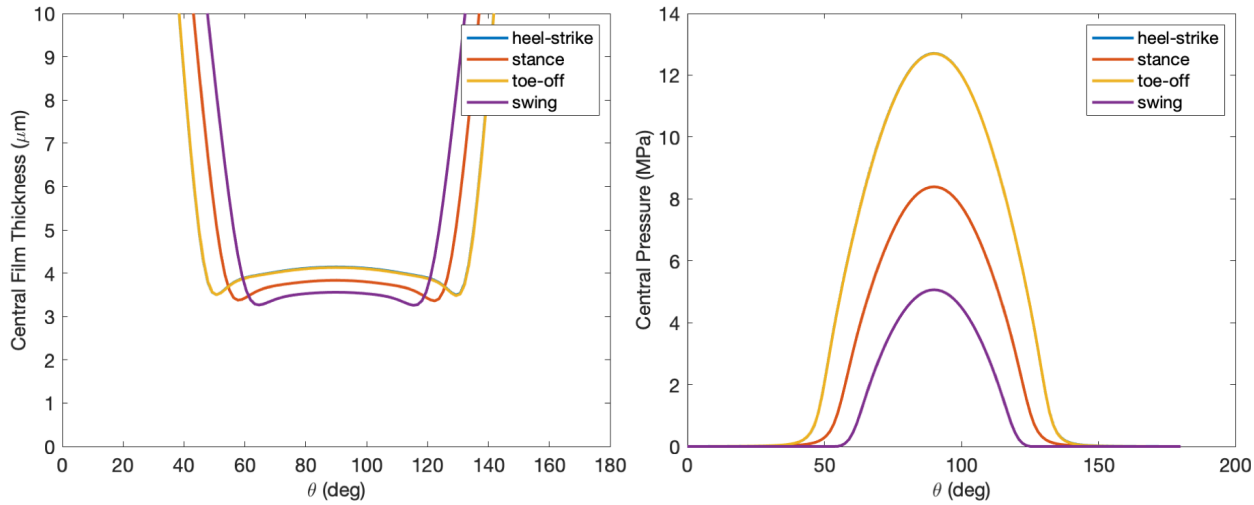

Figure 4.19: The film thickness and pressure distribution at the mid-line in the squeeze direction (normal to the entraining direction) of the UHMWPE cup at the major inflection time points in the gait cycle. Note: heel-strike and toe-off curves overlap.

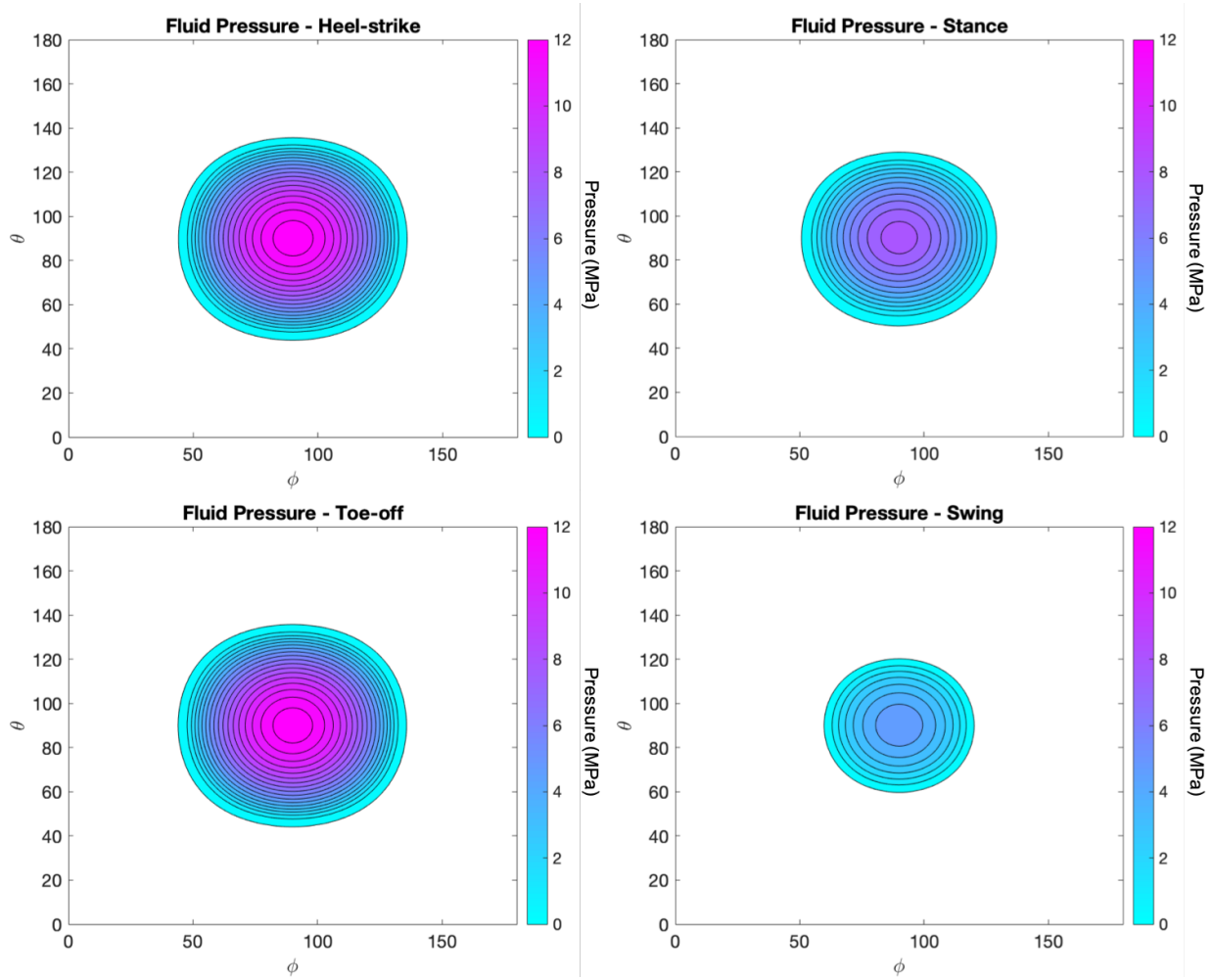

Figure 4.20: Contour plot of the fluid pressure distribution in the UHMWPE acetabular cup at heel-strike (top left), mid-stance (top right), toe-off (bottom left), and swing (bottom right). The pressure is plotted in a 2D projection of θ and ϕ as spherical locations in degrees from 0 to 180 along the arc of the cup.

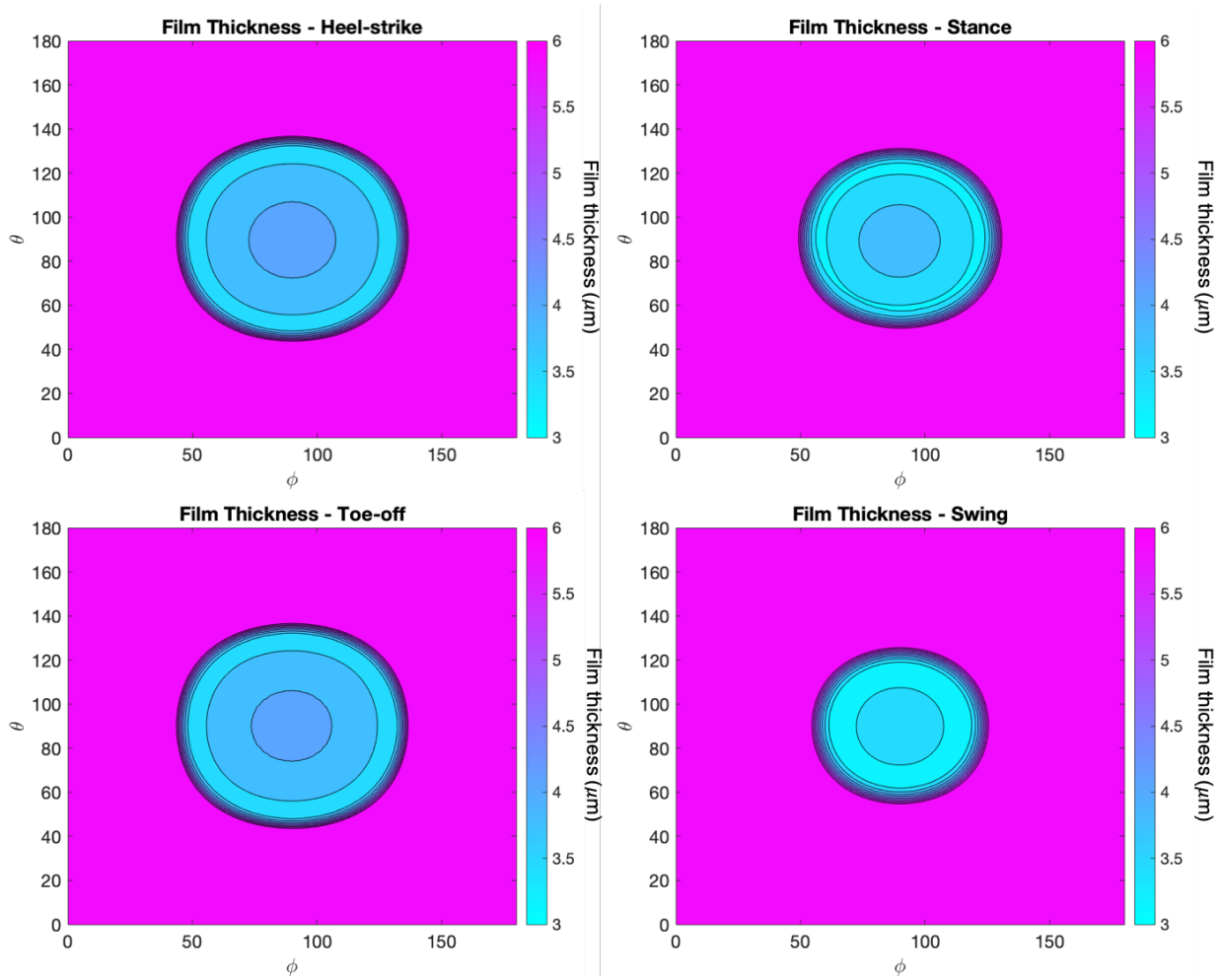

Figure 4.21: Contour plot of the film thickness distribution in the UHMWPE acetabular cup at heel-strike (top left), mid-stance (top right), toe-off (bottom left), and swing (bottom right). The film thickness is plotted in a 2D projection of θ and ϕ as spherical locations in degrees from 0 to 180 along the arc of the cup.

4.6.2 PCU

The maximum fluid pressure predicted in PCU was lower than that predicted for UHMWPE. The maximum fluid pressure at a central cross section was 6.0 MPa and changes in the maximum pressure followed the pattern of changing applied load (Figure 4.22, right). A lower fluid pressure is what is expected with a more compliant material and would create lower contact stresses in the material.

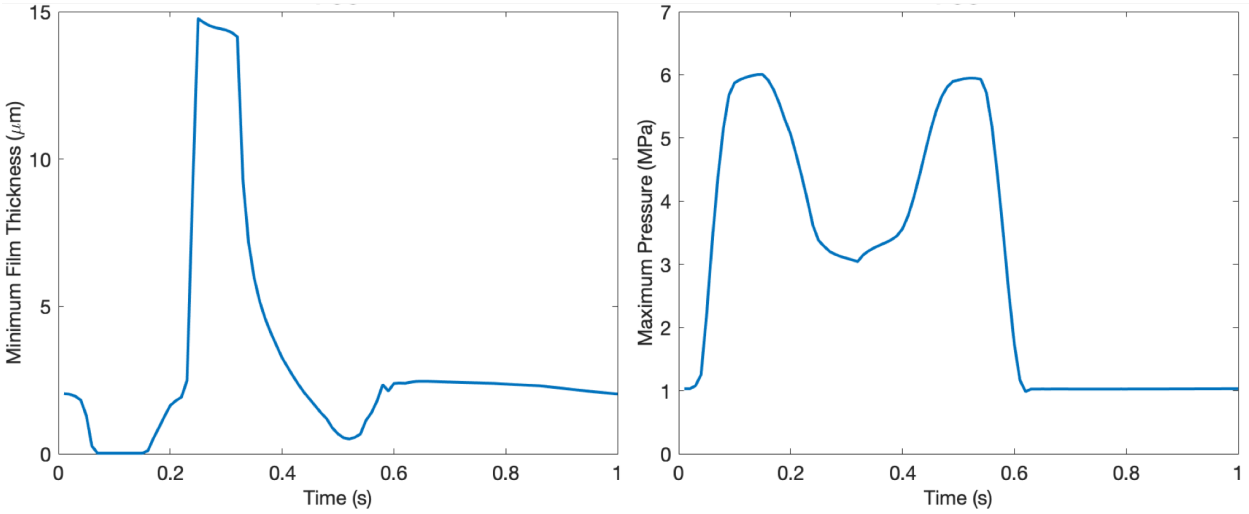

Figure 4.22: The minimum film thickness in the PCU cup throughout the gait cycle (left) and corresponding maximum pressure (right).

The changes in film thickness in PCU relative to those predicted for UHMWPE were large. The range in minimum film thickness at a central cross section for PCU ranged from 0.02 μm (set as a zero limit in the code, representing full contact) to 14.8μm (Figure 4.22, left). These large changes in film thickness throughout the gait cycle are a result of the more compliant behavior of the material and much larger displacement magnitudes. The film thickness was observed to go to zero during heel strike, then rebounds dramatically during stance as the load drops, and drops at a similar rate when reloaded at toe-off, but does not return to zero (0.5 μm). Finally, during the swing phase, although the load drops, a dramatic spike in film thickness is not repeated. This could be due to the reversal in the direction of ω_x. However, it should be noted that throughout the swing phase, rather than maintaining the minimum film thickness, the film thickness slowly decreases over time, suggesting that lubricant is squeezing out faster than it is being pulled in through entraining motion at the low load.

Compared to UHMWPE, the total loaded area of the PCU cup is much greater. At toe-off, where the applied load is maximum, the percent of nodes in PCU where the fluid

thickness is less than 5 μm is 68% compared to 20% in UHMWPE (Figure 4.23). Statistically, this means that, for a an equivalent film thickness, there is more potential for wear with a larger contact area because there is more likelihood that large asperities will be present in a larger area to come into contact.

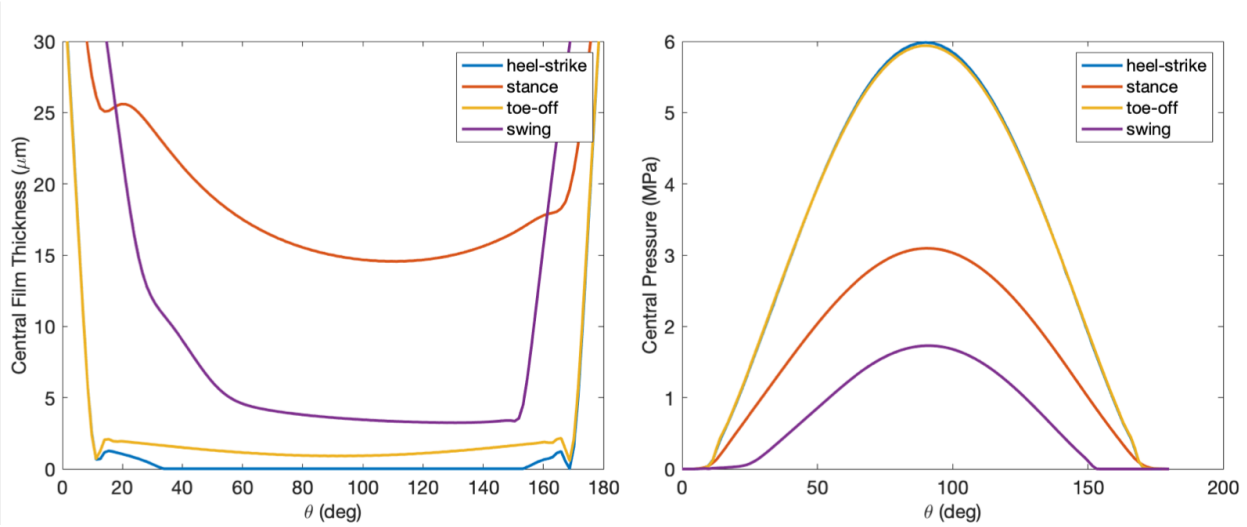

Figure 4.23: The film thickness and pressure distribution at the mid-line in the entraining direction of the PCU cup at the major inflection time points in the gait cycle. Note: heel-strike and toe-off curves overlap in the pressure distributions.

The pressure distributions at each timepoint in the gait cycle is symmetric around the center (Figure 4.23 & 4.24, right, and Figure 4.25). One exception is seen in the swing phase of the gait cycle (Figure 4.26). In contrast, the film thickness distributions are not symmetric in the entraining direction and are lower at the inlet than the outlet (Figure 4.23, left). This behavior is typical of EHL distributions with a minimum film thickness near the inlet. In the direction normal to the entraining direction, the squeeze direction, the distribution is less directed, but asymmetry can still be observed (Figure 4.24). The minimum film thickness distributions show that the minimum film thickness at each time point in the gait cycle does not occur in the same region or occur in the location of highest pressure. For example, in the swing phase, the minimum film thickness occurs not only at the edge of the cup, but it is off the central axis (Figure 4.26). The presence of a minimum outside of the major loading directions demonstrates the limitation of using an assumption of 1D loading.

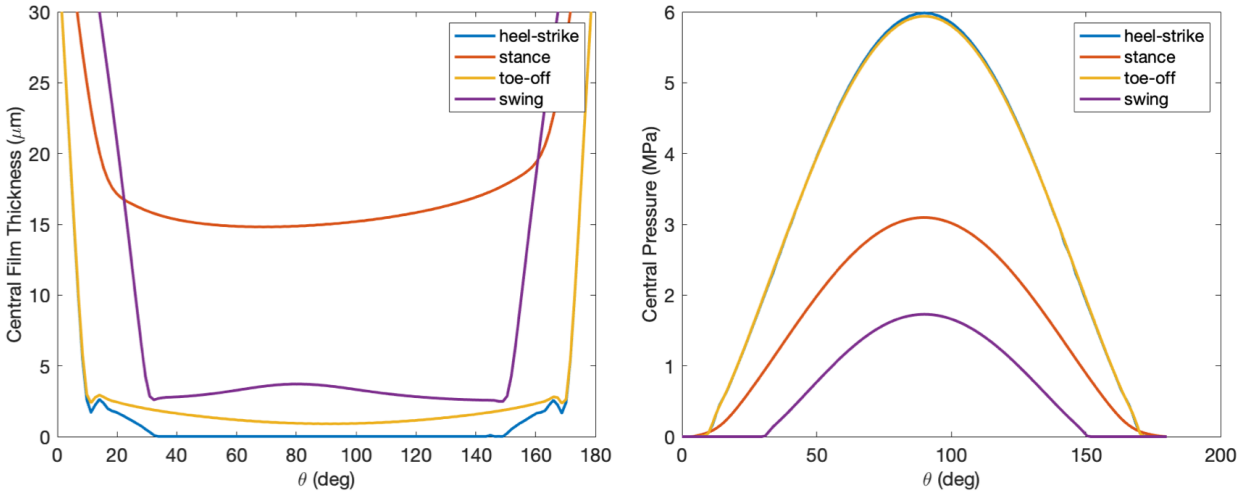

Figure 4.24: The film thickness and pressure distribution at the mid-line in the squeeze direction (normal to the entraining direction) of the PCU cup at the major inflection time points in the gait cycle. Note: heel-strike and toe-off curves overlap in the pressure distributions.

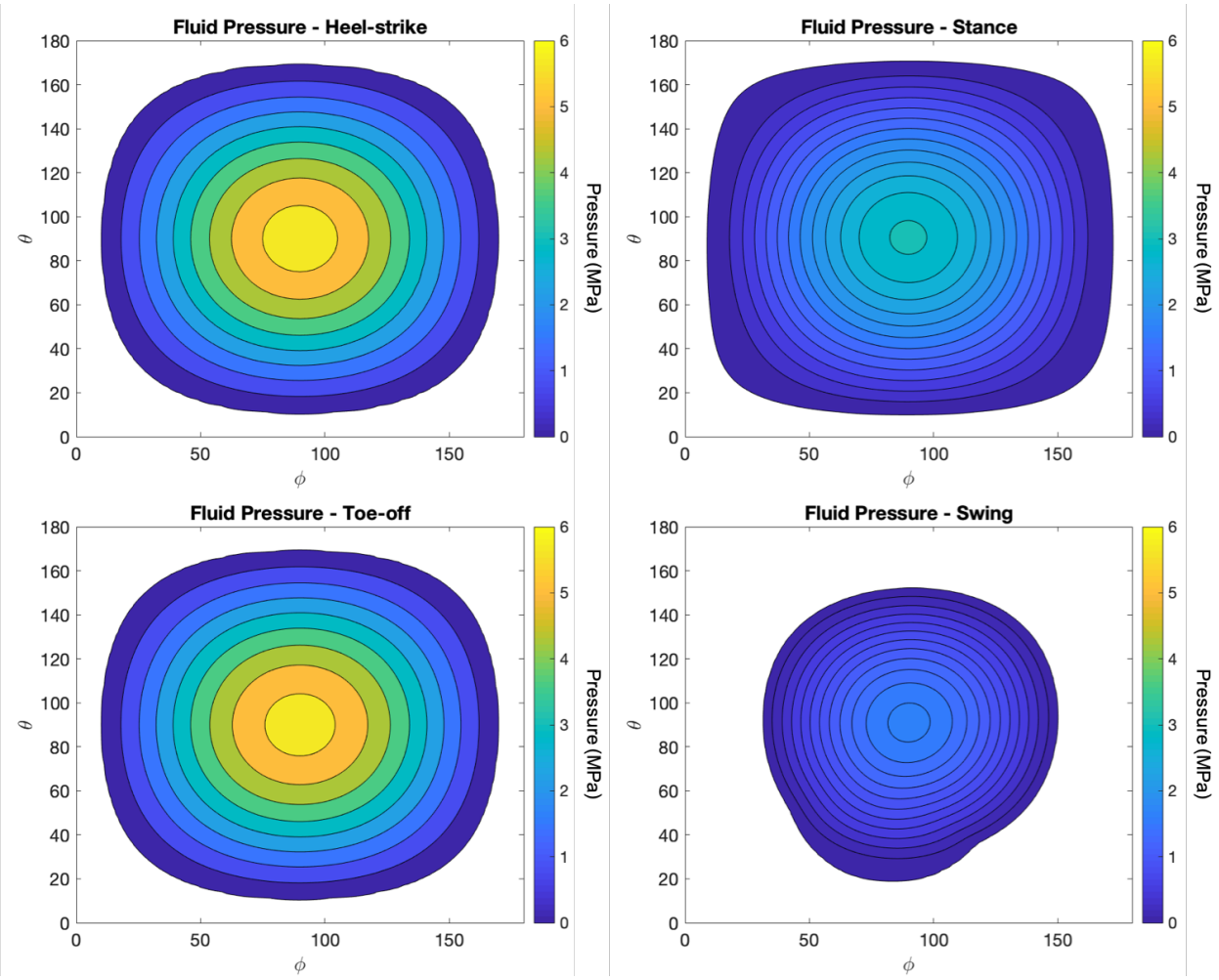

Figure 4.25: Contour plot of the fluid pressure distribution in the PCU acetabular cup at heel-strike (top left), mid-stance (top right), toe-off (bottom left), and swing (bottom right). The pressure is plotted in a 2D projection of θ and ϕ as spherical locations in degrees from 0 to 180 along the arc of the cup.

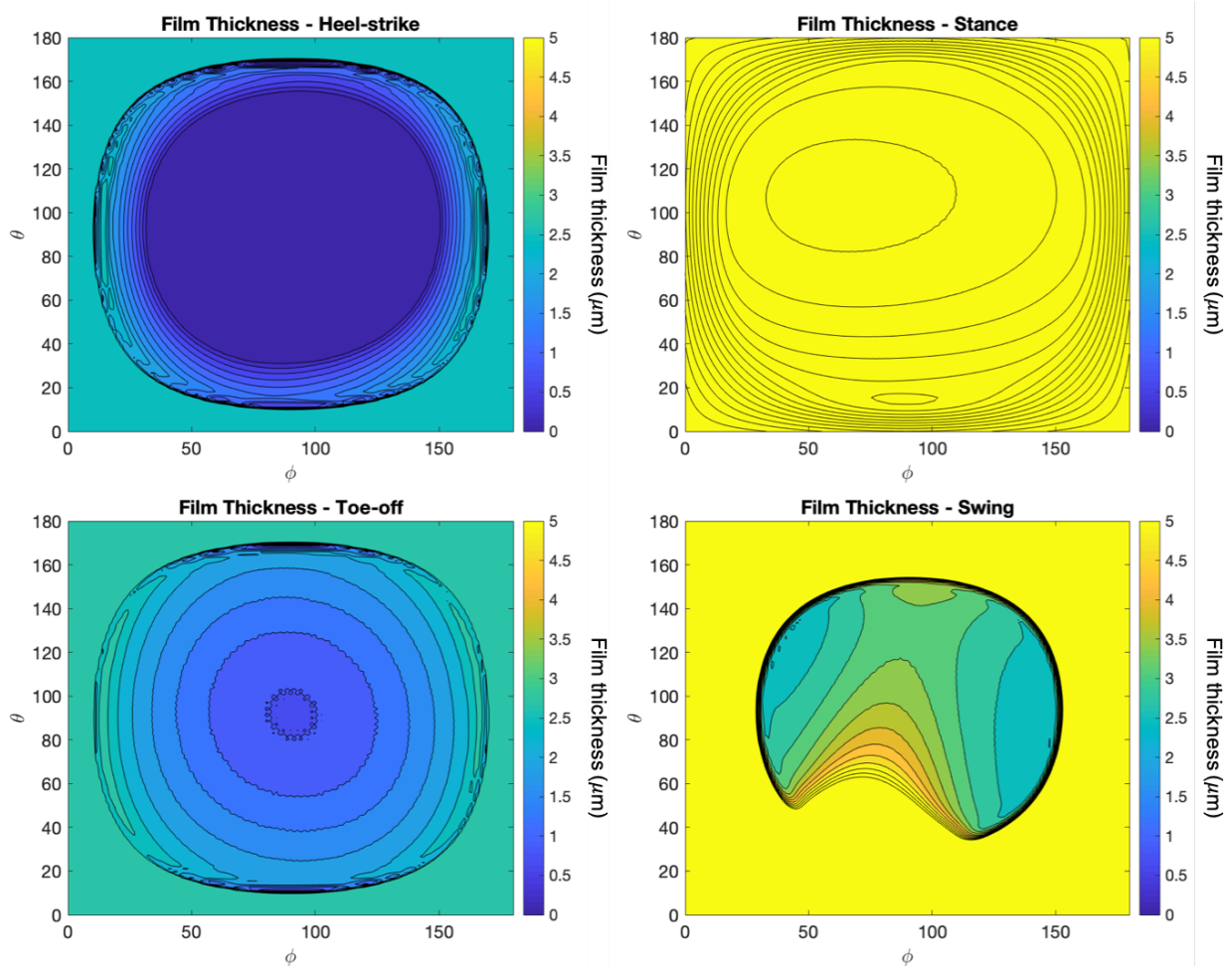

Figure 4.26: Contour plot of the film thickness distribution in the PCU acetabular cup at heel-strike (top left), mid-stance (top right), toe-off (bottom left), and swing (bottom right). The film thickness is plotted in a 2D projection of θ and ϕ as spherical locations in degrees from 0 to 180 along the arc of the cup.

4.7 Discussion

PCU has been marketed as a 'cartilage-like' material that was predicted to maintain full-fluid lubrication regimes to alleviate the wear challenges that limit the life-span of current total joint replacements. This was based on studies of 1D-steady state EHL modeling that predicted fluid film thicknesses of 0.1 - 0.4 μm [68]. The study presented in this chapter contradicts the findings from the 1D-steady state model and predicts a lower minimum film thickness in PCU compared to UHMWPE.

The film thicknesses predicted in UHMWPE in this study (2.5 - 3.8 μm) are higher than those found in a similar study by Lu et al (approximately 0.5 μm) [161]. This is likely due to the difference in geometry. The cup radius in our study was 17 mm for direct geometric comparison to the PCU cup compared to clinically-sized 14 mm cup in the Lu et al. study. A larger radius leads to an increased contact area and thicker lubricant films. The loading patterns used were different between the two studies. The Lu et al. study used the Leeds ProSim gait cycle data which differs from the ISO 14242 load pattern in that it only incorporates flexion and extension, but not internal-external rotation and adduction-abduction. Finally, they also only simulated one 'start-up' gait cycle and did not look at steady state gait.

The film thickness results of this study do not directly correlate to wear, but the lubrication regime indirectly relates to friction and surface interactions that can be correlated to wear performance. The lubrication regime is dictated by both the lubricant film thickness and the surface roughness. Previous studies have determined that UHMWPE operates in a mixed mode lubrication regime. Film thicknesses have been predicted to be between 0.2 - 0.5 μm compared to the surface roughness that is on the order of 0.1 - 2.5 μm [129]. Therefore, the higher asperities are likely to be in contact with the opposing material while lower areas are supported by the lubricant and remain separated.

The average surface roughness of PCU has been reported to be between 0.06 and 0.8 μm using atomic force microscopy and profilometry respectively, and measured each to be significantly reduced following 20 million cycles of wear in a simulator study [71]. Since previous studies predicted lubricant thicknesses over 0.16 - 0.36 μm it was predicted to operate in full-fluid lubrication [68]. Based on the results of this study PCU is predicted to operate in between boundary lubrication (at heel-strike, $h = 0.02$ μm) and full-fluid lubrication (at stance and swing, $h > 2$ μm) depending on the stage of the gait cycle. This suggests that the wear potential of a PCU bearing surface is greater than that of UHMWPE early in the gait cycle during peak loads at heel-strike and toe-off. Not only is the lubricant regime more likely to cause wear, but the total contact area is also greater in PCU during those critical time points than at any time-point in the gait cycle. Based on the relations of Archard's wear law, that increases the wear rate.

The time points that this model predicts high film thicknesses (mid-stance) PCU couples would be operating in full-fluid lubrication regimes and little wear would be predicted. However, these regions of high film thickness are likely overestimated because of the instantaneous response of the linear elastic material model. Due to the highly viscoelastic behavior of PCU, it is likely that the elastic recovery would be delayed due to creep in the material during loading. Because of the time delay in the material response, the change in fluid thickness would likely not be as dramatic because the elastic response would not be as great. This is a limitation of the current study. A study by Lu et al. incorporated the influence of viscoelastic material behavior of UHMWPE [161]. Their study showed significant influence of the viscoelastic material response, however the parameterized approach using a single relaxation time model cannot be directly compared to predict the influence of viscoelastic material response on PCU. Another study by Putignano et al. showed that incorporating viscoelasticity into and EHL model reduced the film thickness due to the lag in deformation response [162]. However, we hypothesize that adding the viscoelastic material properties to PCU would reduce the magnitude of the changes in the film thickness.

This study demonstrates the importance of considering the full 3D loading environment and transient nature of the problem in predicting lubrication regimes in total joint replacements. By utilizing a 3D-transient we predict much less optimistic tribological characteristics in compliant bearing couples. The results from this study better align with the experimental results that showed little improvement in PCU wear behavior compared to the clinical standard of crosslinked UHMWPE. Our results further align with the fact that in lubrication, start-stop behavior and reversals in velocities pose the greatest challenge. By introducing 3D motion we more accurately capture these time points when motion is reversed and take into account the impact of the squeeze-effect.

The value of EHL modeling is the ability to probe lubricant film behavior that is difficult or impossible to directly measure. The same fact is also a main limitation of EHL, the challenge of experimental validation. EHL modeling is a very mature field which has led to the development of these highly complex nonlinear models. However, the only method for direct validation is using white light interferometry. This technique requires one of the surfaces in the contact couple to be optically clear and flat so that the film thickness can be measured based on the refraction of light. EHL models have been extensively validated using this method. These validations provide a strong basis for the validity of EHL models of systems with different geometries (i.e. ball-in-socket) and couple materials that are not optically clear (i.e. UHMWPE). Without the possibility for direct experimental validation, whole models can be validated against previously published models, and pieces of the models can be validated separately. For example, the elastic deformation approximation of our EHL model was validated against a commercially available FE model of the same applied pressure. Future work will model the same geometry as presented by Lu et al. to test our results for UHMWPE [161].

This study is a first look at the impact of 3D-transient loading on the lubrication mechanics in a PCU total hip replacement. Future studies will look at the full range of clinically available geometries for both PCU and UHMPWE to look at the influence of geometry on the film thickness in these implants. Next, a study of a range of moduli for PCU will be modeled. One of the benefits of PCU is that the chemistry allows for highly 'tuneable' properties. We have only modeled an implant with the properties of the 80A formulations of PCU. It is possible that a mid-range modulus provides the benefit of greater deformation without such extreme loading areas and swings in film thickness. Additionally, the incorporation of the nonlinear and viscoelastic material properties of PCU into the EHL model would improve the fidelity of the model. A linear elastic assumption for such large displacements in an elastomer is only a first approximation. Future studies will work to solve the problem at a more physiologically relevant viscosity. This study used 0.01 Pa·s while physiological viscosities are typically reported to be 0.001 Pa·s.

4.8 Conclusions

This study uses a 3D-transient EHL model to predict the lubricant film thickness in compliant acetabular cups for hip implants. In contrast to the results of 1D-steady state models, we predict a lower film thickness for a soft material compared to the current clinical standard, UHMWPE. The regions where there was a reversal of flexion-extension motion had the lowest film thickness. These results are in agreement with *in vitro* wear studies that showed higher wear than predicted with full-fluid lubrication. The results of this model explain the discrepancy between the predicted and actual wear performance of PCU acetabular cups. Moving forward, a 3D-transient EHL model of the hip can be used as a tool to test the wear potential of novel material and geometric implant designs. It can also be used to gain a more mechanistic understanding of the challenge of wear in total joint replacement.

Chapter 5

Conclusions

This thesis evaluated the mechanical performance, with respect to fatigue, structural organization, and lubrication, of PCU with respect to its use in long-term implantable orthopedic device applications. In the first chapter, we motivated the need to find a solution to make total joint replacements (TJR) last longer to serve a growing patient population with increasing demands on the device performance. Using an alternative, more compliant material, like the elastomeric PCU, was proposed as a potential solution to the leading challenge of wear related failures in TJR. In addition to wear performance, TJR applications also require high fatigue performance of a material.

In the second chapter we study the impact of loading, frequency, hydration, and thermal annealing on the mechanisms of fatigue crack growth in PCU. We found that the mechanisms of fatigue crack growth in PCU are highly time-dependent and impacted by hydration. A brittle failure mechanism was induced when samples were unloaded and allowed to relax compared to those continuously loaded. Testing at higher frequencies led to the formation of multiple crack tips, less crazing, and out of plane crack growth. Hydration led to more ductile behavior and less crazing. Each of these mechanisms points to a strong dependence on the organization of the material at the crack tip. With hydration, disrupted order in the hard domains led to a much different response than with more order in the dry condition. Similarly, the brittle failure points to a time-dependent reorganization of the structure in the highly stressed process zone ahead of the crack tip that strongly influences the fracture behavior. Clinically, the highly complex behavior of fatigue crack growth in PCU may lead to challenges in predicting failure. The *in vivo* performance of PCU under highly variable loading, in magnitude, direction, and rate, could lead to unpredictable fatigue failures. Therefore, more work is needed to understand the clinical relevance of these mechanisms and work to understand the structural mechanisms in PCU that are controlling the crack growth and fracture behavior.

In Chapter 3, we sought to test the hypothesis that the time dependent failure behavior was related to the changing structural organization of PCU. To do so, we used differential scanning calorimetry (DSC), Fourier transform infrared spectroscopy (FTIR), and small an-

gle X-ray scattering (SAXS) to investigate the structural organization of PCU as a function of annealing temperature and applied strain. We found that annealing significantly changed the tensile mechanical response of the material. Based on indirect measures of hydrogen bonding from DSC and FTIR, increasing annealing corresponded with increasing order in the hard domain and, from tensile testing, increasing ductility in the material. This trend was reversed with increasing strain, showing a decrease in hydrogen bonding with increasing strain. A lack of resolution in the indirect DSC and FTIR measurements and in SAXS was limited to resolve differences within very large changes in uniaxial strain. Therefore, it is unlikely that more subtle changes in response to fatigue at a highly concentrated and constrained stress state, like that at the crack tip, would be resolved. Without the ability to directly measure the structural shifts, further fatigue characterization becomes more important to design against fatigue and fracture in implant applications.

In the fourth chapter we revisit the hypothesized wear improvements of more compliant materials, like PCU, in total hip replacements. Early elastohydrodynamic lubrication (EHL) models, that assumed 1D-steady state loading, predicted improved lubrication regimes in materials with lower moduli than the current standard UHMWPE. However, *in vitro* wear simulation studies did not show as significant a benefit as predicted. We applied a 3D-transient lubrication model to PCU hip implants to investigate the disconnect between the model and the experimental studies. In contrast to previous studies, we predicted a lower minimum lubricant film thickness in PCU compared to UHMWPE, suggesting a less optimistic wear performance. This finding aligns better with what has been reported in experimental studies and early clinical case studies.

5.1 Future Work

This thesis highlighted the complex mechanical response of PCU with respect to its use in implantable medical devices. Due to the complex behavior that was observed, further work is encouraged to better understand the potential clinical implications of what was observed.

5.1.1 Fatigue

Future work should aim to explore the time dependent impact on the fatigue crack growth mechanisms in PCU. Most importantly, we recommend looking at the limits of the brittle fracture transition following unloading. We observed this only after a certain crack lengths. For example brittle fracture was not observed upon reloading after the first day at very low crack lengths. Only after 2 - 3 relaxation cycles was brittle fracture observed. As the crack grows, the plastic zone grows in front of the crack tip. Therefore, we hypothesize that there is a critical size of process zone where the material undergoes structural changes to induce

this behavior.

The next steps would be to also look at relaxation periods more regularly interspersed in testing. Rather than unloading overnight, the test could be intermittently stopped for a given period of time at regular intervals to look at the interaction between relaxation, crack growth rate, and crack growth mechanisms.

In line with time-dependent impact on fatigue performance of PCU, creep effects should also be studied. Especially at slow physiologically relevant frequencies (0.5 - 2 Hz), the contribution of creep relative to fatigue should be investigated. This could be done with static creep studies of the same compact tension geometry, through different loading curves (i.e. square waves with different hold times, or looking at the relative contribution of K_{max} versus ΔK on crack growth.

Moving forward, for clinical applications, the impact of temperature should also be considered with hydrated testing at 37°C. Additionally, studies of the softer grades of Bionate®, such as 80A should be investigated.

5.1.2 PCU Structure-Function Relationships

In order to study the two-way relationship between structural organization and the mechanical properties of PCU, and the relationship between applied strain and the structural organization of PCU, alternative methods should be established to probe the structure of PCU. DSC and FTIR do not provide direct measures of structure and the resolution is not good enough to differentiate subtle changes. Moving forward, direct measurements with 2D-SAXS would allow for direct quantification of structures [123].

Beyond directly establishing relationships between structure and function in PCU for clinical applications, it is important to consider the potential impact of structural changes as a result of processes known to occur in a medical implant. For example, making sure that end use characterizations are done with consideration of all thermal processes that the device would undergo post molding, such as sterilization, that could change the structural organization. Similarly, characterizing changes in the mechanical properties following high-cycle loading would also indirectly study any potential structural changes induced in the material.

5.1.3 Lubrication Modeling

Future work in EHL modeling of PCU in hip implants will seek to validate the current model by comparing to clinical geometries that have previously been published for UHMWPE (28

mm radius) [161, 68] and PCU [68]. We modeled the smallest clinically available geometry of a PCU acetabular cup. The largest size should also be modeled to understand the impact of cup radius on the lubrication thickness predictions. Additionally, the Tribofit® PCU acetabular cup is indicated for implantation with or without a metal backing. Our finite element models predicted a significant influence on the material deformation between a cup with rigid backing (i.e. metal backed) or a cup with a foundation with generalized material properties for bone. Therefore, the impact of foregoing the metal backing on the lubrication performance could be evaluated.

This study compared the clinically available PCU acetabular cup to the clinical standard, UHMWPE. One of the attributes of PCU's is their 'tuneable' modulus. Therefore, a parametric study of varying the modulus within the range available for PCU (20 - 1000 MPa) could look at potential designs that could optimize the modulus for lubrication properties. It is possible that this current material modulus is too low and an optimum solution is somewhere between Bionate® 80A and UHMWPE. In such a parameterized design study, the cup thickness, radius, and femoral head clearance should also be considered.

One major limitation of this study is the assumption of a linear elastic material model for PCU, a highly nonlinear and viscoelastic material. Recent studies have incorporated viscoelastic material properties into the EHL model [161, 162]. They have found that the viscoelastic response reduced the minimum film thickness in certain applications. Many finite element studies have included the nonlinear hyperelasticity of PCU. As a rubber-like elastomer, PCU is commonly modeled using the Mooney-Rivlin constitutive model for hyperelasticity. The Mooney-Rivlin model gives the stain energy density (W) as a function of the strain invariants ($\bar{I}_1$, $\bar{I}_2$, $\bar{I}_3$). Different model fits utilize from 2 to 9 model coefficients. Most commonly, a two parameter model (C_{10} and C_{01}) is used for PCU using only the first two strain invariants (Equation 5.1).

$$W = C_{10}(\bar{I}_1 - 3) + C_{01}(\bar{I}_2 - 3) \tag{5.1}$$

The Mooney-Rivlin constitutive model for rubber elastomers has been widely applied to finite element modeling of PCU in biomedical devices [93, 118, 87, 58]. Three studies reference the manufacturer for a two term Mooney-Rivlin model using $C_{10} = 2.912$ and $C_{01} = -1.025$ [118, 87, 93], while Ghaill et al. published different parameters for a 2 and 3-term model fit [58]. This model captures the nonlinear stress strain relationship of PCU, but does not capture the time dependent viscoelastic behavior of PCU. Work by Beckmann et al. captured both the hyperelasticity of PCU and the viscoelastic relaxation and creep of the material with the Yeoh model of hyperelasticity and the Bergström-Boyce model through a parallel rheological framework in ABAQUS [64].

Future work should focus on implementing a more accurate constitutive model for PCU. Both the nonlinear and viscoelastic material response are important for accurately predicting the lubrication regime which is dominated by the elastic deformation.

5.2 Summary

PCU has been proposed as a novel biomaterial for use in load bearing applications, like orthopedics. Due to the highly complex and dynamic structural organization of PCU, the mechanical performance of the material is similarly nuanced. This poses many challenges to predicting the long-term performance of this material *in vivo*. This thesis characterizes elements of the fatigue, fracture, and wear performance of PCU. Looking toward clinical applications, work should continue to understand the consequences of the complex mechanical behavior of PCU on device performance.

Bibliography

[1] Mow, V. C., Holmes, M. H., and Lai, W. M., 1984. "Fluid transport and mechanical properties of articular cartilage: A review". *Jounal of Biomechanics,* **17**(5), pp. 377–394.

[2] O'Connell, G., Garcia, J., and Amir, J., 2017. "3D Bioprinting: New Directions in Articular Cartilage Tissue Engineering". *ACS Biomaterials Science and Engineering.*

[3] Basalo, I., Chen, F., Hung, C., and Ateshian, G., 2006. "Frictional response of bovine articular cartilage under creep loading following proteoglycan digestion with chondroitinase ABC". *Journal of Biomechanical Engineering,* **128**(1), pp. 131–134.

[4] Bhardwaj, N., Devi, D., and Mandal, B. B., 2015. "Tissue-Engineered Cartilage : The Crossroads of Biomaterials , Cells and Stimulating Factors". *Macromolecular Bioscience,* **15**, pp. 153–182.

[5] Setton, L. A., Elliot, D. M., and Mow, V. C., 1999. "Altered mechanics of cartilage with osteoarthritis : human osteoarthritis and an experimental model of joint degeneration". *Osteoarthritis and Cartilage,* **7**, pp. 2–14.

[6] Whatley, B. R., and Wen, X., 2012. "Intervertebral disc (IVD): Structure , degeneration , repair and regeneration". *Materials Science & Engineering C,* **32**, pp. 61–77.

[7] Roughley, P. J., 2004. "Biology of Intervertebral Disc Aging and Degeneration Involvement of the Extracellular Matrix". *Spine,* **29**(23), pp. 2691–2699.

[8] Newell, N., Little, J., Christou, A., Adams, M., Adam, C., and Masouros, S., 2017. "Biomechanics of the human intervertebral disc: A review of testing techniques and results". *Journal of the mechanical behavior of biomedical materials,* **69**, pp. 420–434.

[9] Arden, N., and Nevitt, M. C., 2006. "Osteoarthritis : Epidemiology". *Best Practice & Research Clinical Rheumatology,* **20**(1), pp. 3–25.

[10] Pruitt, L., and Chakravartula, A., 2011. *Mechanics of Biomaterials: Fundamentals for Implant Design*, 1 ed. Cambridge University Press, New York.

[11] Helmick, C. G., Felson, D. T., Lawrence, R. C., Gabriel, S., Hirsch, R., Kwoh, C. K., Liang, M. H., Kremers, H. M., Mayes, M. D., Merkel, P. A., Pillemer, S. R., and Reveille, J. D., 2008. "Estimates of the Prevalence of Arthritis and Other Rheumatic Conditions in the United States Part I". *Arthritis and Rheumatism,* **58**(1), pp. 15–25.

[12] Kurtz, S. M., Ong, K. L., Lau, E., and Bozic, K. J., 2014. "Impact of the economic downturn on total joint replacement demand in the united states: updated projections to 2021". *JBJS,* **96**(8), pp. 624–630.

[13] Kurtz, S. M., Lau, E., Ong, K., Zhao, K., Kelly, M., and Bozic, K. J., 2009. "Future young patient demand for primary and revision joint replacement: National projections from 2010 to 2030". *Clinical Orthopaedics and Related Research,* **467**(10), pp. 2606–2612.

[14] Sonntag, R., Reinders, J., and Kretzer, J. P., 2012. "What's next? Alternative materials for articulation in total joint replacement". *Acta Biomaterialia,* **8**(7), pp. 2434–2441.

[15] Kurtz, S. M., 2004. *The UHMWPE handbook: ultra-high molecular weight polyethylene in total joint replacement*. Academic press.

[16] Chevalier, J., and Gremillard, L., 2009. "Ceramics for medical applications: A picture for the next 20 years". *Journal of the European Ceramic Society,* **29**(7), pp. 1245 – 1255. Special Issue on Advanced Materials.

[17] Bartel, D., Wright, T., and Burstein, A., 1986. "Stresses in polyethylene components for total joint replacement". *Symposion Ultrahochmolekulares Polyethylen (UHMWPE) als Biomaterial,* **14**.

[18] , 2018. "Biological evaluation of medical devices". *ISO Standard,* **ISO10993**.

[19] Smith, R. A., and Hallab, N. J., 2009. "In vitro macrophage response to polyethylene and polycarbonate-urethane particles". *Journal of Biomedical Materials Research - Part A,* **93**(1), pp. 347–355.

[20] Clarke, I. C., Lazennec, J. Y., Smith, E. J., Sugano, N., McEntire, B. J., and Pezzotti, G., 2016. "Ceramic-on-ceramic bearings: Simulator wear compared to clinical retrieval data". In *Materials for Total Joint Arthroplasty: Biotribology of Potential Bearings*. World Scientific, pp. 85–131.

[21] Amanatullah, D. F., Sucher, M. G., Bonadurer, G. F., Pereira, G. C., and Taunton, M. J., 2016. "Metal in total hip arthroplasty: Wear particles, biology, and diagnosis". *Orthopedics,* **39**(6), pp. 371–379.

[22] Silverman, E. J., Ashley, B., and Sheth, N. P., 2016. "Metal-on-metal total hip arthroplasty: is there still a role in 2016?". *Current Reviews in Musculoskeletal Medicine,* **9**(1), Mar, pp. 93–96.

[23] Willert, H., Bertram, H., and Buchhorn, G., 1990. "Osteolysis in alloarthroplasty of the hip. the role of ultra-high molecular weight polyethylene wear particles". *Clinical Orthopaedics and Related Research*(258), September, p. 95107.

[24] Goodman, S. B., Ma, T., Chiu, R., Ramachandran, R., and Smith, R. L., 2006. "Effects of orthopaedic wear particles on osteoprogenitor cells". *Biomaterials,* **27**(36), pp. 6096 – 6101. Biomaterials and Stem Cells.

[25] Jacobs, J. J., Hallab, N. J., Urban, R. M., and Wimmer, M. A., 2006. "Wear particles". *JBJS,* **88**, pp. 99–102.

[26] Hangody, L., Dobos, J., Baló, E., Pánics, G., Hangody, L. R., and Berkes, I., 2010. "Clinical experiences with autologous osteochondral mosaicplasty in an athletic population: a 17-year prospective multicenter study". *The American journal of sports medicine,* **38**(6), pp. 1125–1133.

[27] Bentley, G., Biant, L., Carrington, R., Akmal, M., Goldberg, A., Williams, A., Skinner, J., and Pringle, J., 2003. "A prospective, randomised comparison of autologous chondrocyte implantation versus mosaicplasty for osteochondral defects in the knee". *The Journal of bone and joint surgery. British volume,* **85**(2), pp. 223–230.

[28] Magnussen, R. A., Dunn, W. R., Carey, J. L., and Spindler, K. P., 2008. "Treatment of focal articular cartilage defects in the knee". *Clinical orthopaedics and related research,* **466**(4), pp. 952–962.

[29] Erickson, B. J., Locker, P. H., Cvetanovich, G. L., Tilton, A. K., Gitelis, M. E., Weber, A. E., Yanke, A. B., and Cole, B. J., 2017. "Prospective clinical outcomes following microfracture surgery for isolated and multi-site defects: Mid-term follow-up". *Orthopaedic Journal of Sports Medicine,* **5**(7_suppl6), p. 2325967117S00340.

[30] Mithoefer, K., McAdams, T., Williams, R. J., Kreuz, P. C., and Mandelbaum, B. R., 2009. "Clinical efficacy of the microfracture technique for articular cartilage repair in the knee: An evidence-based systematic analysis". *The American Journal of Sports Medicine,* **37**(10), pp. 2053–2063. PMID: 19251676.

[31] O'Connell, G., Lima, E. G., Bian, L., Chahine, N. O., Albro, M. B., Cook, J. L., Ateschian, G. A., and Hung, C. T., 2012. "Toward engineering a biological joint replacement". *Jounal of Knee Surgery,* **25**(3), pp. 187–196.

[32] Bhumiratana, S., Eton, R. E., Oungoulian, S. R., Wan, L. Q., and Ateshian, G. A., 2014. "Large , stratified , and mechanically functional human cartilage grown in vitro by mesenchymal condensation". *PNAS,* **111**(19), pp. 6940–6945.

[33] Bian, L., Angione, S. L., Ng, K. W., Lima, E. G., Williams, D. Y., Mao, D. Q., Ateshian, G. A., and Hung, C. T., 2009. "Influence of decreasing nutrient path length on the development of engineered cartilage". *Osteoarthritis and Cartilage,* **17**, pp. 677–685.

[34] Nims, R. J., Cigan, A. D., Durney, K. M., Jones, B. K., O'Neill, J. D., Law, W.-S. A., Vunjak-Novakovic, G., Hung, C. T.-h., and Ateshian, G. A., 2017. "Constrained cage culture improves engineered cartilage functional properties by enhancing collagen network stability". *Tissue Engineering Part A*, p. ten.TEA.2016.0467.

[35] Ford, A., Chui, W., Zeng, A., Nandy, A., Lindenburg, E., Carraro, C., Kazakia, G., Alliston, T., and O'Connell, G., 2018. "A modular approach to creating large engineered cartilage surfaces". *Journal of Biomechanics,* **67**, pp. 177–183.

[36] Huang, B. J., Hu, J. C., and Athanasiou, K. A., 2016. "Cell-based tissue engineering strategies used in the clinical repair of articular cartilage". *Biomaterials,* **98**, pp. 1–22.

[37] Atwood, S. A., Citters, D. W. V., Patten, E. W., Furmanski, J., Ries, M. D., and Pruitt, L. A., 2011. "Tradeoffs amongst fatigue , wear , and oxidation resistance of cross-linked ultra-high molecular weight polyethylene". *Journal of the Mechanical Behavior of Biomedical Materials,* **4**(7), pp. 1033–1045.

[38] Ansari, F., Ries, M. D., and Pruitt, L., 2016. "Effect of processing , sterilization and crosslinking on UHMWPE fatigue fracture and fatigue wear mechanisms in joint arthroplasty". *Journal of the Mechanical Behavior of Biomedical Materials,* **53**, pp. 329–340.

[39] Pruitt, L. A., 2005. "Deformation, yielding, fracture and fatigue behavior of conventional and highly cross-linked ultra high molecular weight polyethylene". *Biomaterials,* **26**(8), pp. 905–915.

[40] Stokes, K., and McVenes, R., 1995. "Polyurethane Elastomer Biostability". *Journal of Biomaterials Applications,* **9**, pp. 321–354.

[41] Kurtz, S. M., Siskey, R., and Reitman, M., 2010. "Accelerated aging, natural aging, and small punch testing of gamma-air sterilized polycarbonate urethane acetabular components". *Journal of Biomedical Materials Research - Part B Applied Biomaterials,* **93**(2), pp. 442–447.

[42] Howard, G. T., 2002. "Biodegradation of polyurethane: A review". *International Biodeterioration and Biodegradation,* **49**(4), pp. 245–252.

[43] Christenson, E. M., Anderson, J. M., and Hiltner, A., 2007. "Biodegradation mechanisms of polyurethane elastomers". *Corrosion Engineering, Science and Technology,* **42**(4), pp. 312–323.

[44] Santerre, J. P., Woodhouse, K., Laroche, G., and Labow, R. S., 2005. "Understanding the biodegradation of polyurethanes: From classical implants to tissue engineering materials". *Biomaterials,* **26**(35), pp. 7457–7470.

[45] Tanzi, M. C., Mantovani, D., Petrini, P., Guidoin, R., and Laroche, G., 1997. "Chemical stability of polyether urethanes versus polycarbonate urethanes". *Journal of Biomedical Materials Research,* **36**(4), pp. 550–559.

[46] Tanzi, C. M., Fare, S., and Petrini, P., 2000. "In vitro stability of polyether and polycarbonate urethanes". *Journal of Biomaterials Applications,* **14**, pp. 325–348.

[47] Khan, I., Smith, N., Jones, E., Finch, D. S., and Cameron, R. E., 2005. "Analysis and evaluation of a biomedical polycarbonate urethane tested in an in vitro study and an ovine arthroplasty model. Part I: Materials selection and evaluation". *Biomaterials,* **26**(6), pp. 621–631.

[48] Chandy, T., Van Hee, J., Nettekoven, W., and Johnson, J., 2009. "Long-term in vitro stability assessment of polycarbonate urethane micro catheters: Resistance to oxidation and stress cracking". *Journal of Biomedical Materials Research - Part B Applied Biomaterials,* **89**(2), pp. 314–324.

[49] Christenson, E. M., Dadsetan, M., Wiggins, M., Anderson, J. M., and Hiltner, A., 2004. "Poly(carbonate urethane) and poly(ether urethane) biodegradation:In vivo studies". *Journal of Biomedical Materials Research,* **69A**(3), pp. 407–416.

[50] Wiggins, M. J., MacEwan, M., Anderson, J. M., and Hiltner, A., 2004. "Effect of soft-segment chemistry on polyurethane biostability during in vitro fatigue loading.". *Journal of biomedical materials research. Part A,* **68**, pp. 668–683.

[51] Eceiza, A., Martin, M., de la Caba, K., Kortaberria, G., Gabilondo, N., Corcuera, M., and Mondragon, I., 2008. "Thermoplastic Polyurethane Elastomers Based on Polycarbonate Diols With Different Soft Segment Molecular Weight and Chemical Structure: Mechanical and Thermal Properties". *Polymer engineering and Science,* **10**, pp. 297–306.

[52] Guo, J., Zhao, M., Ti, Y., and Wang, B., 2007. "Study on structure and performance of polycarbonate urethane synthesized via different copolymerization methods". *Journal of Materials Science,* **42**, pp. 5508–5515.

[53] Martin, D. J., Meijs, G. F., Gunatillake, R. A., and McCarthy, S. J., 1997. "The effect of average soft segment length on morphology and properties of a series of polyurethane elastomers. ii. saxs-dsc annealing study". *Journal of Applied Polymer Science,* **64**, pp. 803–817.

[54] Cipriani, E., Zanetti, M., Brunella, V., Costa, L., and Bracco, P., 2012. "Thermoplastic polyurethanes with polycarbonate soft phase: Effect of thermal treatment on phase morphology". *Polymer Degradation and Stability,* **97**(9), pp. 1794–1800.

[55] Martin, D. J., Meijs, G. F., Renwick, G. M., McCarthy, S. J., and Gunatillake, P. A., 1996. "The effect of average soft segment length on morphology and properties of a series of polyurethane elastomers. 1. characterization of the series". *Journal of Applied Polymer Science,* **62**, pp. 1377–1386.

[56] Geary, C., Birkinshaw, C., and Jones, E., 2008. "Characterisation of Bionate polycarbonate polyurethanes for orthopaedic applications". *Journal of Materials Science: Materials in Medicine,* **19**(11), pp. 3355–3363.

[57] Ford, A. C., Gramling, H., Li, S. C., Sov, J. V., Srinivasan, A., and Pruitt, L. A., 2018. "Micromechanisms of fatigue crack growth in polycarbonate polyurethane: time dependent and hydration effects". *Journal of the Mechanical Behavior of Biomedical Materials,* **79**, mar, pp. 324–331.

[58] Ghaill, N. N. A., and Little, E. G., 2008. "Determination of the mechanical properties of bionate 80a and bionate 75d for the stress analysis of cushion form bearings". *Proceedings of the Institution of Mechanical Engineers, Part H: Journal of Engineering in Medicine,* **222**(5), may, pp. 683–694.

[59] Kanaca, Y., 2017. "Tribological testing of potential hemiarthoplasty materials using a custom-designed multi-directional reciprocating rig". PhD thesis, Imperial College London.

[60] Khan, I., Smith, N., Jones, E., Finch, D. S., and Cameron, R. E., 2005. "Analysis and evaluation of a biomedical polycarbonate urethane tested in an in vitro study and an ovine arthroplasty model. Part II: In vivo investigation". *Biomaterials,* **26**(6), pp. 621–631.

[61] Gramling, H., Srinivasan, A., and Pruitt, L., 2015. "Mechanical characterization and a computational wear model for polycarbonate urethane as a bearing material". In Summer Biomechanics, Bioengineering, and Biotransport Conference.

[62] Xu, L. C., Runt, J., and Siedlecki, C. A., 2010. "Dynamics of hydrated polyurethane biomaterials: Surface microphase restructuring, protein activity and platelet adhesion". *Acta Biomaterialia,* **6**(6), pp. 1938–1947.

[63] Lawless, B. M., Barnes, S. C., Espino, D. M., and Shepard, D. E., 2016. "Viscoelastic properties of a spinal posterior dynamic stabilisation device". *Jounal of the Mechanical Behavior of Biomedical Materials,* **59**, pp. 519–526.

[64] Beckmann, A., Heider, Y., Stoffel, M., and Markert, B., 2018. "Assessment of the viscoelastic mechancial properties of polycarbonate urethane for medical devices". *Journal of the Mechanical Behavior of Biomedical Materials,* **82**, pp. 1–8.

[65] Shemesh, M., Asher, R., Zylberberg, E., Guilak, F., Linder-Ganz, E., and Elsner, J. J., 2014. "Viscoelastic properties of synthetic meniscus implant". *Journal of the Mechanical Behavior of Biomedical Materials,* **29**, pp. 42–55.

[66] Benzel, E. C., Lieberman, I. H., Ross, E. R., Linovitz, R. J., Kuras, J., and Zimmers, K., 2011. "Mechanical characterization of a viscoelastic disc for lumbar total disc replacement". *Journal of Medical Devices,* **5**(1), p. 011005.

[67] Flanagan, S., 2010. "Friction, lubrication and wear of total joint replacements". PhD thesis, University of Limerick.

[68] Wang, F., Liu, F., and Jin, Z., 2004. "A general elastohydrodynamic lubrication analysis of and artificial hip joints employing a compliant layered and socket under steady state rotation". *Proc. Instn Mech Engrs Part H: Jounal of Engineering in Medicine,* **218**, pp. 283–291.

[69] , 2008. Tribofit acetabular buffer: Design rationale, training manual. online. Active Implants Corporation.

[70] Elsner, J. J., Mezape, Y., Hakshur, K., Shemesh, M., Linder-Ganz, E., Shterling, A., and Eliaz, N., 2010. "Wear rate evaluation of a novel polycarbonate-urethane cushion form bearing for artificial hip joints". *Acta Biomaterialia,* **6**(12), pp. 4698–4707.

[71] Elsner, J. J., Shemesh, M., Mezape, Y., Levenshtein, M., Hakshur, K., Shterling, A., Linder-Ganz, E., and Eliaz, N., 2011. "Long-term evaluation of a compliant cushion form acetabular bearing for hip joint replacement: A 20 million cycles wear simulation". *Journal of Orthopaedic Research,* **29**(12), pp. 1859–1866.

[72] St. John, K., and Gupta, M., 2012. "Evaluation of the wear performance of a polycarbonate-urethane acetabular component in a hip joint simulator and comparison with UHMWPE and cross-linked UHMWPE". *Journal of Biomaterials Applications,* **27**(1), pp. 55–65.

[73] Scholes, S. C., Burgess, I. C., Marsden, H. R., Unsworth, A., Jones, E., and Smith, N., 2006. "Compliant layer acetabular cups: Friction testing of a range of materials and designs for a new generation of prosthesis that mimics the natural joint". *Proceedings of the Institution of Mechanical Engineers, Part H: Journal of Engineering in Medicine,* **220**(5), may, pp. 583–596.

[74] Dowson, D., Fischer, J., Jin, Z., Auger, D., and Jobbins, B., 1991. "Design considerations for cushino form bearing in artificial hip joints". *Journal of Engineering in Medicine,* **205**, pp. 59–68.

[75] Auger, D., Dowson, D., Fisher, J., and Jin, Z., 1993. "Friction and lubrication in cushion form bearings for artificial hip joints". *Proceedings of the Institution of Mechanical Engineers, Part H: Journal of Engineering in Medicine,* **207**(1), pp. 25–33.

[76] Siebert, W. E., Mai, S., and Kurtz, S., 2008. "Retrieval analysis of a polycarbonate-urethane acetabular cup: a case report.". *Journal of long-term effects of medical implants,* **18**(1), pp. 69–74.

[77] Wippermann, B., Kurtz, S., Hallab, N., and Treharne, R., 2008. "Explantation and analysis of the first retrieved human acetabular cup made of polycarbonate urethane: a case report". *Journal of long-term effects of medical implants,* **18**(1), pp. 75–83.

[78] Ianuzzi, A., Kurtz, S. M., Kane, W., Shah, P., Siskey, R., van Ooij, A., Bindal, R., Ross, R., Lanman, T., Büttner-Janz, K., and Isaza, J., 2010. "In vivo deformation, surface damage, and biostability of retrieved Dynesys systems.". *Spine,* **35**(23), pp. E1310–E1316.

[79] Cipriani, E., Bracco, P., Kurtz, S. M., Costa, L., and Zanetti, M., 2013. "In-vivo degradation of poly(carbonate-urethane) based spine implants". *Polymer Degradation and Stability,* **98**(6), pp. 1225–1235.

[80] St. John, K. R., 2014. "The use of polyurethane materials in the surgery of the spine: A review". *Spine Journal,* **14**(12), pp. 3038–3047.

[81] Anderson, P. a., Rouleau, J. P., Bryan, V. E., and Carlson, C. S., 2003. "Wear analysis of the Bryan Cervical Disc prosthesis.". *Spine,* **28**(20), pp. S186–S194.

[82] Cao, J.-m., Zhang, Y.-z., Shen, Y., and Ding, W.-y., 2010. "Complications of Bryan cervical disc replacement.". *Orthopaedic surgery,* **2**(2), pp. 86–93.

[83] Inc., D. B., 2012. "Bionate (r) thermoplastic polycarbonate polyurethane (pcu)". *Product Data Sheet*.

[84] Luo, Y., McCann, L., Ingham, E., Jin, Z.-M., Ge, S., and Fisher, J., 2009. "Polyurethane as a potential knee hemiarthroplasty biomaterial: An in-vitro simulation of its tribological performance". *Proceedings of the Institution of Mechanical Engineers, Part H: Journal of Engineering in Medicine,* **224**, pp. 415–425.

[85] Kretzer, J. P., Jakubowitz, E., Reinders, J., Lietz, E., Moradi, B., Hofmann, K., and Sonntag, R., 2011. "Wear analysis of unicondylar mobile bearing and fixed bearing knee systems: A knee simulator study". *Acta Biomaterialia,* **7**, pp. 710–715.

[86] Kanca, Y., Milner, P., Dini, D., and Amis, A. A., 2018. "Tribological evaluation of biomedical polycarbonate urethanes against articular cartilage". *Journal of the Mechanical Behavior of Biomedical Materials,* **82**, jun, pp. 394–402.

[87] Elsner, J. J., Eliaz, N., and Linder-Ganz, E., 2016. "The use of polyurethanes in joint replacement". *Materials for Total Joint Arthroplasty: Biotribology of Potential Bearings*, pp. 259–298.

[88] Carbone, A., Howie, D. W., Mcgee, M., Field, J., Pearcy, M., Biomed, C., Smith, N., and Jones, E., 2006. "Aging Performance of a Compliant Layer Bearing Acetabular Prosthesis in an Ovine Hip Arthroplasty Model". *The Journal of Arthroplasty,* **21**(6).

[89] Biant, L. C., Gascoyne, T. C., Bohm, E. R. ., and Moran, M., 2016. "Retrieval analysis of a failed TriboFit polycarbonate urethane acetabular buffer". *Proceedings of the Institution of Mechanical Engineers, Part H: Journal of Engineering in Medicine,* **230**(3), feb, pp. 251–256.

[90] Giannini, S., Chiarello, E., Cadossi, M., Luciani, D., and Tedesco, G., 2011. "Prosthetic surgery in fragility ostopathy". *Aging Clinical and Experimental Reserach,* **23**(2), pp. 40–42.

[91] Moroni, A., Nocco, E., Hoque, M., Diremigio, E., Buffoli, D., Cantù, F., Catalani, S., and Apostoli, P., 2011. "Cushion bearings versus large diameter head metal-on-metal bearings in total hip arthroplasty: a short-term metal ion study". *Archives of Orthopaedic and Trauma Surgery,* **132**(1), aug, pp. 123–129.

[92] Cadossi, M., Chiarello, E., Savarino, L., Tedesco, G., Baldini, N., Faldini, C., and Giannini, S., 2013. "A comparison of hemiarthroplasty with a novel polycarbonate-urethane acetabular component for displaced intracapsular fractures of the femoral neck". *Bone and Joint Journal,* **95**(B), pp. 509–515.

[93] Elsner, J. J., Portnoy, S., Zur, G., Guilak, F., Shterling, A., and Linder-Ganz, E., 2010. "Design of a free-floating polycarbonate-urethane meniscal implant using finite element modeling and experimental validation". *Journal of Biomechanical Engineering,* **132**(9), p. 095001.

[94] Vrancken, A. C., Hannink, G., Madej, W., Verdonschot, N., van Tienen, T. G., and Buma, P., 2017. "In vivo performance of a novel, anatomically shaped, total meniscal prosthesis made of polycarbonate urethane: a 12-month evaluation in goats". *The American Journal of Sports Medicine,* **45**(12), jul, pp. 2824–2834.

[95] Linder-Ganz, E., Elsner, J. J., Danino, A., Guilak, F., and Shterling, A., 2010. "A novel quantitative approach for evaluating contact mechanics of meniscal replacements". *Journal of biomechanical engineering,* **132**(2), p. 024501.

[96] Zur, G., Linder-Ganz, E., Elsner, J. J., Shani, J., Brenner, O., Agar, G., Hershman, E. B., Arnoczky, S. P., Guilak, F., and Shterling, A., 2010. "Chondroprotective effects of a polycarbonate-urethane meniscal implant: histopathological results in a sheep model". *Knee Surgery, Sports Traumatology, Arthroscopy,* **19**(2), jul, pp. 255–263.

[97] Kurtz, S. M., Steinbeck, M., Ianuzzi, A., van Ooij, A., Punt, I. M., Isaza, J., and Ross, E., 2009. "Retrieval analysis of motion preserving spinal devices and periprosthetic tissues". *SAS Journal,* **3**(4), pp. 161–177.

[98] Anderson, P. a., Sasso, R. C., Rouleau, J. P., Carlson, C. S., and Goffin, J., 2004. "The Bryan Cervical Disc: wear properties and early clinical results.". *The spine journal : official journal of the North American Spine Society,* **4**(6 Suppl), pp. 303S–309S.

[99] Fan, H., Wu, S., Wu, Z., Wang, Z., and Guo, Z., 2012. "Implant failure of Bryan cervical disc due to broken polyurethane sheath: a case report.". *Spine,* **37**(13), pp. E814—-6.

[100] Lazennec, J. Y., Aaron, A., Brusson, A., Rakover, J. P., and Rousseau, M. A., 2013. "The LP-ESP?? lumbar disc prosthesis with 6 degrees of freedom: Development and 7 years of clinical experience". *European Journal of Orthopaedic Surgery and Traumatology,* **23**(2), pp. 131–143.

[101] Furmanski, J., Anderson, M., Bal, S., Greenwald, A. S., Halley, D., Penenberg, B., Ries, M., and Pruitt, L., 2009. "Clinical fracture of cross-linked uhmwpe acetabular liners". *Biomaterials,* **30**(29), pp. 5572–5582.

[102] Anderson, T., 2005. "Linear elastic fracture mechanics". *Fracture Mechanics. Fundamentals and Applications*, pp. 31–96.

[103] Hertzberg, R. W., and Manson, J. A., 1980. *Fatigue of Engineering Plastics*. Academic press.

[104] Connelly, G., Rimnac, C., Wright, T., Hertzberg, R., and Manson, J., 1984. "Fatigue crack propagation behavior of ultrahigh molecular weight polyethylene". *Journal of Orthopedic Research,* **2**, pp. 119–125.

[105] Baker, D., Bellare, A., and Pruitt, L., 2003. "The effects of degree of crosslinking on the fatigue crack initiation and propagation resistance of orthopedic-grade polyethylene". *Journal of Biomedical Materials Research Part A,* **66.1**, pp. 146–154.

[106] Baker, D., Hastings, R., and Pruitt, L., 2000. "Study of fatigue resistance of chemical and radiation crosslinked medical grade ultrahigh molecular weight polyethylene". *Journal of Biomedical Materials Research,* **46.4**, pp. 573–581.

[107] Bradford, L., Baker, D., Ries, M. D., and Pruitt, L. A., 2004. "Fatigue crack propagation resistance of highly crosslinked polyethylene". *Clinical Orthopaedics and Related Research*(429), pp. 68–72.

[108] Furmanski, J., and Pruitt, L. A., 2007. "Peak stress intensity dictates fatigue crack propagation in UHMWPE". *Polymer,* **48**(12), jun, pp. 3512–3519.

[109] Miller, A. T., Safranski, D. L., Smith, K. E., Guldberg, R. E., and Gall, K., 2016. "Compressive cyclic ratcheting and fatigue of synthetic, soft biomedical polymers in solution". *Journal of the Mechancial Behavior of Biomedical Materials,* **54**, pp. 268–282.

[110] Miller, A. T., Safranski, D. L., Wood, C., Guldberg, R. E., and Gall, K., 2017. "Deformation and fatigue of tough 3d printed elastomer scaffolds processed by fused deposition modeling and continuous liquid interface production". *Journal of the Mechanical Behavior of Biomedical Materials,* **75**, nov, pp. 1–13.

[111] Miller, A. T., Safranski, D. L., Smith, K. E., Sycks, D. G., Guldberg, R. E., and Gall, K., 2017. "Fatigue of injection molded and 3d printed polycarbonate urethane in solution". *Polymer,* **108**, jan, pp. 121–134.

[112] Wiggins, M. J., Anderson, J. M., and Hiltner, A., 2003. "Effect of strain and strain rate on fatigue-accelerated biodegradation of polyurethane.". *Journal of biomedical materials research. Part A,* **66**(3), pp. 463–475.

[113] Wiggins, M. J., Anderson, J. M., and Hiltner, A., 2003. "Biodegradation of polyurethane under fatigue loading.". *Journal of biomedical materials research. Part A,* **65**, pp. 524–535.

[114] Shibayama, M., Kawauchi, T., Kotani, T., Nomura, S., and Matsuda, T., 1986. "Structure and Properties of Fatigued Segmented Poly(urethaneurea)s I. Segment Orientation Mechanism due to Fatigue". *Polymer Journal,* **18**(10), pp. 719–733.

[115] Shibayama, M., Ohki, Y., Kotani, T., and Nomura, S., 1986. "Structure and Properties of Fatigued Segmented Poly(urethaneurea)s II. Structural Analyses of Fatigue Mechanicsm". *Polymer Journal,* **19**(9), pp. 1067–1080.

[116] Flannery, M., Jones, E., and Birkinshaw, C., 2010. "Compliant layer knee bearings. Part II: Preliminary wear assessment". *Wear,* **269**(5-6), pp. 331–338.

[117] Jones, E., Scholes, S. C., Burgess, I. C., Ash, H. E., and Unsworth, A., 2008. "Compliant layer bearings in artificial joints. Part 1: the effects of different manufacturing techniques on the interface strength between an elastomeric layer and a rigid substrate". *Proceedings of the Institution of Mechanical Engineers. Part H, Journal of engineering in medicine,* **222**, pp. 853–864.

[118] Gabarre, S., Herrera, A., Mateo, J., Ibarz, E., Lobo-escolar, A., and Gracia, L., 2014. "Study of the Polycarbonate-Urethane / Metal Contact in Different Positions during Gait Cycle". *BioMed Research International.*

[119] Majd, S. E., Kuijer, R., Schmidt, T. A., and Sharma, P. K., 2015. "Role of hydrophobicity on the adsorption of synovial fluid proteins and biolubrication of polycarbonate urethanes: Materials for permanent meniscus implants". *Materials and Design,* **83**, pp. 514–521.

[120] Jimenez, G., Asai, S., Shishido, A., and Sumita, M., 2000. "Effect of the soft segment on the fatigue behavior of segmented polyurethanes". *European Polymer Journal,* **36**, pp. 2039–2050.

[121] Smith, T. L., 1965. "Deformation and failure of plastics and elastomers". *Polymer Engineering & Science,* **5**(4), pp. 270–279.

[122] Speckhard, T. A., Gibson, P. E., Cooper, S. L., Chang, V. S. C., and Kennedy, J. P., 1985. "Properties of polyisobutylene polyurethane block copolymers: 2 macroglycols produced by the 'inifer' technique". *Polymer,* **26**(1), pp. 55–69.

[123] Kojio, K., Matsuo, K., Motokucho, S., Yoshinaga, K., Shimodaira, Y., and Kimura, K., 2001. "Simultaneous small-angle x-ray scattering/wide-angle x-ray diffraction study of the microdomain structure of polyurethane elastomers during mechanical deformation". *Polymer Journal,* **43**, pp. 692–699.

[124] Spirkova, M., Pavlicevic, J., Strachota, A., Poreba, R., Bera, O., Kapralkova, L., Baldrian, J., Slouf, M., Lazic, N., and Budinski-Simendic, J., 2011. "Novel polycarbonate-based polyurethane elastomers: Composition-property relationship". *European Polymer Journal,* **47**(5), pp. 959–972.

[125] Kimura, I., 1974. "Morphology and Deformation Mechanism of Segmented Poly(urethaneureas) in Relation to Spherulitic Crystalline Texture". *Macromolecules,* **7**(3), pp. 355–363.

[126] McLean, R. S., and Sauer, B. B., 1997. "Tapping-mode AFM studies using phase detection for resolution of nanophases in segmented polyurethanes and other block copolymers". *Macromolecules,* **30**(26), pp. 8314–8317.

[127] Callister, W., 2003. *Material Science and Engineering, an Introduction*, Vol. 6. John Wiley & Sons, Inc.

[128] Jin, Z., Dowson, D., Fisher, J., Rimmer, D., Wilkinson, R., and Jobbins, B., 1994. "Measurement of lubricating film thickness in low elastic modulus lined bearings, with particular reference to models of cushion form bearings for total joint replacements: Part 1: steady state entraining motion". *Proceedings of the Institution of Mechanical Engineers, Part J: Journal of Engineering Tribology,* **208**(3), pp. 207–212.

[129] Mattei, L., Puccio, F. D., Piccigallo, B., and Ciulli, E., 2011. "Lubrication and wear modeling of artificial hip joints: A review". *Tribology International,* **44**, pp. 532–549.

[130] Jones, E., Scholes, S. C., Burgess, I. C., Ash, H. E., and Unsworth, A., 2008. "Compliant layer bearings in artificial joints. Part 1: the effects of different manufacturing techniques on the interface strength between an elastomeric layer and a rigid substrate". *Proceedings of the Institution of Mechanical Engineers. Part H, Journal of engineering in medicine,* **222**, pp. 853–864.

[131] Scholes, S., Unsworth, A., and Jones, E., 2007. "Polyurethane unicondylar knee prostheses: simulator wear tests and lubrication studies". *Physics in Medicine and Biology,* **52**, pp. 197–212.

[132] , 2018. "Implants for surgery - wear of total hip-joint prostheses part 1: Loading and displacement parameters for wear-testing machines and corresponding environmental conditions for tests". *ISO Standard,* **ISO 14242-1**.

[133] Schwartz, C. J., and Bahadur, S., 2007. "Development and testing of a novel joint wear simulator and investigation of the viability of an elastomeric polyurethane for total-joint arthroplasty devices". *Wear,* **262**, pp. 331–339.

[134] Komvopoulos, K., 1998. "Fundamentals of tribology and contact mechanics". *Tribology Research Program, Department of Mechanical Engineering, UC Berkeley.*

[135] Archard, J., 1953. "Contact and rubbing of flat surfaces". *Journal of applied physics,* **24.8**, pp. 981–988.

[136] Wu, J. S.-S., Hung, J.-P., Shu, C.-S., and Chen, J.-H., 2003. "The computer simulation of wear behavior appearing in total hip prosthesis". *Computer Methods and Programs in Biomedicine,* **70**, pp. 81–91.

[137] Teoh, S., Chan, W., and Thampuran, R., 2002. "An elasto-plastic finite element model for polyethylene wear in total and hip arthroplasty". *Journal of Biomechanics,* **35**, pp. 323–330.

[138] Liu, F., Galvin, A., Jin, Z., and Fisher, J., 2010. "A new formulation for the prediction of polyethylene wear in artificial hip joints". *Proceedings of the Institution of Mechanical Engineers, Part H: Journal of Engineering in Medicine,* **225**, pp. 16–24.

[139] Liu, F., Fisher, J., and Jin, Z., 2012. "Computational modelling of polyethylene wear and creep in total hip joint replacements: effect of the bearing clearance and diameter". *Proceedings of the Institution of Mechanical Engineers, Part J: Journal of Engineering Tribology,* **226**(6), mar, pp. 552–563.

[140] Wang, A., Sun, D., Stark, C., and Dumbleton, J., 1995. "Wear mechanisms of uhmwpe and in total joint replacements". *Wear*(181-183), pp. 241–249.

[141] Liu, F., Leslie, I., Williams, S., Fisher, J., and Jin, Z., 2008. "Development of computational wear simulation of metal-on-metal hip resurfacing replacements". *Journal of Biomechanics,* **41**(3), pp. 686–694.

[142] Gao, L., Dowson, D., and Hewson, R. W., 2017. "Predictive wear modeling of the articulating metal-on-metal hip replacements". *Journal of Biomedical Materials Research Part B: Applied Biomaterials,* **105**(3), pp. 497–506.

[143] Gao, L., Hua, Z., and Hewson, R., 2018. "Can a "pre-worn" bearing surface geometry reduce the wear of metal-on-metal hip replacements? – a numerical wear simulation study". *Wear,* **406-407**, jul, pp. 13–21.

[144] Venner, C. H., and Lubrecht, A. A., 2000. *Multi-level methods in lubrication*, Vol. 37. Elsevier.

[145] Jalali-Vahid, D., Jagatia, M., Jin, Z., and Dowson, D., 2000. "Elastohydrodynamic lubrication analysis of uhmwpe and hip joint replacements". *Thinning Films and Tribological Interfaces*, pp. 329–339.

[146] Jin, Z., and Dowson, D., 1999. "A full numerical analysis of hydrodynamic lubrication and in artificial hip joint replacements constructed from and hard materials". *Proc Instn Mech Engrs*, pp. 355–370.

[147] Gao, L., Wang, F., Yang, P., and Jin, Z., 2009. "Effect of 3d physiological loading and motion on elastohydrodynamic lubrication of metal-on-metal total hip replacements". *Medical Engineering & Physics,* **31**(6), jul, pp. 720–729.

[148] Wang, F., and Jin, Z., 2004. "Prediction of elastic deformation of acetabular cups and femoral heads for lubrication analysis of artificial and hip joints". *Proc. Instn Mech. Engrs Part J: Journal of Engineering Tribology,* **218**, pp. 201–209.

[149] Jin, Z. M., and Dowson, D., 2005. "Elastohydrodynamic lubrication in biological systems". *Proceedings of the Institution of Mechanical Engineers, Part J: Journal of Engineering Tribology,* **219**(5), may, pp. 367–380.

[150] Jin, Z. M., Dowson, D., and Fisher, J., 1993. "Wear and friction of medical grade polyurethane sliding on smooth metal counterfaces". *Wear,* **162-164**(PART A), pp. 627–630.

[151] Moghani, T., Butler, J. P., Li-Wen Lin, J., and Loring, S. H., 2007. "Finite element simulation of elastohydrodynamic lubrication of soft biological tissues". *Computers & Structures,* **85**(11-14), jun, pp. 1114–1120.

[152] Wang, F., and Jin, Z., 2006. "Lubrication modeling of artificial hip joints". *IUTAM Symposium on Elastohydrodynamics and Microelastohydrodynamics*, pp. 385–396.

[153] Jin, Z., 2006. "Theoretical studies of elastohydrodynamic lubrication of artificial hip joints". *Proceedings of the Institution of Mechanical Engineers, Part J: Journal of Engineering Tribology,* **220**(8), aug, pp. 719–727.

[154] Dumbleton, J. H., 1981. *Tribology of natural and artificial joints*, Vol. 3. Elsevier.

[155] Liu, F., Jin, Z., Hirt, F., Rieker, C., Roberts, P., and Grigoris, P., 2006. "Transient elastohydrodynamic lubrication analysis of metal-on-metal hip implant under simulated walking conditions". *Journal of Biomechanics,* **39**, pp. 905–914.

[156] Bergmann, G., Deuretzbacher, G., Heller, M., Graichen, F., Rohlmann, A., Strauss, J., and Duda, G., 2001. "Hip contact forces and gait patterns from routine activities". *Journal of biomechanics,* **34**(7), pp. 859–871.

[157] Jalali-Vahid, D., and Jin, Z., 2002. "Transient elastohydrodynamic lubrication analysis of and ultra-high molecular weight polyethylene hip joint and replacements". *Proc. Instn Mech Engrs Part C: Journal of Mechanical Engineering Science,* **216**, pp. 409–420.

[158] Jagatia, M., and Jin, Z., 2001. "Elastohydrodynamic lubrication analysis of and metal-on-metal hip prostheses under steady state and entraining motion". *Proc. Instn Mech Engrs,* **215**, pp. 531–541.

[159] Udofia, I., and Jin, Z., 2003. "Elastohydrodynamic lubrication analysis of metal-on-metal hip-resurfacing prostheses". *Journal of Biomechanics,* **36**, pp. 537–544.

[160] Auger, D., Dowson, D., and Fisher, J., 1995. "Cushion form bearing for total knee joint replacement part 1: design, friction and lubrication". *Proc Insta Mech Engrs,* **29**, pp. 73–81.

[161] Lu, X., Meng, Q., Wang, J., and Jin, Z., 2018. "Transient viscoelastic lubrication analyses of UHMWPE hip replacements". *Tribology International,* **128**, dec, pp. 271–278.

[162] Putignano, C., and Dini, D., 2017. "Soft matter lubrication: does solid viscoelasticity matter?". *ACS applied materials & interfaces,* **9**(48), pp. 42287–42295.